Current Debates on Natural and Engineering Sciences

3

Editors

Hikmet Y. ÇOĞUN

Zeynel KARACAGİL

Contents

A Comparative Analysis of Helmholtz Principle in Extractive Automatic Document Summarization

Ahmet Toprak[1]
Metin Turan[2]

Introduction

The enormous amount of data available on the internet today has reached unpredictable volumes; therefore, it is not possible using human power in order to efficiently sift useful information from it now. The demand for automated tools that can understand, index, classify and present text documents clearly and concisely has increased greatly in recent years. One solution to this problem is to use automatic document summarization techniques. Automatic document summarization is one of the Natural Language Processing (NLP) research fields that extracts important information in an input document and is actively studied as well as machine translation. Especially, the importance of the research is increasing because digitized text data grow rapidly. Figure 1 shows the system architecture of an automatic document summarization.
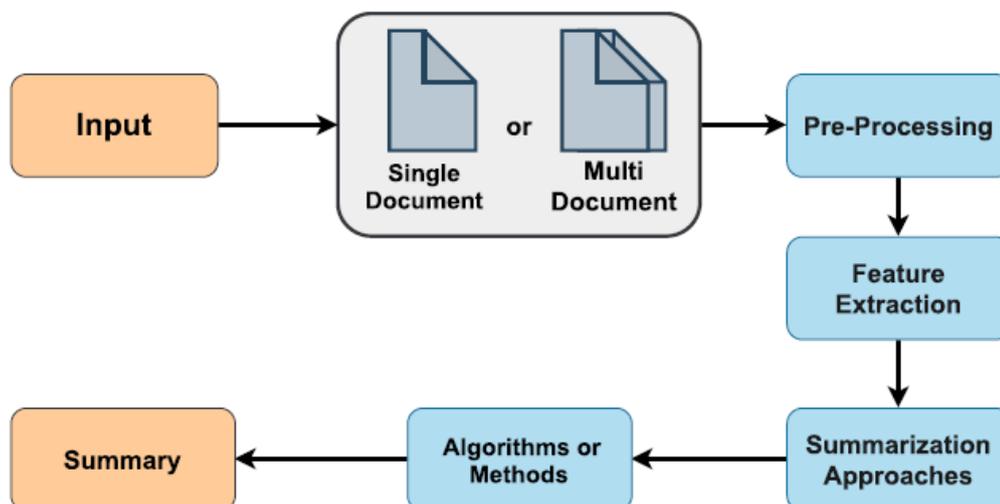
Figure 1. Automatic document summarization system architecture (Boorugu et al., 2020)

Automatic document summarization can be divided into a single-document summarization and a multi-document summarization according to the type of input data. Its details are given in Figure 2.

---

[1] Ahmet Toprak, Istanbul Commerce University, Computer Engineering
[2] Metin Turan, Istanbul Commerce University, Computer Engineering
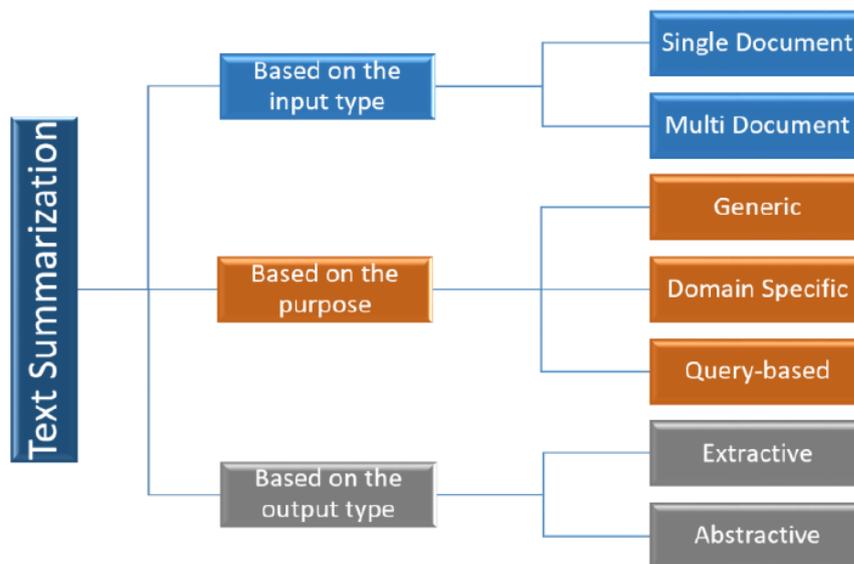
Figure 2. Text summarization types (Mridha et al., 2021)

Automatic document summarization also can be divided into extractive and abstractive summarization depending on the way of extracting important information from input data. The extractive summarization model is a model of selecting sentences according to the importance of the sentence in the input document. Abstractive summarization model is a model of generating words for the summary based on the input document. For abstractive summarization, several variant models based on the sequence-to-sequence model have been proposed (Kim et al., 2019).

In this study, a Helmholtz-based extractive summarization approach is proposed to create an automatic extractive summarization system. CNN Daily/Mail data set was used to evaluate the proposed approach. This data set includes both the original full-text documents and the summary documents of these original documents produced by human summarizers. First of all, the original documents in the data set that the user wanted to summarize were taken into the data preprocessing process. After data preprocessing, inferential summaries of the original documents were created using well-known techniques in the literature, BertSum (Bidirectional Encoder Representation from Transformer), Luhn and SumBasic, and the proposed Helmholtz principle based model. The ratio of the summary to be extracted was obtained from the division of the word count of the document in the summary in the data set to the word count of the original document. Using this ratio, the similarity of the summary document obtained from each algorithm and the original summary document in the CNN Daily/Mail data set was calculated using the Spacy text similarity algorithm. When the summary documents obtained were examined in terms of average Spacy text similarity rates, it was seen that the proposed Helmholtz principle based model achieved acceptable results. The obtained results are shared in detail in the Experiments section. The main purpose of this study is to create an automatic document summarization system without requiring human intervention on a specialized problem.

The organization of the remaining paper is as follows: In the second section, document summarization researches in literature or studies covering methods applied in this study are mentioned. In the third section, used methods in the document summarization study are explained in detail. In the last section, the results are commented on and future studies are discussed.

Literature Review

In 2009, the study by Chen et al. (Chen et al., 2009) proposes a multi-document news summary system that summarizes local news based on the need for a personal handheld PDA (Personal Digital Assistant) device based on the user's location. The proposed system has an automatic news summary based on the mean k-NN (k-Nearest Neighbors) classifier. According to the experimental results in multi-document summary and user location determination, a success rate of up to 86% in news summary and up to 90% in the accuracy of user location awareness scheme has been achieved. In addition, the proposed average k-NN classifier for determining a user's location in the Taiwan region has better results than the four machine learning schemes tested in this study (BP neural networks, naïve Bayesian classifier, Lin's support vector machine (LIBSVM), and original k-NN classifier). production is emphasized. The experimental results indicate that the proposed system can be successfully applied in real-world applications for personalized location-based news services.

In 2014, the study by Pal et al. (Pal et al., 2014), the text summarization method with unsupervised learning-based Simplified Lesk algorithm is proposed. The importance of a sentence in a text to be summarized is evaluated with the help of the Simplified Lesk algorithm. WordNet is used as an online dictionary of meanings. With the proposed approach, all sentences of a text are weighted separately using the Simplified Lesk algorithm and sorted in descending order of weight. Then, a certain number of sentences are selected from this ordered list, according to the given summarization percentage. When the results were examined, the recommended approach gives the best results in summarizing up to 50% of the original text. It is also stated that it achieves satisfactory results even when summarizing up to 25% of the original text.

In 2016, the study by Alsaedi et al. (Alsaedi et al., 2016) proposed a method to summarize microblogging documents by selecting the most representative posts for real-world events (clusters). The study noted that in recent years there has been an increased interest in real-world event summary using data that is publicly available through social networking services such as Twitter and Facebook, and people use these channels to communicate with others, express their opinions, and comment on a wide variety of real-world events. In this study, three techniques (Temporal TF-IDF, Retweet Voting Approach, Temporal Centroid Method) are presented to summarize microblogging documents. Temporal TF-IDF is based on subtracting the highest weighted terms determined by TF-IDF (Term Frequency–Inverse Document Frequency) weighting for two consecutive periods. Retweet Voting Approach considers the highest number of retweets received on a post in a given time as the criterion for finding the most representative post in a single time. This method reflects users' choices when deciding which message is the most "valuable". The Temporal Centroid Method selects the posts corresponding to each cluster centroid as the summary of that cluster according to the time dimension. The abstracts produced were compared to both human-generated abstracts and the summary results of similar leading abstraction systems. Rouge-1 was used to evaluate the summary text. When the results were examined, the Rouge-1 score was obtained as 0.4453. Experimental results show that the proposed Temporal TF-IDF method outperforms all other hashing systems for both English and non-English languages.

In 2016, the study by Li et al. (Li et al., 2016), an automatic summarization method of Tibetan language is proposed. The proposed method consists of a combination of keyword processing based on the TextRank algorithm and the detection of the relationship between sentences based on the LexRank algorithm. The frequency of a sentence is calculated by including word positions, word lengths, and contents. In the experiments, summaries of a document were created by combining the TextRank algorithm first, then the LexRank algorithm, and finally the LexRank and

TextRank algorithms. The Rouge metric was used to evaluate the summarization. Experimental results show that the combination of TextRank and LexRank algorithms of single-document auto summarization in Tibetan gives better results and accuracy reaches 80%.

In 2016, the study by ShafieiBavani et al. (ShafieiBavani et al., 2016), a summary method based on abstractive query-focused multi-document summarization (QMDS) using multi-sentence compression (MSC) is proposed for multiple news sources. With the proposed method, a new summary text is created that represents the core of the content of the source documents. The proposed method consists of four stages. In the first stage, semantic similarities between the sentences and the input query were determined. In the second stage, sentence pruning was used to filter out fewer query-related sentences. In the third stage, the sentences related to the query were clustered using a graphical clustering algorithm. In the fourth and final stage, abstractive summarization of the clusters was achieved through an MSC approach based on word graphics, which takes into account the grammatical structure of the produced summaries and important keywords. DUC 2005, DUC 2006, and DUC 2007 datasets, which are query-oriented benchmark datasets, were used in the experiments. The Rouge-1 Rouge-2 Rouge-SU4 metrics were used to evaluate the summary. In the DUC 2005 dataset, Rouge-1 Rouge-2 Rouge-SU4 values were obtained as 0.41980, 0.08725, 0.13941, respectively, while in the DUC 2006 data set it was 0.44871, 0.14208, 0.17602, and in the DUC 2007 data set it was 0.47641, 0.15415, 0.18573. It is stated that the proposed approach outperforms other existing approaches.

There are studies on the Turkish language in the field of text summarization. One of these studies was the study by Demirci and his team in 2017 (Demirci et al., 2017). In this study, multi-document summarization (MDS) system is recommended for Turkish news. The proposed MDS system aims to create a single document for previously collected multi-document news. The data set was collected from various Turkish news sources via Real Simple Syndication (RSS). The news are divided into clusters according to their topics. The cosine similarity metric was used for the clustering process. Latent Semantic Analysis (LSA) was used to summarize multiple documents. TF-IDF metric was used to select sentences with higher significance in the texts. The Rouge metric was used to evaluate the performance of the system. Results show that the average recall and precision percentage of this system is about 43%. In the study, it was stated that the number of sentences and the summarization rate affected the accuracy rate.

In 2019, the study by Karakoc et al (Karakoc et al., 2019), Turkish news headlines were predicted by using the encoder-decoder model, which is one of the deep learning methods. While estimating the news headlines, the interpretation-based text summarization method was used. The system is trained with iterative neural networks by developing an encoder-decoder model. Word embeddings in news texts at the training stage were obtained by using the FastText algorithm, which has been widely used in the literature in recent years. The system was tested separately by training the first sentence, the first two sentences, and the whole of the news text. Rouge-1 (Recall Oriented Understudy of Gisting Assessment) score and semantic similarity were used to evaluate the performance of the system, and Rouge-1 and similarity values were obtained as 0.20 and 0.51, respectively. The results of the experiment indicated that the model trained with the whole news text was more successful than other similar models.

Method

The working topology of the proposed Helmholtz principle based extractive summarization model is as in Figure 3. All steps in topology will be covered under separate headings.
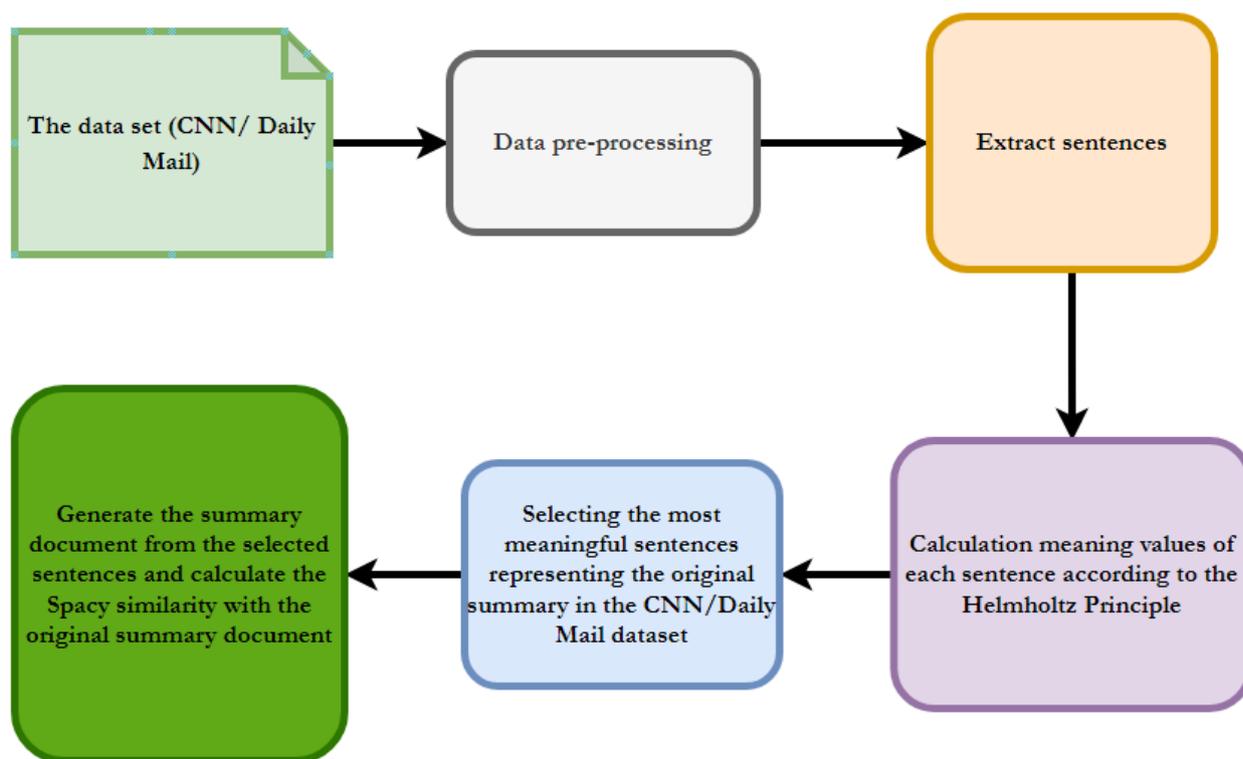
Figure 3. The topology of the proposed approach

The Data Set

In this study, the CNN Daily/Mail data set was used to evaluate the accuracy of the proposed model. CNN Daily/Mail is a data set for text summarization. Human-generated abstractive summary bullets were generated from news stories in CNN and Daily Mail websites as questions (with one of the entities hidden), and stories as the corresponding passages from which the system is expected to answer the fill-in-the-blank question. The authors released the scripts that crawl, extract and generate pairs of passages and questions from these websites. In all, the corpus has 287,113 training pairs, 13,368 validation pairs, and 11,490 test pairs, as defined by their scripts. The source documents in the training set have 766 words spanning 29.74 sentences on average while the summaries consist of 53 words and 3.72 sentences (Kaggle, 2022).

Data Pre-processing

Data pre-processing is a step in the data mining and data analysis process that takes raw data and transforms it into a format that can be understood and analyzed by computers and used for machine learning. It is also an important step in data mining as we cannot work with raw data. The quality of the data should be checked before applied to the machine learning or data mining algorithms. Data pre-processing includes data cleaning, data integration, data transformation, and data reduction (Nadzurah et al., 2018). The details of the steps applied in data pre-processing are given in Figure 4.
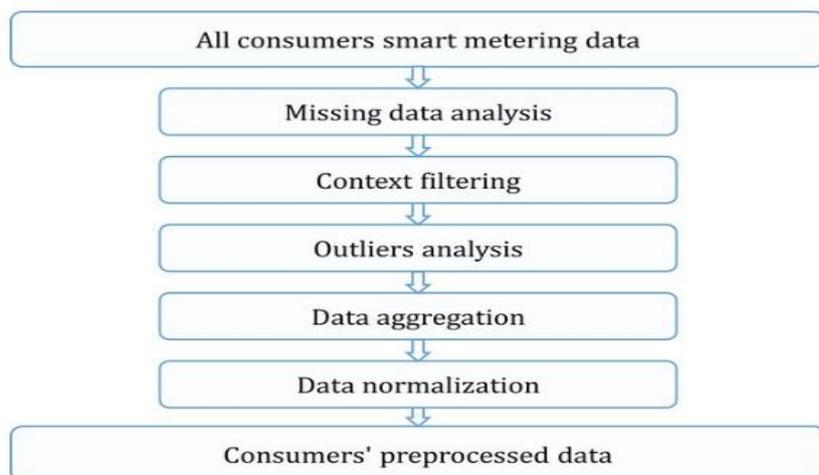
Figure 4. Data preprocessing steps (Fernandes et al., 2017).

Proposed Helmholtz-based Extractive Summarization Algorithm

In the proposed model, the original full-text documents in the CNN Daily/Mail data set were evaluated on a sentence basis. The meaning values of the words in each sentence were calculated. Helmholtz principle (Dadachev et al., 2010; Dadachev et al., 2012; Toprak et al., 2019) was used to calculate the meaning values of words. Then, the words whose meaning values were calculated were collected on a sentence basis. The sentences with the highest meaning value were selected according to the determined summary length ratio parameter value and added to the summary document. Then, the Spacy text similarity of this generated summary document and the original summary document in the CNN Daily/Mail data set was calculated.

Summarization Algorithms Used in This Study

In order to compare and evaluate the proposed model in this study, algorithms that are widely known in the literature BertSum, Luhn, and SumBasic are used. These algorithms perform extractive summarization.

BertSum extractive summarization algorithm assigns scores to each sentence that represents how much value that sentence adds to the overall document (Yadav et al., 2022). Scores of each node or vertex are decided by either a "voting" or "recommendation" system, where each node or vertex votes for all others. The importance of a node/vertex is decided based on the votes received. The value of each vote also depends on the importance of the node casting it. The sentences with the highest scores are then collected and rearranged to give the overall summary of the article.

Luhn extractive summarization algorithm was proposed by Hans Peter Luhn in 1958. This algorithm is one of the first studies in the field of text summarization. The algorithm is based on TD-IDF metrics. According to the Luhn extractive summarization algorithm, some words are frequently used while the subject is being detailed by the author. Frequent use of the word shows the importance of that word for writing. The more frequently a word is found in a text, the more importance can be given to each of these words. The basic steps of the Luhn algorithm are as follows (Victor et al., 2019).

In the first stage, the important words in the document are determined. The frequency of the words in the document is calculated, the most and least frequent words are ignored.

- Weight is calculated for each sentence in the text. Weight values are score values for sentences. In order to find the score value, the window size value must be calculated first. The window shows you the distance value between two important words in the sentence.

- These score values calculated for each sentence are ranked and then sentence selection is made.

SumBasic is a multi-document summarization method that determines a frequency distribution of words over every document, determines the average probability of each sentence based on its word composition, and takes the best scoring sentence of the most frequent word until the desired summary length has been reached (Nenkova et al., 2005). In a non-redundancy step, every iteration updates the probability of the most frequent word by multiplying it by itself and updating the assigned weights of the sentences correspondingly.

The variations implemented were:

- Orig: The original version, including the non-redundancy update of the word scores.

- best_avg: A version of the system that picks the sentence that has the highest average probability in Step 2, skipping Step 3.

- simplified: A simplified version of the system that holds the word scores constant and does not incorporate the non-redundancy update.

- leading, which takes the leading sentences of one of the articles, up until the word length limit is reached.

Summaries were generated by these algorithms for each of the original full-text documents in the CNN Daily/Mail data set. The success rates of the generated summaries are discussed in detail in the Experiments section.

Determining the Size of the Summary Document

The length of the summary document to be generated with the extractive summarization algorithms was calculated with reference to the CNN Daily/Mail data set. The summary length ratio was determined by dividing the total number of words of the original full-text document to be summarized by the number of words in the original summary document. The flow through an example scenario would be as follows.

When it is desired to generate a summary of the original full-text in the CNN Daily/Mail data set;

F(t) = Total word count of the original full-text document (CNN Daily/Mail) = 3000

S(t) = Total number of words in the original summary document = 300

G(t) = Summary length ratio = S(t) / F(t)

G(t) = 300 /3000 = 10 (10%).

Calculation of Similarity Rate

In this study, the similarities of the summary documents generated by BertSum, Luhn, SumBasic, and proposed model with the original full-text documents found in the CNN Daily/Mail data set were calculated using the Spacy text similarity algorithm.

Spacy is a free, open-source library for advanced NLP in Python. Word similarity is a number between 0 to 1 which tells us how close two words are, semantically. This is done by finding similarities between word vectors in the vector space. Spacy, one of the fastest NLP libraries widely used today, provides a simple method for this task. Spacy supports two methods to find word similarity: using context-sensitive tensors, and using word vectors.

Experiments

In each experiment, the success rates of the summary documents produced by extractive summarization algorithms for a different number of documents selected in the CNN Daily/Mail data set are shared with reference to Spacy text similarity.

Experiment I

In Experiment I, summaries of 10 original full-text documents selected from the CNN Daily/Mail data set were generated with each extractive summarization algorithm. The similarities between the summary document generated by each summarization algorithm and the original summary document were calculated. The average Spacy text similarity rates obtained by the algorithms are given in Table 1.

Table 1 - The Success Rates Obtained with 10 Documents Selected from the CNN Daily/Mail Data Set

Extractive Summarization Algorithm	Average Similarity Rate (%)
BertSum	41.2
Luhn	29.7
SumBasic	35.6
Proposed Helmholtz-Based	38.2

Experiment II

In Experiment II, summaries of 50 original full-text documents selected from the CNN Daily/Mail data set were generated with each extractive summarization algorithm. The similarities between the summary document generated by each summarization algorithm and the original summary document were calculated. The average Spacy text similarity rates obtained by the algorithms are given in Table 2.

Table 2 - The Success Rates Obtained with 50 Documents Selected from the CNN Daily/Mail Data Set

Extractive Summarization Algorithm	Average Similarity Rate (%)
BertSum	40.1
Luhn	28.2
SumBasic	34.1
Proposed Helmholtz-Based	36.9

Experiment III

In Experiment III, summaries of 100 original full-text documents selected from the CNN Daily/Mail data set were generated with each extractive summarization algorithm. The similarities between the summary document generated by each summarization algorithm and the original summary document were calculated. The average Spacy text similarity rates obtained by the algorithms are given in Table 3.

Table 3 - The Success Rates Obtained with 100 Documents Selected from the CNN Daily/Mail Data Set

Extractive Summarization Algorithm	Average Similarity Rate (%)
BertSum	39.3
Luhn	27.5
SumBasic	33.2
Proposed Helmholtz-Based	36.1

Conclusions and Recommendations

In this study, a Helmholtz principle is proposed as selective metric in extractive summarization model. CNN Daily/Mail data set was used to evaluate this proposed model. In this dataset, there are both original full-text documents and summary documents of these original full-text documents produced by human summarizers. The proposed model in the study was compared with the BertSum, Luhn, and SumBasic extractive summarization algorithms known in the literature.

The summaries of the original full-text documents in different numbers selected from the CNN Daily/Mail data set were produced with extractive summarization algorithms. The similarities of the produced summaries with the original summary documents in the CNN Daily/Mail data set were calculated using the Spacy text similarity algorithm.

When the results obtained in the experiments are examined, the extractive summarization algorithm that reaches the highest average Spacy text similarity rate is BertSum with 41.2%. The

proposed Helmholtz-based extractive summarization approach also achieved the highest average Spacy text similarity rate in Experiment I, 38.2%. Then, respectively, the SumBasic and Luhn algorithms obtained the highest average Spacy text similarity rate.

It is also seen from the experiments that when the number of documents to be summarized is increased, the average Spacy text similarity rate decreases. Of note, the highest average success rates were obtained in Experiment I. However, it is considerable that Helmholtz principle is selective to evaluate units in a text for importance in extractive summarization, consequently it can be adaptable to specific NLP tasks for similar purpose.

As a continuation of this study, the following studies that are thought to contribute to the literature can be discussed.

- The results obtained by using a different data set instead of the CNN Daily/Mail data set used in this study can be evaluated comparatively.
- The proposed model can also be compared with other third-party algorithms known in the literature (LexRank, TextRank, Kullback-Leiber Divergence, Latent Semantic Analysis etc.).

References

A. Li, T. Jiang, Q. Wang and H. Yu, "The Mixture of Textrank and Lexrank Techniques of Single Document Automatic Summarization Research in Tibetan," 2016 8th International Conference on Intelligent Human-Machine Systems and Cybernetics (IHMSC), 2016, pp. 514-519, doi: 10.1109/IHMSC.2016.278.

A. R. Pal and D. Saha, "An approach to automatic text summarization using WordNet," 2014 IEEE International Advance Computing Conference (IACC), 2014, pp. 1169-1173, doi: 10.1109/IAdCC.2014.6779492.

A. Toprak and M. Turan, "English Automatic Dictionary Creation with Natural Language Processing," 2019 Innovations in Intelligent Systems and Applications Conference (ASYU), 2019, pp. 1-6, doi: 10.1109/ASYU48272.2019.8946431.

B. Dadachev, A. Balinsky, H. Balinsky and S. Simske, "On the Helmholtz Principle for Data Mining," Third International Conference on Emerging Security Technologies (EST), Lisbon, Portekiz, 2012.

B. Dadachev, A. Balinsky, H. Balinsky and S. Simske, "On Helmholtz's Principle for Documents Processing," Proceedings of the 10th ACM Symposium on Document Engineering, Manchester, England, ss. 283-286, 2010.

Boorugu, Ravali & Ramesh, G. (2020). A Survey on NLP based Text Summarization for Summarizing Product Reviews. 352-356. 10.1109/ICIRCA48905.2020.9183355.

C. Chen, C. Hong and S. Chen, "Intelligent Location-Based Mobile News Service System with Automatic News Summarization," 2009 International Conference on Environmental Science and Information Application Technology, 2009, pp. 527-530, doi: 10.1109/ESIAT.2009.485.

E. Karakoc and B. Yılmaz, "Deep Learning Based Abstractive Turkish News Summarization," 2019 27th Signal Processing and Communications Applications Conference (SIU), 2019, pp. 1-4, doi: 10.1109/SIU.2019.8806510.

E. ShafieiBavani, M. Ebrahimi, R. Wong and F. Chen, "A Query-Based Summarization Service from Multiple News Sources," 2016 IEEE International Conference on Services Computing (SCC), 2016, pp. 42-49, doi: 10.1109/SCC.2016.13.

F. Demirci, E. Karabudak and B. İlgen, "Multi-document summarization for Turkish news," 2017 International Artificial Intelligence and Data Processing Symposium (IDAP), 2017, pp. 1-5, doi: 10.1109/IDAP.2017.8090189.

Fernandes, Marta & Viegas, Joaquim & Vieira, Susana & Sousa, João. (2017). Segmentation of Residential Gas Consumers Using Clustering Analysis. Energies. 10. 2047. 10.3390/en10122047.

H. Kim and S. Lee, "A Context based Coverage Model for Abstractive Document Summarization," 2019 International Conference on Information and Communication Technology Convergence (ICTC), 2019, pp. 1129-1132, doi: 10.1109/ICTC46691.2019.8939704.

https://www.kaggle.com/gowrishankarp/newspaper-text-summarization-cnn-dailymail

M. F. Mridha, A. A. Lima, K. Nur, S. C. Das, M. Hasan and M. M. Kabir, "A Survey of Automatic Text Summarization: Progress, Process and Challenges," in IEEE Access, vol. 9, pp. 156043-156070, 2021, doi: 10.1109/ACCESS.2021.3129786.

N. Alsaedi, P. Burnap and O. Rana, "Temporal TF-IDF: A High Performance Approach for Event Summarization in Twitter," 2016 IEEE/WIC/ACM International Conference on Web Intelligence (WI), 2016, pp. 515-521, doi: 10.1109/WI.2016.0087.

Nenkova, Ani & Vanderwende, Lucy. (2005). The impact of frequency on summarization.

Victor, Domínguez & Fidalgo, Eduardo & Biswas, R. & Alegre, Enrique & Fernández-Robles, Laura. (2019). Application of Extractive Text Summarization Algorithms to Speech-to-Text Media. 10.1007/978-3-030-29859-3_46.

Yadav, Divakar & Lalit, Naman & Kaushik, Riya & Singh, Yogendra & Mohit, & Dinesh, & Yadav, Arun Kumar & Bhadane, Kishor & Kumar, Adarsh & Khan, Baseem. (2022). Qualitative Analysis of Text Summarization Techniques and Its Applications in Health Domain. Computational Intelligence and Neuroscience. Early Access. Early Access. 10.1155/2022/3411881.

Z.A. Nadzurah, A.R. Ismail, N. Emran, "Performance Analysis of Machine Learning Algorithms for Missing Value Imputation," International Journal of Advanced Computer Science and Applications, Vol. 9, Issue. 6, pp. 442-447, 2018.

The Effect of Break Draft, Roving Hank and Cot Diameter on Physical Properties of Yarn in Ring Spinning

Ahmet ZEYBEK[1]

Introduction

Ring spinning is the most widely used (Goyal, 2019) and the oldest technology (Bakhsh et al., 2020) to produce yarn worldwide. However, the drawbacks of this system cannot be underestimated. Production in ring spinning systems has various limits that affect the yarn quality such as low speed, requiring additional processes (winding, roving, etc.), excessive heat and dissipation in travelers (Bakash et al., 2020; Goyal, 2019). For these reasons, it is essential to do process control to eliminate any unfavorable situation in the final yarn quality. The sequential flow in the spinning process makes it fundamental to control each process as the performance of the machines in the spinning line consecutively affects each other (Ghosh & Majumdar, 2012).

Spinning back zone draft (break draft), roving hank and cot diameter are three process parameters that affect the quality of produced yarn in the spinning process. Combining these three factors in appropriate scales is quite important to obtain better yarn quality (Bakhsh et al., 2020; Ghane et al., 2008; Su & Jiang, 2004). In the drafting process, necessary drafts are adjusted for attenuating fibers in roving. Furthermore, the economy of the machine is directly influenced by the final break rate and thickness of the roving hank since these can increase yarn quality and decrease cost in production (Ghodke et al., 2021). Similarly, the front cot diameter affects the strength of the yarn in the spinning process and plays an important role in fiber cohesion (Ghane et al., 2008; Xu, 2005). Thus, finding optimal processes among them is the question that needs to be investigated to have better yarn quality at low costs.

Studies found that high levels of drafting can cause breakages and irregularity in yarn, and reduce yarn strength (Su & Jiang, 2004). Especially, as Bakhsh et al. (2020) state, the correct adjustment in the break draft is essential as the evenness in the yarn quality highly depends on this process. In Khan et al. (2020)'s study, in which they investigated the effect of roving number and break draft ratio on compact ring yarn quality, coarser roving was found to increase yarn irregularities (U%) and IPI values as this type of roving need higher draft ratio which causes a poorer control on floating fibers. Moreover, they stated that in coarser roving, the increased break draft ratio led to a decrease in yarn irregularity and improved yarn strength while in finer roving high break draft ratio increased yarn unevenness.

In a study conducted by Zeybek (2020) on cot diameter and yarn quality, the cot hardness was kept constant and the effect of two different cot diameters on the physical properties of yarn was investigated. The results revealed that using bigger diameters, especially in the front cot can lead to better yarn qualities.

In this study, the effect of break draft ratio, roving hank and cot diameter on the physical properties of yarn in terms of the quality parameters in ring spinning has been investigated.

---

[1] Doktor,

Regression analysis has been used to understand the effect of these three independent factors on the irregularities, hairiness, IPI values and strength of ring spinning cotton yarn. This research will help characterize the variability of ring process settings to optimize the quality of the yarn.

Materials and Method

Cotton fiber samples, which were created by taking samples from various parts of the cotton blend used in the study, were measured with the Uster HVI 1000 test device. The HVI test system has great importance in determining fiber properties and establishing a standardization with a single device (Bedez Ute, 2012). The measurements were carried out at 20±2°C temperature and 65±2% relative humidity (standard atmospheric conditions) and three tests were performed for each sample taken in the test system. The average values found as a result of these measurements are shown in Table 1.

Table 1. Uster HVI 1000 measurement values of the cotton fiber

	Mean	Standard Deviation
Spinning Consistency Index	147	5,0
Micronaire (μg/inch)	4,80	0,11
UHML (mm)	30,17	0,47
Maturity Index	0,86	0,01
Uniformity Index (%)	84,3	0,6
Short Fiber Index (%)	8,1	0,7
Strength (g/tex)	31,3	0,2
Elongation (%)	4,4	0,1
Reflectance (Rd)	75,5	0,9
Yellowness (+b)	8,3	0,3

These machines were used respectively in the production of the samples in this study; UniFloc A-11, UniClean B-11, UniMix B 7/3, UniFlex B 60, Card C 70, Draw frame SB-D 45, UniLap E 30, Comber E 86, Draw Frame RSB-D 30, Roving F 16, and Ring G 33.

In the sample production, 10 roving bobbins with a length of 500 meters were produced from the blend used, and yarn samples with the number Ne 30/1 were produced from these roving bobbins. A total of 80 cops were produced on the ring spinning machine, 10 for each combination. In order to eliminate the machine-related reasons that may cause different results in the measurements of the combed ring yarns produced in the ring spinning machine in cop form with the Uster Tester 4 device, the production was carried out using the same spindles of the roving and

ring spinning machines. The parameters set for this study in the sample yarn production are presented in Table 2.

Table 2. Parameters for the sample yarn production

Yarn number	Parameters in yarn production	
Ne 30/1	Card, 1. and 2. Draw Frame Sliver (Ne)	0,120
	Roving Hank (Ne)	0,90 – 1,20
	Roving Twist (T/inch)	1,28
	Yarn Twist (T/m)	798
	Ring Speed (rpm)	14500
	Break draft (G33)	1,14 – 1,19
	Ring traveler type and ISO number	PM Udr Saphir – 40,0
	Pin spacer size (mm)	3,50
	Cot diameter (mm)	28,20 – 30,30
	Cot hardness (shore)	63

As seen in Table 2, two different values were set for the chosen parameters of the spinning system roving hank (Ne), for break draft (G33), and for cot diameter (mm). The coded levels and their actual values are presented in Table 3.

Table 3. Independent factors and their values

Factor with symbol	Coded values and actual values	
	-1	1
Break Draft, X1	1.14	1.19
Roving Hank, X2	0.90	1.20
Cot Diameter, X3	28.20	30.30

Results and Discussion

The mean values of irregularity, IPI values, hairiness and strength of the yarns produced through independent variable in different values (coded as -1 and 1) are presented in Table 4.

Table 4. The mean values of the physical properties of yarn in terms of quality parameters

Factors			Physical Properties of Yarn (Means)					
X1	X2	X3	CVm (%)	Thin (-50%/km)	Thick (+50%/km)	Neps (+200%/km)	H	Tenacity (cN/tex)
-1,00	-1,00	1,00	11,57	,50	4,00	12,00	5,41	17,55
-1,00	-1,00	-1,00	11,69	1,30	8,80	15,80	5,37	17,61
1,00	-1,00	1,00	11,54	2,30	6,80	15,80	5,54	17,14
-1,00	1,00	-1,00	11,79	2,80	7,00	14,30	5,26	17,37
1,00	1,00	1,00	11,63	1,50	5,30	12,50	4,90	17,23
1,00	1,00	-1,00	11,97	,50	6,80	14,80	5,09	17,56
1,00	-1,00	-1,00	11,81	4,50	11,30	15,00	5,27	17,36
-1,00	1,00	1,00	11,61	1,00	3,50	11,50	5,27	17,06

The results of the regression analysis to understand the effect of break draft, roving hank and cot diameter on physical properties of yarn are presented in Table 5 below.

Table 5. The results of regression analysis on the factors affecting physical properties of yarn

Depen. Variables	Indepen. Variables	B	Stand .Dev.	β	T	p	Pairwise r	Partial R	R	R²	F	p
CVm(%)	Constant	11.701	.022		529.115	.000			.946	.895	11.334	.020*
	X1	.036	.022	.266	1.639	.177	.266	.634				
	X2	.049	.022	.358	2.204	.092	.358	.741				
	X3	-.114	.022	-.834	-5.114	.007*	-.834	-.932				
Thin (-50%/km)	Constant	1.800	.525		3.426	.027			.561	.315	.613	.641
	X1	.400	.525	.315	.761	.489	.315	.356				
	X2	-.350	.525	-.276	-.666	.542	-.276	-.316				
	X3	-.475	.525	-.374	-.904	.417	-.374	-.412				
Thick (+50%/km)	Constant	6.688	.397		16.843	.000			.943	.888	10.604	.023*
	X1	.862	.397	.363	2.172	.096	.363	.736				
	X2	-1.038	.397	-.437	-2.613	.059	-.437	-.794				
	X3	-1.788	.397	-.752	-.4.502	.011*	-.752	-.914				
Neps (+200%/km)	Constant	13.963	.440		31.759	.000			.837	.701	3.129	.150
	X1	.563	.440	.350	1.279	.270	.350	.539				
	X2	-.687	.440	-.427	-1.564	.193	-.427	-.616				
	X3	-1.013	.440	-.629	-2.303	.083	-.629	-.755				
H	Constant	5.264	.054		97.197	.000			.809	.654	2.725	.196
	X1	-.064	.054	-.346	-1.177	.304	-.346	-.507				
	X2	-.134	.054	-.726	-2.470	.069	-.726	-.777				
	X3	.016	.054	.088	.300	.779	.088	.148				
Tenacity (cN/tex)	Constant	17.360	.069		251.266	.000			.693	.480	1.233	.407
	X1	-.038	.069	-.196	-.543	.616	-.196	-.262				
	X2	-.055	.069	-.287	-.796	.471	-.287	-.370				
	X3	-.115	.069	-.600	-1.664	.171	-.600	-.640				

When the pairwise and partial correlations between independent variables and CVm (%) values are examined, it has been found that there is a positive but low relationship between break draft and CVm (%) mean value (r=.26). However, when other variables are taken under control the correlation between these two variables has been calculated as r=63. There is a positive and low-level relationship between roving hank and CVm (%) mean value (r=35), but when the other two variables are taken under control this relationship is calculated as r=74. When the relationship between cot diameter and CVm (%) values is investigated, a negative and high-level relationship is observed (r=-.83) and when the other variables are taken under control this relationship is observed as r=-.93. Break draft, roving hank and cot diameter, all together, have a significant and high level correlation with CVm (%) mean value, R=.946, R2=.895, p<.05. These three independent variables explain 89% of the variance in CVm (%) value. According to the standardized regression coefficient (β), the order of importance of the independent variables on CVm (%) mean value is; cot diameter, roving hank and break draft. When the T-Test results on the significance of regression coefficients are examined, it can be noticed that only cot diameter has a significant effect on CVm (%) values.

The physical properties of yarn can be affected by the variation of mass per unit along the yarn and this is generally defined as yarn irregularity or unevenness (Eyasu et al., 2018). As Bakhsh et al. (2020) stated, setting the correct ratio in the break draft plays an important role in yarn quality as the incorrect ratio can increase the irregularity in the final product. The analysis results demonstrated that the combinations defined in this study for break draft ratio, roving hank and cot diameter have a significant effect on CVm (%) values. In other words, the optimum results have been obtained by the combination of (X1:1, X2: -1, X3:1), i.e. break draft ratio= 1.19, roving hank= 0.90 and cot diameter= 30.30 (Mean Value=11.54). The results also revealed that cot diameter

plays a crucial role in yarn irregularity as the bigger the diameter gets the lesser will be the CVm (%) values. This result supports the previous findings on cot diameter and yarn irregularity (Ghane et al., 2008; Xu, 2005, Zeybek, 2020).

The pairwise and partial correlations between independent variables and Thin (-50%/km) mean value are examined, a low level and positive relationship is found between break draft and Thin (-50%/km) mean value (r=.31) and a similar result is obtained when the other variables are taken under control r=.35. Furthermore, there are also low level but negative relationships between roving hank (r=-.27) and Thin (-50%/km) mean value, and between cot diameter (r=-.35) and Thin (-50%/km) mean value. The correlations are calculated as r=-.31 for roving hank and Thin (-50%/km) and as r=-.41 for cot diameter and Thin (-50%/km) when the other variables are taken under control. The three independent variables have a medium level correlation between Thin (-50%/km) mean value, which is not a statistically significant result, R=.56, R2=31, p>.05. They, all together, explain only the 31% of the variance on Thin (-50%/km) value. According to the standardized regression coefficient (β), the order of importance of the independent variables on Thin (-50%/km) values is; cot diameter, break draft and roving hank. When the T-Test results on the significance of regression coefficients are examined, it is found that all three independent variables do not have a significant effect on Thin (-50%/km) values.

The correlations for Thick (+50%/km) show that in terms of pairwise and partial correlations, there is a positive and low level relationship between break draft and Thick (+50%/km) mean values (r=.36). However, when other variables are taken under control this relationship increases by r=.73. The relationship between roving hank and Thick (+50%/km) values demonstrates a negative and medium relationship (r=-.43) and when other variables are taken under control the relationship between the two is observed as r= -.79. There is a negative but high level relationship between cot diameter and Thick (+50%/km) values (r=-.75) and when other independent variables are taken under control, this relationship is even higher as r=-.91. Break draft ratio, roving hank and cot diameter together have a significant positive and high level correlation between Thick (+50%/km) values, R=.94, R2=.88, p<.05. Altogether, they explain the 88% of the variance in Thick (+50%/km) values. The standardized regression coefficient (β) indicates that in terms of the order of importance on Thick (+50%/km) values cot diameter comes first followed by roving hank and break draft. Moreover, the T-test results on the significance of regression coefficients show that only cot diameter has a significant effect on Thick (+50%/km) values.

The regression analysis on Neps (+200%/km) values reveals that between break draft and Neps (+200%/km) values, the pairwise correlation indicates a low level positive relationship (r=.35) and this becomes r=.53 in partial correlation. A negative and medium level relationship is observed between roving hank and Neps (+200%/km) values (r=-.42) and when other independent variables are taken under control, the relationship is as r=-.61. The pairwise correlation between cot diameter and Neps (+200%/km) values show a similar relationship, i.e. there is a medium level and negative relationship (r=-.62). When other variables are taken under control, this relationship between them is as r=-.75. The three independent variables together have a high level positive correlation between Neps (+200%/km) values, but this correlation is statistically significant, R=.83, R2=.70, p >.05. They have been found to explain the 70% of the variance in Neps (+200%/km) values. According to the standardized regression coefficient (β), the order of importance of the independent variables on Neps (+200%/km) values is: cot diameter, roving hank and break draft. As the T-Test results suggest, none of the independent variables has a significant effect on Neps (+200%/km) values in terms of the significance of regression coefficients.

Imperfection is usually defined as the extremes in variation in yarn and these are thin/thick places and neps (Eyasu et al., 2018). According to the regression analysis results, the combinations of independent variable values do not have a significant effect on Thin (-50%/km) and Neps (+200%/km) values. However, the combinations defined in this study for these variables were found to affect significantly Thick (+50%/km) values in the sample cotton yarns. That is, the optimum quality was obtained by (X1: -1, X2: 1, X3: 1) combination concerning Thick (+50%/km) values (Mean Value=3.5). This indicates that choosing a smaller break draft ratio and roving hank, and a bigger cot diameter can lead to a better yarn quality. Furthermore, similar to CVm (%) results, only cot diameter was found to have a significant effect on Thick (+50%/km) values and there is a negative correlation between the two variables. Although no statistically significant effect was observed between cot diameter and Thin (-50%/km) and Neps (+200%/km) values, again cot diameter has the highest regression coefficient (β) values. Thus, cot diameter can be considered as an important factor in the physical properties of cotton yarns, especially for IPI values.

The correlations for hairiness (H) values indicate that for both break draft (pairwise r=-. 34 and partial r=-.50 and cot diameter (pairwise r=.08 and partial r=.14) the relationship is low. However, there is a negative high relationship between roving hank (r=-.72) and H values and when the other independent variables are taken under control, the relationship is as r=-.77. The three independent variables have a high level and positive correlation with H values, but this correlation is not statistically significant, R=.80; R2=.65, p>.05. These variables explain 65% of the variance in H values. According to the standardized regression coefficient (β), the order of importance of the independent variables on H values is: roving hank, break draft and cot diameter. The T-Test on the significance of the regression coefficients indicates that no independent variables have a significant effect on H values.

Hairiness is defined as the abundance of fiber loops or ends that moves freely which not only affects yarn quality but also deteriorates the performances of consecutive processes in spinning (Eyasu et al., 2018). According to the results found in this study, the defined combinations of the independent variable values did not show any significant effect on hairiness values. The main function of cot is to support the drafting process by applying equal pressure on the fiber surface. Thus, instead of the cot diameter, hairiness is anticipated to be affected mostly by other factors such as the roving hank and the relationship between ring diameter and travelers. As found in the results of this study, roving hank is the most important factor among all three independent variables according to the standardized regression coefficient (β).

Finally, the regression analysis on Tenacity (cN/tex) values reveals that all independent variables have a negative pairwise relationship with Tenacity (cN/tex) values while the relationship with the variables break draft (pairwise r=-.19 and partial r=-.26) and roving hank (pairwise r=-.28 and partial r=-.37) is quite low, it is in medium level with cot diameter (pairwise r=-.60 and partial r=-.64). The independent variables, together, have a medium level positive correlation with Tenacity (cN/tex) values, but this correlation is not statistically significant, R=.69, R2=.48, p>.05. They explain 48% of the variance in Tenacity (cN/tex) values. According to the standardized regression coefficient (β), the order of importance of the independent variables on Tenacity (cN/tex) values is: cot diameter, roving hank and break draft. When the T-Test results on the significance of regression coefficients are examined, none of the independent variables are found to have a significant effect on Tenacity (cN/tex) values.

Conclusion

This study aimed to investigate the effect of break draft ratio, roving hank and cot diameter on cotton yarn quality parameters in ring spinning. The results revealed that, for the value combinations defined in this study for independent variables, significant findings were found only for CVm (%) and Thick (+50%/km) values; i.e. higher and bigger ratios in break draft, roving hank and cot diameter lead to low irregularity and lower ratios in break draft and roving hank and bigger cot diameter lead to lower thick places in the yarn.

REFERENCES

Bakhsh, N., Khan, M. Q., Ahmad, A., & Hassan, T. (2020). Recent advancements in cotton spinning. In Cotton Science and Processing Technology (pp. 143-164). Springer, Singapore.

Bedez Ute, T. (2012). Sirospun Pamuk İpliklerinde İplik Özellikleri İle Lif Özellikleri Arasındaki İlişkinin Fonksiyonel Olarak Tahminlenmesi Üzerine Bir Araştırma. Doktora Tezi, Ege Üniversitesi, Fen Bilimleri Enstitüsü, İzmir.

Eyasu, F., Sakthivel, S., & Bewuket, T. (2018). Effect of spinning top front roller rubber cots shore hardness on yarn quality. International Journal of Industrial Engineering, 2(1), 7-14.

Ghane, M., Semnani, D., Saghafi, R., and Beigzadeh, H. (2008). Optimization of top roller diameter of ring machine to enhance yarn evenness by using artificial intelligence. Indian Journal of Fibre and Textile Research, 33, 365-370.

Ghodke, V., Singh, H., Wadwankar, A., Patil, N., & Kulkarni, K. (2021). Brief overview of the automation process in speed frame machine. International Research Journal of Modernization in Engineering Technology and Science, 3(9), 119-123.

Ghosh, A. & Majumdar, A. (2012). Process control in drawframe, comber, and speed frame. In Process control in textile manufacturing (pp. 158-190). Woodhead Publishing, USA.

Goyal, A. (2019). Yarn Formation and Recent Developments. In Fibres to Smart Textiles (pp. 31-61). CRC Press.

Khan, M. K. R., Hasan, M. M., & Haque, A. K. M. M. (2020). Investigating the effects of some process parameters on the quality of coarse compact yarn produced from carded roving. J Textile Eng Fashion Technol, 6(6), 251-255.

Su, C. I., & Jiang, J. Y. (2004). Fine count yarn spun with a high draft ratio. Textile Research Journal, 74(2), 123-126.

Xu, Z. G. L. (2005). Spinning Test of Big Diameter Spinning Top Roller [J]. Cotton Textile Technology, 9.

Zeybek, A. (2020). Ön ve Arka Manşon Çapı Farklılıklarının Karde Ring İplik Kalite Parametreleri Üzerine Etkisi. Uluslararası Doğu Anadolu Fen Mühendislik ve Tasarım Dergisi, 2(2), 380-400.

Artificial Neural Network-Based Stock Market Forecast

Bilal GÜREVİN [1]
Emin GÜNEY [2]
Samed KALKAN [3]

Introduction

As human beings open their eyes to life due to their nature, they live in the sense of curiosity to learn the information they do not know. As human beings open their eyes to life due to their nature, they live in the sense of curiosity to learn the information they do not know. Because the past is the future field, this search provides the basis for the formation of prediction ability and, therefore, the construction of prediction models.

While making predictions, human beings analyze the information they have learned and their past experiences and thus try to comment on the future. In the prediction models, more reasonable interpretations can be made about the future by processing the information obtained in the past through statistical procedures and transforming them into data.

Finance and investment sectors stand out among the sectors where the need for forecasting is felt the most. Many traditional forecasting models used in these sectors have been used as guiding tools for decision makers for decades. It is an undeniable fact that the algorithms used in artificial intelligence together with the advancing technology and the contribution of these traditional models to the further prediction power brought by them is an undeniable fact. Artificial neural networks, one of the artificial intelligence tools, are among the most used models for prediction.

In this study, it is tried to predict the BIST-100 index, which is a prominent indicator in the financial sector, using artificial neural networks. Based on the fact that the economy is a whole of relations, the selected macroeconomic indicators that guide the markets, and among these indicators, the data related to the manufacturing sector, which have been tested in the literature at the point of causality and relationship criteria, are used as input data. By including studies showing the link between causality and relationship between indicators, selected indicators of the TSI (Turkey Statistical Institute) and Central (Central Bank of the Republic of Turkey) monthly periodical data, compiled the data set has been demonstrated artificial neural networks forecast results with the help of the software tool.

Related Works

When the literature about financial investment instruments is examined, it is thought that macroeconomic indicators are related to many indices and indicators in the stock market, and it is

[1] PhD Cand., Sakarya University of Applied Sciences, Department of Mechatronic Engineering, Orcıd: 0000-0003-4035-2759
[2] PhD Cand., Sakarya University of Applied Sciences, Department of Computer Engineering, Orcıd: 0000-0003-0098-9018
[3] Industrial Engineering, Sakarya University, Department of Industrial Engineering, Orcıd:

seen that many studies have been carried out on the causality and relationship between macroeconomic indicators and financial indicators.

Sayılgan ve Süslü has examined the interaction of macroeconomic factors with stock earnings in Turkey and developing country markets (Sayılgan et al., 2011). Masuduzzaman has investigated whether there is a relationship between the German and UK consumer price index, industrial production index, exchange rates and interest rates in the short and long term, and determined the interaction between selected indicators and stock indices (Masuduzzaman, 2012). In her study, Koyuncu mentioned the significant effect of the industrial production index on BIST-100 by expressing the relationship between the BIST-100 index, IPI (Industrial Production Index), real economic growth, interest rates and inflation rates (Koyuncu, 2018).

Hacıhasanoğlu and Soydaş emphasized that changes in macroeconomics will affect stock market indices (Erk et al., 2011). Uzun and Gungor mentioned that stocks in the stock market are affected by selected macroeconomic indicators and that their effects in developed countries and developing countries are different and there is no consensus on the relationship direction and level of indicators and as a result they stated that there is an interaction between the stock market and macro indicators at various levels (Uzun et al., n.d.). Herve et al. used the industrial production index, consumer price index, real exchange rate and money supply as indicators in their study, where they subjected the economic indicators to the causality tests in the literature, especially in Ivory Coast (Herve et al., 2011). Dizdarlar and Derindere examined the effects of economic indicators on the BIST-100 index by considering 14 factors including capacity utilization rate, industrial production index and consumer price index. They mentioned that there is a relationship between selected economic indicators(Dizdarlar et al., 2008).

Akkum and Vuran concluded that the relationship between the industrial production index and the stock market index was not as expected in their study based on the data of a number of companies (Vuran et al., 2005). In the study conducted by Kaya, Çömlekçi et al., The relationship between BIST-100 index and macroeconomic indicators was examined, and the industrial production index and 3 other indicators were used. As a result, they stated that they could not find a statistically significant relationship between stock indices, interest rate and industrial production index(V. Kaya et al., 2013) . In their study, Aktaş and Akdağ examined the effects of indicators such as interest rate, consumer price index, exchange rate, unemployment rate, industrial production index, export amount, capacity utilization rate, gold prices, consumer confidence index and crude oil prices on the stock market index and they showed that they were in interaction (Aktaş et al., 2013). In her article, Ay examined the causality relationship and argued that there is a long-term interaction between the real sector confidence index (IACI) and the industrial capacity utilization rate (CUR), which are macroeconomic indicators that allow the increase and decrease in production activities (Ay, 2019).

Eyüboğlu and Eyüboğlu, examining the relationship between economic confidence index data and 3 different Borsa Istanbul indices (BIST-100, BIST-Sinai, BIST-services), they stated that there is a long-term relationship between the indices (Eyüboğlu et al., n.d.). Fattah and Kocabıyık in their article investigated the relationship between macroeconomic variables and the BIST-100 index, they concluded that the consumer price index has an effect on stock market stocks (Kocabıyık et al., 2020).

In the studies of Coşkun et al mentioned that the industrial production index is an indicator of economic activities and therefore will affect the future cash flow and stock markets while examining the relationship of macroeconomic indicators with the stock index (Coskun et al., 2016). Küçükçaylı and Akıncı stated that there is a relationship between various indicators, examining the

interaction between consumer confidence index, industrial production index, BIST-100 index, as well as some other economic indicators (Küçükçaylı et al., 2018).

On the other hand, Bremmer concluded that there is a short-term relationship between stock indices and consumer confidence index, but there is no long-term interaction in his test with 9 of the stock market stock indices in addition to the consumer confidence index indicator (Bremmer, 2008). Topuz investigated the relationship between consumer confidence index and stock values in his study and found that there was a positive correlation tendency between indicators (Topuz, 2011).

As a result of the above literature research, in this study observed relationship between capacity utilization rate belonging to manufacturing sector, industrial production index, real sector confidence index indicators and other macroeconomic indicators such as economic confidence index, consumer price index and consumer confidence index are considered appropriate to be used as input variables in the prediction model. In the light of this information, when we look at the studies on the predictive ability of the artificial neural network (ANN) that we will use as a prediction tool in our study, it is seen that ANN contributes to many different fields and studies on stock market prediction.

Nasuhoğlu analyzed the accuracy of the results using the sales data of the past by creating a forecast model with an artificial neural network (ANN) to control the inventory cost of a pharmacy (Nasuhoğlu, 2019). Kıratlı et al. estimated the sales data, which it took as a sample with the help of selected macroeconomic indicators such as gross domestic product (GDP), real sector confidence index, investment expenditures, consumption expenditures, consumer confidence index, dollar rate and time criteria, with artificial neural networks in order to help decision makers in the automotive industry (Karaatlı et al., 2012).

Avcı examined the daily returns of some stocks in the BIST-30 index in terms of estimation difficulties using Artificial Neural Networks (ANN) Models (A. Emin, n.d.). Kantar stated that ANN performance results were more effective by making a prediction study on the BIST-100 index using selected macroeconomic indicators with the help of artificial neural networks and comparing it with the other model she determined (Kantar, n.d.). On the other hand, Yakut et al. compared the estimation ability of artificial neural networks with support vector machines by using daily data of BIST-50 values of previous periods (Yakut et al., 2014). Çalışkan and Deniz tried to estimate the daily transaction data of 27 stocks determined in the BIST-30 index using the artificial neural network model (Çalışkan et al., 2015).

Methodology

Artificial Neural Networks

Artificial neural networks are a computer system that is based on the learning function of the human brain from experience rather than the algorithmic computational structure of traditional computers, inspired by the highly complex, nonlinear and parallel structure of the human brain. ANN consists of a large number of interconnected process elements called artificial nerve cells. Each link between cells has a weight value, and the artificial neural network calculates through the weights in these connections. The learning function is realized through examples given as an introduction to the network (Öztemel, 2003).

Biological Structure of Artificial Neural Networks

The functioning of the brain, which is the most important decision mechanism of the nervous system, takes place through communication between cells. In the human brain, where there are two types of cells, namely neuron cells and glial cells, the main components of the nervous system and brain functions are composed of three parts: neurons, cell body, dendrite and axon (Saatçioğlu, 2016). The general structure of the biological nerve cell is given in Figure 1.
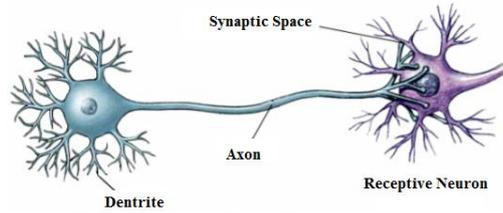

Figure 1. The general structure of the biological nerve cell

The biological nervous system elements and their corresponding functions of the artificial nervous system are given in Table 1. Here, the biological nervous system is divided into parts and the artificial neural network element corresponding to each element is shown.

Table1. Comparison of biological nervous system and artificial nervous system (Öztürk et al., 2018)

Biological Nervous System	Artificial Nervous System
Neuron	Processor Element
Dendrite	Addition Function
Cell Body	Transfer Function
Axons	Artificial Neuron Output
Synapses	Weights

As seen in Figure 2, n data are entered into the existing cell. The data entered into the network is multiplied by the weights and all of the data is collected. After that, the estimate is added and the resulting net decision is obtained. The net input is passed through the activation function and the output of the network is obtained (Öztürk et al., 2018).
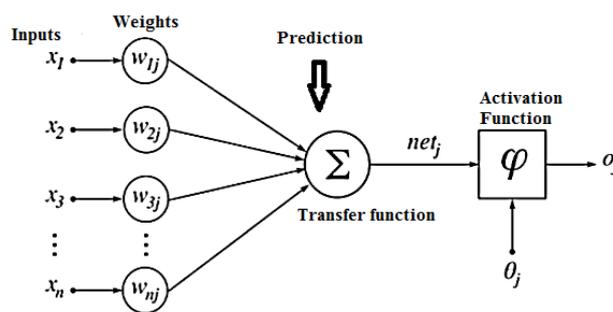
Figure 2. Basic structure of artificial nerve cell (Saatçioğlu, 2016)

Artificial neural networks have a parallel distributed structure that is interconnected. It is similar to the human brain in two ways, although it consists of units that have a natural tendency to store and make available experiential knowledge;

1. Knowledge is acquired by the network through a learning process.

2. Connection values between neurons are used to store information acquired by the network

In the process of training the network in ANN, changing the weight values of the cell element connections is performed. For the learning process of the network, the weight values must be changed repeatedly in order to reach the real value of these random cell values at the beginning. The network has different learning models regarding learning types. Some of these are as follows (Yılmaz, 2019);

- Perceptronlar, Adaline
- Support Vector Machine
- Multilayer Perceptron Models
- Vector Quantization Models (LVQ)
- Hopfield Networks

Structure of Artificial Neural Networks

Artificial nerve cells come together to form an artificial neural network. Although the connection of nerve cells to each other is not random, connections are formed in layers. Generally, cells are in 3 layers. Each layer comes together in parallel to form the network. These layers are:

Input layer: Process elements in this layer are responsible for receiving information from the outside world and transferring it to intermediate layers. In some networks, there is no information processing at the input layer.

Interlayer: Information from the input layer is processed and sent to the output layer. The processing of this information is carried out in intermediate layers. There can be multiple intermediate layers for a network.

Output layer: Process elements in this layer process the information coming from the intermediate layer and produce the output that the network needs to produce for the input set presented from the input layer, and in this way the information is transmitted to the outside world.
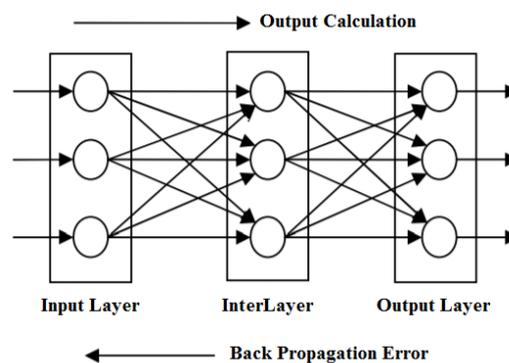
Figure 3. ANN General Network Structure (Çevik et al., 2012)

Artificial neural networks can be classified according to the direction of neural connections;

- Feed Forward ANN; Feed Forward ANN has a single weight layer where the inputs are directly connected to the outputs. In this network, all neurons are directed forward. Each neuron in the layer is connected to another neuron in the next layer without a feedback link (Chauhan et al., 2012).
- Multi Layer Feed Forward ANN; At the input, the input layer consists of one or more hidden layers and an output layer with output nodes from which the error is calculated. The input data is sent from the previous layer to the next layer and finally to the output layer. Such networks are

called Multi Layer Feed Forward ANN (Chauhan et al., 2012). Figure 4 shows a multilayer feed forward network structure with 3 neurons in the input layer, 6 neurons in a single hidden layer, and 3 neurons in the output layer.

- Feedback ANN; Feedback In ANN, a cell is fed from cells in at least one layer after it, and is a type of network where output and intermediate layer outputs are fed back to input units or previous intermediate layers. This allows entries to be transferred both forward and backward.
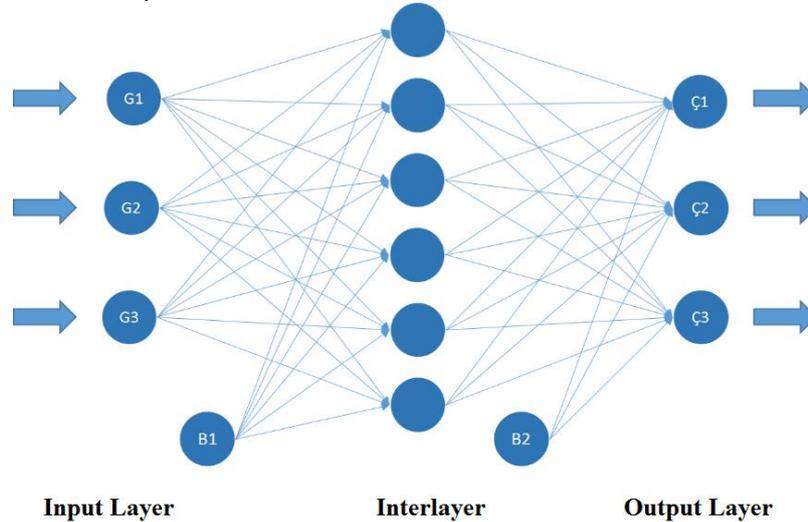
Figure 4. Multi-layer feed forward ANN design
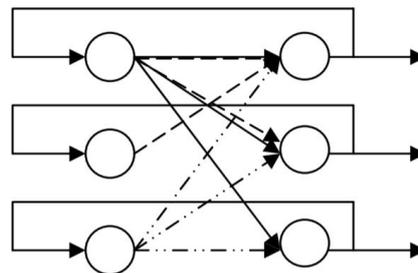
Figure 5. Feedback Network Architecture (İ. Kaya et al., 2005)

Experimental Results

In this study the design of the neural network was done on the Neural Network Tool (NNTool) offered by Matlab® program. In order for ANN to work faster, using Equation 1, normalization was performed in the range of [0 1]. And the results were evaluated by denormalizing again.

As a data set, 158 data of 7 different macroeconomic indicators, including economic confidence index, industrial production index, real sector confidence index, consumer confidence index, capacity utilization rate, consumer price index data, BIST-100 index, were supplied from TUIK, BIST and Central Bank data. Some of the macroeconomic indicator data collected between January 2007 and February 2020 are as shown in Table 2.

The data used in this study are not seasonally adjusted due to the ability of ANN to learn seasonal patterns during training, as the process of seasonalization of the data may eliminate the non-linear feature of the data (Polat et al., n.d.).

Table 2. Instance macroeconomic indicator data of 2007

Years	Months	Economic Confidence Index	Industrial Production Index	Real Sector Confidence Index	Consumer Confidence Index	The capacity utilization rate	Consumer price index	BIST 100 index
2007	January	113,2	60,2	117	78,6	80,4	135,84	41182,55
2007	February	110,4	60,8	113,3	79,5	78,7	136,42	41430,99
2007	March	110,7	70	113,7	79,2	81	137,67	43661,12
2007	April	111,9	66,2	115,9	80,4	82,1	139,33	44984,45
2007	May	106,1	71,4	106,8	81,7	82,8	140,03	47081,49
2007	June	109,7	70,7	109,7	80,9	83,8	139,69	47093,67
2007	July	111	69,2	111,1	82,3	84,1	138,67	52824,89
2007	August	113,7	68,5	113,8	85	81,8	138,7	50198,6
2007	September	112,4	70,9	110,8	83,9	82,9	140,13	54044,22
2007	October	109,5	70,3	108	83	83	142,67	57615,72
2007	November	108,9	75,3	109	79,3	82,5	145,45	54213,82
2007	December	110,4	68	110,5	80,7	80,7	145,77	55538,13

$$X' = \frac{X - X_{min}}{X_{max} - X_{min}}$$

(1)

As the input of the network, 142 data sets consisting of economic confidence index, industrial production index, real sector confidence index, consumer confidence index, capacity confidence index and CPI data were created. It is aimed to estimate 142 BIST-100 index values at the exit. As the test data set, 16 data sets that have never been shown to the network before and expected to forecast by network outputs were used. Looking at the design of the artificial neural network, there is an input layer consisting of 6 neurons, an intermediate layer and an output layer consisting of 1 neuron (Figure 6). Different results were observed by trying the number of neurons in the intermediate layer between 14-20. The number of iterations was determined as 1000. Levenberg-Marquardt as training function and sigmoid transfer function as activation function were used.

There are some indicators used in the performance evaluation of the artificial neural network. MAE, RMSE, MSE, MAPE, R2 values are the main indicators. Since R2 represents accuracy, it is expected to be high. On the other hand, MAE, RMSE, MSE values are expected to be low since they express the error (Gültepe, 2019; Kantar, n.d.). R2 and MSE values are expressed in Table 3 in order to make the best performance evaluation. Looking at the table, the highest educational success was achieved in the interlayer with 19 neurons, the highest verification success in the interlayer with 19 neurons, the highest test success in the interlayer with 15 neurons, and the lowest MSE value in the design with 17 neurons.
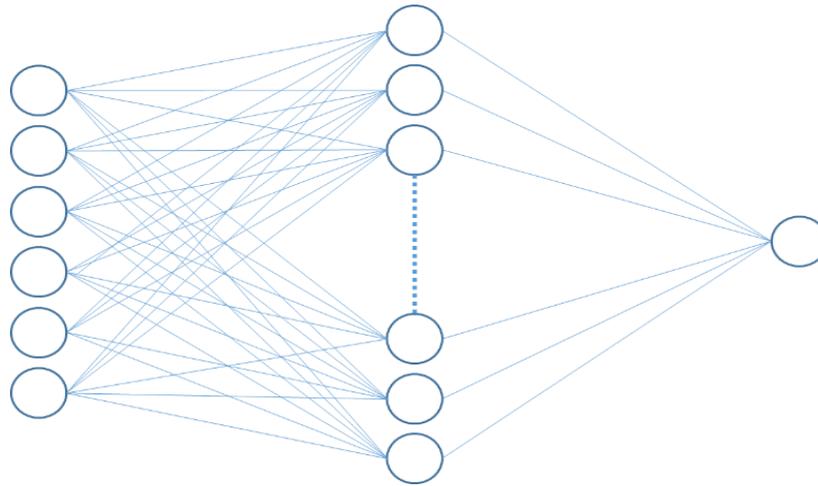
Figure 6. Network topology used in ANN design

Table 3.Regression and MSE outputs

Neuron	Training R	Verification R	Test R	Common R	MSE
14	0.976	0.971	0.973	0.974	0.0024
15	0.973	0.956	0.988	0.973	0.0046
16	0.977	0.960	0.973	0.973	0.0039
17	0.964	0.984	0.978	0.969	0.0017
18	0.971	0.966	0.982	0.972	0.0042
19	0.984	0.985	0.983	0.983	0.0020
20	0.975	0.971	0.977	0.973	0.0037

On the other hand, in the literature, MAPE error rate is defined as "very good" if it is below 10%, and "good" if it is between 10% and 20% (Aslay et al., 2013). In this design, the system performance can be described as good according to the MAPE error value of 15% in Table 4.

Table 4. Error indications

MAE	0,12913237
RMSE	0,161739872
MAPE	0,151930796

Table 5 shows some of the ANN output values obtained by using BIST-100 index values and different neuron numbers. Outputs and expected outputs of 16 BIST-100 index test data estimated by ANN are as shown in Figure 7.
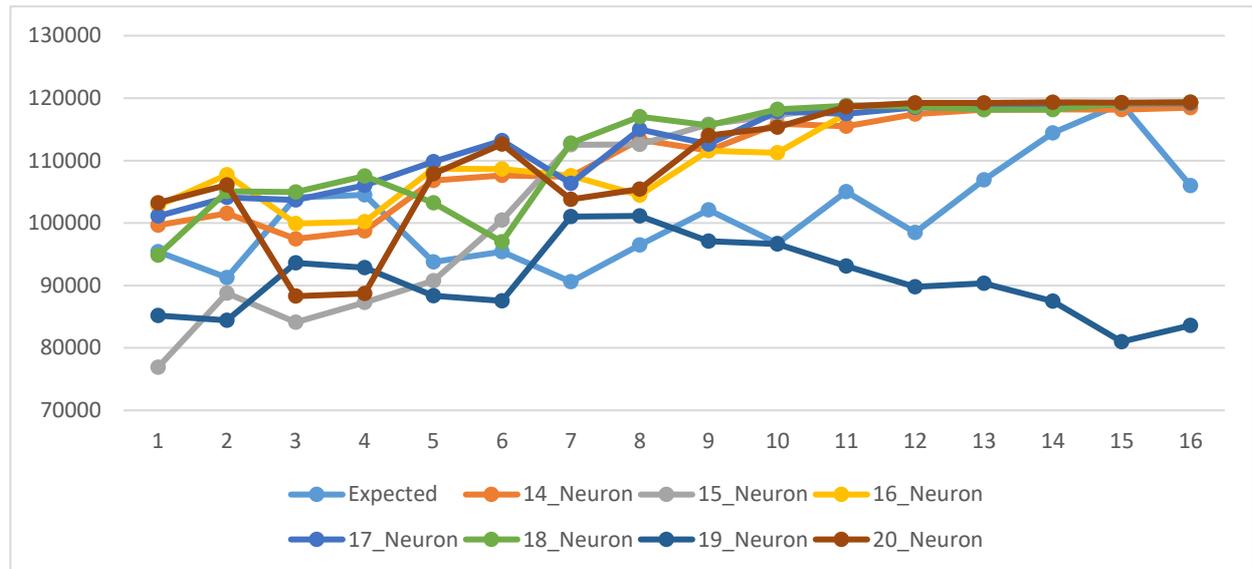
Figure 7. Graphical representation of network outputs with different neuron numbers.

Table 5.Network outputs with different number of neurons

Expected BIST 100	14_Neuron	15_ Neuron	16_ Neuron	17_ Neuron	18_ Neuron	19_ Neuron	20_ Neuron
95416,03001	99626,44088	76896,78811	102761,6282	101113,4725	94838,04941	85203,23958	103213,6023
91270,47997	101518,0027	88759,49948	107742,9367	104107,4838	105094,479	84418,73287	106114,9394
104074,22	97472,25083	84089,49356	99919,08956	103674,549	104989,3707	93597,84694	88280,59886
104529,93	98752,30721	87259,88061	100238,0547	106041,3548	107506,5899	92863,78531	88714,47789
93784,18001	106797,6727	90746,40245	108682,1674	109825,6138	103249,9089	88358,96403	107856,4136
95415,56998	107604,6642	100458,9535	108639,8637	113197,5794	96994,20843	87534,17284	112621,84551
90589,72997	107403,0593	112520,6731	107567,1162	106334,2097	112808,5974	101019,379	103805,0047
96485,32001	113375,7686	112565,5519	104471,1411	114991,9669	117046,4639	101139,6079	105414,6465

Conclusions

In this study, macroeconomic indicators such as economic confidence index, industrial production index, real sector confidence index, consumer confidence index, capacity utilization rate, consumer price index data, BIST-100 index, which are found to have causality and relationships, It is aimed to show the relationship between the output values of the model and the actual values by presenting the prediction model with the artificial neural networks with strong predictive direction. As a data set, 158 data of economic confidence index, industrial production index, real sector confidence index, consumer confidence index, capacity utilization ratio,

consumer price index, BIST-100 index between 2007 January and February 2020 are included in the model.

While some researchers state that the interaction of macroeconomic values, which is stated to have an interaction in the literature, on the BIST-100 index is consistent, it is seen by the research results that the same indicators do not interact by others. When we look at Figure 7 where the criteria we have determined based on these expressions the artificial neural network is trained and the estimation harmony of the estimation outputs with the real values is shown it is seen that the predicted values make serious deviations after a certain trend of harmony with the stock market index. Changes in the number of neurons in the model show that this change affects the predictive power of the model. However, even the model with 19 neurons that are fully compatible among the changes in the number of neurons was not sufficient to catch the trend of perfect harmony with the real values. Looking at the model from this point of view, the situations considered for the causes of incompatibility can be a suggestion for new study topics to investigate and strengthen this model. These situations,

- It can be stated that not every macroeconomic indicator with causality and relationship interaction is suitable for the BIST-100 index. In this viewpoint, the data set that constitutes the input variables should be free from the effects that would cause deviations by using the necessary statistical tools, and the model should be tried again. As a result, if the harmony trend is still not caught, input variables should be rearranged.
- In this study, the possibility of making changes in the parameters provided to us by the Matlab® NNTool that we use in the prediction model is limited. More advanced uses of this tool provide flexibility in these parameters, and if a new study is done in this way, more harmonious results can be obtained.
- Other than normalization, no purification process was done in the data set. The fact that the data set is made in the long term may cause seasonal effects to cause deviation. The new seasonally adjusted data set can contribute to achieving forecast trend fit.

Apart from the reasons mentioned above, factors not stated here may cause the trend of adjustment to deteriorate. It is suggested that all of these reasons will contribute to the development of the model proposed in the study and will be useful for the development of forecasting models among macroeconomic indicators.

However, if there is no margin of error in this prediction model, which is made with the indicators whose interaction is revealed as a result of the literature research, this article will have put forward a supportive result for the studies that incorrectly express the harmony between the relevant indicators.

References

A. Emin. (n.d.). Yapay Sinir Ağları Modelleri ile Hisse Senedi Piyasası Tahminleri: Literatür Analizi ve İMKB-30 Endeksi Üzerine Bir Uygulama. İstanbul Üniversitesi İktisat Fakültesi Mecmuası, 59(1), 55-108.

Aktaş, M., & Akdağ, S. (2013). Türkiye'de Ekonomik Faktörlerin Hisse Senedi Fiyatları ile İlişkilerinin Araştırılması. In International Journal Social Science Research (Issue 2).

Aslay, F., & Özen, Ü. (2013). Meteorolojik Parametreler Kullanılarak Yapay Sinir Ağları ile Toprak Sıcaklığının Tahmini. Politeknik Dergisi Journal of Polytechnic Cilt, 16(4), 139–145. doi: 10.2339/2013.16.4

Ay, B. (2019). İmalat Sanayi Kapasite Kullanım Oranı ve Reel Kesim Güven Endeksi Arasındaki İlişki: Türkiye İçin Ampirik Bir Çalışma. The Journal of Social Science. doi: 10.30520/tjsosci.525025

Bremmer, D. (2008). Consumer confidence and stock prices. In 72nd Annual Meeting of the Midwest Economics Association Hyatt Regency, Chicago, Illinois.

Çalışkan, M. M. T., & Deniz, D. (2015). Yapay Sinir Ağlarıyla Hisse Senedi Fiyatları ve Yönlerinin Tahmini. Eskişehir Osmangazi Üniversitesi İİBF Dergisi, 10(3), 177-194.

Çevik, K. K., & Dandıl, E. (2012). Yapay sinir ağları için net platformunda görsel bir eğitim yazılımının geliştirilmesi. Bilişim Teknolojileri Dergisi, 5(1), 19-28.

Chauhan, S., & Prema, K. v. (2012). Car classification using artificial neural network. Int. J. Sci. Res. Publ, 2(12), 1-4.

Coskun, M., Kiraci, K., & Muhammed, U. (2016). Seçilmis Makroekonomik Degiskenlerle Hisse Senedi Fiyatlari Arasindaki Iliski: Türkiye Üzerine Ampirik Bir Inceleme/Relationship Between Stock Prices and Selected Macroeconomic Variables: An Empirical Study. Finans Politik & Ekonomik Yorumlar, 53(616), 61.

Dizdarlar, H. I., & Derindere, S. (2008). Hisse senedi endeksini etkileyen faktörler: imkb 100 endeksini etkileyen makro ekonomik göstergeler üzerine bir araştırma. Yönetim Dergisi: İstanbul Üniversitesi İşletme Fakültesi İşletme İktisadı Enstitüsü, 19(61), 113-124.

Erk, H., & Soytaş, U. (2011). Bileşik öncü gösterge ve sektörel endeksler arasındaki ilişki. Dokuz Eylül Üniversitesi İİBF Dergisi, 79–91.

Eyüboğlu, K., & Eyüboğlu, S. (n.d.). Ekonomik Güven Endeksi İle Hisse Senedi Fiyatları Arasındaki İlişkinin İncelenmesi: Türkiye Örneği.

Gültepe, Y. (2019). Makine Öğrenmesi Algoritmaları ile Hava Kirliliği Tahmini Üzerine Karşılaştırmalı Bir Değerlendirme. Avrupa Bilim ve Teknoloji Dergisi, (16), 8-15.

Herve, D. B. G., Chanmalai, B., & shen, Y. (2011). The study of causal relationship between stock market indices and macroeconomic variables in Cote d'Ivoire: Evidence from error-correction models and Granger causality test. . International Journal of Business and Management, 6(12), 146.

Kantar, L. (n.d.). Bist 100 Endeksinin Yapay Sinir Ağları ve Arma Modeli ile Tahmini. Muhasebe ve Finans İncelemeleri Dergisi, 3(2), 121-131.

Karaatlı, M., & Halvacıoğlu, Ö. C. (2012). Yapay Sinir Ağları Yöntemi ile Otomobil Satiş Tahmini. Uluslararası Yönetim İktisat ve İşletme Dergisi, 8(17), 87-100.

Kaya, İ., Oktay, S., & Engïn, O. (2005). Kalite Kontrol Problemlerinin Çözümünde Yapay Sinir Ağlarının Kullanımı. In Erciyes Üniversitesi Fen Bilimleri Enstitüsü Dergisi (Vol. 21, Issue 2).

Kaya, V., Kara, O. (2013). Hisse Senedi Getirilerini Etkileyen Makroekonomik Değişkenler 2002-2012 Türkiye Örneği. In Dumlupınar Üniversitesi Sosyal Bilimler Dergisi-Sayı.

Kocabıyık, T., & Fattah, A. (2020). Makroekonomik Değişkenlerin Borsa Endeksleri Üzerine Etkisi: Türkiye ve ABD Karşılaştırması. Finansal Araştırmalar ve Çalışmalar Dergisi. doi: 10.14784/marufacd.691108

Koyuncu, T. (2018). BİST-100 Endeksinin Makroekonomik Değişkenler ile İlişkisi: Ampirik Bir Çalışma. Finans Ekonomi ve Sosyal Araştırmalar Dergisi. doi: 10.29106/fesa.423051

Masuduzzaman, S. M. (2012). Impact of the macroeconomic variables on the stock market returns: The case of Germany and the United Kingdom. Global Journal of Management and Business Research 12.16.

Mumcu Küçükçaylı, F., & Yüce Akıncı, G. (2018). 17. Uik Tüketici Güveninin Makroekonomik Belirleyicileri: Bir Zaman Serisi Analizi. Uluslararası İktisadi ve İdari İncelemeler Dergisi. doi: 10.18092/ulikidince.433056

Nasuhoğlu, H. (2019). Eczacılık sektöründe yapay sinir ağları ve zaman serileri analizi ile talep tahmini. (Master's Thesis, Maltepe Üniversitesi, Fen Bilimleri Enstitüsü).

Öztemel, E. (2003). Yapay sinir ağlari. PapatyaYayincilik, Istanbul.

Öztürk, K., & Şahin, M. E. (2018). Yapay Sinir Ağları ve Yapay Zekâ'ya Genel Bir Bakış. 6(2), 25–36.

Polat, O., & Temurlenk, S. (n.d.). YSA Metodolojisi ile Makroekonomik Zaman Serilerinde Öngörü Modellemesi. Retrieved from http://www.tcmb.gov.tr/yeni/duyuru/2010/DUY2010-03.htm

Saatçioğlu, D. (2016). Yapay Sinir Ağları Yöntemi İle Aralıklı Talep Tahmini. Beykoz Akademi Dergisi, 4(1), 1–32. doi: 10.14514/byk.m.21478082.2016.4/1.1-32

Sayılgan, G., & Süslü, C. (2011). Makroekonomik Faktörlerin Hisse Senedi Getirilerine Etkisi: Türkiye ve Gelişmekte Olan Piyasalar Üzerine Bir İnceleme. BDDK Bankacılık ve Finansal Piyasalar Dergisi, 5(1), 73–96.

Uzun, U., & Güngör, B. (n.d.). Borsa Endeksleri ile Ülkelerin Seçilmiş Makroekonomik Göstergeleri Arasındaki İlişkinin Uluslararası Boyutta İncelenmesi.

Volkan Topuz, Y. (2011). Tüketc Güven ve Hsse Sened Fyatları Arasındak Nedensellk Lşks: Türkye Örneğğ * The Causalıty Relatıon Between Consumer Confidence And Stock Prıces: Case Of Turkey Öz (Vol. 7).

Vuran, B., & Akkum, T. (2005). Türk sermaye piyasasındaki hisse senedi getirilerini etkileyen makroekonomik faktörlerin Arbitraj Fiyatlama Modeli ile analizi. İktisat İşletme ve Finans, 20(233), 28-45.

Yakut, E., Elmas, B., Selahattin, Y. (2014). Yapay Sinir Ağları Ve Destek Vektör Makineleri Yöntemleriyle Borsa Endeksi Tahmini Predicting Stock-Exchange Index Usıng Methods Of Neural Networks And Support Vector Machınes. In Suleyman Demirel University The Journal of Faculty of Economics and Administrative Sciences Y (Vol. 19, Issue 1).

Yılmaz, B. (2019). Maliyet Fonksiyonun Belirlenmesinde Yapay Sinir Ağı Modellerinin Kullanımı. Muhasebe ve Finansman Dergisi, 329–344.

Effects of Carbofuran on Egg Production and Heart Rate in *Daphnia magna* (Crustacea: Cladocera)

Buket Çağla BÖLÜKBAŞI[1]
Esra AKAT[2]

Introduction

Carbofuran is a type of pesticide used as an insecticide, nematicide, and acaricide in agricultural lands. It is soluble in water and moderately persistent in soil. Carbofuran can cause health problems such as diarrhea, increased blood pressure, breathing difficulty, vomiting, sweating. at high doses, deaths have been reported due to respiratory problems (Kuswandi et al., 2017; Shanthamma et al., 2022).

Daphnia genus known as the water fleas has a key role in the food web of freshwater ecosystems such as ponds, lakes, and streams (Mergeay et al., 2006), since they are the food source of invertebrates and fish. Water fleas feed on algae, protozoans, bacteria, cyanobacteria, and small particles suspended in the water. In addition, daphnids improve water quality as they consume algae (Tatarazako and Oda, 2007; Dietrich et al., 2010).

Daphnia generally serves as a model organism in biological experiments (Ebert, 2005). Hypersensitive behavioral and physiological responses of water fleas are the parameters used as biomarkers of the effects of chemical substances. Additionally, they were used in distinct research approaches such as eco/toxicology, ecology, reproductive and ageing biology, and evolution (Barata et al., 2005; Ebert, 2005). Currently, testing with the use of *D. magna* is one of the most widely used ways in the toxicity evaluation of pharmaceuticals including antidepressants, anti-inflammatory drugs, antibiotics, anticancer drugs, beta-blockers, and lipid-regulating agents (Villegas-Navarro et al., 2003).

Daphnia is a colorless animal due to the transparent chitinous carapace. This feature allows for examining the heart rate via light microscope. Its heart is myogenic and has circadian rhythm initiated in the cardiac muscular tissue (Kaas et al., 2009). *Daphnia*'s heart has high sensitivity to various factors. Therefore, it is one of the most widely used physiological parameter in toxicology tests. This study was designed to understand the effects of Carbofuran on non-target organism, *D. magna*. The effects of Carbofuran on egg production and heart rate of *D. magna* were analyzed.

Material and Methods

The present study was performed with *D. magna* which we have cultured in the laboratory for more than three years. Water fleas were maintained in aerated fresh water at temperature of 20-22 °C with a 14 h light and 10 h dark cycle. Stock solutions were prepared by dissolving Carbofuran in fresh water. Three different concentrations of Carbofuran (3, 6, 12 μg/L) were diluted from the stock solution. The culture medium was renewed every day. Water fleas were fed with a mixture of

---

[1] Undergraduate Student, Ege University, Biology
[2] Assoc. Prof. Dr., Ege University, Biology

Spirulina microalgae and TetraPond fish food once a day. Each beaker contained 60 mL solution and ten daphnids. All experimental samples were made in triplicate. Ten adults (older than 14 d) were used for heart rate analysis. Each daphnid was transferred on a slide with a drop of the culture medium and examined by light microscopy. Heartbeats of each daphnid were recorded in slow motion by a video camera for 10 seconds. Changes in heart rate of *D. magna* were examined for 96 h. Additionally, a 21-day reproductive test was carried out with neonates (<24 h). The number of eggs per individual in each experimental group was noted. Data were presented as mean with standard deviation. The differences were compared for statistical significance by one-way ANOVA with post hoc analysis using Tukey test. Statistical evaluations were carried out via PASW statistics (SPSS) 18 software. We set the significance level at $p<0.05$.

Results

The effects of Carbofuran on heart rate and egg production of *D. magna* were evaluated in this study. Heart contractions were visually counted by slowing down the speed of video playback. The number of eggs per individual was also counted in each group for 21 days. *D. magna* has 10 pairs of appendages which are antennae, antennules, maxillae, and mandibles followed by 5 thoracic limbs on the trunk. Additionally, there is a pair of abdominal claws at the end of the abdomen. The heart of *D. magna* is located dorsally and in front of the brood chamber (Figure 1). The water fleas, which were not exposed to any chemicals, lived for 35-40 days under laboratory conditions.

Figure 1. Adult *Daphnia magna* of control group. The spherical heart is located on the dorsum of animal and in front of the brood chamber. There is one egg in the brood chamber. Scale bar = 500 μm

As a result of the exposure to Carbofuran, an increase in the heart rate was examined depend on concentration gradients. Heart rate changes were statistically significant in the high-dose group compared to control. The highest heart rate was examined in the high-dose group at 72 h. Although the heart rate increased in the first 72 hours in the treatment groups, it was observed that the heart rate tended to decrease at the 96th hour. The heart rate of the low-dose group was similar to that observed in control. Data related to heart rate (mean ± s.d.) for each group were presented in Table 1.

The eggs were observed in the brood chamber located dorsally beneath the carapace of *D. magna*. The embryos hatched from the eggs after about 1 day at 20-22 °C but they remained in the brood chamber for further development. After 2-3 days, the young individuals were released by the mother daphnid from the brood chamber. Although the newborn looked more or less like the

adult daphnid, the brood chamber was not developed in newborn individuals. The period of first brood and first egg production took 9-10 days in the control group, whereas they were 12-13 days in the high and medium-dose groups. The number of neonates per water flea also decreased prominently in all treatment groups. Generally, exposure to Carbofuran gave rise to a decrease in egg production of treatment groups. The lowest egg production was mainly observed in the high-dose group. Our values were presented in the bar chart (Figure 2).

Experimental Groups	24 h	48 h	72 h	96 h
Control	358.8±18.14	395.4±63.27	380.2±30.61	360±37.30
3 µg/L	364±27.27	392.6±26.75	406.2±41.11	376±16
6 µg/L	412±32.12	420.2±33.35	419.4±68.51	382±41.47
12 µg/L	445.4±20.99	464±41.08	477.4±42.84	409.2±41.16

Table 1. The mean and standard deviation (mean ± s.d.) of *Daphnia magna* heart rate in the control group and treatment groups with different concentrations of Carbofuran were presented.
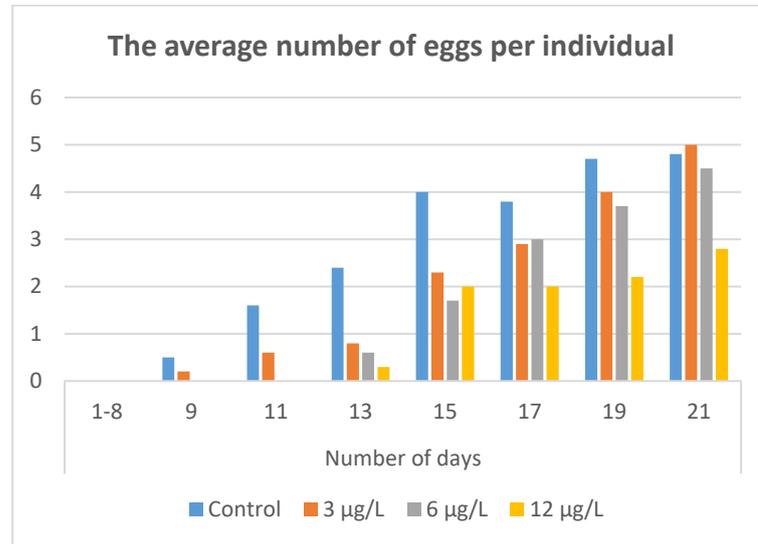
Figure 2. The graph shows the average number of eggs per individual in the control group and the treated groups with different concentrations of Carbofuran for 21 days.

Discussion

Daphnia, *Moina,* and *Ceriodaphnia* among the cladocerans have been mainly used in aquatic toxicity assessments for a long time (Thorp and Covich, 2009). Cladocera has an open circulatory system as opposed to the closed circulation of vertebrates. *Daphnia*'s heart has no chambers or valves (Monahan-Earley et al., 2013). Due to their high sensitivity, the effects of environmental factors on the heart rate of daphnids have been examined in many studies. In this study, the effects of different concentrations of Carbofuran on *D. magna* were evaluated in terms of physiological parameters including variability of the heart rate and egg production.

After exposure to Carbofuran, an increase in heart rate of treatment groups was observed compared to the control group, depending on the concentration levels of this compound. The most increased heart rate was observed after 72 h in water fleas treated with 12 µg/L (477.4±42.84 bpm). Bownik et al. (2017) reported that stimulated heart rate at 25 mg/L and 50 mg/L of the

neonicotinoid insecticide acetamiprid on the other hand, reducing effect at its highest concentration (100 mg/L). The most decreased heart rate was observed after 48 h in water fleas treated with 100 mg/L (132 ± 40 bpm). The daphnids exposed to acetamiprid at 25 mg/L showed stimulated heart rate compared to the control (445 ± 25 bpm). The highest heart rates were indicated after 24 h (538 ± 20 bpm) and 48 h (502 ± 32 bpm), however it reduced to 380 ± 55 bpm after 72 h. Similar stimulatory effects were also reported at 50 mg/L, however the reduction of heart rate was more prominent at 72 h (300 ± 45 bpm).

Contrary to our findings, a decrease in heart rate was observed in some studies. Bownik and Szabelak (2021) reported that fipronil at concentrations 1 μg/L, 10 μg/L, and 100 μg/L reduced water flea heart rate after a 24 h exposure, when compared to the control. Reduce heart rate may result from a direct interaction of fipronil with receptors for gamma aminobutyric acid and glutamic acid in neurons regulating cardiac activity of daphnid. Another study also showed that an organochlorine pesticide, Methoxychlor reduced the heartbeat in *D. magna*. After 24 h of exposure, prominent decreases in heart rate were observed between the control and 10 μg/L, 1 μg/L and 10 μg/L, 2.5 and 10 μg/L, 5 and 10 μg/L treatment groups, respectively.

D. magna bioassays are very important in providing valid estimates relevant toxicity of pesticides on aquatic communities and serve as a useful indicator for water quality. Developmental and reproductive phases in *D. magna* were affected by toxaphene, acetochlor, and cyanazine at different concentrations found in surface waters (Kashian and Dodson, 2002). There are diverse pathways in which pollution can affect the life cycle of *D. magna*. Our results showed that very early-stage *D. magna* (neonates <24 h) reduced egg production after 21 days of exposure to Carbofuran. The lowest egg production was mainly observed in the high-dose group. Additionally, compared to the control group, the day of first egg production were considerably delayed in the high and medium-dose groups. A similar result was noted by Aksakal (2019). After exposure to thifluzamide the period of the first brood and first egg production were significantly delayed in a dose-dependent effect. The first brood days and the first egg production days were 6.2 and 8.2 days in the control groups, whereas they were 8.4 and 10.1 days in the 2.5 mg/L thifluzamide treatment groups, respectively. The number of neonates per water flea also decreased prominently in all treatment groups. Another study showed that significant reduction of egg production in the water flea *D. magna* in the lowest exposure concentrations of 0.50, 0.08 and 0.40 mg/ L, for Diclofenac, Acetaminophen, and Ibuprofen, respectively (Du et al., 2016). It was also reported that Fenoxycarb had a significant negative impact on survival of the hatched individuals of *D. magna* (Navis et al., 2013). Marcial and Hagiwara (2007) noted that a euryhaline rotifer, *Brachionus plicatilis* hatching rates were severely affected by diazinon.

Conclusion

The current study revealed that Carbofuran alters egg production and heart rate of *D. magna*. Our results also demonstrate that physiological parameters such as the heart rate and egg production may be considered as sensitive, early biomarkers of toxicity in the cladocerans.

Acknowledgements

References

Aksakal, F. İ. (2019). Acute and chronic effects of thifluzamide on *Daphnia magna*. Turk J Zool, 43(6), 554-559.

Barata, C., Varo, I., Navarro, J.C., Arun, S., Porte, C. (2005). Antioxidant enzyme activities and lipid peroxidation in the freshwater cladoceran *Daphnia magna* exposed to redox cycling compounds. Comp. Biochem. Physiol. C Toxicol. Pharmacol. 140 (2), 175–186.

Bownik, A., Pawłocik, M., Sokołowska, N. (2017). Effects of neonicotinoid insecticide acetamiprid on swimming velocity, heart rate and thoracic limb movement of *Daphnia magna*. Pol. J. Nat. Sci, 32, 481-493.

Bownik, A., Szabelak, A. (2021). Short-term effects of pesticide fipronil on behavioral and physiological endpoints of *Daphnia magna*. Environ Sci Pollut Res, 28(25), 33254-33264.

Dietrich, S., Ploessl, F., Bracher, F., Laforsch, C. (2010). Single and combined toxicity of pharmaceuticals at environmentally relevant concentrations in *Daphnia magna*–a multi-generational study. Chemosphere 79 (1), 60–66.

Du, J., Mei, C. F., Ying, G. G., Xu, M. Y. (2016). Toxicity thresholds for diclofenac, acetaminophen and ibuprofen in the water flea *Daphnia magna*. Bull Environ Contam Toxicol, 97(1), 84-90.

Ebert, D. (2005). Ecology, Epidemiology, and Evolution of Parasitism in *Daphnia*. National Library of Medicine (US), National Center for Biotechnology Information, Bethesda (MD) http://www.ncbi.nlm.nih.gov/entrez/query.fcgi?db=Books.

Kaas, B., Krishnarao, K., Marion, E., Stuckey, L., Kohn, R. (2009). Effects of melatonin and ethanol on the heart rate of *Daphnia magna*. Impulse 1–8.

Kashian, D. R., Dodson, S. I. (2002). Effects of common-use pesticides on developmental and reproductive processes in *Daphnia*. Toxicol Ind Health, 18(5), 225-235.

Kuswandi, B., Futra, D., Heng, L. Y. (2017). Nanosensors for the detection of food contaminants. In Nanotechnology applications in food (pp. 307-333). Academic Press.

Marcial HS, Hagiwara A (2007) Effect of diazinon on life stages and resting egg hatchability of rotifer *Brachionus plicatilis*. Hydrobiologia 593(1),219-225

Mergeay, J., Declerck, S., Verschuren, D., de Meester, L. (2006). *Daphnia* community analysis in shallow Kenyan lakes and ponds using dormant eggs in surface sediments. Freshw Biol 51, 399–411.

Monahan-Earley, R.; Dvorak, A.M.; Aird, W.C. (2013). Evolutionary origins of the blood vascular system and endothelium. J Thromb Haemost 11, 46-66.

Navis, S., Waterkeyn, A., Voet, T., De Meester, L., Brendonck, L. (2013). Pesticide exposure impacts not only hatching of dormant eggs, but also hatchling survival and performance in the water flea *Daphnia magna*. Ecotoxicology, 22(5), 803-814.

Shanthamma, S., Leena, M. M., Moses, J. A., Anandharamakrishnan, C. (2022). Potential applications of nanosensors in the food supply chain. In Food Engineering Innovations Across the Food Supply Chain (pp. 369-388). Academic Press.

Tatarazako, N., Oda, S. (2007). The water flea *Daphnia magna* (Crustacea, Cladocera) as a test species for screening and evaluation of chemicals with endocrine disrupting effects on crustaceans. Ecotoxicology 16 (1), 197–203.

Thorp, J.H., Covich, A.P. (2009). Ecology and Classification of North American Freshwater Invertebrates; Academic press: Cambridge, MA, USA.

Villegas-Navarro, A., Rosas-L, E., Reyes, J.L. (2003). The heart of *Daphnia magna*: effects of four cardioactive drugs. Comp Biochem Physiol C Toxicol Pharmacol 136(2), 127-134.

Predicting Explosive Weight from Explosion Data with Artificial Intelligence Methods

Dilan ONAT ALAKUŞ[1]
İbrahim TÜRKOĞLU [2]

Introduction

Explosion events originating from explosives are divided into two as controlled and uncontrolled explosions. Examples of controlled explosions are road construction, building destruction, mine blasting etc. explosions. Terrorist attacks and ammunition explosions can be given as examples for uncontrolled explosions. An image of an explosion event is given in Figure 1.

Figure 1. An explosion event

An ignition source, explosive material (solid, liquid, gas) and oxygen are required for an explosion to occur. The combination of these three sources is called the explosion triangle. The effects of an explosion can be grouped under three main headings. These are effects on humans (injuries, deaths, temporary deafness), effects on structures (destruction, glass bursts) and effects on the environment (ground shaking, thermal effects, chemical events). The types of explosion effects are given in Figure 2.

---

[1] Research Assistant, Kirklareli University, Software Engineering, Orcid: 0000-0002-4748-3412
[2] Professor, Firat University, Software Engineering, Orcid: 0000-0003-4938-4167
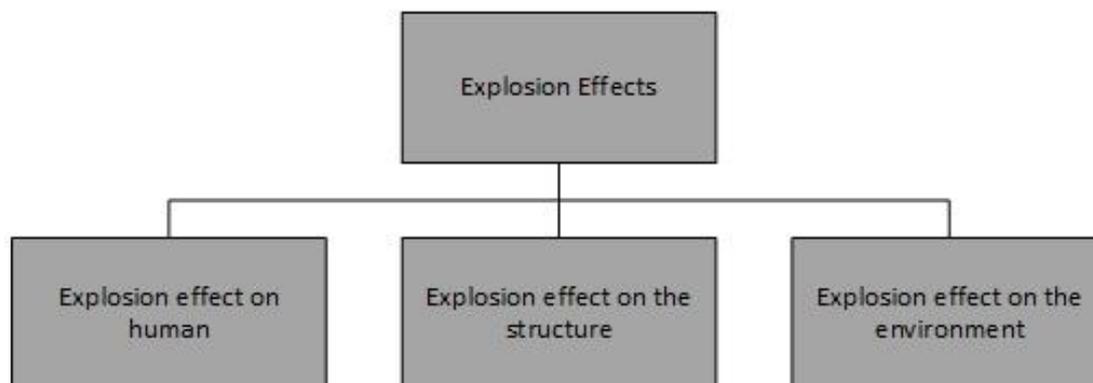
Figure 2. Types of explosion effects

Explosions occur in 3 different ways according to explosive positioning. These are free air blasts, air blasts, and surface blasts. In free air explosions, the explosive is detonated in the air and strikes the structure before it reaches the surface. The blast wave is outward and spherical. In air explosions, the explosive is detonated in the air and reaches the structure after hitting the ground. After hitting the ground, a Mach wave is formed. The blast wave is outward and spherical as in a free air blast. Surface explosions are detonated on the ground or very close to the ground. The blast wave propagates hemispherical and outward. With today's technologies, the explosions mentioned are carried out in a controlled manner and explosion data is obtained. The weight of the explosive is known in advance when these detonations are performed. However, in a possible explosion or uncontrolled explosions, the weight of the explosive is unknown, and its damages can only be determined after the explosion occurs. For these reasons, it is aimed to use artificial intelligence methods to determine the explosive weight and to provide solutions to the mentioned problems.

In this study, the surface explosion was scenarioized and the weight of the explosive was estimated by using artificial intelligence methods. The study consists of three stages. In the first stage, the data of the surface explosion was generated using the Kingery-Bulmash method and the data set was prepared. In the second stage, classification was carried out using the generated data set. In this context, SVM (Support Vector Machines), KNN (K-Nearest Neighbor) and ANN (Artificial Neural Networks) were used in the study. At the last stage, the classification results were examined, and the performances of the classifiers were evaluated. The performance of the classifiers was only measured by the accuracy evaluation criterion. The important points of the study can be expressed as follows;

- In this study, the explosion data set was generated using the Kingery-Bulmash method.
- The generated data set was analyzed using artificial intelligence methods and practical solutions were developed for the mentioned problems.

The remainder of the study is organized as follows. In the second section, various studies carried out with explosion data were examined and the results of these studies were evaluated. In the third section, materials and methods used in the study were emphasized. In the fourth section, the results of the application were given, and the performances of the classifiers were examined. In this section, the performances of the classifiers were compared, and the results were discussed. In the last section, the result of the study was evaluated, and the applications planned for future studies were mentioned.

RELATED STUDIES

In this section of the study, similar studies in the literature are mentioned. Artificial intelligence models used in the studies, prediction performances of these models and simulations are examined. In the study (Silay and Karaci, 2021: 303-315), the researchers estimated the pressure wave parameters with deep learning. Within the scope of the study, firstly simulation was developed, and explosive effect analysis was performed with this simulation. With this simulation, the extreme pressure waves that emerged after the explosion in the environment were accurately predicted and their effects on both people and structures were analyzed. In addition, the pressure data generated, and the explosion was determined using DNN (Deep Neural Network). The pressures of explosions between 1 and 5 meters were estimated and the performance of the classifier was determined by MSE (Mean Squared Error). The MSE value of 20.84 was obtained with the DNN model at the end of the study. In another study, researchers designed an early warning system by developing a shock wave diagram-based deep learning model (Yang et al., 2021: 102862). In the study, firstly, a shock wave diagram was converted into digital expressions by means of a decoder. Then, using CNN (Convolutional Neural Network) architecture, edge extraction was done, and edges were determined. Finally, the ReLU (Rectified Linear Unit) activation function was applied, and important information was obtained. In this way, the features were obtained, and the classification process was carried out. In the classification step, LSTM (Long/Short Term Memory) and SVM were used. The performances of the classifiers were determined by the accuracy evaluation criterion. At the end of the study, the accuracy of the estimation process performed with the LSTM model was 92%, while this rate decreased to 72% with the SVM. In the study (Mohr et al., 2019: 253-260), the researchers determined the damage of the explosions in the city by simulation. In the first stage of the study, aerial images were used and separated into classes by semantic segmentation. Then, the 3D model was created, and the geometric structure of the model was designed. 1, 10, 100 and 1000 kg explosives were simulated in the study. During the estimation process, broken windows and glass were estimated. At the end of the study, 46 windows for 1kg explosives, 105 windows for 10 kg explosives, 319 windows for 100 kg explosives and 363 windows for 1000 kg explosives were estimated as a broken at the end of the study.

MATERIAL AND METHODS

In this study, surface explosion scenarios were created, and the data set was generated by calculating the blast loads using the empirical methods available in the literature. The Kingery-Bulmash method was used while generating the data set. TNT (Trinitrotoluene) explosive type has been standardized as a widely used explosive type in many test explosions and explosion experiments (Grisaro and Edri, 2017: 199-220). For this reason, the calculation of blast loads for explosions originating from different explosives. Different explosives are calculated using the TNT equivalence given in Equation 1.

$$W = W_{exp} \left. H_{exp}^d \middle/ H_{TNT}^d \right. \qquad (1)$$

In the Equation 1, W value is TNT equivalent weight, W_{exp} value is the weight of the explosive, H_{exp}^d value is detonation temperature of the explosive and H_{TNT}^d TNT detonation temperature.

In the generated data set, there are 9 features; time of arrival, incident pressure, reflected pressure, reflected pulse, incident pulse, positive phase duration, shock front velocity, distance, and scaled distance. In addition to these, there are 10 labels in total in the data set. Explosion data up to 40 meters distance were created for each weight and a total of 4,000 data were used. The incident pressure in the data set represents the peak pressure caused by the explosion. The reflected pressure indicates the pressure reflected from the surface of the object it hits in front of the blast wave, while the reflected impulse indicates the pressure at which the explosion acts on the object if there is an object in front of the blast wave. The incident impulse is the impulse resulting from the explosion overpressure. Furthermore, the positive phase time represents the duration of the explosion in the positive phase. Shock front velocity is the velocity of the shock wave resulting from the explosion. Scaled distance is the ratio of the distance between the detonation point and the measurement point to the cube root of the explosive weight. Distance is expressed in meters and weight is expressed in kilograms. In Equation 2, the formula of the scaled distance is given.

$$Z = R / \sqrt[3]{W} \tag{2}$$

In the Equation 2, the Z value is the scaled distance, the R value is the distance to the explosion point, and the W value is the explosive weight.

While creating the explosion scenario, there are many methods to calculate the blast loads. These methods are Kingery and Graham, Brode, Henry, and Kingery-Bulmash. The method chosen in this study is based on whether the detonation is a free air burst, air burst or surface explosion, as well as the weight and distance of the explosive. Kingery and Graham presented equations for calculating blast loads based on a large database of experimental blasts. These data are global air burst loads from chemical explosions and cover the scaled distance $Z > 0.5$ m/kg$^{1/3}$ (Karlos et al., 2016: 409-429). One of the first researchers to publish the relationships for the calculation of explosion parameters was Brode in 1955 (Brode, 1955: 766-775). He published equations in which the peak positive incident pressure, scaled distance in m/kg$^{1/3}$, and the peak overpressure in bar is measured for near-field and mid- to far-field bursts. Henry method was published a set of equations for the calculation of detonation parameters, based on an extensive experimental database. These quasi-experimental equations are similar to those introduced by Brode and relate the peak event overpressure to scaled distance m/kg$^{1/3}$ (Karlos et al., 2016: 409-429). The most accepted method in the field of engineering is the Kingery-Bulmash method. They used polynomial formulations for calculations of both spherical and hemispherical detonation waves. Equations are derived from data from explosive tests using explosive weights from 1 kg to 400,000 kg. For hemispherical detonation waves it can be applied up to the scaled distance $Z=0.05$ m/kg$^{1/3}$. The Kingery-Bulmash general polynomial form is given in Table 1.

Table 1. Kingery-Bulmash general polynomial form

Common algorithm of T = distance in m	C_0, 1, 2, ……. n= constants
$U = K_0 + K_1 * T$	K_0, 1, 2, ……. = constants
$Y = C_0 + C_1 U_1 + C_2 U_2 C_3 U_3 + \cdots, C_n U_n$	

The experimental data generated within the scope of the study were analyzed and classified by various artificial intelligence methods. For this purpose, ANN, KNN, and SVM were used. Artificial intelligence is used effectively today. One of the biggest reasons why it is popular is that data can be obtained more quickly and easily and the hardware needs that can analyze this data can be met (Goodfellow et al., 2018). In addition to these, the use and success of artificial intelligence methods in complex and large data sets are also effective in this sense. Deep learning and machine learning algorithms are at the forefront of artificial intelligence methods. The biggest difference

between deep learning and machine learning algorithms is that features are obtained manually in machine learning (Santur, 2020: 561-570). In cases where the number of data is small, it is easy to obtain the features manually and the complexity is reduced. In addition, deep learning algorithms lose their effectiveness when the number of data does not have enough labels. For these reasons, machine learning algorithms were used rather than deep learning algorithms in the study.

ANNs are computer systems developed with the aim of automatically performing the abilities of the human brain, such as deriving new information, creating, and discovering new information through learning, without any help. Artificial neurons come together to form the ANN. An ANN has an input layer, a hidden layer or layers, and an output layer. Today, ANN is used in computational finance, image processing and computer vision, computational biology, power generation, automotive, natural language processing, etc. Although the KNN algorithm is a learning-based algorithm, it is a method based on transferring data that are close to each other to the same class or cluster. In learning-based algorithms, the learning process is carried out depending on the data in the training set. Each new sample arriving in the data space is compared with the data in the training set and placed in the class or cluster it belongs to according to similarity. Since the KNN algorithm is an easy and understandable algorithm, it is one of the algorithms used in the studies. It is a method used in various fields such as data mining, pattern recognition and security. One of the biggest advantages of the KNN algorithm is that it gives successful results on data containing noise. In addition, it was determined that the algorithm gave successful results as the number of data increased. Among the disadvantages, it can be shown that the classification success depends on the chosen distance calculation method and the k value. Since the distance between the data is calculated one by one, there may be reductions in the performance of the classification. SVM is a machine learning algorithm based on statistical learning theory and developed with consulting learning technique. It was first introduced by Vapnik in 1995, and it was aimed to solve classification problems with pattern recognition (Vapnik, 2000). It was used for the separation of only two-class linear data in the early times, but today it can be used to distinguish both non-linear and multi-class data. The basis of the classification process with SVM is the separation of the data belonging to two different classes with a defined boundary, namely the hyper-plane. With SVM, the most suitable plane is determined by selecting the data at the extreme point in the training data set. These selected data are called support vectors. Choosing the most appropriate hyper-plane positively supports classification and discrimination performance, resulting in more effective results. In short, SVM performs classification by calculating the maximum distance between support vectors (Abe, 2010). The flow chart of the study is given in Figure 3.
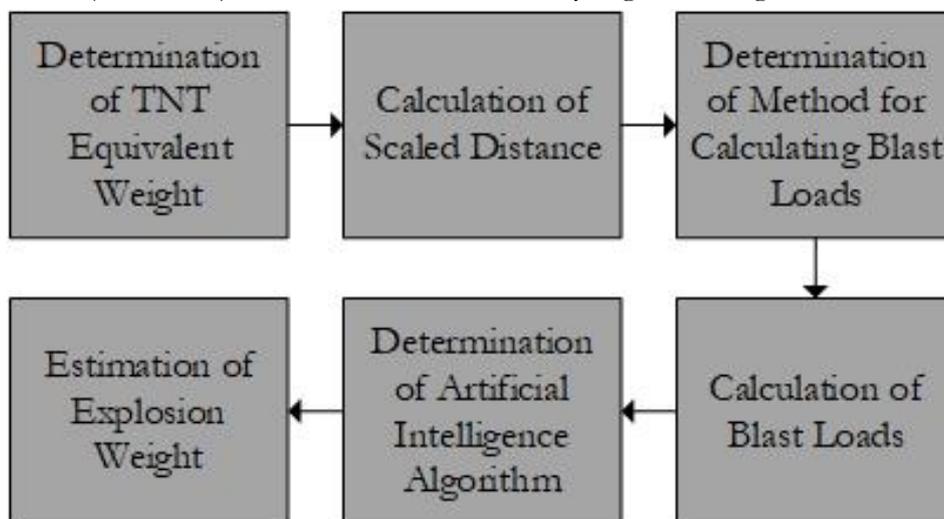

Figure 3. Flow chart of the study

APPLICATION RESULTS AND DISCUSSION

In this study, a controlled surface explosion event is performed. The Kingery-Bulmash method was used to calculate the blast loads. The data were generated by calculating the blast loads and scaled distance within 1-40 meters, during and after the explosion, using a TNT explosive in the range of 1-10 kg. Obtained blast loads are time of arrival (ms), incident pressure (ip/kPa), reflected pressure (rp/kPa), reflected impulse (ri/kPa), incident impulse (i/kPa-ms), positive phase time (ms), shock front velocity (m/s) and scaled distance. Machine learning methods were used to train the data and the performances of the classifiers were determined by the accuracy evaluation criterion. The accuracy values of the classifiers are given in Table 2.

Table 2. Classification results

Classification Method	Accuracy Value
KNN	44.87%
ANN	81.54%
SVM	91.02%

According to the classification results in Table 2, the highest performance was obtained with the SVM classifier, and an accuracy of 91.02% was calculated with this classifier. Then, the ANN algorithm performed an effective classification and the accuracy score of this classifier was 81.54%. The most unsuccessful and ineffective classification process was obtained with the KNN algorithm. The accuracy score obtained with the KNN algorithm was 44.87%. One of the biggest reasons underlying the low results of the KNN algorithm is due to the parameters of the KNN algorithm. There are two main factors in the KNN algorithm: distance and neighborhood value. It is necessary to determine the most effective values for these two parameters. In addition, the KNN algorithm is more effective in data containing noise (Alakus, 2018). In addition, the increase in the number of data positively affects the performance of this algorithm. Determining the ideal parameters and increasing the number of data can increase the performance of this classifier. Although the ANN classifier is not as effective as SVM, it has performed a successful classification process. Changing the activation and sum functions used in the ANN classifier can positively affect the performance of this method. In addition to these, the number of neurons used, the optimization method and the number of iterations also affect the performance of the algorithm. By determining the ideal values for these parameters, an increase in the ANN classifier can be observed. One of the reasons for the high performance of the SVM classifier may be it is a classification algorithm, without parameters. It does not need a specific parameter as in KNN and ANN classifiers. In addition, it has achieved an effective classification because they can model complex decision boundaries and work with a large number of independent variables. In addition to these, there is no memorization as in ANN. Due to these advantages, the highest performance may have been obtained with the SVM classifier. The contributions of the study to the literature can be summarized as follows;

- With this study, surface explosion was simulated, and a data set was generated with the Kingery-Bulmash method.
- With this study, scenarioized explosion data were classified and estimated. In this way, the weight of an explosive of unknown class was estimated.

CONCLUSION

In this study, a surface explosion scenario was created, and the data set was generated. After that, the data were classified with artificial intelligent algorithms. The study consisted of three stages. In the first stage, the data set was formed using the Kingery-Bulmash method. There are 9 features and 10 classes in total in the data set. The explosive type was determined as TNT. In the second stage of the study, artificial intelligence algorithms were determined, and classification was performed. Algorithms used within the scope of the study are SVM, ANN and KNN algorithms. In the last stage, the performances of the used classifiers were evaluated, and the accuracy evaluation criterion was used. At the end of the study, the lowest classification process was performed with the KNN algorithm and an accuracy of 44.87% was obtained. In the classification process performed with the ANN classifier, an accuracy score of 81.54% was calculated. The most effective classification process was carried out with the SVM algorithm. With this algorithm, an accuracy of 91.02% was achieved. With this study, the data generated for the explosion scenario were classified and estimated. In line with the results obtained in this study, the explosions will not need to be simulated and the weights of the new explosives will be estimated before the explosion event occurs with machine learning approaches. In addition to these, the data set generated in the study will be developed for future studies and the number of data will be increased. In this way, there will be no need to create a data set, which is costly in terms of time and labor, and researchers will be able to access this data set.

ACKNOWLEDGMENT

REFERENCES

Abe, S. (2010). Support vector machines for pattern classification. Springer

Alakus, TB. (2018). Emotion detection based on EEG signals by applying signal processing and classification techniques. Firat University, Graduate School of Natural and Applied Sciences

Brode, HL. (1955). Numerical solutions of spherical blast waves. Journal of Applied Physics, 26(6), 766-775

Goodfellow, I., Bengio, Y. and Courville, A. (2018). Deep learning. MIT Press

Grisaro, HY. and Edri, IE. (2017). Numerical investigation of explosive bare charge equivalent weight. International Journal of Protective Structures, 8(2), 199-220. doi: 10.1177/2041419617700256

Karlos, V. Solomos, G. and Larcher, M. (2016). Analysis of the blast wave decay coefficient in the Friedlander equation using the Kingery-Bulmash data. International Journal of Protective Structures, 7(3), 409-429. doi: 10.1177/2041419616659572

Mohr, L., Benauer, R., Leitl, P. and Fraundorfer, F. (2019). Damage estimation of explosions in urban environments by simulation. The International Archives of the Photogrammetry, Remote Sensing and Spatial Information Sciences, 42, 253-260. doi: 10.5194/isprs-archives-XLII-3-W8-253-2019

Santur, Y. (2020). Improving sentiment classification performance using deep learning and undersampling approaches. Fırat University of Journal of Engineering Science, 32(2), 561-570. doi: 10.35234/fumbd.759131

Silay, R. and Karacı, A. (2021). Development of explosive impact analysis simulation software and prediction of pressure wave parameters with deep learning, Duzce University Journal of Science and Technology, 9(6), 303-315. doi: 10.29130/dubited.1014063

Vapnik, VN. (2000). The nature of statistical learning theory. Springer

Yang, H., Du, L. and Mohammadi, J. (2021). A shock wave diagram based deep learning model for early alerting an upcoming public event. Transportation Research Part C, 122. doi: 10.1016/j.trc.2020.102862

Analysis of Tungsten Disulfide Contribution to the Reflected Phase of the Four-Arm Bilayer Nanoantenna Structure

Duygu GÜMÜŞCÜ[1]
Ekin ASLAN[2]
Erdem ASLAN[3]

Introduction

Metamaterials, which are artificial electromagnetic media, consist of metalic or dielectric periodic subwavelength structures. Metasurfaces, which are planar versions of metamaterials, can locally change the light phase, while transmitting or reflecting (Z.-J. Yang et al., 2017: 1–50).

Metasurfaces consist of subwavelength nanostructure arrangements. These arrays are considered as pixels of a desired phase. A flat surface yielding a phase pattern $\phi(x, y)$ required to obtain the desired beamform is divided into individual pixels denoted by ϕ_{ij} as seen in Figure 1, where each pixel ensures a local phase cell (Scheuer, 2017: 137–152).
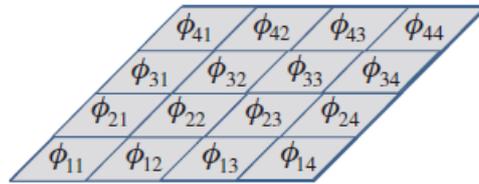
Figure 1. Metasurface phase diagram.

Metasurface designs are realized for beamforming and holography applications. While performing these designs, firstly, it is necessary to design the appropriate phase gradient required to obtain the desired beam shape. Thenit is necessary to design different nanostructures for each phase pixel needed to obtain a target phase shift in the range of $[0,2\pi]$ (Scheuer, 2017: 137–152). Metamolecules derived must be placed on the surface to achieve the desired phase change according to the type of application.

In this study, it is aimed to design different metacells creating a phase gradient in the range of $[0,2\pi]$ by partially coating Au (gold) nanoscatterers with WS_2 (tungsten disulfide). In this scope of work, with the metasurfaces designed by going beyond the diffraction surfaces, both the resonative behaviors will be controlled and the targeted local phase will be achieved with the designs in different geometries.

---

[1] Student, Kayseri University, Department of Electrical and Electronics Engineering, Orcıd: 0000-0002-5666-9665

[2] 2Assist. Prof, Kayseri University, Department of Electrical and Electronics Engineering, Orcıd: 0000-0003-0933-7796

[3] 3Assist. Prof, Erciyes University, Department of Electrical and Electronics Engineering, Orcıd: 0000-0001-6829-9000

Method

The monolayer state of WS_2 is considered in the study (Ermolaev, 2020: 1402). Analyzes are made in the visible region. And simulations of nanoscatterers are made between 365-800 nm wavelengths using the finite difference in time method (FDTD; Finite-difference time-omain) (Aslan and Turkmen, 2017: 259). The Au dielectric function is from Palik, 1985 and the WS_2 dielectric permittivity data is from G. A. Ermolaev, 2020. In the study, the metamolecules are placed in the $xy -$plane and their dimensions in the x and y directions are chosen as Px and Py, and they are called periodicity parameters. A plane wave is placed on the $z -$axis in the system and the width of its source is determined as Px and Py. To obtain a more accurate simulation, a special mesh region will be created to cover the structure 5 nm outside the edges of the structure. The x and y dimensions of the cubes in which the nanoscatter is divided spatially are chosen as 10 nm and the z dimension is 7 nm. In order to measure reflectance and transmission in the far field, power monitors are placed in the far areas of the building, symmetrically to each other. The limits of the monitors are chosen the same as the limits of the FDTD. Throughout the simulations, periodic boundary conditions are used along the $x -$and $y -$axes and perfectly matched layers are used along the $z -$axis. The nanoscattering unit cell is brightened by a plane wave with $y -$polarization in the $z -$direction.

In this study, the antenna design is made in the geometry where the perspective and profile diagram is shown in Figure 2. With the change in the angle between the arms and the rotation of the structure, the phase can be changed in the range of $0 \leq \phi < 2\pi$. The aim of the study is to obtain higher resolution phase steps in the range of $0 \leq \phi < 2\pi$ with the amplitude value kept as high and constant as possible.
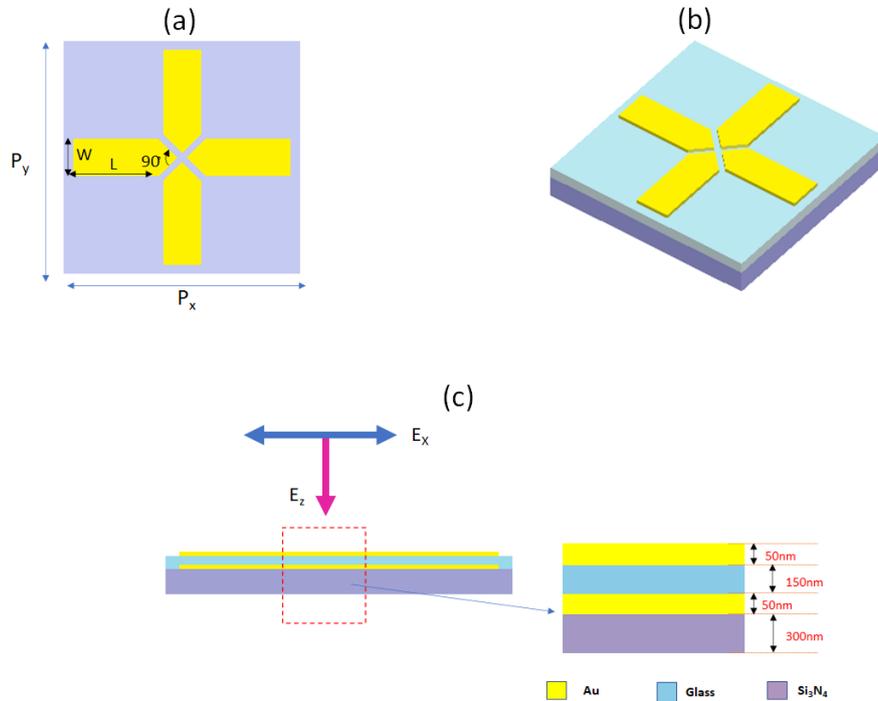

Figure 2. The designed basic antenna structure (a) topview (b) perspective and (c) side views.

Two Au antenna layers are placed on the Si3N4 (silicon nitride) membrane in Figure 2. SiO2 (silicon dioxide) glass material is used between them. And the analysis of these two antenna layers was carried out. Here L is the length of the nanoantenna arms, W is the width of the nanoantenna

arms, and C is the distance between the arms. The angle of the pointed ends of the lower wavelength antenna arms is taken as 90°. The thicknesses of Si_3N_4, SiO_2 and Au layers are adjusted as 300 nm, 150 nm and 200 nm, respectively. While controlling the resonative behavior with the under layer of the antennas in the design, it is aimed to obtain the targeted local phase with the given rotations with the top layer.

Results and Discussions

The reflection and transmission responses of the basic antenna structure are analyzed for different geometric parameters in Figure 3. Based on this graph, the geometric parameters of the design were taken as $L = 900$ nm, $W = 400$ nm, C = 50 nm and $P_x = P_y = 2500$ nm. The reflection and transmission spectra obtained for the selected geometric parameters $L = 900$ nm, $W = 400$ nm, $C = 50$ nm and $P_x = P_y = 2500$ nm are presented in Figure 4. Considering the relevant spectrum, good resonative behaviors are shown at 488 nm wavelength, it is deemed appropriate to choose these parameters.
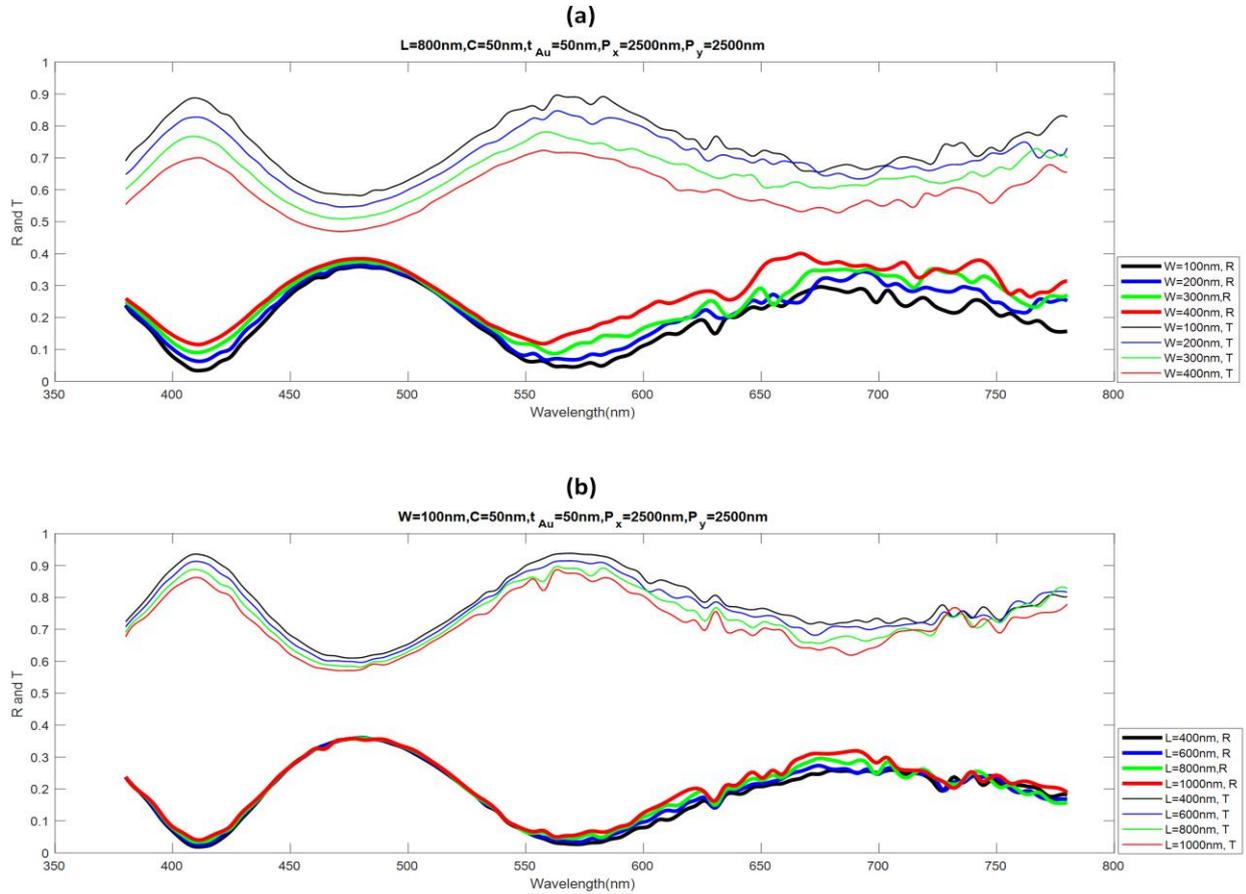

Figure 3. Reflectance and transmittance spectra of the basic antenna structure for different geometric parameters.
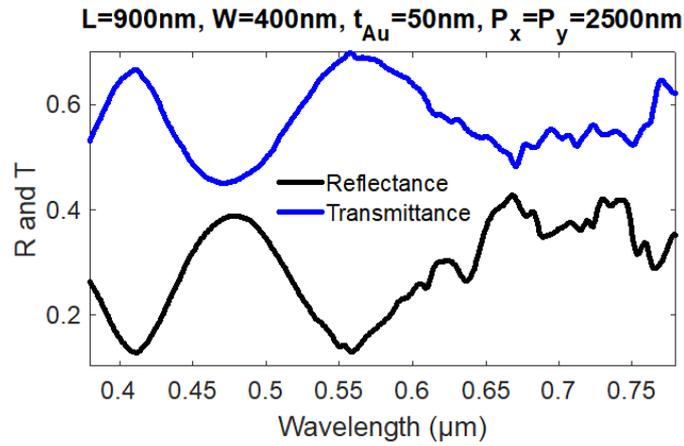
Figure 4. Reflectance and transmittance spectra obtained for geometric parameters L = 900 nm, W = 400 nm, C = 50 nm and P_x = P_y = 2500 nm.

The top antenna layer is supported with WS_2 material to provide higher resolution local phase values at high and constant resonance amplitude values (Figure 5). Transition metal dichalcogenides named as van der Waals materials such as WS_2 have large transmittance values in the visible spectral ranges and can support well-defined Mie resonances because they are patterned (Babicheva and Moloney, 2019a: 2106–2112).

(a)   **(b)**
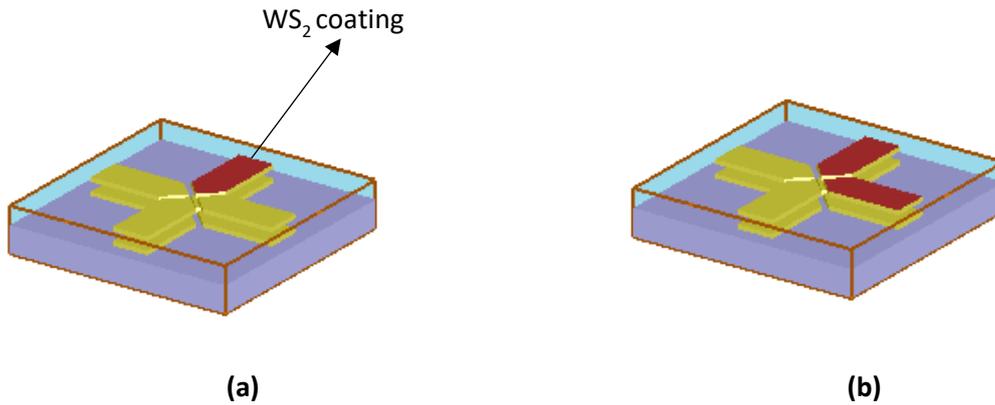
Figure 5. (a) Antenna design with one arm of the top antenna layer supported by WS_2 (b) Antenna design with two arms of the top antenna layer supported by WS_2

Resonant electric field distributions will be used to determine the phase difference of the related antennas. These distributions are shown in Figure 6. Here, the block on the left represents the structureless simulation environment. Number-1-block expresses the electromagnetic propagation caused by the basic antenna structure, resonant wavelengths (Figure 6) at 488 nm, with geometric parameters L = 900 nm W = 400 nm, C = 50nm and P_x = P_y = 2500 nm.
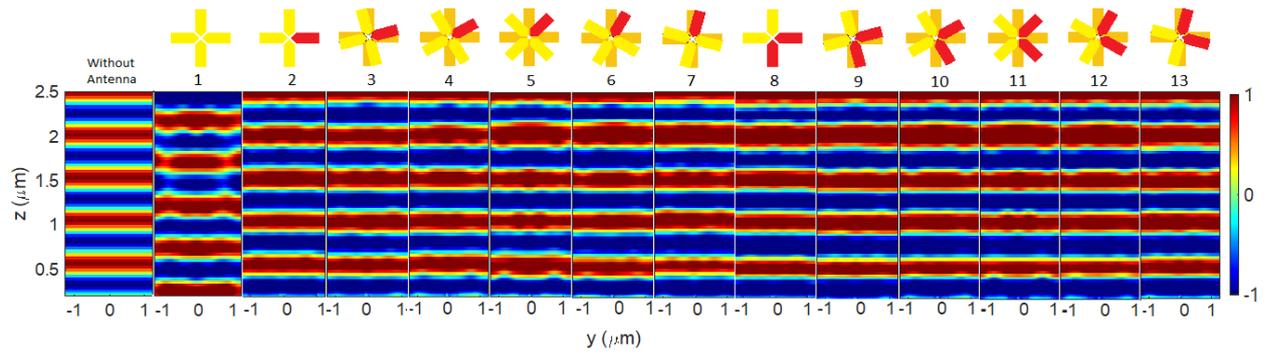
Figure 6. Electric field distributions according to rotation-based antenna types

Blocks 2, 3, 4, 5, 6, 7 shown in Figure 6 contains antenna structure of the unrotated upper antenna layer in which single arm coated with WS_2 monolayer and 15°, 30°, 45°, 60°, 75° rotated ones, respectively. Blocks 8, 9, 10, 11, 12, 13 represents electromagnetic propagation of unrotated antenna structure in which two arms coated with WS_2 film and ones with rotations of 15°, 30°, 45°, 60°, 75°, respectively.

In these spreads, the real values of the E_y distributions formed in the yz −plane ($x = 0$) are obtained. E_x and E_z distributions are not evaluated because they show very small values and do not provide information about the phase difference. Phase difference is calculated only based on the source propagation simulation results and by determining the maximum positive electric field values of the other antennas. Accordingly, where z_1 and z_2 being the maximum positive electric field position taken as the basis and the next maximum positive electric field location, resonant wavelength has been confirmed as $z_2 - z_1 = 488nm$ from the mere source propagation, (Figure 7). Then, in order to calculate the phase difference (PD_{ATENNA}) caused by the antennas; by determining the position $z_1^{antenna}$ of the closest maximum positive electric field value on the field map of the related antenna structure, the difference $z_1^{antenna} - z_1$ is determined. Lastly $PD_{ATENNA} = (z_1^{antenna} - z_1) * 2\pi/(z_2 - z_1)$ equation is used via a direct proportion.
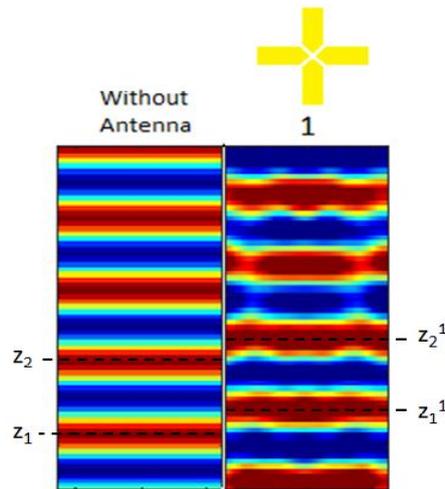
Figure 7. Determination of phase difference from field distributions caused by source only and basic antenna structure

Phase analyzes are carried out by making calculations as above according to all antenna types. Phase difference graph is drawn by using phase analysis values calculated according to different antenna types (Figure 8). The x −axis represents the rotational and non-rotational antenna types

supported by WS$_2$, and the $y-$axis represents the phase difference values obtained from the analyzes of these antennas. As seen in the graph, the coated antennas provide a phase difference with respect to the base antenna, but no significant phase difference can be observed between the coated antennas. By changing the angles between the arms, analyzes are continuing in order to obtain phase values that divide the range of [0,2π] regularly.
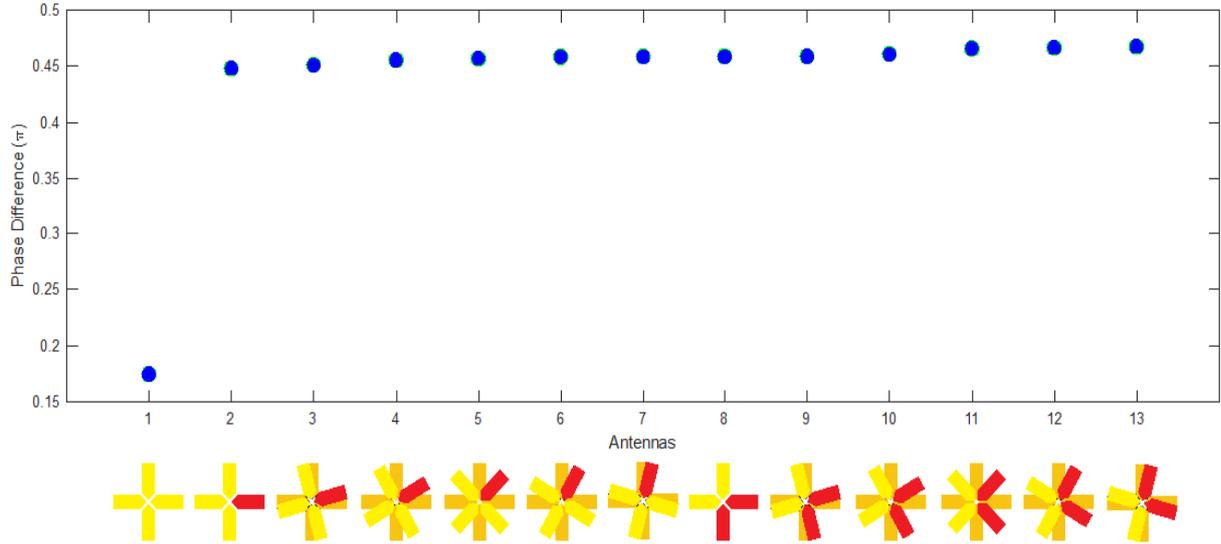

Figure 8. Phase difference graph created by different antenna types

Acknowledgement

References

Aslan, E., Turkmen, M. 2017. "Square fractal-like nanoapertures for SEIRA spectroscopy: An analytical, numerical and experimental study". Sensors and Actuators, A: Physical, 259.

Babicheva, V. E., Evlyukhin, A. B. 2018. "Metasurfaces with Electric Quadrupole and Magnetic Dipole Resonant Coupling". ACS Photonics, 5(5), 2022–2033.

Babicheva, V. E., Gamage, S., Zhen, L., Cronin, S. B., Yakovlev, V. S., Abate, Y. 2018. "Near-Field Surface Waves in Few-Layer MoS2". ACS Photonics, 5(6), 2106–2112.

Babicheva, V. E., Moloney, J. V. 2019a. "Lattice Resonances in Transdimensional WS2 Nanoantenna Arrays". Applied Sciences, 9(10).

Ermolaev, G. A., Yakubovsky, D. I., Stebunov, Y. V, Arsenin, A. V, Volkov, V. S. 2020. "Spectral ellipsometry of monolayer transition metal dichalcogenides: Analysis of excitonic peaks in dispersion". Journal of Vacuum Science & Technology B, 38(1), 14002.

Palik, E. D. 1985. "Handbook of optical constants of solids". Orlando : Academic Press, 1985. Tarihinde adresinden erişildi https://search.library.wisc.edu/catalog/999554063402121

Scheuer, J. 2017. "Metasurfaces-based holography and beam shaping: engineering the phase profile of light". Nanophotonics, 6(1), 137–152.

Yang, W., Xiao, S., Song, Q., Liu, Y., Wu, Y., Wang, S., Tsai, D.-P. 2020. "All-dielectric metasurface for high-performance structural color". Nature Communications, 11(1), 1864.

Yang, Z.-J., Jiang, R., Zhuo, X., Xie, Y.-M., Wang, J., Lin, H.-Q. 2017. "Dielectric nanoresonators for light manipulation". Physics Reports, 701, 1–50.

Zhang, H., Abhiraman, B., Zhang, Q., Miao, J., Jo, K., Roccasecca, S., Jariwala, D. 2020. "Hybrid exciton-plasmon-polaritons in van der Waals semiconductor gratings". Nature Communications, 11(1), 3552.

On Arithmetic Functions

Emre ÖZTÜRK[1]

Introduction

Arithmetic functions have rather rich properties and very useful tool for both in number theory and algebra. Furthermore, they have many implementations in science such as computer science, cryptography, graph theory etc. The essential arithmetic functions are multiplicative and additive functions. Some fundamental multiplicative functions are sigma function, tau (divisor) function, Euler totient function, Möbius function, Dedekind psi function etc. For more details, see (Long, 1972) and (Pettofrezzo & Byrkit, 1970). In (Sierpinski, 1964), Sierpinski stated the following inequalities:

$$\varphi(n) \leq n - \sqrt{n}, \qquad (1.1)$$

if n is a composite natural number, and

$$d(n) \leq 2\sqrt{n}, \qquad (1.2)$$

if n is a natural number. From (1.1) and (1.2) we have,

$$\varphi(n) + d(n) \leq n + \sqrt{n}, \qquad (1.3)$$

where n is composite integer.

In this study, we improve (1.3) by extending n to for all-natural numbers, and we give the following result:

Let n be a positive integer. Then,

$$\varphi(n) + d(n) \leq n + 1, \qquad (1.4)$$

where $\varphi(n)$ is Euler's totient function, and d is the number of positive divisor function.

Moreover, we give nice relations about the elementary arithmetic functions which are Euler's totient function, number of divisor function, and sum of divisor function.

These functions also related with Riemann-Zeta function, Möbius function etc. The implementations of arithmetic functions in number theory and other sciences can be play crucial role, especially understanding the primes and their distributions. The results that obtained in the study will be useful for who works on prime numbers and its applications.

---

[1] Emre Öztürk, Dr., Turkish Court of Accounts, Department of Data Analysis

Method

Let us give some definitions and their properties of well-known arithmetic functions in number theory.

Definition 2.1 Let $n \geq 1$ be a natural number. Number of integers m that satisfy $1 \leq m \leq n$ and $(m, n) = 1$ is shown by $\phi(n)$ where ϕ is called as Euler's totient function.

Example 2.2 If we take $n = 10$, then $\phi(n) = 4$. Because 1,3,7,9 are coprime with 10.

Example 2.3 For big numbers n, we can use Euler's identity. Let $n = p_1^{m_1} p_2^{m_2} \dots p_k^{m_k}$ where $p_1, p_2, \dots p_k$ are distinct primes. Then,
$$\phi(n) = p_1^{m_1-1}(p_1 - 1) p_2^{m_2-1}(p_2 - 1) \dots p_k^{m_k-1}(p_k - 1).$$
So, we can easily calculate $\phi(288)$. Since $288 = 2^5 3^2$,
$$\phi(288) = 2^4 \times 3 \times 2 = 96.$$

Definition 2.4 The cototient of n is defined as $n - \phi(n)$ such that it counts the number of positive integers less than or equal to n that have at least one prime factor in common with n (Browkin & Schinzel, 1995).

Remark. Since $\phi(n) \leq n - \sqrt{n}$ (Sierpinski, 1964), cototient of composite positive integers are always greater than its own square root.

Definition 2.5 Let the divisor function $\sigma_k(n)$ for n an integer is defined as the sum of the kth powers of the (positive integer) divisors of n,
$$\sigma_k(n) = \sum_{d|n} d^k.$$

The function $\sigma_0(n)$ satisfies the identity:
$$\sigma_0(p_1^{a_1} p_2^{a_2} \dots) = (a_1 + 1)(a_2 + 1) \dots$$
where the p_i are distinct primes and $p_1^{a_1} p_2^{a_2} \dots$ is the prime factorization of a number n. In this study we use the notations $d(n)$ and $\sigma(n)$, instead of $\sigma_0(n)$ and $\sigma_1(n)$, respectively (Weisstein, 2022).

Example 2.6 If we factor $n = 72$, it is written $n = 72 = 2^3 \times 3^2$. Then, number of the positive divisor of n can be given by
$$\sigma_0(72) = (3 + 1)(2 + 1) = 12.$$

Theorem 2.7 Let G be a finite cylic group and $|G| = m$. Number of different subgroups of G is equal to number of positive divisors of m (Fraleigh, 1982).

Theorem 2.8 Every cylic group of finite order n is a isomorphic to the additive group $\mathbb{Z}_n$ (Fraleigh, 1982).

Theorem 2.9 Any element a^m of a finite cylic group G of order n is a generator of G if and only if $(m, n) = 1$ (Fraleigh, 1982).

Applications in number and group theory

Theorem 3.1 Let n be a positive integer. Then,
$$\varphi(n) + d(n) \leq n + 1,$$

where φ is Euler's totient function, and d is the number of positive divisors function. In the case of prime numbers n the equality holds.

Proof. Let us show the case of inequality first. Let $\mathbb{Z}_n = \{0,1,2,...,n-1\}$ be a finite additive group $(|\mathbb{Z}_n| = n < \infty)$ and S be a set of different subgroups of $\mathbb{Z}_n$ that is not include $\mathbb{Z}_n$. From Theorem 2.8, magnitude of subgroups of $\mathbb{Z}_n$ is given by $d(n)$. Therefore, the norm of S can be given by $|S| = d(n) - 1$. Let $m \in \mathbb{Z}_n$ and $\langle m \rangle = \mathbb{Z}_n$. From Theorem 2.9 number of elements m is given by $\phi(n)$. Also, these elements are generate group of $\mathbb{Z}_n$ and the other elements are generate subgroups of $\mathbb{Z}_n$ which is not included $\mathbb{Z}_n$ and number of this elements are equal to cototient of n. Some subgroups of $\mathbb{Z}_n$ can be identical, therefore number of subgroups of $\mathbb{Z}_n$ which is not included $\mathbb{Z}_n$ is greater than number of different subgroups of $\mathbb{Z}_n$ (not included $\mathbb{Z}_n$). Hence $|S|$ is smaller than the cototient of n which follows $d(n) + \phi(n) \leq n + 1$. Furthermore, if n is a prime number then $\phi(n) = n - 1$, $d(n) = 2$ and so $\phi(n) + d(n) = n + 1$ which holds the equality.

Corollary 3.2 By Theorem 3.1, the following results can be obtain:

$(a)\ \lim_{n \to \infty} \dfrac{\phi(n) + d(n)}{n} \leq 1,$

$(b)\ \lim_{n \to \infty} \left(\dfrac{\phi(n) + d(n)}{n} \right)^n \leq e,$ *where e is Euler constant.*

Example 3.3 Here we give a *Maple* procedure for testing big positive numbers whether satisfies the inequality or not:

with(numtheory):

$test := proc(n)$

if $tau(n) + phi(n) \leq n + 1$ then 'true' else 'false' fi;
end:
test ("enter your number");

Now, according to (Vargas & Shashank, 2013), we give two lemmas:

Lemma 3.4 Let p is a prime number and $p|n$. Then, $\phi(pn) = p\phi(n)$.

Lemma 3.5 Let p is a prime number and $p \nmid n$. Then, $\phi(pn) = (p-1)\phi(n)$.

Theorem 3.6 Let p is a prime number and $p|n$. Then,

$$d(n) \leq \frac{k+1}{k+2}\big(pn + 1 - p\phi(n)\big),$$

where k is a positive integer.

Proof. Let $p|n$. From Theorem 3.1 we write
$$\varphi(pn) + d(pn) \leq pn + 1, \qquad (3.1)$$

From Lemma 3.4, Eq. (3.1) becomes
$$p\varphi(n) + d(pn) \leq pn + 1, \qquad (3.2)$$

Let $n = p_1^{k_1} p_2^{k_2} ... p_m^{k_m}$, then the number of divisors is $d(n) = (k_1 + 1)(k_2 + 1)...(k_m + 1)$. Without loss of generality, we assume $p = p_1$. Thus, we get $pn = p_1^{k_1+1} p_2^{k_2} ... p_m^{k_m}$ and
$$d(pn) = (k_1 + 2)(k_2 + 1)...(k_m + 1) = d(n) + \frac{d(n)}{k_1 + 1}.$$

If we arrange Eq. (3.2), we obtain the intended.

Theorem 3.7 Let p is a prime number and $p \nmid n$. Then,

$$d(n) \leq \frac{1}{2}\big(pn + 1 - (p-1)\phi(n)\big).$$

Proof. Let $p \nmid n$. From Lemma 3.5, it is written $\phi(pn) = (p-1)\phi(n)$. Let $n = p_1{}^{k_1}p_2{}^{k_2} \dots p_m{}^{k_m}$, and $p = p_{m+1}$. Therefore,

$$pn = p_1{}^{k_1}p_2{}^{k_2} \dots p_m{}^{k_m}p_{m+1}. \qquad (3.3)$$

From Eq. (3.3), we obtain $d(pn) = 2d(n)$ and so $\varphi(pn) + d(pn) = (p-1)\varphi(n) + 2d(n)$. Easily seen the inequality.

Corollary 3.8 If n is odd number. Then,

$$\varphi(n) + 2d(n) \leq 2n + 1.$$

Proof. If we take $p = 2$, it is obvious $p \nmid n$. From Theorem 3.7, we get the intended.

Now, according to (Pakapongpun, 2018), we give the following lemma:

Lemma 3.9 If $n = 2p$ and p is prime then, $\sigma(n) = n + \phi(n) + d(n)$.

Theorem 3.10 Let $n = 2p$ and p is prime. The following statement is true:

$$\sigma(n) \leq 2n + 1.$$

Proof. Since $n = 2p$ and p is prime, $\sigma(n) = n + \phi(n) + d(n)$. Thus, we obtain $\sigma(n) - n = \phi(n) + d(n)$. From Theorem 3.1, the inequality is easily seen.

Theorem 3.11 Let $n = 3p$ and p is prime, where $p \neq 3$. The following statement is true:

$$\sigma(n) \leq 2n + 2.$$

Proof. Since $n = 3p$ and p is prime $(p \neq 3)$, $\sigma(n) = 2(\phi(n) + d(n))$ (Pakapongpun, 2018). Thus, we obtain $\phi(n) + d(n) = \frac{1}{2}\sigma(n)$. From Theorem 3.1, we get the inequality.

Theorem 3.12 Let $n = 1$ or $n = p$ is prime. Then the following satisfies:

$$n - 1 \leq \sigma(n) - d(n).$$

Proof. Since $n = 1$ or $n = p$ is prime, $\sigma(n) + \phi(n) = 2n$ (Pakapongpun, 2018). Thus, we obtain $\phi(n) = 2n - \sigma(n)$. From Theorem 3.1, we get the intended.

An application in field theory

Theorem 4.1 Let (p, q) be a twin prime pair such that $q > p$. Let splitting fields of $x^p - 1 \in \mathbb{Q}[x]$ and $x^q - 1 \in \mathbb{Q}[x]$ polynomials be K and K', respectively. The following statements are true:

(a) There exists $\sigma, \zeta \in \mathbb{C}$ such that $K = \mathbb{Q}(\sigma)$ and $K' = \mathbb{Q}(\zeta)$,

(b) K/K' is an normal extension.

Proof. First, we show that $\big(\phi(p), \phi(q)\big) = 2$ when (p, q) is twin prime. Since $p < q$, it is obvious $q = p + 2$. Also, $\phi(p) = p - 1$ and $\phi(q) = q - 1$. Since p and q are odd, $\phi(p)$ and $\phi(q)$ are even. Then, we can write $p - 1 = 2k$ and $q - 1 = 2t$ such that k and t are positive integers. Thus, it is written $t = k + 1$. Therefore, $(k, t) = (k, k+1) = 1$ i.e., $(k, t) = 1$. It follows that,

$$\big(\phi(p), \phi(q)\big) = (p - 1, q - 1) = (2k, 2t) = 2(k, t) = 2 \qquad (4.1)$$

Now we can determine K and K'. The roots of the polynomial $x^p - 1 = 0$ can be given by

$$\sigma, \sigma^2, \dots, \sigma^{p-1}, \sigma^p = 1,$$

where $\sigma = e^{\frac{2\pi i}{p}}$. Since $K = \mathbb{Q}(\sigma, \sigma^2, \dots \sigma^{p-1}) = \mathbb{Q}(\sigma)$ and irreducible polynomial $irr(\sigma, \mathbb{Q}) = x^{p-1} + \cdots + x + 1$, we have $[\mathbb{Q}(\sigma):\mathbb{Q}] = p - 1$. Similarly, the roots of the polynomial $x^q - 1 = 0$ can be given by

$$\zeta, \zeta^2, \dots, \zeta^{q-1}, \zeta^q = 1,$$

where $\zeta = e^{\frac{2\pi i}{q}}$. Hence, we obtain $K' = \mathbb{Q}(\zeta)$, and $irr(\zeta, \mathbb{Q}) = x^{q-1} + \cdots + x + 1$. It is obvious that $[\mathbb{Q}(\zeta):\mathbb{Q}] = q - 1$ and $\mathbb{Q}(\sigma)$ is a finite extension of $\mathbb{Q}$, and $\mathbb{Q}(\zeta)$ as well. Therefore, $\mathbb{Q}(\zeta)$ is a finite extension of $\mathbb{Q}(\sigma)$. Let us show this. Assume that $\mathbb{Q}(\zeta)$ is an infinite extension of $\mathbb{Q}(\sigma)$. Then, $\mathbb{Q}(\zeta)$ is also infinite extension of $\mathbb{Q}$. But, it contradicts with $[\mathbb{Q}(\zeta):\mathbb{Q}] = q - 1 < \infty$. So, $\mathbb{Q}(\zeta)$ is finite extension of $\mathbb{Q}(\sigma)$. Assume that $[\mathbb{Q}(\zeta):\mathbb{Q}] = \alpha$. This implies $[\mathbb{Q}(\zeta):\mathbb{Q}] = [\mathbb{Q}(\zeta):\mathbb{Q}(\sigma)] \times [\mathbb{Q}(\sigma):\mathbb{Q}]$, which means $q - 1 = \alpha(p - 1)$. From Eq. (4.1) there exists $x, y \in \mathbb{Z}$ such that $(p-1)x + (q-1)y = 2$. If we arrange some equations, it follows $(p-1)(x + \alpha y) = 2$, which means $(p-1)|2$. Since $p > 2$, we get $p = 3$ and so $q = 5$. These results reveal that $\alpha = \frac{q-1}{p-1} = 2$. As a result, $[\mathbb{Q}(\zeta):\mathbb{Q}(\sigma)] = 2$ and K/K' is an normal extension.

References

Browkin, J., & Schinzel, A. (1995). On integers not of the form n-phi(n). *Colloq. Math.*, 55-58.

Burton, D. M. (1989). *Elementary Number Theory, 4th ed.* Boston: Allyn and Bacon.

Fraleigh, J. B. (1982). *A first course in abstract algebra.* Reading, Mass: Addison-Wesley Pub. Co.

Hardy, G. H., & Wright, E. M. (1979). *An Introduction to the Theory of Numbers, 5th ed.* Oxford: Oxford University Press.

Long, C. T. (1972). *Elementary Introduction to Number Theory (2nd ed.).* Lexington: D. C. Heath and Company.

Ore, Ø. (1988). *Number Theory and Its History.* New York: Dover.

Pakapongpun, A. (2018). The relation among Euler's phi function, tau function, and sigma function. *International Journal of Pure and Applied Mathematics*, 675-684.

Pettofrezzo, A. J., & Byrkit, D. R. (1970). *Elements of Number Theory.* Englewood Cliffs: Prentice Hall.

Sierpinski, W. (1964). *Elementary Theory of Numbers.* Warszawa.

Vargas, J., & Shashank, C. (2013). Proof of Euler's Phi Function Formula. *Rose-Hulman Undergraduate Mathematics Journal.*

Weisstein, E. W. (2022, May 1). *Divisor Function. From MathWorld--A Wolfram Web Resource.* Wolfram: https://mathworld.wolfram.com/DivisorFunction.html adresinden alındı

On Row Co-divisors and Column Co-divisors in Regular Square Matrices

Hasan KELEŞ[1]

Introductıon

This section is about row column co-divisor definitions in matrices. This study consists of a comparison between column co-divisors defined in 2010 and row co-dividers newly defined in March-2021. In column co-divisor definition, two regular square matrices are calculated by taking the determinant by replacing all the columns of the first with the columns of the second matrix, respectively. For the same matrices, in the definition of row co-divisor, the rows of the first of the two matrices, which also have the same conditions, are defined by taking their determinants by replacing the rows of the second matrix, respectively. The common aspects of these two definitions are examined. Examples of different situations are given. The meanings of the concepts known in the literature and some of the features that may be related to these two were discussed. In two definitions, it is determined that there are new approaches that can bring to the literature. It is investigated whether there are new accounts that are the same or different on a matrix.

It is concluded that new, rapid results were obtained in the local and even holistic comparison of the matrices obtained from the systems. Therefore, it is expected to make a significant contribution to the comparison of technological solutions. On the contrary, this approach allows observing mass solutions, variation between local solutions.

Here, it is aimed to compare each component of the first matrix with each component of the second matrix. This is made a great contribution to us in comparing the images obtained in imaging, especially in health and safety areas, with reality. Beyond horizontal and vertical comparison, new situations are possible.

Let F be a field and $M_n(F) = \left\{ \left[a_{ij} \right]_n \middle| a_{ij} \in F, n \in \square^+ \right\}$. Also, the transpose of $A \in M_n(F)$ is denoted by A^T.

Let A and B be two regular square matrices of order n. The determinant of the new matrix obtained by writing the ith row of the matrix A on the jth row of the matrix B is called the *co-divisor by row* of the matrix A by the row on the matrix B. It is denoted by $\underset{ij}{AB}$. Their number is n^2. The matrix co-divisor by row is $\left[\left(\underset{ij}{AB} \right)_{ij} \right]$ (Keleş, 2022).

Hasan Keleş, Öğretim Görevlisi, Karadeniz Technical Üniversity, Department of Mathematics

column-by-column co-divisors are denoted by ${}_{B}^{A}i_{j}$ and column-by-column co-divisors matrix as $\left[\left({}_{B}^{A}i_{j} \right)_{ij} \right]$ (Keleş, 2010,2015, 2018).

The following lemmas and theorems that have been proved before are given.

Lemma 1. Let F be a field, $M_{n}(F) = \left\{ \left[a_{ij} \right]_{n} \big| a_{ij} \in F, n \in \square^{+} \right\}$ and $A, B \in M_{n}(F)$. Then,

$$\frac{1}{|A|} \left[\left(\underset{ij}{AB} \right)_{ij} \right] = \left(\frac{B^{T}}{A^{T}} \right)^{T}$$ (Keleş, 2022).

Theorem 1. Let F be a field, $M_{n}(F) = \left\{ \left[a_{ij} \right]_{n} \big| a_{ij} \in F, n \in \square^{+} \right\}$ and $A, B \in M_{n}(F)$. Then,

$$\frac{A}{B} = \frac{B^{T}}{A^{T}} .$$

Theorem 2. Let F be a field, $M_{n}(F) = \left\{ \left[a_{ij} \right]_{n} \big| a_{ij} \in F, n \in \square^{+} \right\}$ and $A, B \in M_{n}(F)$. Then, solution of the linear matrix equation $XA = B$;

$$X = \left(\frac{B^{T}}{A^{T}} \right)^{T} .$$

Lemma 2. Let F be a field, $M_{n}(F) = \left\{ \left[a_{ij} \right]_{n} \big| a_{ij} \in F, n \in \square^{+} \right\}$ and $A, B, C \in M_{n}(F)$, where $|C| \neq 0$. Then,

i. $\left[\left({}_{B}^{A}i_{j} \right)_{ij} \right] = \frac{1}{|C|} \left[\left({}_{B}^{C}i_{j} \right)_{ij} \right] \left[\left({}_{C}^{A}i_{j} \right)_{ij} \right].$

ii. $\left[\left({}_{B}^{A}i_{j} \right)_{ij} \right] = A \left[\left({}_{B}^{I}i_{j} \right)_{ij} \right].$

Theorem 3. Let $M_{n}(F) = \left\{ \left[a_{ij} \right]_{n} \big| a_{ij} \in F, n \in \square^{+} \right\}$ be and $C_{ij}(A) = (-1)^{i+j} M_{ij}(A)$ be, where $M_{ij}(A)$ is the minor of a_{ij}. If $A \in M_{n}(F)$ with $|A| \neq 0$, let I or I_{n} be the unit matrix. Then

i. ${}_{A}^{I}i_{j} = C_{ij}(A).$

ii. ${}_{I}^{A}i_{j} = a_{ij}$ where $i, j = 1, \dots, n.$

iii. ${}_{A}^{A}i_{j} = \begin{cases} |A|, i = j \\ 0, i \neq j \end{cases}$

In this section, the similarities, equality or differences between $\left[\left(\dfrac{A}{B}i\,j\right)_{ij}\right]$ and $\left[\left(\dfrac{AB}{ij}\right)_{ij}\right]$, which

form the basis of the solution of equations, $XA = B$ and $AX = B$ formed by the square matrices of A and B are examined.

The row and column co-divisors of second-order square matrices $A = \begin{bmatrix} a_{11} & a_{12} \\ a_{21} & a_{22} \end{bmatrix}$ and

$B = \begin{bmatrix} b_{11} & b_{12} \\ b_{21} & b_{22} \end{bmatrix}$ are given below.

$$\underset{11}{AB} = \begin{vmatrix} a_{11} & a_{12} \\ b_{21} & b_{22} \end{vmatrix} = a_{11}b_{22} - a_{12}b_{21}$$

$$\underset{12}{AB} = \begin{vmatrix} b_{11} & b_{12} \\ a_{11} & a_{12} \end{vmatrix} = b_{11}a_{12} - a_{11}b_{12}$$

$$\underset{21}{AB} = \begin{vmatrix} a_{21} & a_{22} \\ b_{21} & b_{22} \end{vmatrix} = a_{21}b_{22} - b_{21}a_{22}$$

$$\underset{22}{AB} = \begin{vmatrix} b_{11} & b_{12} \\ a_{21} & a_{22} \end{vmatrix} = b_{11}a_{22} - a_{21}b_{12}$$

$$\dfrac{A}{B}{}^1{}_1 = \begin{vmatrix} a_{11} & b_{12} \\ a_{21} & b_{22} \end{vmatrix} = a_{11}b_{22} - a_{21}b_{12}$$

$$\dfrac{A}{B}{}^1{}_2 = \begin{vmatrix} b_{11} & a_{11} \\ b_{21} & a_{21} \end{vmatrix} = b_{11}a_{21} - b_{21}a_{11}$$

$$\dfrac{A}{B}{}^2{}_1 = \begin{vmatrix} a_{12} & b_{12} \\ a_{22} & b_{22} \end{vmatrix} = a_{12}b_{22} - a_{22}b_{12}$$

$$\dfrac{A}{B}{}^2{}_2 = \begin{vmatrix} b_{11} & a_{12} \\ b_{21} & a_{22} \end{vmatrix} = b_{11}a_{22} - a_{12}b_{21}$$

$$\left[\left(\dfrac{AB}{ij}\right)_{ij}\right] = \begin{bmatrix} a_{11}b_{22} - a_{12}b_{21} & b_{11}a_{12} - a_{11}b_{12} \\ a_{21}b_{22} - b_{21}a_{22} & b_{11}a_{22} - a_{21}b_{12} \end{bmatrix}$$

$$\left[\left(\dfrac{A}{B}i\,j\right)_{ij}\right] = \begin{bmatrix} a_{11}b_{22} - a_{21}b_{12} & b_{11}a_{21} - b_{21}a_{11} \\ a_{12}b_{22} - a_{22}b_{12} & b_{11}a_{22} - a_{12}b_{21} \end{bmatrix}$$

Lemma 1. Let $A, B \in M_n(F)$ be regular matrices. Then

$$\left[\left(\dfrac{A^T}{B^T}i\,j\right)_{ij}\right] = \left[\left(\dfrac{AB}{ij}\right)_{ij}\right]^T.$$

Proof. Let the regular matrices $A, B \in M_2(F)$ be given

$$\left[\left(\begin{smallmatrix}A^T\\B^T\end{smallmatrix} i\, j\right)_{ij}\right]=\begin{bmatrix} a_{11}b_{22}-a_{12}b_{21} & a_{21}b_{22}-a_{22}b_{21} \\ a_{12}b_{11}-a_{11}b_{12} & a_{22}b_{11}-a_{21}b_{12} \end{bmatrix}$$

$$\left[\left(\begin{smallmatrix}AB\\ij\end{smallmatrix}\right)_{ij}\right]^{T}==\begin{bmatrix} a_{11}b_{22}-a_{12}b_{21} & a_{21}b_{22}-a_{22}b_{21} \\ a_{12}b_{11}-a_{11}b_{12} & a_{22}b_{11}-a_{21}b_{12} \end{bmatrix}.$$

Lemma 2. Let F be a field, $M_n(F)=\left\{\left[a_{ij}\right]_n \middle| a_{ij}\in F, n\in\square^+\right\}$ and $A,B,C\in M_n(F)$, where $|C|\neq 0$. Then,

   i. $\left[\left(\begin{smallmatrix}AB\\ij\end{smallmatrix}\right)_{ij}\right]^{T}=\dfrac{1}{|C|}\left[\left(\begin{smallmatrix}C\\B^T\end{smallmatrix} i\, j\right)_{ij}\right]\left[\left(\begin{smallmatrix}A^T\\C\end{smallmatrix} i\, j\right)_{ij}\right].$

   ii. $\left[\left(\begin{smallmatrix}AB\\ij\end{smallmatrix}\right)_{ij}\right]^{T}=A^{T}\left[\left(\begin{smallmatrix}I\\B^T\end{smallmatrix} i\, j\right)_{ij}\right].$

Proof. Let the regular matrices $A,B,C\in M_2(F)$ be given, where $|C|\neq 0$. Its proof is obtained from Lemma 2 given in the Introduction and Lemma 1 in the second part.

Theorem 3. Let $M_n(F)=\left\{\left[a_{ij}\right]_n \middle| a_{ij}\in F, n\in\square^+\right\}$ be and $C_{ij}(A)=(-1)^{i+j} M_{ij}(A)$ be, where $M_{ij}(A)$ is the minor of a_{ij}. If $A\in M_n(F)$ with $|A|\neq 0$, let I or I_n be the unit matrix. Then

i. $\begin{smallmatrix}I_n\\A^T\end{smallmatrix} i_j = I_n A \underset{ji}{}.$

ii. $A I_n \underset{ji}{} = a_{ji}$, where $i=1,\cdots,n$ and $j=1,\cdots,n$.

iii. $A A \underset{ij}{} = \begin{cases} |A|, i=j \\ 0, i\neq j \end{cases}$

Proof. For a matrix A that satisfies the hypothesis of the theorem

   i. $\begin{smallmatrix}I_n\\A^T\end{smallmatrix} i_j = C_{ij}\left(A^T\right)= I_n A \underset{ji}{}.$

   ii. $\begin{smallmatrix}A^T\\I_n\end{smallmatrix} i_j = a_{ji} = A I_n \underset{ji}{}.$

   iii. $\begin{smallmatrix}A\\A\end{smallmatrix} i_j = A A \underset{ij}{} = \begin{cases} |A|, i=j \\ 0, i\neq j \end{cases}.$

References

Keles, H., (**2010).** The Rational Matrices, **New Trends in Nanotechnology and Nonlinear**

Dynamical Systems, paper58**, Ankara**.

Rafael Bru,, Maria T. Gassó,, Isabel Giménez, and José A. Scott, (2015). The Hadamard Product

of a Nonsingular General H-Matrix and Its Inverse Transpose Is Diagonally Dominant, Hindawi Publishing Corporation Journal of Applied Mathematics Volume, Article ID 264680, 6 pages.

Keleş, H., (2018). ON MATRIX DIVISION AND RATIONAL MATRICES, SOI: 1.1/IM

DOI: 10.15863/IM, International Scientific Journal Intelligent Mathematics, 1(7).

Keleş, H., (2015). Lineer Cebire Giriş-I-, Bordo yayınları, Trabzon, Turkiye.

James A. Mingo and Mihai Popa, (2019). Freeness and The Partial Transposes of Wishart

Random Matrices, Canad. J. Math. Vol. 71 (3), pp. 659–681, http://dx.doi.org/10.4153/CJM-2018-002-2 ©Canadian.

Keleş, H., (2022). On The Relationship between Transpose and Division,

https://www.internationalistanbulcongress.com/

Some Relationships between Functions Demand-Supply and Loss-Profit

Hasan Keleş[1]

Introduction

This section consists of two main parts.

First part is about the demand and supply function, which is one of the functions of a single variable, which is frequently used in economic, economic, business, financial, applications of mathematics. In the calculation of the equilibrium point, $f_D(x)$ demand and $f_S(x)$ supply functions,

$$f_D(x) = f_S(x)$$

using the equation, for $\forall x \geq 0$;

$$\frac{f_D(x)}{x} = \frac{f_S(x)}{x}$$

Here, the representations of $L(x), P(x), I(x), E(x)$, are considered as loss function, profit function, income function and expense function, respectively. Different from the market calculations, the known situations in the real structure were studied on the concepts that were initially considered as linear functions on the plane by using mathematical operations. Some of the cases where the results of the concepts of average demand and average supply were examined. In an economic activity, the importance of the demand and supply functions is as important as the profit and loss. In addition, profit and loss functions were obtained in relation to the concepts of average demand and average supply. The direct relationship between the loss function and the demand function was obtained. Namely, it was calculated that the derivative of the expression obtained by multiplying the loss function by the unit corresponds to the demand. It was also concluded that to obtain the profit, the integral of the difference between supply and demand must be twice. Univariate function results between profit, loss, unit, demand and supply functions were obtained. It became intuitively clear that it could be a function of two variables involving demand and supply. Although the equilibrium point is associated with demand and supply functions, it has been observed that profit and loss functions can also be calculated. Thus, it was perceived that the averages should not be kept constant in constantly changing market applications.

In this study, the functional relationship between the profit and loss function and the demand and supply function in the plane of demand and supply functions, which form the basis of economic, financial and even business activities, is emphasized. The activity of demand and supply is the study of how buyers and sellers interact to determine transaction prices and quantities. As will be seen, prices determine both the quantity of the next activity and the price for the buyer of the unit and the cost for the seller of that unit at the same time.

---

[1] Hasan Keleş, Öğretim Görevlisi, Karadeniz Technical Üniversity, Department of Mathematics

The second part is about profit and loss functions.

the cases where the profit and loss functions are equal or different, which are one of the functions of one variable, which are frequently used in economic, economic, business, financial, ... applications of mathematics are discussed. Here, the representations of , $L(x), P(x), I(x),$ $E(x)$ are considered as loss function, profit function, income function and expense function, respectively. While calculating break-even points from $I(x) = E(x)$ the remainder of the economic activity consists of situations where the $I(x)$ and $E(x)$ functions are not equal. The fact that the control, management and planning of this activity took place in this area determined the direction of the study. Briefly, for the demand functions $f_D(x)$ and supply functions $f_S(x)$, the situation where the income and expense functions are not equal [4,5].

$$xf_D(x) \neq xf_S(x)$$
$$I(x) \neq E(x)$$
$$E_{av}(x) \neq I_{av}(x).$$

Scientific and technological developments make the benefit and necessity of profit and loss account in financial reporting even more important by increasing the development of increasingly complex activities, increasing the interest in business performance for solution-oriented economic, financial and economic dynamic information. This situation increases the interest in mathematics, which produces more systematic and even predictable solutions instead of local solutions. This article is studied in terms of revealing the planar and even spatial structures necessary for the management of the market economy in the real sense and producing solutions.

At the beginning, it is examined how the profit and loss functions of income and expenses are calculated when the demand and supply (price) are known. It has been researched that the increase or restriction of continuous production is fixed results, so the turmoil of profit-making in societies made economic activity unworkable after a while. As a result of this, it is increased the necessity and importance of the analysis and planning of complex economic structures. Although there is limited study in mathematical calculations, it is important that activities in the life principle of this subject develop more clear and measurable concepts. It is observed that there can be infinite concepts, considering that partial calculations are replaced by another calculation after a while.
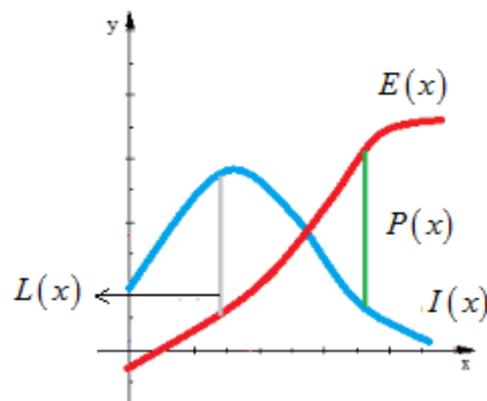
Chapter 1. Functions Demand and Supply

The acceleration of technological developments and the push of producers to production concerns naturally lead consumers to vital concerns. Producers' and consumers' foresight of profit and loss necessitate their dependence on demand-supply functions. Hence, "how are the profit and loss functions expressed in terms of demand and supply (price) functions?" obliges the question. This study focuses on this question and seeks an answer to this question on the plane. A linear demand and supply functions were studied by transforming them into simple hyperbolic functions, starting from the averages of demand and supply.

Figure 1.   Figure 2.
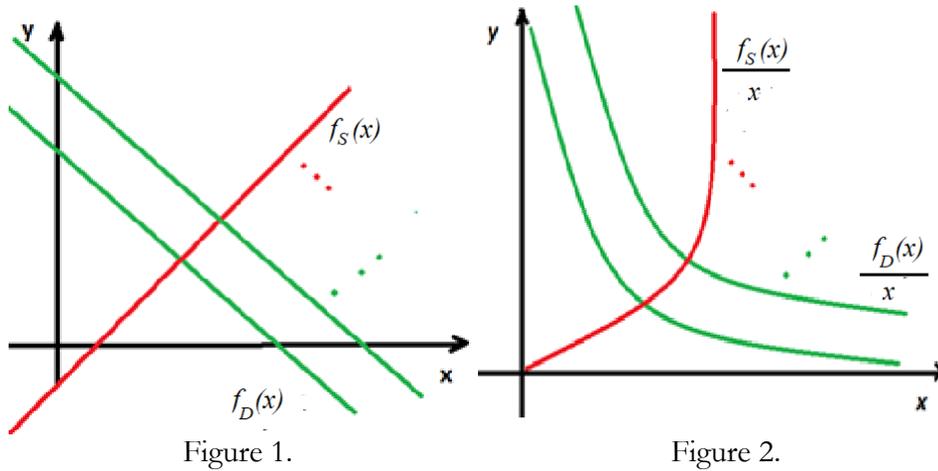
Examples are given. The results were reinforced with some other economic functions. This provides an environment where investors can gain their trust. At the same time, it also eliminates the scarcity anxiety of consumers. Although the result of an activity is very important for investors and consumers, the planning of demand and supply is at least as important as this.

As x units; For $m_1 < 0, n_1 > 0$ the linear $f_D(x) = m_1 x + n_1$ demand function,
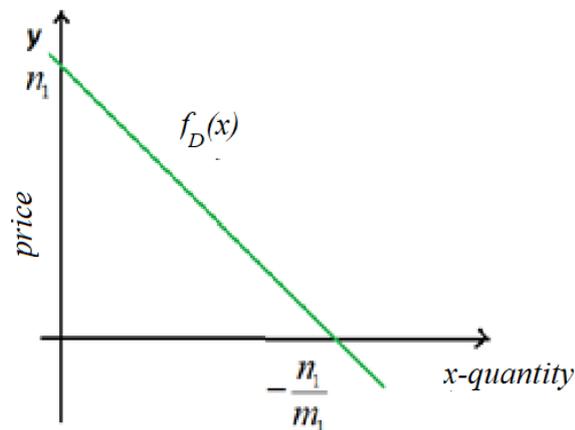
Figure 3.

and for the linear supply function, $f_S(x) = m_2 x + n_2$, where $m_2 > 0$.
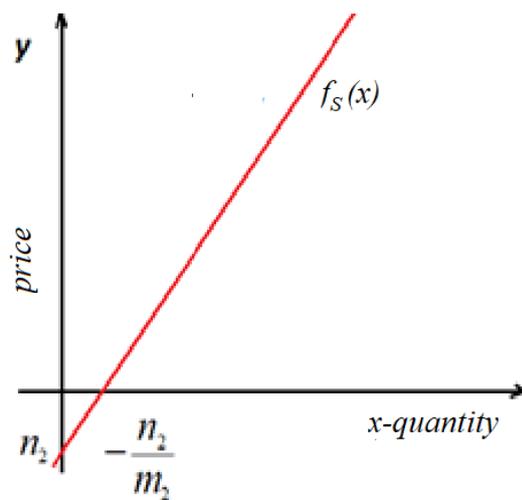
Figure 4.

The average demand and the average supply functions are given below, respectively.

$$f_{D,avr}(x) = \frac{f_T(x)}{x} = \frac{m_1 x + n_1}{x} = m_1 + \frac{n_1}{x},$$

$$f_{S,avr}(x) = \frac{f_A(x)}{x} = m_2 + \frac{n_2}{x}.$$

they become average simple hyperbolic functions.

Example 1.1. Demand and supply functions, respectively, $f_D(x) = 4000 - x$, $f_S(x) = -200 + 2x$.
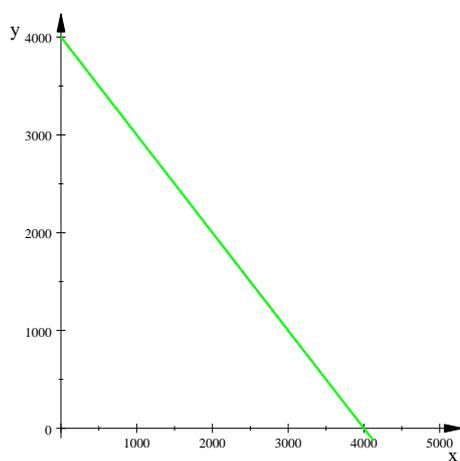
Figure 5.
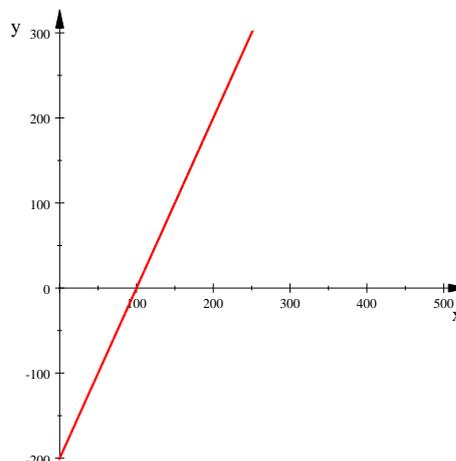
Figure 6.
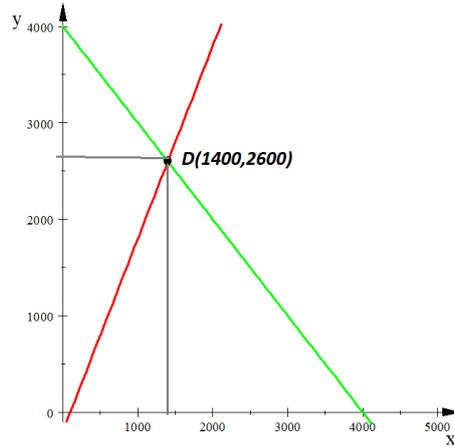
Figure 7.

average demand and average supply functions, respectively;

$$f_{D,avr}(x) = -1 + \frac{4000}{x}, \ f_{S,avr}(x) = 2 - \frac{200}{x}.$$
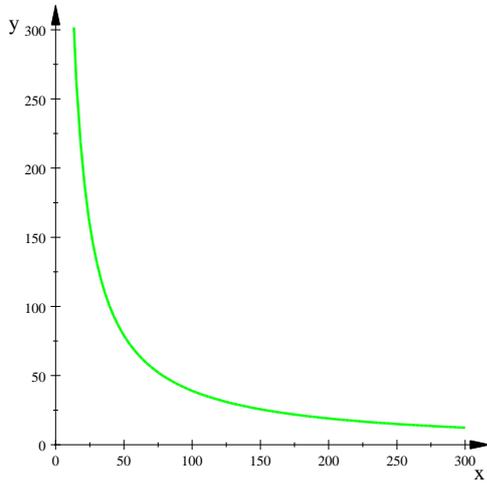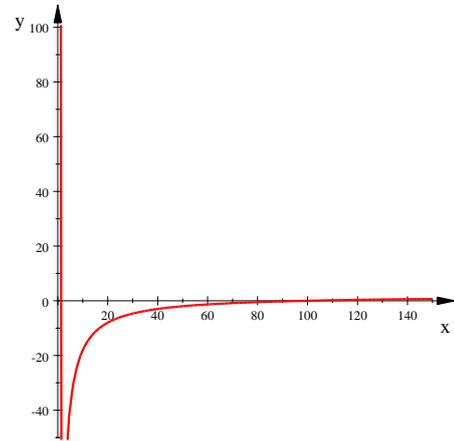
Figure 8.   Figure 9.

$$f_{D,avr}(x) = f_{S,avr}(x).$$

The following proposition without proof is given.

Proposition 1.1. If any given demand $f_D(x)$ and supply $f_S(x)$ functions, respecttively, then,

$$E(x) = xf_D(x), I(x) = xf_S(x).$$

Lemma 1.1. For given the demand $f_D(x)$ and supply $f_S(x)$ functions,

    i.   If $f_D(x) \ge f_S(x)$ then,

$$L(x) = x\big[f_D(x) - f_S(x) \big].$$

    ii.   If $f_D(x) \ge f_S(x)$ then,

$$P(x) = x\big[f_S(x) - f_D(x) \big].$$

74

Proof. The proof is clear from the equation given below.

$$P(x) = E(x) - I(x) \geq 0,$$
$$L(x) = I(x) - E(x).$$

Lemma 1.2. Let $f_{D,avr}(x)$ be the demand and $f_{S,avr}(x)$ A be the average functions of supply. If $f_{D,avr}(x) = f_{S,avr}(x)$ then,

    i. $L(x) = 2\int \dfrac{(f_S(x) - f_D(x))}{x} dx$.

    ii. $P(x) = \dfrac{1}{x}\int L(x) dx$.

Proof.

$$\frac{d}{dx}\left(\frac{f_D(x)}{x}\right) = \frac{d}{dx}\left(\frac{f_S(x)}{x}\right)$$
$$\frac{xf_D{}'(x) - f_D(x)}{x^2} = \frac{xf_S{}'(x) - f_S(x)}{x^2}.$$

    i. $xf_D{}'(x) - f_D(x) - xf_S{}'(x) + f_S(x) = 0$

$$x(f_D(x) - f_S(x))' - f_D(x) + f_S(x) = 0$$
$$x(f_D(x) - f_S(x))' - f_D(x) + f_S(x) + f_D(x) - f_D(x) + f_S(x) - f_S(x) = 0$$
$$x(f_D(x) - f_S(x))' + f_D(x) - f_S(x) + 2(f_S(x) - f_D(x)) = 0$$
$$\frac{d}{dx}[xL(x)] = 2(f_S(x) - f_D(x))$$
$$L(x) = \frac{2}{x}\int(f_S(x) - f_D(x)) dx .$$

    ii.   It is proved similarly.

Proposition 1.2. For a differentiable demand function $f_D(x)$, the extreme points of the $E(x) = xf_D(x)$ function are

$$\frac{d}{dx}E(x) = 0$$
$$xf_D{}'(x) + f_D(x) = 0$$
$$x = -\frac{f_D(x)}{f_D{}'(x)}, \text{ where } f_D{}'(x) \neq 0 .$$

Example 1.2. The critical point of the expense function $E(x) = 6x - x^2$ for the demand function $f_D(x) = 6 - x$, where $x = 3$ is the critical point fort his fonction.

$$f_D'(x) = -\frac{f_D(x)}{x}$$

$$f_D(x) = -\int \frac{f_D(x)}{x} dx$$

$$f_D(x) = -x + 6\ln x + C$$

$$C = 0.59167.$$

$$f_D(x) = -x + 6\ln x - 0.59167$$

The graph of the two functions is given below,
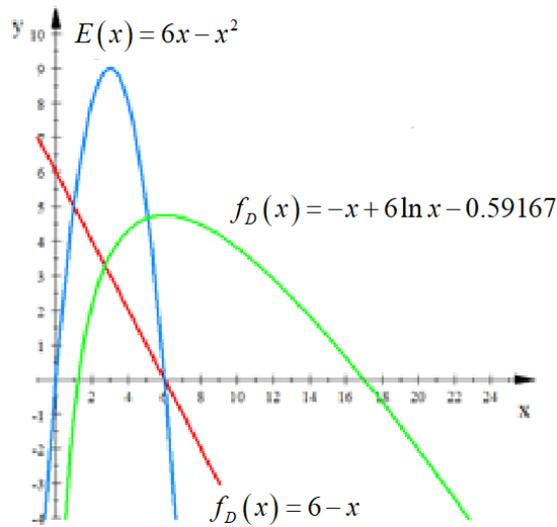
Figure 10.

The solution of the critical points of the function $f_D(x) = -x + 6\ln x - 0.59167$ is the set

$$\square \cap \left\{ \exp{-1.0 \mathrm{LambertW}\left(k, -\frac{1}{3}e^{-\frac{54083}{60000}} - 0.90138\right)} \middle\| k \in \square \right\}$$ and and numerical solution is

$x = 9.4386$.

Not. By obtaining different functions, different critical points were determined.

Chapter 2. Functions Profit and Loss

The profit and loss formula the application of mathematical science in other vital areas in order to determine the price of a commodity in the markets and to understand how profitable a business is necessitated. Each product has a cost price and a selling price. Based on the values of these prices, the profit or loss for a particular product is calculated. This, in turn, helps the realization of the plan to some extent, as well as the achievements achieved and the steps to be taken afterwards. Although the situations where the income and expense functions are equal are fundamental, it is important to consider the situations where they are different in observing the before and after situations of profit or loss.

$$\overbrace{\hspace{6cm}}^{I(x),E(x)}$$

$$I(x) = E(x) \qquad\qquad I(x) \neq E(x)$$

Here, if $I(x) = E(x)$, income and expense are equal, it determines the balance of the activity in terms of profit and loss. It also aims at the break-even point (Keleş, 2022).

If $I(x) \neq E(x)$ then quantitative ability observes the outcome of the achievements, most importantly, after the activity. This is intuition or how people will behave in the next step, hence production, consumption, social life, etc. it even guides previous logical theories. Therefore, at this stage, the path of the economic impression is determined. Almost all economic systems and theories are based on the well-known principle of profit and loss. This, in turn, affects social depression and economic crises. If there is a social society that is devoid of calculation, it will deprive the other socio-economic society it is established relations with from the results of quantitative logic.
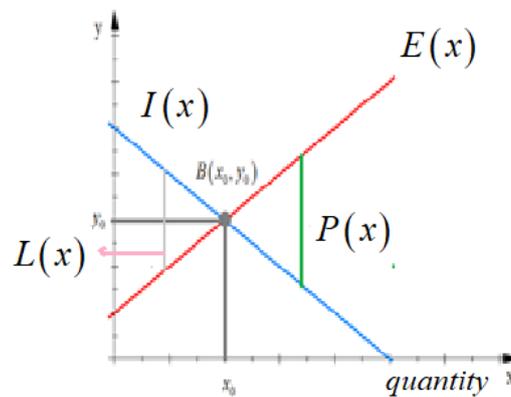
Figure 1.

If the expense and income functions are linear and the average income and average expense functions become simple hyperbolic functions.
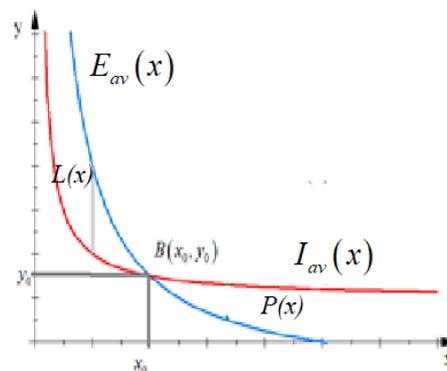
Figure 2.

This explains that the demand and supply functions at the equilibrium point are constant. In this study, mostly demand and supply functions were handled linearly. Thus, the functions were calculated as quadratic.

As $x-$unit; a quadratic expense function is $E(x)=m_1x^2+n_1x$ for $m_1<0, n_1>0$.
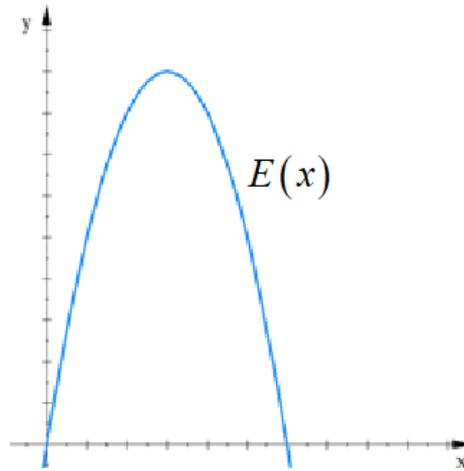
Figure 3.

and a quadratic income function $I(x)=m_2x^2+n_2x$ for $m_2>0$.
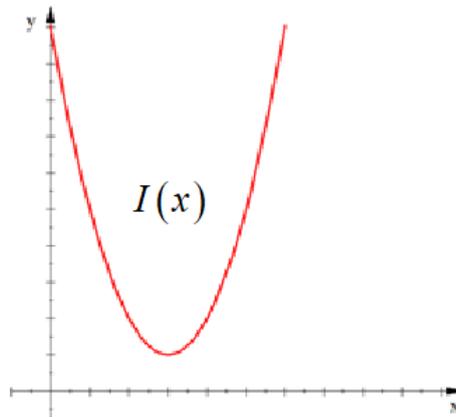
Figure 4.

In the graph below, the closest and farthest components of the two curves in the plane are given.
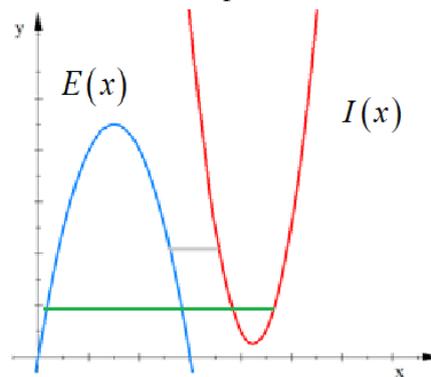
Figure 5.

Therefore, the profit and loss functions are

$$P(x)=I(x)-E(x)$$
$$L(x)=E(x)-I(x).$$

Lemma 2.1. Let the $I(x)$ income and $E(x)$ expense functions have first derivatives and be given continuously.

    i.   If $E(x) > I(x)$ then

$$Z(x) = -x \int \frac{Z(x)}{x^2} dx .$$

    ii.   If $I(x) > E(x)$ then

$$K(x) = -x \int \frac{K(x)}{x^2} dx .$$

Proof.

    i.

$$\frac{d}{dx} L(x) = \frac{L(x)}{x} + x \frac{d}{dx}\left(\frac{L(x)}{x} \right) = 0$$

$$\frac{d}{dx}\left(\frac{L(x)}{x} \right) = -\frac{L(x)}{x^2}$$

$$L(x) = -x \int \frac{L(x)}{x^2} dx .$$

    ii.   The proof is similar.

Corollary 2.1. $P(x) = -L(x)$.

Example 2.1. At the critical point $x = 4$ for functions $L(x) = 16x - 2x^2$ and $P(x) = 2x^2 - 16x$ with the same demand and supply in an economic transaction

$$x \int \frac{L(x)}{x^2} dx = -2x^2 + 16x \ln x + C$$

$$C = -88,723$$

$$x \int \frac{L(x)}{x^2} dx = -2x^2 + 16x \ln x - 88.723$$

$$L(x) = 16x - 2x^2$$
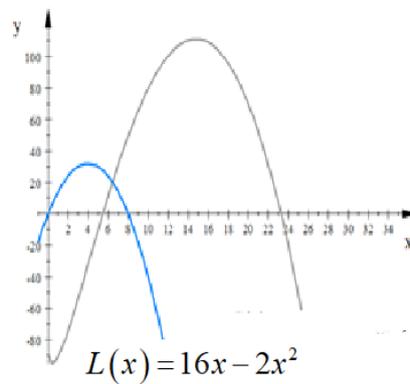
Figure 6.

Lemma 2.2. Let the loss and profit functions be $L(x)$ and $P(x)$.

    i.   If $\dfrac{d}{dx} L(x) = 0$ then

$$x = -\frac{E(x)}{E'(x)}.$$

ii.   If $\frac{d}{dx}P(x)=0$ then

$$x = -\frac{I(x)}{I'(x)}.$$

Proof. The proofs are clearly obtained from the literature.

References

Richard V. Eastin, PhD, and Gary L. Arbogast, CFA Richard V. Eastin, (2019). Demand and Supply Analysis: Introduction by PhD, is at the University of Southern California (USA). Gary L. Arbogast, CFA (USA).

Bulanichev, V.A., and Serkov, L.A., (2006). Model approach of functioning of higher educational institutions as self-organizing systems, Information Technologies, 3, pp. 68 – 73.

Jeffrey M. Perloff. (2017). Microeconomics: Theory and Applications with Calculus (The Pearson Series in Economics), 4th edition Published by Pearson.

Keleş H., (2022). On Reflections of Profit and Loss Functions, INTERNATIONAL CURRENT RESEARCH SYMPOSIUM 2022 (ICRS'22), CONFERENCE PROCEEDINGS, ISBN: 978-605-74014-4-1, pages 223-228, F E B R U A R Y 2 1 - 2 2.

Keleş H., (2022). On Reflections of Demand and Supply Functions, INTERNATIONAL CURRENT RESEARCH SYMPOSIUM (2022). (ICRS'22), CONFERENCE PROCEEDINGS, ISBN: 978-605-74014-4-1, pages 217-222, F E B R U A R Y 2 1 - 2 2.

Trend Analysis of Somali Precipitation Data

Hodo ABDILAHI[1]
Turgay PARTAL[2]

Introduction

Water is one of the most vital substances on our planet. Population growth has led to increased water consumption due to the global climate change. Many African countries, including Somalia are among the most affected by climate change and are also not part of the richest countries in terms of water.

Trend analysis and homogeneity tests was studied by many researchers in last years (**Gocic and Trajkovic, 2013; Topuz, 2017**). Özkoca (2018) studied homogeneity tests and trend method of Mann-Kendall and Sen for annual average precipitation and annual average of temperature data in the Central Black Sea region between 1975-2013. In the results of the study, an increasing precipitation an increase of temperature on the coasts and a decrease in the interior areas were detected. Rustum et al (2017) conducted a long-term study of trend analysis of Shire basin in Malawi from 1952-2010. In their study, the non-parametric Mann-Kendall test were used to determine the importance of the trends, and Sen's slope Method were used to determine the magnitude of the trends. They concluded that 20 years of precipitation increased, although monthly precipitation had an increasing trend in winter (November-April) and decreasing trend in summer (May-October). During the winter months, the monthly trend analysis emerged as a rising trend across all sites. Tokgöz and Partal (2020) applied trend analysis on the precipitation and temperature data of 16 stations of the years 1960-2015 in the Black sea region. In their study, Mann-Kendall and Innovative Sen Method were used to find trend analysis. As a result annual precipitation and annual temperature in the Black Sea region showed an overall increasing trend. Oğuztürk and Yıldız (2014) studied drought analysis in different time periods in Kırıkkale province. They used the standardized precipitation index (SPI) to analyze drought status. They determined that the SPI data are compatible with the climatic conditions observed in the study area.

In this study, the trends of annual precipitation data of Somalia, which is one of the regions most affected by climate change and located in East Africa, were examined. Fort his purpose, Mann-Kendall, Sen slope and Sen's innovative methods were used. It's important to carry out this research, especially in a region where precipitation is very rare and limited such as Somalia. Very few studies have been carried out in Somalia's climate change. This study will make an important contribution to the literatüre.

MATERIAL AND METHODS

This section gives information about the study area. Trend analysis of annual precipitation data for 10 stations in Somalia were performed using different trend tests. The average of annual rainfall in Somalia is 267mm. In this study the data of 10 meteorological observation stations in North and East regions in Somalia were used. The map of the stations was given in Figure1

---

[1] Student, Ondokuz Mayis University, Civil Engineering.
[2] Prof. Dr.Turgay PARTAL, Ondokuz Mayis University, Civil Engineering.
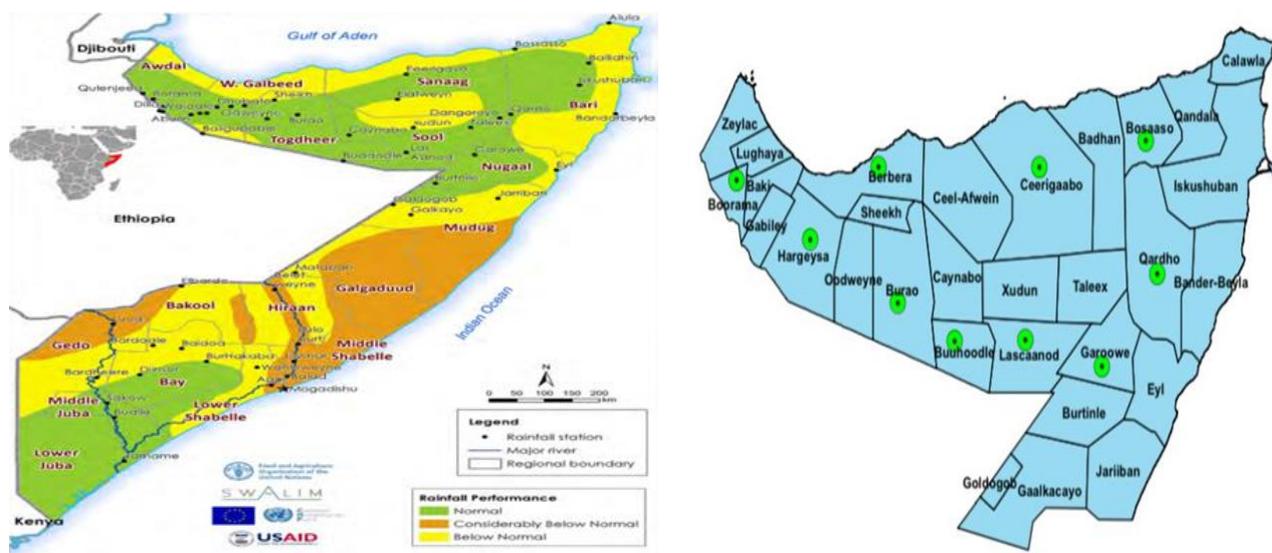
Figure 1: Map of Somalia

Table:1 Information of the Stations Examined in the Study

Station Name	Observation Years	Height (m)	Latitude	Longitude	Average of yearly total Precipitation	Auto-correlation
Borama	1981-2019	1.454	9,9360°N	43,1844°E	548	0,235
Hargeisa	1981-2019	1.334	9,5624°N	44,0770°E	726	0,385
Berbera	1981-2019	3	10,4348°N	45,0140°E	38.5	0,222
Bur'o	1981-2019	1.037	9,5259°N	45,5346°E	123	-0,069
Buhodle	1981-2019	672	8,2363°N	46,3385°E	193.7	-0,134
Erigavo	1981-2019	2.470	10,6150°N	47,3658°E	120.93	-0,289
Las'anod	1981-2019	691	8,4760°N	47,3658°E	52.27	-0,237
Garowe	1981-2019	4.000	8,4084°N	48,4837°E	123	-0,324
Qardho	1981-2019	802	9,5116°N	49,0868°E	96	-0,289
Bosaso	1981-2019	15	11,2755°N	49,1879°E	91.95	0,00

Homogeneity Tests

The use of homogeneous series in studies on climate change plays a very important role (Zaifoğlu et al. 2017). Changes in homogeneous series are due to climate and meteorological changes (Conrad and Pollak, 1950). In other words, non-climate changes can distrupt the homogeneity of time series. Relocation of measuring station, exposure to environmental factors, instrumentation and setting errors affect the homogeneity of climate data. For this reason, it's

important to homogeneity of the data obtained from the stations in studies related to climate change characteristics.

Alexanderson's Standart Normal Homogeneity Test (SNHT) was effectively used to examine various climate and hydrological factors (Alexanderson, 1986). The data were distributed separately and randomly according to the H0 hypothesis accepted for this test. It is sensitive to detecting breaks or distortions on the test very set at the beginning and end. Buishand test is sensitive to detecting time deviations in the center (Wijngaard et al. 2003). When the data series is homogeneous, the test statistic value will be equal to 0, since time series will not have a systemic deviation. On the other hand, the Pettit test was developed by Pettit (1979) to determine the point of change in a time series. This non-parametric method is used to explore the change point on a monthly or annual scale (Pettit,1979). According to test, zero hypothesis has a random and independent distribution of the series. The alternative shows that there is sudden change in defending. If the test statistic exceeds the critic value, the H0 hypothesis is rejected. According to the Ho hypothesis in the Von-Neumann test, the data is not randomly distributed. The time series is distributed according to alternative hypothesis. This test does not define a particular place where homogeneity is disrupted and does not provide information about when homogeneity is disrupted (Winjngaard, 2003).

Mann-Kendall Test-

The Mann-Kendall test was developed by Mann (1945) and Kendall (1975). This test is independent of the distribution of the random variable and is a non-parametric test. Due to this feature, Mann-Kendall test is widely used especially on hydrometeorological data. According to this test, the H0 hypothesis accepts that there is no trend in a time series, while the H1 non-hypothesis accepts that there is a trend (Beyazit, 1996).

Sgn (x_i-x_j) =1; if $x_j > x_i$

$\qquad$ 0; if $x_j = x_i$

$\qquad$ -1; if $x_j < x_i$

$$S = \sum_{i=1}^{n-1\Sigma} \sum_{j=i+1}^{n\Sigma} sg \qquad (1)$$

If the time data length is n>10, it is assumed that the data are normally distributed and variance is calculated as in equation 2

$$var(s) = \frac{n(n-1)(2n+5)-\sum_{i=1}^{k} t_i(t_i-1)(2t+5)}{18} \qquad (2)$$

$$z = \begin{cases} \frac{s-1}{\sqrt{Var(s)}}; Eğer S > 0 \\ 0; Eğer S = 0 \\ \frac{s+1}{\sqrt{Var(s)}}; Eğer S < 0 \end{cases} \qquad (3)$$

If the absolute value of the z value calculated as a result of equation (2) is greater than the z value determined at the α significance level, the H0 hypothesis is rejected, that is there is a significant trend in the time series. If it is small, the H0 hypothesis is accepted, that is there is no significant trend in the time series. If the MK test statistical value (s) is positive, it is determined that there is an increasing trend and if it is negative there is a decreasing trend (Yu et al, 1993).

Sen's Slope Test

This method is a non-parametric test developed by Sen (1968). This test calculates both the lineer rate of change and the intersection according to Sen's method. Likewise, this method is used to calculate the magnitude of the change in the variable (the amount of increase or decrease precipitation over period). Here, the number of data and the first data at times j and k are xj and xk (j>).

$$N = N(\frac{n-1}{2}) \tag{4}$$

Periodically Qi parameter

$$Qi = \frac{xj - xk}{(j-k)(i=1....,N)} \tag{5}$$

The median of the Qi values calculated according to the Sen method gives the inclination of the linear trend.

Innovation Sen Method

Innovative Sen method, is a new trend analysis, was first introduced by Sen (2012). In this method, the time series is divided in two equal parts and each part is sorted from the smallest to the largest starting from the first date. Then according to the cartesian coordinate system, the first of the two data columns (xi) is placed on the X axis and the other (xj) Y axis. If the data is collected on the 1:1 ideal line (45° line), there is no trend in the time series.
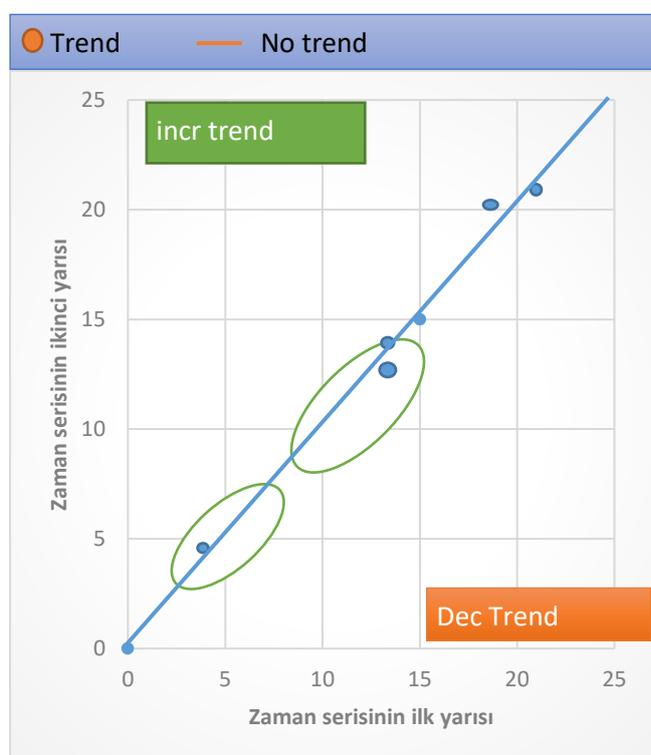
Figure 2: Data display in cartesian coordinates

Standardized Precipitation Index (SPI)

The Standardized Precipitation Index (SPI) was developed by McKee et al. (1993) to quantify the precipitation deficit for several time scales. These time scales reflect different water resources. The SPI is defined for each of the time scale difference between the monthly precipitation on a 3,6- or 13-month time scale (xi) and ($\bar{x}$), divided by the standard deviation (s).

$$SPI = \frac{xi - \bar{x}}{s}$$
(6)

Where xi is the monthly rainfall amount and $\bar{x}$, s is the mean and standard deviation of rainfall calculated from the whole time series of monthly values.

Table 2: SPI Classifation

SPI Index Value	Drought category
2.0 and above	Extremely wet
1.50 to 1.99	Severe wet
1.00 to 1.49	Moderate wet
0.0 to 0.99	Mild wet
0.0 to -0.99	Mild wet
-1.00 to -1.49	Moderate drought
-1.50 to 1.99	Severe drought
-2.00 to below	Extreme drought

RESULTS AND DISCUSSION

This section summarizes the main research findings of the study

Results of Homogeneity Analysis

In this section, precipitation data were applied for annual average of the 10 stations examined. As indicated in Table 3, the most common homogeneity tests Pettit, SNHT, Buishand and Von-Neumann tests were applied. For these tests, the data were distributed separately and randomly according to the accepted H0 hypothesis accepted. As a result of the study, it was determined that Berbera, Bur'o and Erigavo stations have 2nd class (suspicious homogeneous) data in terms of homogeneity. However, in the remaining 7 stations in the study, Hargeisa, Borama, Buhodle, Las'Anod, Garowe, Qardho and Bosaso stations were became 1st class (homogeneous).

Table 3: Annual precipitation homogeneity results

Station Name	Test Name	Result H0: Accept/Reject	Class
Borama	Pettit SNHT Buishand Von-Neuman	Accept Reject Accept Accept	Class:1. Homogeneous
Hargeisa	Pettit SNHT Buishand Von-Neuman	Accept Reject Accept Accept	Class:1. Homogeneous
Berbera	Pettit SNHT Buishand Von-Neuman	Accept Reject Reject Accept	Class: 2. Suspicious Homogeneous
Bur'o	Pettit SNHT Buishand Von-Neuman	Accept Reject Reject Accept	Class: 2. Suspicious Homogeneous
Buhodle	Pettit SNHT Buishand Von-Neuman	Accept Accept Reject Accept	Class:1. Homogeneous
Erigavo	Pettit SNHT Buishand Von-Neuman	Accept Reject Reject Accept	Class: 2. Suspicious Homogeneous
Las'Anod	Pettit SNHT Buishand Von-Neuman	Accept Accept Accept Accept	Class:1. Homogeneous

Garowe	Pettit SNHT Buishand Von-Neuman	Accept Accept Reject Accept	Class:1. Homogeneous
Qardho	Pettit SNHT Buishand Von-Neuman	Accept Accept Accept Accept	Class:1. Homogeneous
Bosaso	Pettit SNHT Buishand Von-Neuman	Accept Accept Reject Accept	Class:1. Homogeneous

Results of Trend Analysis

Mann Kendall Trend Analysis

Mann-Kendall method findings for annual average precipitation values are given in Table 4. The results were evaluated by comparing the critical z value 1.96 for the 95% confidence level. Accordingly, a statistical significant decreasing trend was determined at 95% confidence level for Borama, Hargeisa, Bur'o, Garowe and Bosaso. Although, an increasing trend was determined in only two stations of the ten stations.

Table 4: Results of Mann-Kendall and Sen's slope tests.

Station Name	MK Test Z Value	Sen's slope (mm/year)	Significant Trend %95	Decision Trend type
Borama	-3,04	-0,461	Yes	Decreasing
Hargeisa	-3,434	-0,886	Yes	Decreasing
Berbera	-1,023	-0,179	No	No Trend
Bur'o	-2,389	-0,578	Yes	Decreasing
Buhodle	0,629	0,106	No	No Trend
Erigavo	-3,042	-0,461	Yes	Decreasing
Las'Anod	0,377	0,072	No	No Trend
Garowe	-0,327	-0,059	No	No Trend
Qardho	-1,383	-0,200	No	No Trend
Bosaso	-2,263	-0,148	Yes	Decreasing

Innovative Sen Trend Analysis

In this section, annual average precipitation data are graphically examined for Innovative Sen trend analysis.
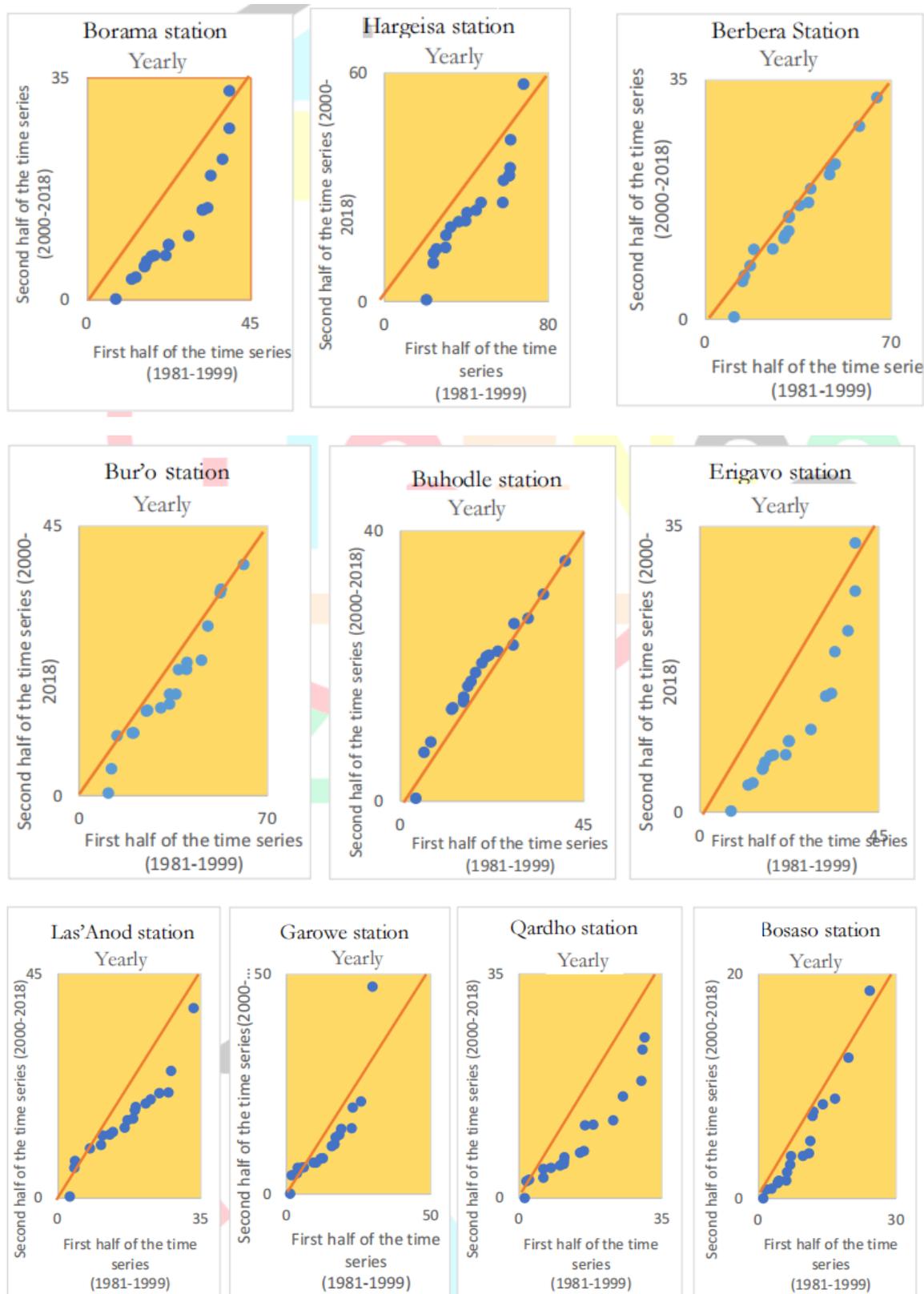
Figure 3: Graphical results of Innovative Sen trend analysis

The precipitation data of 10 meteorological stations in Somalia were studied for the innovation Sen method. The data were split into two classes from 1981 to 1999 and 2000 to 2018. This graphics show us there is a decreasing trend in the average yearly precipitation data at Borama, Hargeisa, Bur'o, Erigavo, Qardho and Bosaso stations. Although, Las'Anod and Garowe stations is determined that there is a middle trend. According the other stations, Berbera station showed that there is no trend.

Results of Standardized Precipitation Index (SPI)

In this section, precipitation data were applied for 12 monthly (annual) standardized precipitation index of the 10 stations. As indicated in Figure 4, Borama, Berbera, Hargeisa, Bur'o, and Erigavo stations showed positive SPI values for the data period from 1981 to 1999, while these stations showed negative SPI values for the data period from 2000 to 2019. Namely, these stations indicated a drought period since 2000. All stations also show a severe drought period for the 2018 and 2019 years.

Erigavo

Las'Anod SPI

Garowe SPI
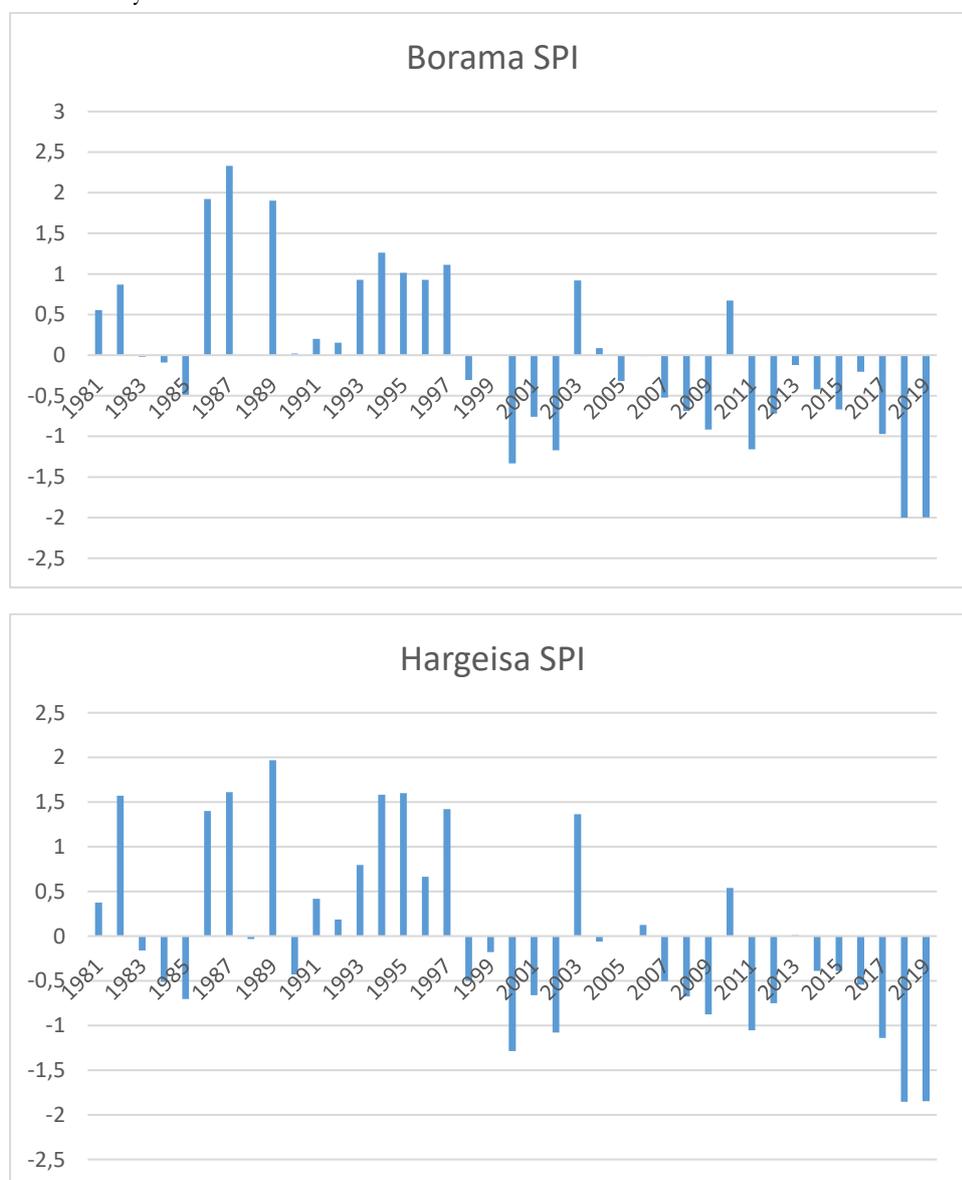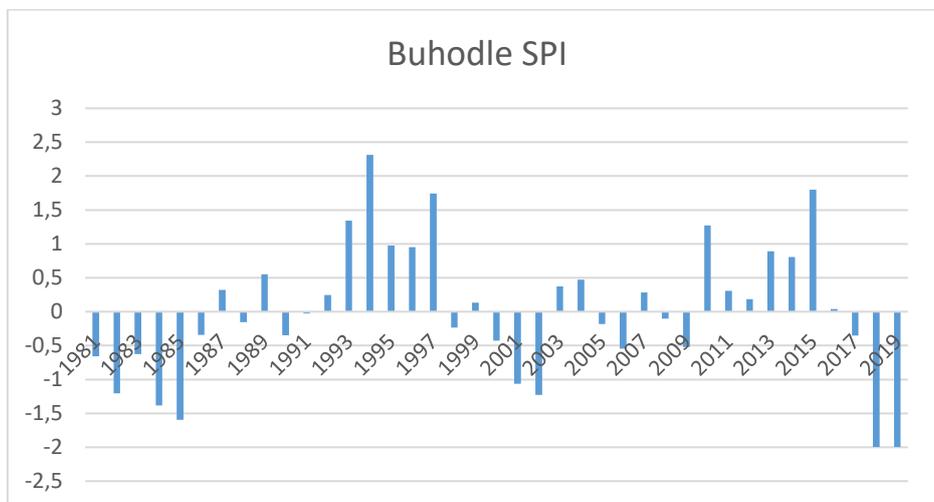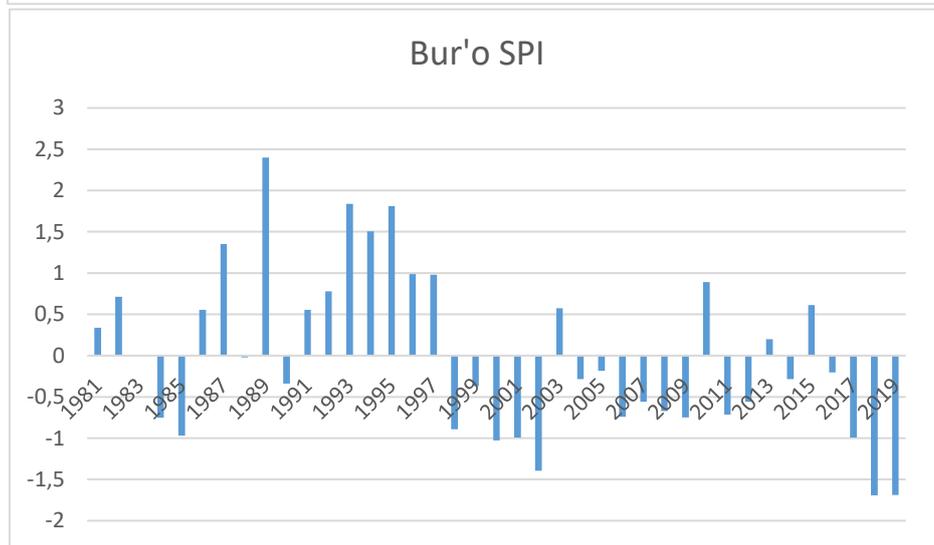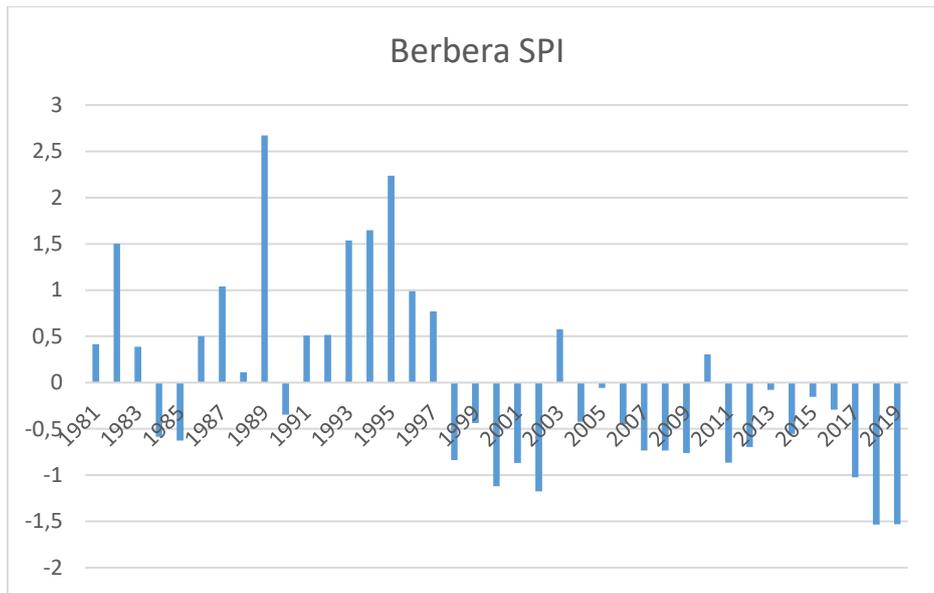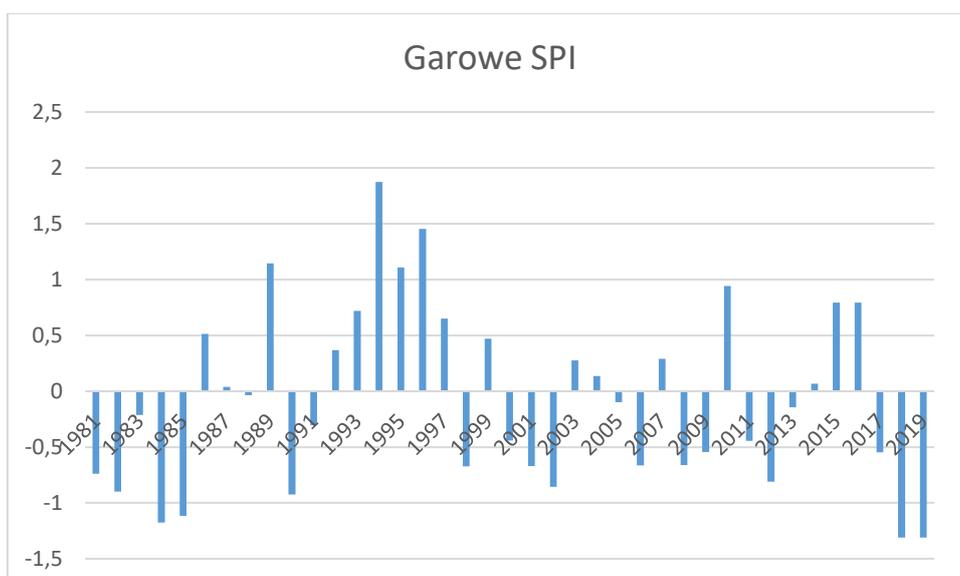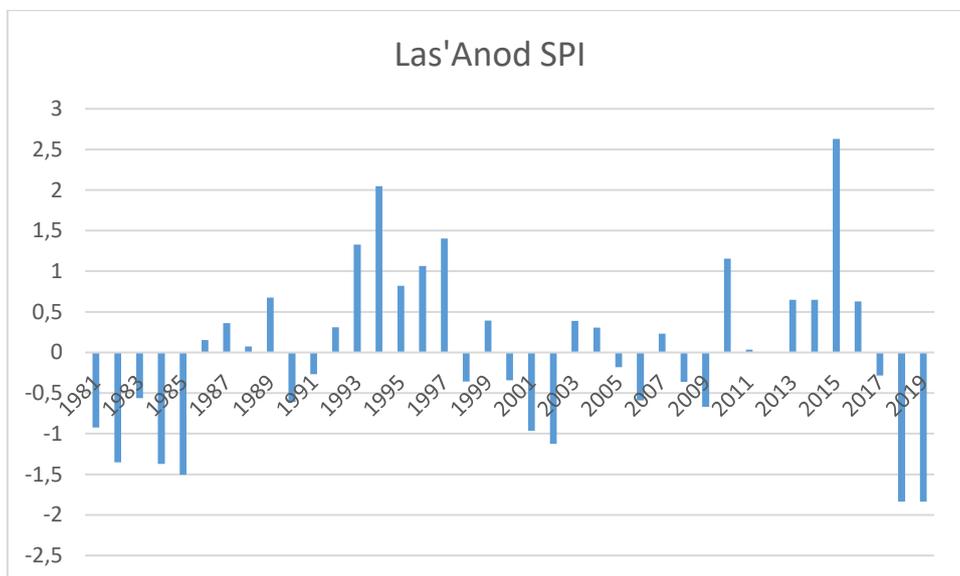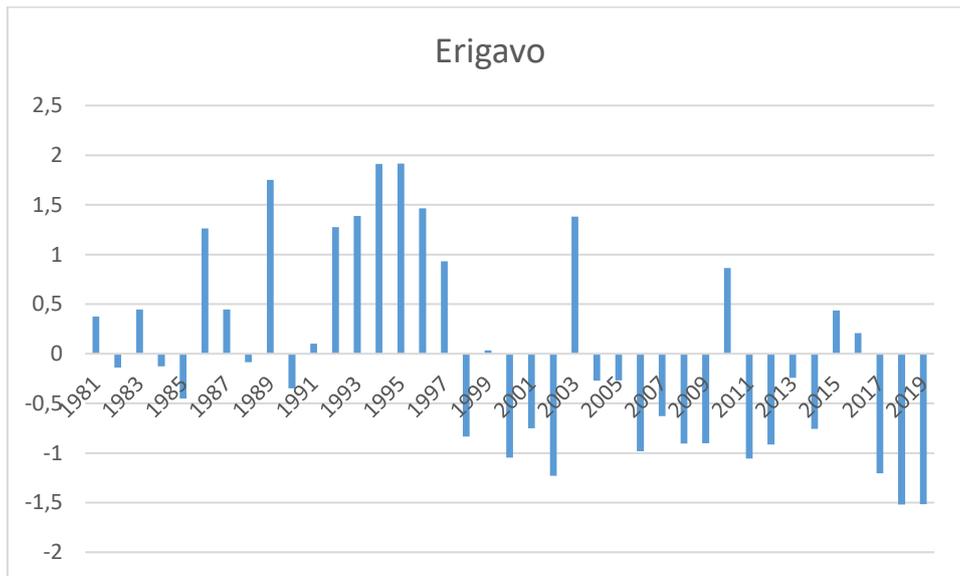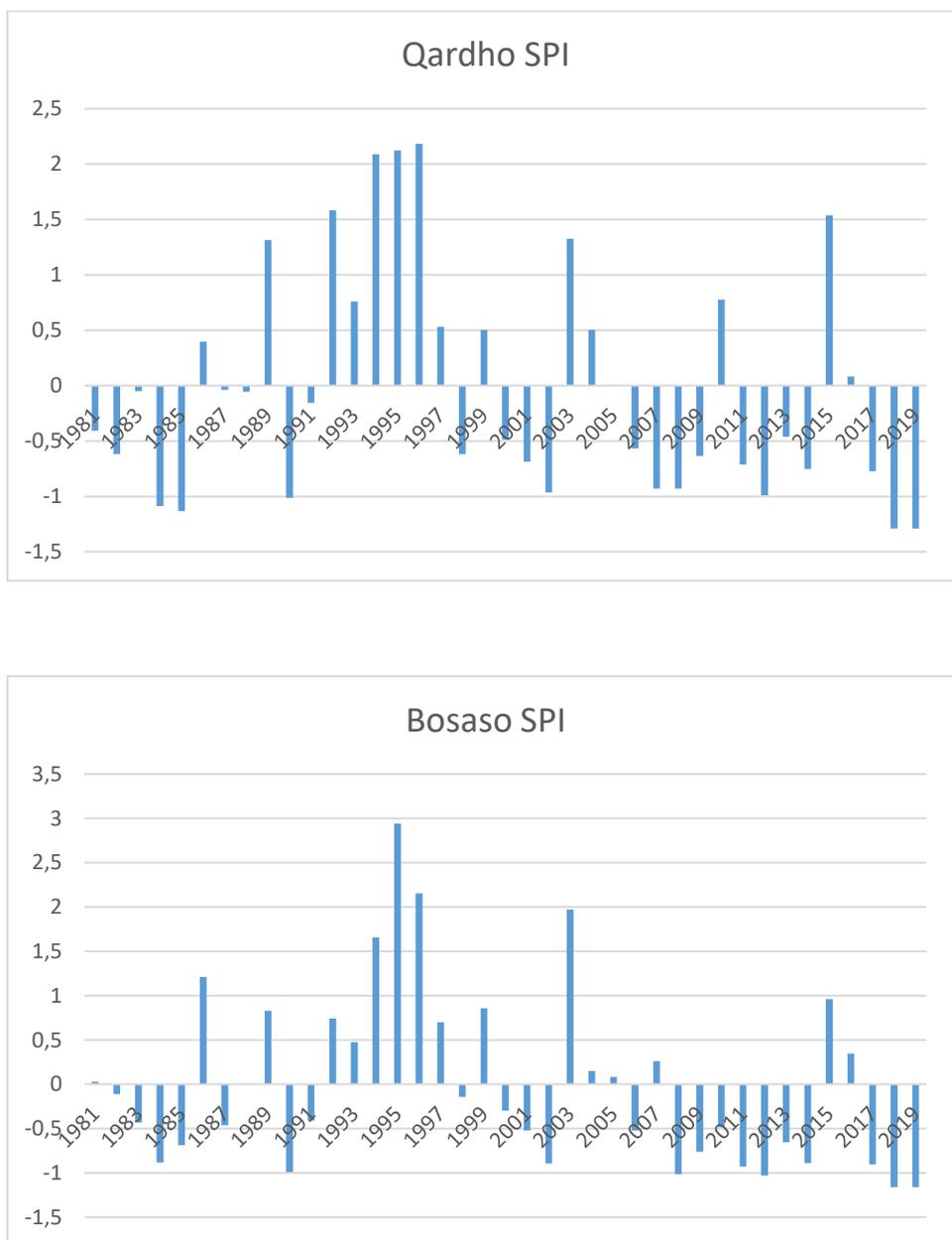
Figure 4: Graphical results of annual SPI

CONCLUSION

In this study, the trend analysis of the annual average precipitation of ten stations of Somalia is examined by using Mann-Kendall test, Sen's slope and Sen innovation test. Also, homogeneous tests of the stations were examined. Homogeneity of the stations were examined by using homogeneity tests (Pettit, SNHT, Buishand and Von-Neumann). In the result three stations of the study became 1st class (non-homogenous) the rest of the seven stations became 2nd class (homogeneous). The results of the trend tests, Mann-Kendall and Sen tests, a decreasing trend tests were determined at 95% confidence level for Borama, Hargeisa, Bur'o, Garowe and Bosaso. Although, an increasing trend was determined in only two stations of the ten stations. However, innovation Sen test method, different slopes were seen for low, medium and high values in the graphical results of the stations between (1981-2018). Decreasing trends were found in most stations. SPI results indicate a drought period for the Somali precipitation data after 2000.

REFFRENCES

Alexandersson H. (1986) A homogeneity test applied to precipitation data. *Journal of Climatology. 6.* 661-675

Bayazıt, M. (1996). İnşaat mühendisliğinde olasılık yöntemleri, *İTÜ İnşaat Fakültesi Matbaası, İstanbul*, 245s.

Conrad V, Pollak LW. (1950) Methods in climatology. *Harvard University Press, Cambridge, Mass 459*

Gocic M, Trajkovic S (2013). Analysis of changes in meteorological variables using Mann-Kendall and Sen's slope estimator statistical tests in Serbia. *Global and Planetary Change. 100, 172-182*

Kendall, MG. (1975). Rank Correlation Methods, *Charles Griffin, London.*

Mann, HB. (1945). Non-Parametric Test Against Trend, *Econometrika,13*, 245-261

McKee, TB. Doesken, NJ. Kleist, J. (1993) The relationship of drought frequency and duration to time scale. In: Preprints Eighth Conf. on Applied Climatology, *Anaheim, American Meteorological Society,* 179–184, 1993

Oğuztürk, G. Yıldız O.(2014). Drought Analysis for Different Time periods in the city of Kırıkkale. International Journal of Engineering Research and Development, 6(2), 19-25.

Özkoca, T. (2015). Orta Karadeniz Kıyı İllerinin Hidrometeorolojik Verilerinin Trend Analizi, *Yüksek Lisans Tezi, Ondokuz Mayıs Üniversitesi, Fen Bilimleri Enstitüsü, Samsun.*

Pettit, A (1979). Anon-parametric approach to the change-point detection. *Applied Statistic* 28: 126-135

Rustum, R, Adeloye, AJ, Mwale, F. (2017). Spatial and temporal Trend Analysis of Long Term rainfall records in data-poor catchments with missing data, a case study of Lower Shire floodplain in Malawi for the Period 1953–2010. *Hydrology and Earth System Sciences Discussions,* 1-30.

Sen, P. K. (1968). Estimates of the regression coefficient based on Kendall's tau. *American Statistical Association Journal 63*, 1379–1389

Şen, Z. (2012). Innovative trend analysis methodology. *Journal of Hydrologic and Engineering 17(9),* 1042-1046.

Tokgöz S, Partal T. (2020). Karadeniz Bölgesinde yıllık yağış ve sıcaklık verilerinin yenilikçi şen ve mann-kendall yöntemleri ile trend analizi. *Journal of the Institute of Science and Technology*, 10(2), 1107-1118.

Topuz, M (2017). Çukurova'da Yağışların Trend Analizi, *Çukurova Araştırmaları Dergisi, 3(1),* 173-181.

Wijngaard, JB Klein, Tank, AMG. Können. GP. (2003). Homogeneity of 20th century European daily temperature and precipitation series. *International Journal of Climatology. 23(6).* 679-692.

Zaifoğlu, H. Akıntuğ, B. Yanmaz, AM. (2017). Quality control, homogeneity analysis, and trends of extreme precipitation indices in Northern Cyprus. *Journal of Hydrologic Engineering, 22* (12).

Extraction and Characterization of Fenugreek Seed Proteins

İzzet TÜRKER [1]
Gamze Nur OLGUN [2]
Hilal İŞLEROĞLU [3]

Introduction

Increasing world population creates the need of alternative protein resources and plant–based proteins are expected to meet this demand of protein diet (Bernardi et al., 2021: 1). Legumes can be excellent protein sources because of their high protein content and low price. Fenugreek (*Trigonella foenum graecum* L.) is a legume which belongs to the Fabaceae family and its seeds have been used as medicines for over 2500 years (Srinivasan, 2006: 203). Fenugreek seeds are also used as spices and flavoring agents for different food formulations. Fenugreek seeds are rich in oil, dietary fiber and also protein. 100 g of fenugreek seed may contain 15-39 g protein and the fenugreek protein have mainly albumin fraction.

The combination of alkaline extraction and isoelectric precipitation methods are frequently used for the extraction of plant proteins from their tissues. The solubility of proteins is increased at alkaline conditions and the lowest solubility of the proteins occurs at the isoelectric point, which is around pH 4-5 for the plant–based proteins (Klupšaitė and Juodeikienė, 2015: 8). Alkaline extraction is carried out by setting the pH of the extraction medium to alkaline and stirring the medium at a constant agitation rate. To reduce extraction time and energy usage, enhance the energy transfer rate and obtain higher extraction yields, ultrasonic-assisted extraction (UAE) technique can be used for the protein extraction from plants (Bernardi et al., 2021: 1458). UAE is considered as a green extraction technique and it is a clean and a novel technology for the extraction of proteins from plant tissues (Ohja et al., 2020: 115663).

In this study, fenugreek seed proteins were extracted using alkaline extraction and UAE. The alkaline extraction conditions (pH level, extraction time, NaCl concentration, solid–solvent ratio) were determined and UAE was also applied to make a comparison in terms of extraction time and extraction yield. Moreover, physicochemical properties such as coagulated protein, water holding capacity, oil holding capacity, foaming properties and emulsion properties of defatted fenugreek seed protein isolates obtained with alkaline extraction and UAE were investigated.

[1] Research Assistant Izzet TURKER, Tokat Gaziosmanpaşa University, Food Engineering Department,
Orcıd ID: 0000-0003-0107-1962
[2] Gamze Nur OLGUN, Tokat Gaziosmanpaşa University, Food Engineering Department,
Orcıd ID: 0000-0002-7046-8341
[3] Assoc. Prof. Dr. Hilal ISLEROGLU, Tokat Gaziosmanpaşa University, Food Engineering Department,
Orcıd ID: 0000-0002-4338-9242

MATERIALS AND METHODS

Material

The fenugreek seeds bought from a store selling regional products in Tokat, Turkey were first combed out to remove foreign matters. After that, fenugreek seeds were powdered using a rotary blender (Sinbo SHB 3020, Turkey). The powdered seeds were screened with a 630 μm sieve and the powder under the sieve was collected. Because of having high fat content (16.15±1.02%) this fraction of the powder was subjected to defatting process with n-Hexane (n-Hexane Ultra-Pure >96%, Tekkim, Turkey) (1:4, w/v). The protein content of the defatted fenugreek seed was determined by Kjeldahl method as 17.13±0.10%.

Alkaline Extraction

To obtain proteins from defatted fenugreek seeds, the alkaline extraction conditions of pH level, extraction time, NaCl concentration and solid–solvent ratio were determined. Firstly, the effect of pH level was determined. Only distilled water was used as solvent and the pH was set with 0.1-1.0 M NaOH after defatting and the distilled water was mixed. To determine the effect of pH to the extraction yield, medium pH level was set to 9.0 and 12.0, and 24 hours of extraction was applied (solid–solvent ratio of 62.5 g defatted fenugreek seed in 1 L water). After determination of the pH level, the effect of the NaCl concentration and the extraction time on extraction yield were also investigated. 0-1 M of NaCl concentrations and 2-8 hours of extraction times were used at the medium pH of 12.0 and 62.5 g/L solid–solvent ratio. Following to the determination of NaCl concentration and extraction time, the effect of solid–solvent ratio was examined and solid–solvent ratio of 20-60 g/L was applied. For all extraction conditions, the protein amount in the aqueous extract was determined with Bradford method (g protein in L solvent) and the extraction yield was determined with Equation 1.

$$\text{Extraction yield (\%)} = \frac{\text{protein amount in the extract}}{\text{initial protein content of the prepared solutions}} \times 100 \tag{1}$$

Ultrasonic-Assisted Extraction

UAE was applied to the defatted fenugreek seeds and the effects of the extraction time and solid–solvent ratio were investigated. The UAE was carried out using a laboratory scale sonicator having ½" diameter probe (Q 500, Q Sonica, 500 W, 20 kHz, USA). An ice bath was used to prevent samples from overheating and extraction temperature was kept at ~ 25°C. At pH 12.0 and 55% ultrasonic amplitude, 10-60 minutes of extraction times were used and the effect of solid–solvent ratio (20-60 g/L) on the extraction yield was also investigated. For the extraction yield, Equation 1 was used.

Production of Protein Isolates

The supernatant phases obtained after different extraction processes having the highest extraction yield were acidified to different pH levels (pH 3.5, 4.0, 4.5 and 5.0) and left to precipitate for 15, 120 and 360 minutes. Precipitation yield was calculated using Equation 2. After determination of precipitation conditions, the samples were subjected to centrifugation and the supernatant phases were discarded. The precipitates were washed with distilled water at pH 4.0. Washed precipitates were then subjected to centrifugation at 6000 rpm for 5 minutes and this washing procedure was repeated for thrice. To obtain powdered protein isolates, precipitates were

dissolved in distilled water having pH 7.2 and these solutions were frozen at -18°C for 12 hours. Following that, freeze drying (Christ Alpha 1-4 LSC Plus, Germany) was applied to the samples for 72 hours. The powdered fenugreek seed protein isolates were used for further analysis.

$$\text{Precipitation yield (\%)}=100-\frac{\text{protein amount of supernatant after precipitation time (g/L)}}{\text{protein amount of the extract (g/L)}}\times 100 \qquad (2)$$

Analysis Methods

Coagulated protein, water holding capacity, oil holding capacity, foaming properties and emulsion properties of the protein isolates obtained from the extracts of alkaline classical extraction and UAE having highest extraction yield were determined. The coagulated protein percentage of the protein isolates were determined with the method of Kramer and Kwee (1977). Water holding capacity of the fenugreek seed protein isolates were determined with the slightly modified version of the method described by Piornos et al. (2015). Foaming properties namely foaming capacity and foam stability were determined using the method of Timilsena et al. (2016) and emulsion properties of the protein isolates namely emulsion stability, emulsion activity and emulsion capacity were determined the methods described by Feyzi et al. (2017).

Statistical Analysis

Comparison of the analysis results for the samples were carried out using the SPSS 21.0 (IBM, USA) package program.

RESULTS AND DISCUSSION

The effect of pH level on the defatted fenugreek seed protein extraction yield, extraction medium was set to pH 9.0 and pH 12.0 and extraction was carried out for 24 hours. Results showed that higher extraction yield was achieved at pH 12.0 than pH 9.0 (Table 1). Feyzi et al. (2017: 31) reported that the solubility of the fenugreek seed proteins had its highest level at higher pH values ($\geq$ pH 10.0). Because of having higher extraction yield ($p<0.05$), pH 12.0 was selected as the extraction medium pH level for the defatted fenugreek seed protein extraction. From this point on, pH 12.0 was used for all different extraction studies.

Table 1. Effect of pH level on the protein extraction yield

Medium pH	Protein content (g/L)	Extraction Yield (%)
9.0	6.63 ($\pm$0.05)	61.92 ($\pm$0.45)[b]
12.0	8.48 ($\pm$0.06)	79.17 ($\pm$0.46)[a]

[a-b] Means with uncommon superscripts within a column are significantly different ($p<0.05$).

To determine the pH level, long extraction times (24 hours) used to minimize the effect of the extraction time. However, determination of extraction time in alkaline extraction that gives the highest extraction yield is required, because different plant materials' protein extraction times could be different. In this study, extraction time (alkaline extraction) having the highest extraction yield was determined to prevent non-efficient use of time. Moreover, different salt concentrations were used to determine the effect of salt (NaCl) on the defatted fenugreek seed extraction yield. The results are shown in Table 2. Results showed that the highest extraction yields were obtained when only distilled water was used (without NaCl) and 4-8 hours of extraction times ($p<0.05$). The solutions prepared without NaCl at extraction times of 4, 6 and 8 hours, there was no statistical

difference between extraction yields ($p>0.05$). For further extractions, extraction time was applied as 4 hours and only distilled water was used (without NaCl).

Table 2. Effect of the extraction times and NaCl concentrations on protein extraction yield

NaCl Concentration (M)	Extraction Time (h)	Protein content (g/L)	Extraction Yield (%)
0.0	2	7.21 (±0.06)	67.35 (±0.54)[b]
	4	8.19 (±0.05)	76.49 (±0.45)[a]
	6	8.31 (±0.06)	77.57 (±0.54)[a]
	8	8.40 (±0.04)	78.47 (±0.36)[a]
0.5	2	5.28 (±0.18)	49.28 (±1.72)[g]
	4	6.80 (±0.19)	63.52 (±1.81)[cd]
	6	7.10 (±0.03)	66.27 (±0.27)[bc]
	8	6.70 (±0.05)	62.56 (±0.45)[d]
1.0	2	6.09 (±0.06)	56.88 (±0.55)[f]
	4	6.99 (±0.02)	65.31 (±0.18)[bcd]
	6	6.39 (±0.10)	59.69 (±0.90)[e]
	8	5.99 (±0.36)	55.92 (±3.34)[f]

[a-g] Means with uncommon superscripts within a column are significantly different ($p<0.05$).

In this study, 20-60 g/L solid-solvent ratio was used to determine the highest extraction yield at pH 12.0, and 4 hours of extraction time. The results were given in Table 3 and it was observed that the highest extraction yield was obtained at 20 and 40 g/L of solid-solvent ratios ($p<0.05$). The extraction yields were reduced at 60 g/L, possibly due to the extraction of more gums than 20 and 40 g/L of solid-solvent ratios which could negatively affect the protein extraction.

Table 3. Effect of the solid-solvent ratio on protein extraction yield

Solid-solvent ratio (g/L)	Protein content (g/L)	Extraction Yield (%)
20	3.12 (±0.02)	91.11 (±0.56)[a]
40	6.21 (±0.08)	90.67 (±1.13)[a]
60	8.40 (±0.02)	78.47 (±0.18)[b]

[a-b] Means with uncommon superscripts within a column are significantly different ($p<0.05$).

After determination of the conditions of alkaline extraction with the highest extraction yields (>90%), UAE was applied to the defatted fenugreek seeds to extract proteins. At 55% amplitude, 10-60 minutes of extraction times were applied for 40 g/L of solid–solvent ratio. The results are shown in Table 4 and it was observed that the highest extraction yields were obtained for the 30 and 45 minutes of extraction times. When UAE was compared with alkaline extraction, it was observed that higher extraction yields were achieved at 8-folds shorter time. The superiority of the UAE for the defatted fenugreek seed protein extraction over alkaline extraction in terms of extraction time and extraction yield was observed.

Table 4. Ultrasonic-assisted extraction of the fenugreek seed proteins

Extraction Time (min)	Protein content (g/L)	Extraction Yield (%)
10	3.92 (±0.00)	57.59 (±0.02)[c]
30	6.50 (±0.01)	95.45 (±0.02)[a]
45	6.61 (±0.00)	97.05 (±0.02)[a]
60	6.17 (±0.01)	90.62 (±0.02)[b]

[a-c] Means with uncommon superscripts within a column are significantly different ($p<0.05$).

To obtain defatted fenugreek seed protein isolate (from the supernatant extracted at pH 12.0, 40 g/L), isoelectric point precipitation technique was used and the effects of precipitation

times and pH values were investigated to obtain the highest precipitation yield. The results are given with Table 5 and the high precipitation yields (>90%) were achieved by isoelectric point precipitation technique (Table 5). According to Table 5, the pH 4.0 and 360 minutes of precipitation time gave the highest precipitation yield ($p < 0.05$). On the other hand, at pH 3.5, fenugreek seed proteins were more soluble than at pH 4.0, 4.5 and 5.0. The results showed that fenugreek seed proteins' isoelectric point was around pH 4.0.

Table 5. Precipitation yields at different precipitation times and pH values

pH	Precipitation Yield (%)		
	15 min	120 min	360 min
3.5	82.08 (±0.16)[dC]	89.49 (±0.03)[dB]	90.09 (±0.03)[dA]
4.0	89.94 (±0.05)[aC]	93.01 (±0.13)[aB]	93.16 (±0.10)[aA]
4.5	89.39 (±0.03)[bC]	91.94 (±0.13)[bB]	92.44 (±0.08)[bA]
5.0	86.94 (±0.10)[cC]	90.46 (±0.14)[cB]	91.25 (±0.15)[cA]

[a-d] Means with uncommon superscripts within a column are significantly different ($p < 0.05$).
[A-C] Means with uncommon superscripts within a line are significantly different ($p < 0.05$).

The characterization results were given in Table 6. Protein isolates obtained with alkaline extraction and UAE were compared. The results showed that water holding capacity, oil holding capacity and foaming properties of the protein isolates obtained with alkaline extraction and UAE were quite similar ($p > 0.05$). On the other hand, emulsifying properties of the protein isolates obtained with UAE were better than that of obtained with alkaline extraction ($p < 0.05$) (Table 6). Flores-Jiménez et al. (2022: 105976) reported that *Pithecellobium dulce* (Roxb.) seed protein isolates' emulsifying properties were enhanced with the application of 20 kHz and 600 W sonication for 30 minutes.

Table 6. Characterization of fenugreek seed protein isolates

Sample	CP (%)	WAC (g/g)	OAC (g/g)	FC (%)	FS (%)	ES (min)	EA (m²/g)	EC (%)
UAE	3.22 (±0.16)[a]	2.44 (±0.16)[a]	1.90 (±0.16)[a]	17.70 (±0.16)[a]	71.92 (±0.16)[a]	33.74 (±0.16)[a]	82.80 (±0.16)[a]	29.39 (±0.16)[a]
ACE	3.19 (±0.16)[a]	2.38 (±0.16)[a]	1.87 (±0.16)[a]	17.50 (±0.16)[a]	71.41 (±0.16)[a]	28.44 (±0.16)[b]	75.30 (±0.16)[b]	25.56 (±0.16)[b]

UAE: ultrasonic-assisted extraction, ACE: alkaline classical extraction, WAC: water holding capacity, OAC: oil holding capacity, FC: foam capacity, FS: foam stability, ES: emulsion stability, EA: emulsion activity, EC: emulsion capacity
[a-b] Means with uncommon superscripts within a column are significantly different ($p < 0.05$).

CONCLUSIONS

In this study, the alkaline extraction and UAE conditions of fenugreek seeds were determined to achieve the highest protein extraction yield and precipitation conditions of the fenugreek seed proteins were also examined. Moreover, coagulated protein, water holding capacity, oil holding capacity, foaming properties and emulsion properties of protein isolates obtained at the highest yields were determined. Results showed that UAE was superior to alkaline extraction in terms of extraction time, extraction yields and protein isolates obtained with UAE method showed better emulsifying properties. By the UAE, fenugreek seed proteins can be extracted at shorter times with higher yields and UAE can be a suitable technology for the protein extraction from fenugreek seeds.

ACKNOWLEDGEMENTS

REFERENCES

Bernardi, S., Lupatini-Menegotto, A. L., Kalschne, D. L., Moraes Flores, É. L., Bittencourt, P. R. S., Colla, E., & Canan, C. (2021). Ultrasound: A suitable technology to improve the extraction and techno-functional properties of vegetable food proteins. *Plant Foods for Human Nutrition*, *76*(1), 1-11. doi: 10.1007/s11130-021-00884-w

Feyzi, S., Varidi, M., Zare, F., & Varidi, M. J. (2017). A comparison of chemical, structural and functional properties of fenugreek (*Trigonella foenum graecum*) protein isolates produced using different defatting solvents. *International Journal of Biological Macromolecules*, *105*, 27-35. doi: 10.1016/j.ijbiomac.2017.06.101

Flores-Jiménez, N. T., Ulloa, J. A., Urías-Silvas, J. E., Ramírez-Ramírez, J. C., Bautista-Rosales, P. U., & Gutiérrez-Leyva, R. (2022). Influence of high-intensity ultrasound on physicochemical and functional properties of a guamuchil *Pithecellobium dulce* (Roxb.) seed protein isolate. *Ultrasonics Sonochemistry*, *84*, 105976. doi: 10.1016/j.ultsonch.2022.105976

Klupšaitė, D., & Juodeikienė, G. (2015). Legume: Composition, protein extraction and functional properties. A review. *Chemical Technology*, *66*(1), 5-12. doi: 10.5755/j01.ct.66.1.12355

Kramer, A., & Kwee, W. H. (1977). Functional and nutritional properties of tomato protein concentrates. *Journal of Food Science*, *42*(1), 207-211. doi: 10.1111/j.1365-2621.1977.tb01253.x

Ojha, K. S., Aznar, R., O'Donnell, C., & Tiwari, B. K. (2020). Ultrasound technology for the extraction of biologically active molecules from plant, animal and marine sources. *TrAC Trends in Analytical Chemistry*, *122*, 115663. doi: 10.1016/j.trac.2019.115663

Piornos, J. A., Burgos-Díaz, C., Ogura, T., Morales, E., Rubilar, M., Maureira-Butler, I., & Salvo-Garrido, H. (2015). Functional and physicochemical properties of a protein isolate from AluProt-CGNA: A novel protein-rich lupin variety (*Lupinus luteus*). *Food Research International*, *76*, 719-724. doi: 10.1016/j.foodres.2015.07.013

Srinivasan, K. (2006). Fenugreek (Trigonella foenum-graecum): A review of health beneficial physiological effects. *Food Reviews International*, *22*(2), 203-224. doi: 10.1080/87559120600586315

Timilsena, Y. P., Adhikari, R., Barrow, C. J., & Adhikari, B. (2016). Physicochemical and functional properties of protein isolate produced from Australian chia seeds. *Food Chemistry*, *212*, 648-656. doi: 10.1016/j.foodchem.2016.06.017

The Numerical Hydrodynamic Investigation of Different Maneuver of a Controllable Pitch Propeller

Kaan AKTAY[1]
Ahmet YURTSEVEN[2]

1.Introduction

Propeller propulsion is of great importance for all commercial or military vessels. The vast majority of marine vehicles have propeller-driven propulsion systems. Controllable pitch propellers are preferred in order to increase high speed and maneuverability in propeller propulsion systems. Controllable pitch propellers are available in many different designs. Apart from the mechanical elements of the system, the hydraulic force that provides the movement of the system is the most important element. It is to analyze the hydraulic force effect created to overcome the resistance force acting on the blades in the sea during the rotation of the propeller and to analyze this force numerically.

For this reason, existing studies in the literature have been examine in order to mathematically examine the force acting on the blades of pitch-controlled propellers.

This article mainly focuses on the mathematical model of the control pitch mechanism for a controllable pitch propeller (CPP), which can realize the propeller blade position change and give suitable information about the oil pressures produced in the CPP hub. In fact, too high pressures may be responsible for the mechanical failure, and then it should always be examine by the ship's automation. Regarding the conventional representation of the few spindle torque data reported in the literature, in the proposed mathematical model, the transport inertia forces and the Coriolis inertia forces acting on the propeller blade are evaluated by considering the ship's roll motion. Propeller speed (including shaft accelerations and decelerations) and blade rotation during pitch change. Because of the introduced procedure, the CPP model was develop as part of a general propulsion simulator representing the dynamic behavior of a twin-screw fast ship. The aim of the study is to represent ship propulsion dynamics with time-domain simulation, where automation designers can develop and test various propulsion control options. A brief description of the simulation approach adopted for ship collision arrest is show at the end of this article. In particular, the drive control action has been studied considering machine performance and constraints, including control pitch mechanism feedback in terms of allowable forces and pressures. (Altosole M. et al. 2011) The Report begins in Chapter 2 with a description of the operation of the CPP. Subsystems thought to be relate to the dynamic behavior of the system are then model. Then, the model was verify by making some measurements on a test bench developed within the scope of this thesis. A comparison is made to verify whether the test bench represents a CPP. In Chapter 3, an overview of observers for nonlinear systems is given and an observer is design. Performance is

[1] Engineer, Yildiz Technic Universty, Depatment of Naval Arc. & Marine Engineer
[2] Ph D., Yildiz Technic Universty, Departmant of Marine Engineering.,

test on the test bench. In Chapter 4, a new control strategy is developed and two new step controllers are design. These new controllers are compare with the traditional proportional controller and the relevant results are give by simulations and experiments. Finally, in Chapter 5 conclusions are drawn and recommendations for future work are formulated. (Dullens F. P. M. et al. 2009) The research described in this paper was conducted to estimate the hydrodynamic and frictional forces of the controllable pitch propeller. (CPP) causes wear problems in the blade bearing. The main equations are Reynolds averaged Navier-Stokes (RANS) and are solve by the Open FOAM solver for the hydrodynamic forces behind the ship's track. Frictional forces are calculated using practical mechanical formulas. To obtain the hydrodynamic coefficients in open water and in the trail behind the propeller, different propagation speeds with constant rotational speed are use for the blades. Results are compare at four different sites. Detailed numerical results of the 3D modeling of the propeller, its hydrodynamic properties, and the possibility of friction motion in the propeller are present. The results show that the probability of friction motion is relate to the pitch. (Tarbiat S. et al. 2014) This study focuses on friction in a controllable pitch propeller (CPP), wear formation in a CPP system, and their interdependence. The author has tried to obtain a general description of the problem that includes the hydrodynamic and mechanical aspects of a CPP, rather than delving into the tribology aspects alone. By doing this, the author concluded that total wear is the result of several wear mechanisms, but friction and sliding wear in the first place. It has been tried to explain the existence of wear because of very high oscillations in the track speed while the ship is cruising at sea. The wear experiments presented in this book show that friction wear is more dangerous than other wear mechanisms in CPP. Finally, based on experiments and previous analysis, the author presents a model of total wear for a CPP. This book is useful for marine engineers had better understand the characteristics and limitations of a CPP in real service conditions. It can also be an example of how to use a multidisciplinary approach to solving a particular problem. It is also helpful for tribologists to get an impression of the problems facing sea people and how they relate to their expertise. (Godjevac M. et al. 2009) The main objective of this study is the development and use of simulation techniques for the design of a naval ship's propulsion control system. The use of such a simulation platform to test the propulsion controller previous to installation on the ship allowed the automation provider to significantly reduce setup time during sea trials. In addition, the simulation platform allowed optimization of propulsion plant performance in terms of responsiveness, fuel consumption, and safety. After sea trials, different models were validate. A good correlation was observe between the experimental and simulated data. Obviously, some differences exist and it is important to understand the reasons for future improvements. (Martelli M. et al. 2014) The aim of this study is to use the CFD (Computational Fluid Dynamics) technique to examine the effects of the pitch ratio on the thrust characteristics of a controllable pitch propeller. The analyzed propeller is in the following design condition: 3.65 m diameter, 200-rpm speed, number of blades 4, average pitch 2,459 m, and pitch ratio 0.6737 at 0.7. The first phase involves networking and refining the designed propeller's domain. The second stage is concerned with defining the initial and boundary conditions of the networked module. In the final stage, various results for the pitch ratio affecting the thrust characteristic of the propeller are calculated and analyzed. The results achieved are the basic design and increased efficiency of the controllable pitch propeller. (Nguyen C. et al. 2018) This article aims to give a brief overview of the design process of an adapted propeller and to give a brief historical development of mathematical models. Discuss the possibilities and limitations of hydrodynamic propeller design. In this process, the blade strength should also be take into account, and in our opinion, it should be do with the available possibilities. It controls the design by taking into account the rules of the classification societies and analyzing it with a finite element approach. This is an important tool for analyzing the fatigue of the blades and components of the controllable system. This article suggested values of some sensitive limits for propeller design constraints since track area and ship structure are the limits given for the design process. A propeller designer is a

job that allows high-end projects such as navy ships and mega yachts to find their limits to fulfill their currently expected specifications. (Zarbock O. et al. 2009)

In this study, the hydrodynamic analysis of the propeller maneuvers of the controllable pitch propeller obtained by modifying a fixed pitch propeller at different starting positions was carried out. In this study, the focus is on the torque value of the blade.

2. The Numerical Methods

2.1. Unsteady RANS Method

The governing equations are the continuity equation and the RANS equations for the unsteady, three dimensional, incompressible flow. The continuity equation can be given as;

$$\frac{\partial U_i}{\partial x_i} = 0 \tag{1}$$

The momentum conservation equations are expressed as;

$$\frac{\partial U_i}{\partial t} + \frac{\partial (U_i U_j)}{\partial x_j} = -\frac{1}{\rho}\frac{\partial P}{\partial x_i} + \frac{\partial}{\partial x_j}\left[\nu\left(\frac{\partial U_i}{\partial x_j} + \frac{\partial U_j}{\partial x_i}\right)\right] - \frac{\partial \overline{u_i' u_j'}}{\partial x_j} \tag{2}$$

2.2. Dimensionless coefficients

The dimensionless coefficients that are frequently used in propeller hydrodynamic studies are the thrust coefficient, thrust coefficient, and torque coefficient.

Progress Coefficient;

$$J = \frac{V_a}{nD} \tag{3}$$

Thrust Coefficient;

$$KT = \frac{T}{\rho n^2 D^4} \tag{4}$$

Torque Coefficient;

$$KQ = \frac{Q}{\rho n^2 D^5} \tag{5}$$

can be defined as.

In addition, apart from the propeller rotation, which is discussed in the results section of the study, the blade torque coefficient obtained by the rotation of the blades around their own axis;

$$KQb = \frac{Q_b}{\rho n^2 D^5} \tag{6}$$

is defined as.

Propeller Coefficient;

$$EFF = \frac{KT}{KQ} \frac{J}{2\pi}$$

(7)

is defined as.

3. Numerical Results

DTMB 4119 model propeller has been select for hydrodynamic performance prediction. The geometrical features of the model propeller have been gave in Table 1. 3-D view of the model propeller has been present in Figure 1. In addition, our modified model, which we prepared to use during the processes, is available in Figure 2.

The numerical results have been compared with the experimental one at J=0.833 for thrust, torque coefficients, and efficiency values. The absolute difference between the results of the present method and experiments for non-dimensional thrust value has been compute as 0.68%. The rest of the analyses have been conducted using optimum grid numbers in open water conditions. The numerical results have been compare with the experimental data in Figure 2. Note that the agreement is good.

Table 1 - Main Particulars of DTMB4119

D (m)	0.3048
Z	3
Blade Section	NACA66 a=0.8
Rotation direction	Right
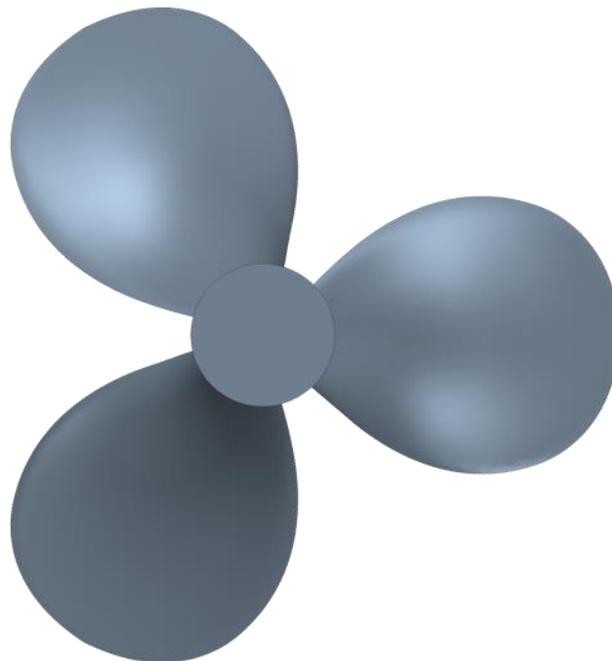
Figure 1 - 3-D view of DTMB 4119 model

3.1.Verification and Validation of the Propeller Hydrodynamic

In the mesh dependency study for the verification of the numerical study, the impulse coefficients in the mesh models with 950000, 1880000, and 4050000 cells were compare and the solution mesh configuration with 1880000 cells was preferred.

For numerical solution validation, the experimental values found in the literature are compare with the numerical solution results as shown in Figure 2. When the numerical thrust coefficient, torque coefficient, and propeller efficiency values are examined, it is seen that they are in well agreement with the experimental data.
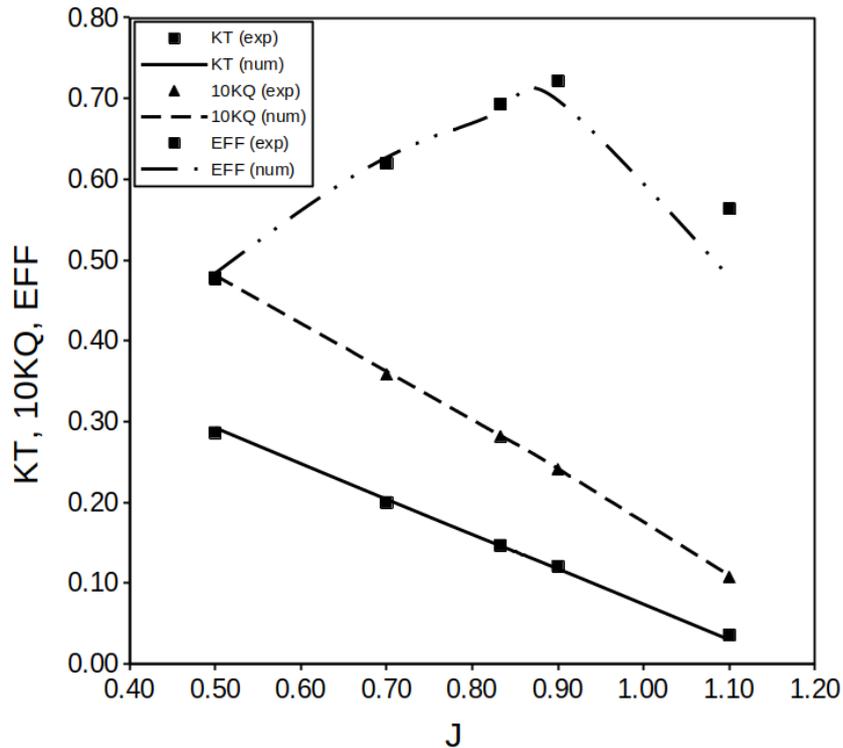
Figure 2 - Comparison of a DTMB 4119 fixed pitch Propeller numerical results with experimental datas (Sezen S. et al. INT-NAM 2018)

3.2.Numerical Model

In the study, the pitch of the DTMB 4119 model propeller, which is a fixed pitch propeller model whose pitch is not controllable, has been made controllable by making updates. The modified propeller used with the updates was named CPP DTMB 4119. The fixed pitch version and the CPP model DTMB 4119 propeller are shown in Figure 3. Movable blades were obtained with minimal changes.
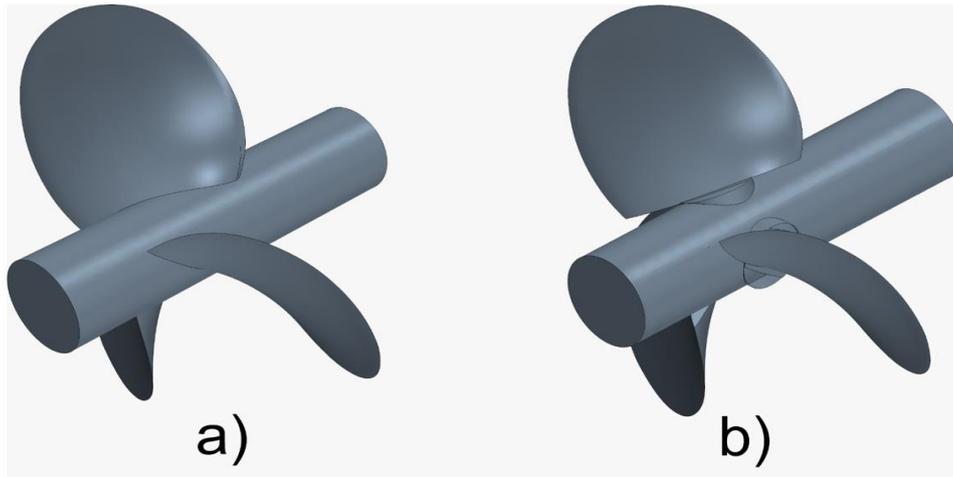
Figure 3 - a) DTMB4119 Fixed Pitch 3-D Model, b) Modify CPP DTMB4119 3-D Model
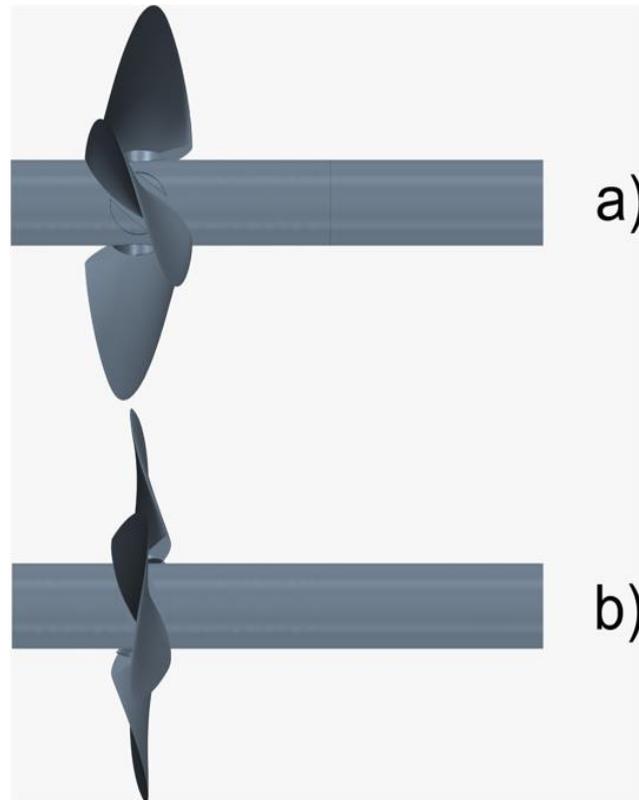
Figure 4 - a) Modify CPP DTMB4119 Full Ahead, b) Modify CPP DTMB4119 Zero Pitch

A study was create for two different starting pitches of the modified CPP-DTMB 4119 propeller.

Figure 4 shows a) the pitch angle of full ahead position the DTMB 4119 propeller in fixed pitch, b) the zero pitch position of the blades to provide maximum frontal area.
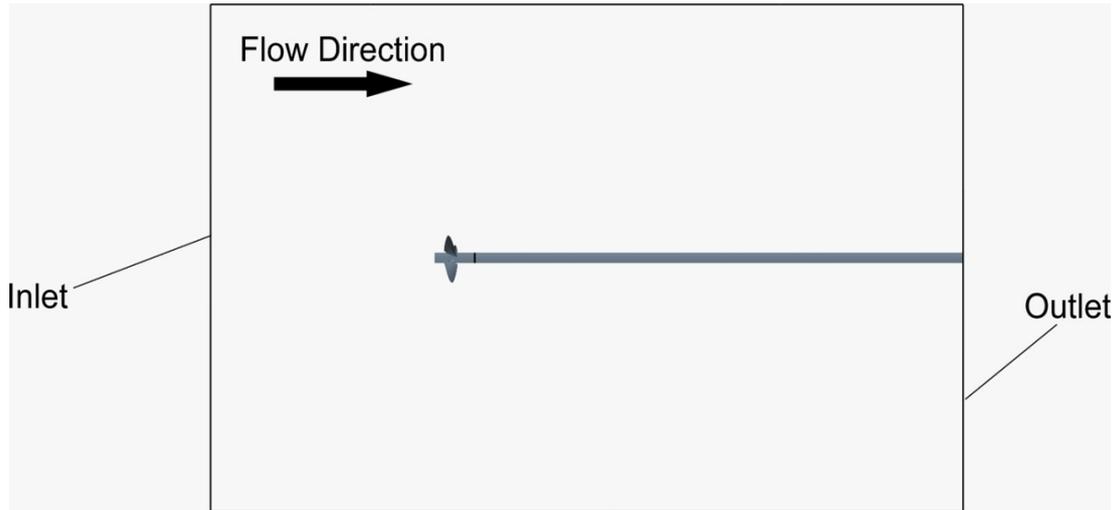
Figure 5 - Image of the Solution Domain

Figure 5. shows the solution volume used during the study. The inlet surface is used with the velocity inlet and the outlet surface with the pressure outlet boundary condition, and all the other outer surfaces are used with the symmetry boundary condition. In the study, the main body of the propeller and the blades are model with the RBM (Rigid Body Motion) movement model, and the movements of the blades around their own axis required for pitch change are model with the Overset movement model.

Figure 6. in the analysis studies we conducted, there is an image of the solution mesh. In the CFD analysis, the zero pitch position made for different blade positions of the propeller and the full ahead position is the mesh in which the analysis is resolved.
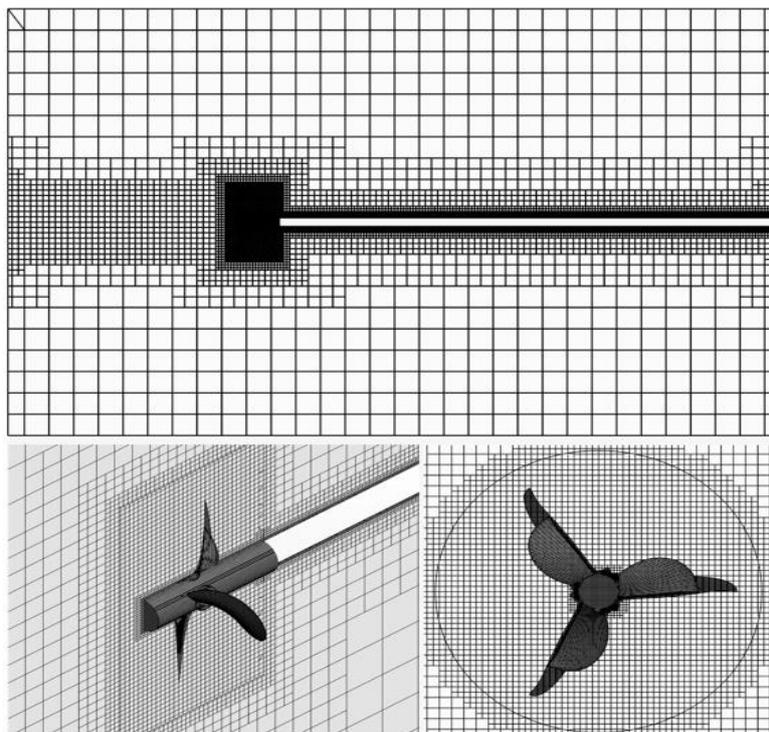
Figure 6 - Solution Mesh Image

In the study, the boundary conditions were chosen to provide five different progression (advance) coefficients: J=0.500, 0.700, 0.833, 0.900, 1.100 in order to be compatible with the experimental data of the fixed pitch model. In order to obtain different propagation coefficients in the analyses, the vessel speed was consider constant and the propeller speed was changed.
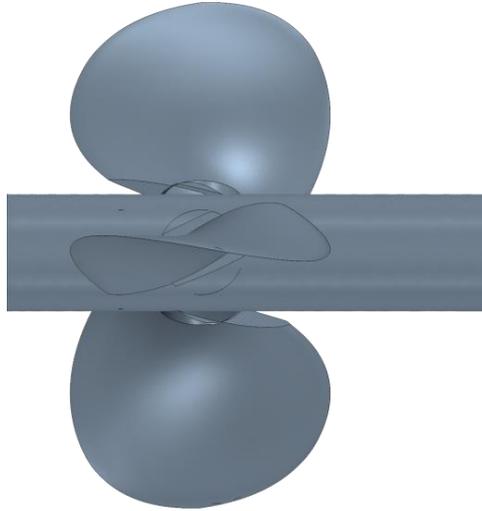
Figure 7 - Feathering Position

Analysis of the transition from full ahead pitch position and zero pitch starting positions to the feathering position, which is the rotated position to provide the minimum frontal area shown in Figure 7, is perform. The transition time to the feathering position is considered equal for both starting positions.

3.3. Hydrodynamic Results

During the transition from the initial position to the feathering position of the CPP DTMB 4119 propeller developed in the study, the torque values of each blade according to its own axis were examined.
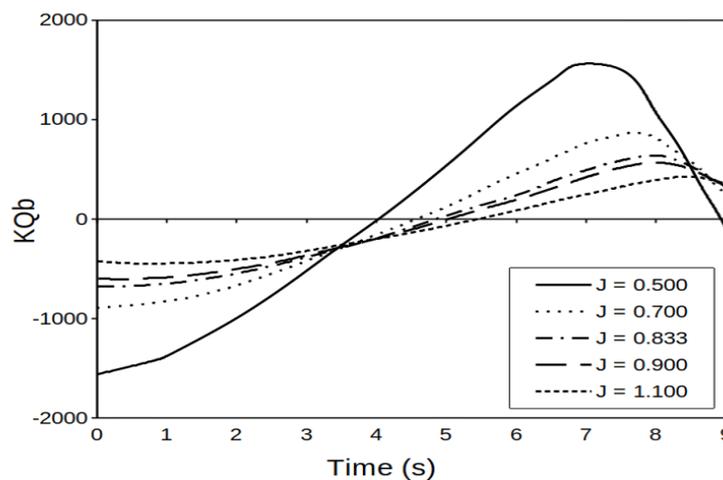
Figure 8 - Torque Coefficient Variation of Blades Around Their Axes for Zero Pitch Position

Figure 8 shows the time-dependent variation of the torque value on the blade during the transition from zero pitch position to feathering position. It is see in the graph that the maximum

blade torque coefficient value decreases with the increase in the feed coefficient. In addition, the time to reach the minimum torque value increased with the increase in the feed rate.
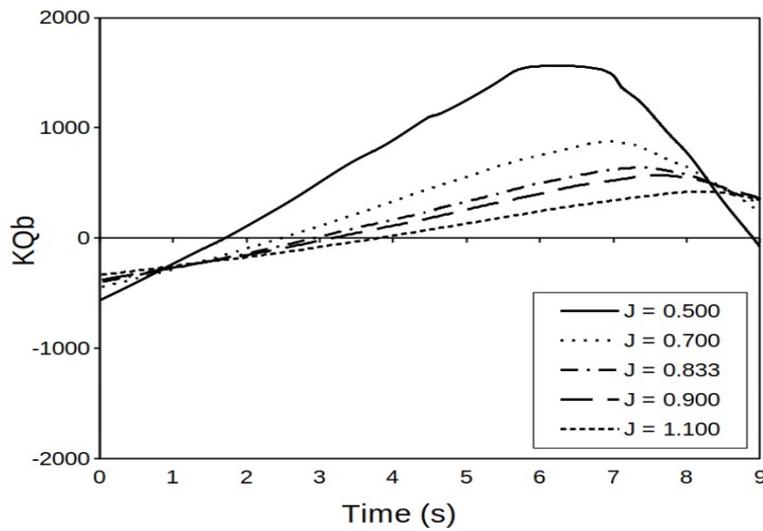
Figure 9 - Torque Coefficient Variation of Blades Around Their Axes for Full Ahead Pitch Position

In Figure 9, the time-dependent variation of the torque value (blade torque coefficient) on the wing during the transition from the full ahead starting position to the feathering position is shown. It has been observed that there is no change in the maximum torque amount between the zero pitch condition and the forward road condition. No difference was observed in the trends of the moment curves, except for a time dependent expansion and contraction.
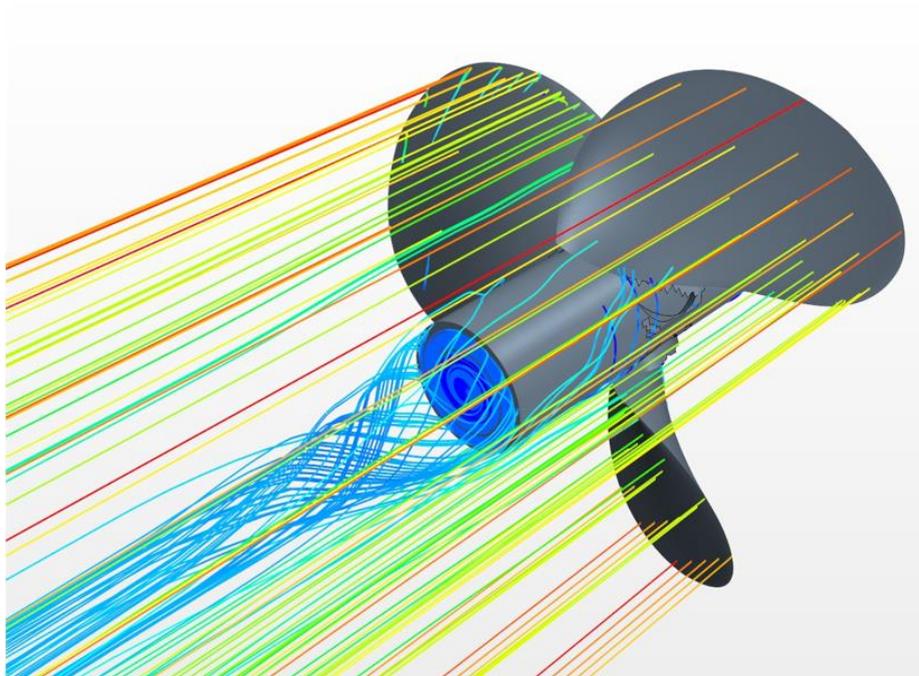
Figure 10 - View of Streamlines for the Full Ahead Position
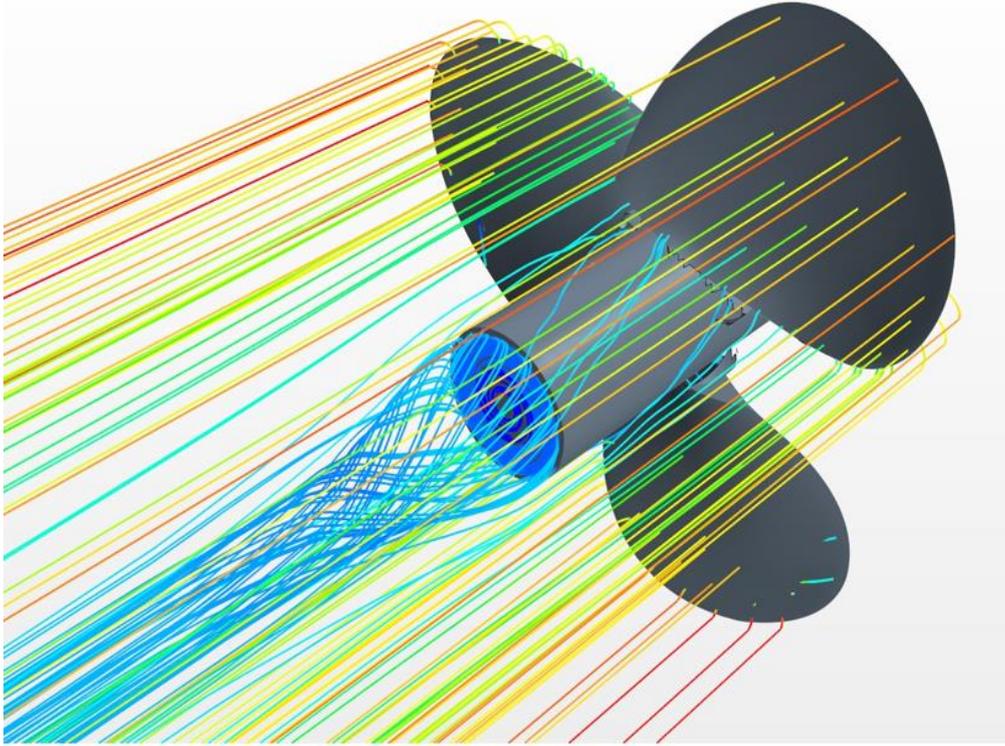
Figure 11 - View of Streamlines for the Zero Pitch Position

In Figures 10 and 11, flow lines visuals are given for full ahead and zero pitch situations, respectively. In general, no difference was observed in the downstream flow behavior for the two initial conditions.

4.Discussion

For the CPP propeller obtained by modifying the fixed pitch DTMB 4119 propeller, the transition from two different starting positions to the feathering position was investigate. In this study, the variation of the torque value on the blade depending on time has been examine. In this context, it has been obtained that the maximum value of the torque value is not affected by the two starting positions, only the same behavior curves expand and contract according to time. It has been observed that the maximum torque values are very much affected by the feed coefficient and the maximum torque value decreases with the increase in the feed rate. In future studies, it is predicted that it will be valuable to examine how the changes in different parameters affect the result in the change of the progression coefficient.

Acknowledgment

REFERENCES

Altosole M[1], Martelli M.[1] & Vignolo S.[2],(2011 September) ''A mathematical model of the propeller pitch change mechanism for the marine propulsion control design '' [1]Department of Naval Architecture and Electrical Engineering, [2]Department of Production Engineering, Thermal Energetic and Mathematical Models, Genoa, Italy

Dullens F.P.M., (2009 Feb.) ''Modeling and control of a controllable pitch propeller'' Technische Universiteit Eindhoven Department Mechanical Engineering Dynamics and Control Group Eindhoven.

Ghassemi S. T. H., & Fadavie M., (2014 July) ''Numerical prediction of hydromechanical behaviour of controllable pitch propeller'' Department of Ocean Engineering, Amirkabir University of Technology, Tehran, Iran.

Godjevac M., (2009) ''Wear and friction in a controllable pitch propeller'' Universiteit Belgrado, Serbia

Martelli M, (2014) ''Marine propulsion simulation'' Chapter-6 Propeller & Pitch Change Mechanism, Pages 46-61. ISBN 978-3-11-040149-3.

Nguyen C.[1], Luong N[2] & Ngo V.[2],(2018)''A study on effects of blade pitch on the hydrodynamic performances of a propeller by using CFD'' Vietnam Marine University[1] Haiphong 180000 Vietnam, Hanoi University[2].

Sezen Savas[1], Delen Cihad[2], Dogrul Ali[1], Bal Sakir[2] (INT-NAM 2018)'' Hydro-Acoustic Performance Prediction of DTMB 4119 Propeller'' Yıldız Technical University, İstanbul, Turkey[1], İstanbul Technical University, İstanbul, Turkey[2]

Zarbock O., (2009) ''Controllable pitch propellers for future warships & mega yachts'' Andritz Hydro, Ravensburg, Germany

Biofuel Production Potential of Turkey

Koç Mehmet Tuğrul[1]

Introduction

The use of alternative renewable energy sources is becoming widespread due to the negative environmental effects of the intensive use of traditional energy sources and their contribution to global warming. In addition, it is necessary to evaluate the contribution to rural development through the reduction of foreign dependency in energy and the support to be given to agricultural products in this context. Bioethanol and biodiesel, which are in the biofuels group, are among the most rapidly expanding alternatives. Increasing biodiesel production from renewable energy sources is considered as an alternative to reduce the negative effects of fossil fuel use in the world, especially diesel fuel use.

In the biological carbon cycle of agricultural biofuels, increasing photosynthesis with CO_2 and accelerating the carbon cycle limits the increase in the greenhouse effect. The idea of using herbal products as motor fuel is not a new idea. As a matter of fact, the inventor of the diesel engine, German Rudolph Diesel, first started the engine he developed at the World Fair held in Paris in 1898 with peanut oil. Henry Ford designed his 1908T car to use ethanol and built an ethanol plant. However, the problems encountered at that time, and especially the prevalence and cheapness of oil, put biofuels off the agenda. The use of ethanol in automobiles continued until 1940, then it was stopped due to the availability of cheap gasoline (Songstad et. al., 2009). However, the instability of oil prices, the prominence of its strategic aspect, the excessive use of petroleum products, especially gasoline and diesel fuels, to pose a great risk for the environment, started the search for alternative and renewable energy and biofuels came to the fore again.

Increasing environmental awareness, obligations arising from international agreements on reducing greenhouse gas emissions, the EU's obligatory biofuel contribution and the financial supports (tax privileges) it provides and its ease of production encourage biofuel production. On the other hand, demand-related increases in raw material prices, high plant production costs and limited cultivation areas are the factors hindering biofuel production.

In order to create a sustainable agricultural structure in agricultural production and to support organic agriculture, it is possible to evaluate the barren areas that are not suitable for agricultural production of plants that can be biofuel raw materials. In order to reduce foreign dependency in energy, it would be appropriate to support the development of new production technologies for biofuel production from by-products without disrupting agricultural production. Thus, used plant and animal origin wastes will be brought into the economy without harming the environment.

Studies show that the most economical bioethanol is produced from sugar beet, sugar cane, corn and wheat, and biodiesel is produced from rapeseed, soybean and palm oil. However, with the improvement studies to be carried out on plants, which are the basic production materials,

[1] Assoc. Prof. Dr., Eskişehir Osmangazi University, Faculty of Agriculture, Department of Biosystems Engineering, Orcid: 0000-0003-2111-4050

these products can be taken to a higher level and the economic level of other products can be increased.

1 121 Mt of corn was produced in the world in 2020, and the USA, which is the largest producer, realizes 27% of its total exports. Corn consumption in the same period was 1 145 Mt. There is a balance in terms of corn, which has an important place in nutrition. Turkey realized 6 million tons of corn production in 2020 against 640 thousand hectares of corn cultivation area. In the same period, the average yield is around 9.4 t ha^{-1}. Turkey is not a self-sufficient country in corn, and imports around 3 million tons of corn annually due to the increase in the demand for feed raw materials parallel to the increase in egg and poultry production and the number of cattle (Agriculture-Orman, 2020a).

World wheat production in 2020 was 774 and consumption was 766 Mt. Global production is at a record level of 790 Mt, while consumption is expected to increase to 787 Mt. Turkey wheat cultivation area constitutes 3.2% of the world wheat cultivation area as of 2020/21 production season. This area also constitutes 44% of the total cultivated grain area in Turkey. In our country, wheat cultivation in 2020 is 692 thousand hectares, total production is 20.5 million tons. Domestic wheat use in the 2019/2020 marketing year is 20 million tons and the adequacy is 89.5% (Agriculture-Forest, 2020b).

Approximately 76% (127 Mt) of world sugar production is produced from sugar cane, and 24% (39.6 Mt) is produced from sugar beet (USDA, 2020a). Sugar produced from sugarcane is less costly because of the low cost of producing and processing sugarcane, which is usually grown in tropical and sub-tropical regions. A significant part of the world's sugar need is provided from sugar cane. World sugar production decreased by 4.4% in 2019/20, from 174 million tons to 169.6 million tons. Turkey is in the 5th place among the countries producing beet sugar with a cultivation area of 307 thousand ha and 18.9 Mt of beet production, and the average yield is around 6.1 t ha^{-1}. Turkey produced a total of 2.7 million tons of sugar in 2020, of which 2 633 thousand tons of beet sugar production and 67 thousand tons of SBS. Research shows that the most important consumer countries are also the leading countries in terms of production. While India, EU, China, USA, Brazil, Russia, Indonesia, Pakistan, Mexico and Egypt are the leading sugar consumers, East Asia is the continent that consumes sugar at the highest level. Turkey ranks 11th in the world with 3 million tons (Crop report, 2020a).

According to FAO 2018 data, 368.2 Mt of potatoes were produced in 17.6 million hectares of land in the world. 27.4% of the world potato cultivation areas are in China, 12.2% in India and 7.5% in Russia, these three countries account for 43.8% of the world potato production. Turkey has suitable conditions for potato cultivation, and potato production was carried out on an area of 140.000 ha in 2019. According to the data of 2020, 3.9 Mt consumption was realized against 4.6 Mt potato production in Turkey (TUIK, 2020). Although Turkey is a country that can meet its needs in potato production, it also imports for the purpose of price balancing in the domestic market (Crop report, 2020b).

MATERIAL and METHOD

Bioethanol

Bioethanol is a clean and renewable energy source produced from various agricultural products. The amount of carbon dioxide released as a result of the combustion of this fuel is quite low compared to coal, oil and natural gas. It can be produced with ethanol, petroleum or biomass. When ethanol is produced with biomass, it is called bioethanol. Bioethanol and petroleum-

produced ethanol are chemically identical. The general raw materials of bioethanol are biomass products such as corn, sugar beet and algae. Raw materials are digested with various bacteria by fermentation. As a result of this process, bioethanol and carbon dioxide are released.

Ethanol has a high octane number and is used as an octane booster in gasoline. This feature allows engines to be designed with a higher compression factor. Although ethanol contains less energy per liter than gasoline, it causes less energy loss when used as fuel, meaning that ethanol fueled vehicles have better performance. Besides alcohol-based beverages, ethanol is used as an alternative fuel in internal combustion engines. It can be mixed with gasoline, such as biodiesel, in certain proportions, and all current gasoline engines in automobiles can operate with a gasoline-ethanol mixture with 10% ethanol. However, since ethanol has a lower energy density than gasoline, more ethanol must be burned to produce the same amount of energy as 1 liter of gasoline produces. The amount of energy per unit volume of ethanol is 34% less than gasoline. Therefore, 1.5 liters of ethanol has the same energy production capacity as 1 liter of gasoline. When bioethanol is burned, it causes much less emissions than conventional fuels used in transportation. Since the carbon dioxide released during the fermentation and combustion of bioethanol is used for the cultivation of agricultural raw materials required for the production of bioethanol, this fuel is seen as a renewable energy source. In the researches, it has been observed that the carbon monoxide emission in fuels mixed with 5-7% bioethanol is reduced by 15-40% (Adıgüzel, 2013).

The agricultural raw materials used by the countries in the production of biofuels are determined entirely depending on their own conditions. In the production of bioethanol, grain types such as corn, wheat, barley, triticale, maize, sorghum containing starch and or sugar, vegetable products such as sugar beet, molasses, sugarcane, potatoes, and vermicelli are used as raw materials. Bioethanol emerges as a result of the fermentation process applied after the conversion of starch in agricultural products into sugar. Oxygen makes up 35% of the chemical composition of bioethanol. Its octane is 113 and its freezing point is -114 °C. It can be mixed with gasoline directly (Horuz et. al., 2015).
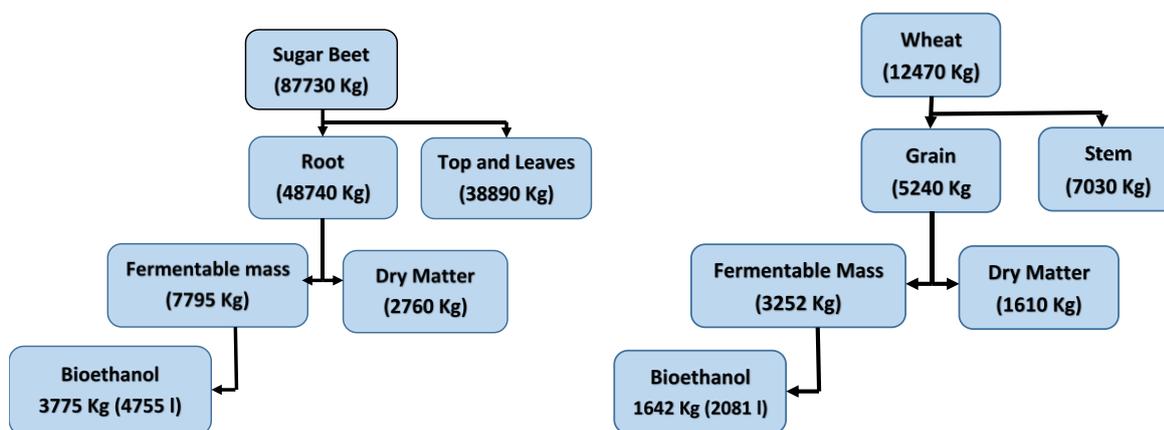
Figure 1 - The amount of bioethanol that can be produced from 1 ha area

The first application in the field of biofuels started with bioethanol. Bioethanol production in the USA in 2004 is 10.3 million tons. In the USA, the mixture of bioethanol, which is generally produced from corn, with gasoline is made at a rate of 10%. DDGS (Dried Distillers Grain with Solubles) remaining in bioethanol production is a good animal feed because it contains 30% protein and 6-10% oil. In the USA, where the use of bioethanol is increasingly widespread. E85 application is aimed at in the region and the use of bioethanol has been made compulsory by legal regulation in order to reduce air pollution in large residential areas.

Bioethanol produced from cereals is considered environmentally beneficial because it is carbon neutral. However, considering the environmental emissions caused by the fertilizer and energy used to produce the grains used in the production of bioethanol, this production technique is not completely carbon neutral and is indirectly considered a carbon neutral product since it stands out as a low carbon emission choice compared to gasoline (Melikoğlu et al. al., 2011). In our country, bioethanol is mainly produced from molasses in sugar factories. The capacities of the existing bioethanol production plants in Turkey are given in Table 1 (İçöz et. al., 2009; Horuz et. al., 2015).

Table 1 - Bioethanol factories in Turkey

Ethanol plant	Crop	Production capacity (×1000 m³ year⁻¹)
Eskişehir	Sugar beet	21.0
Turhal	Sugar beet	14.0
Malatya	Sugar beet	12.5
Erzurum	Sugar beet	12.5
Çumra	Sugar beet	84.0
Tarkim (M. Kemalpaşa)	Wheat-Corn	40.0
Tezkim (Adana)	Wheat-Corn	26.0

Biodiesel

Biodiesel is an alternative energy source obtained from domestic and renewable biological resources such as vegetable and animal oils and used as fuel in diesel engines. Biodiesel is easily biodegradable and non-toxic in nature, and is environmentally friendly because it has low emission values when burned. In addition, the amount of unburned hydrocarbons produced during the combustion process is lower than diesel fuel.

Table 2 - Emission values of biodiesel

	B100	B20
Unburned hydrocarbons	% -93	% -30
Carbon monoxide	% -50	% -20
Particulate matter	% -30	% -22
NOx (nitrogen oxides)	% +13	% +2
Sulfates	% -100	% -20
PAH* (carcinogenic substances)	% -80	% -13
nPAH (nitrated PAHs)	% -90	% -50
Effect of hydrocarbons on the ozone layer	% -50	% -10

* Polycyclic aromatic hydrocarbons

Biodiesel can be used both pure and mixed with diesel fuel in proportions expressing the mixture ratios such as B5, B20, B50 and B100. Comparative values of the emission values that may arise in case of using pure biodiesel (B100) and 20% (B20) biodiesel with diesel fuels are given in Table 2.

Biodiesel is close to diesel fuel in terms of efficiency and engine performance. On the other hand, it has advantages such as reducing dependence on fossil fuels in energy, being able to be produced from agricultural products and waste, not containing toxic waste, and reducing the pollution load of exhaust emissions due to its rapid dissolution in nature.

Biofuels in the World and the European Union

Due to the COVID-19 experienced in 2020, the use of disinfectants, especially for health purposes, has increased, and there has been a 10% decrease in demand for ethanol, especially for fuel. The market share of the USA, which met half of the ethanol exports before the pandemic, decreased to 43% due to the decreasing fuel demand and the prominence of some countries such as China and Brazil in the trade of medicinal products (Figure 2). With the increase in population and income, the mobility of people and the demand for fuel increase accordingly. However, ethanol blended gasoline falls short of meeting the increasing demand for mobility, while reducing greenhouse gas emissions. Increased public transport, improved fuel efficiency, lifestyle changes including teleworking, and alternatives such as electric motors are all factors in meeting the fuel requirement of ethanol.
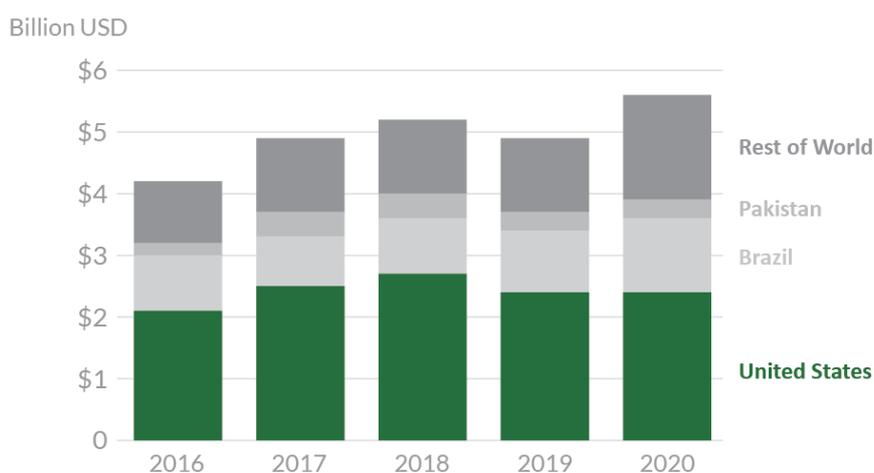
Figure 2 - Global Ethanol Exports (USDA, 2020b)

The EU has increased its target of 10% for the use of renewable energy in transport for 2020 to 14% for 2030 (Table 3). The EU has set an upper limit of 7% for food-based biofuels, which is estimated at 4.6% in 2019, and a target of 3.5% for non-food-based biofuels. Such advanced biofuels, mostly made from agricultural, forestry and municipal waste, are currently 0.2 percent and are projected to increase mainly due to tallow oil. The EU has set the production target of biofuels produced by blending waste fats and oils, which is currently 1%, to be 1.7% for 2030 (GAIN, 2019). EU bioethanol production was around 5.5 billion liters in 2019 despite the increase in corn and wheat prices (Table 4-5). EU biofuels goals set out in Directive 2003/30/EC (indicative goals) and in the RED 2009/28/EC (mandatory goals) further pushed the use of biofuel.

Table 3 - Statement in relation to marketing strategy of biofuels (%) as stated in the national renewable energy action plans (NREAPs) (Kampman, 2013)

	2005	2010	2015	2020
France		5.75	7.0	7.0
Germany		5.25	6.25	6.25
U.K.		3.5	4.5	5.0
Hungary			4.8	4.8
Belgium	4.0	4.0	4.0	4.0
Netherlands			3.5	3.5
Spain			6.5	6.5
Poland		6.2	7.1	7.1
Austria	2.5	5.75	6.25	8.45
Italy		4.0	4.5	5.0

Romania	6.0	7.0	9.0	10.0
Latvia		5.0	5.75	5.75
Lithuania	2.0	5.75	7.0	7.0
Ireland		4.0	6.0	6.0
Estonia			5.0	5.0
Denmark	0.75	3.35	5.75	5.75
Czech Republic			5.0	5.0
Bulgaria	2.0	3.5	8.0	10.0

Table 4 - EU bioethanol production data for 2019

(Million liters)	Ethanol
Production	6 180
Fuel Production	5 505
Consumption	5 950
Number of Refineries*	60
Capacity Use (%)	71
Feedstock use for bioethanol	(1 000 MT)
Wheat	5 665
Corn	5 000
Barley	430
Rye	418
Triticale	720
Sugar Beet	8 145
Cellulosic Biomass	50

*Two of them are cellulosic ethanol production refineries.

The EU is the world's largest producer of biodiesel, holding approximately 75 percent of the biofuels market. Biodiesel is also the most important biofuel adopted by the transport sector in the 1990s and developed in the EU. In 2018, France, Germany, Spain, Sweden and Italy were the largest consumers of biodiesel, accounting for 63 percent of total EU biodiesel consumption. However, biodiesel consumption varies due to legislative changes and tax regulations in countries (Table 6). EU biodiesel consumption is expected to increase by 3% for 2019 (GAIN, 2019).

Table 5 - Biofuel production and consumption amounts in some countries in 2019 (million liters)

	Ethanol		Biodiesel	
Countries	Production	Consumption	Production*	Consumption
France	1 000	880	1 778	3 025
Germany	785	1 505	3 000	2 600
U.K.	695	925	490	1 200
Hungary	645	-	-	-
Belgium	645	-	490	610
Netherlands	565	305	2 268	-
Spain	522	350	2 340	2 275
Poland	265	340	1 000	970
Austria	235	-	330	600
Italy	-	260	877	1,360
Sweden	-	205	200	1,610
Finland	-	-	-	400
Portugal	-	-	410	-
Others	-	-	370	2 730
Total	5 505	5 950	14 150	17 380

*HVO + FAME (Fatty acid methyl ester)

RESULT and DISCUSSION

Biofuel in Turkey

In the Regulation on Technical Criteria to be Applied in the Petroleum Market of the Official Gazette dated September 10, 2004 and numbered 25579, how and by whom the biodiesel will be mixed with diesel fuel, and in Article 9, it has been explained by whom the biodiesel can be produced. Since Turkey is an economically and technologically developing country, the consumption rate varies according to energy sources. For this reason, the state is trying to benefit from all natural resources for energy production in order to ensure stable energy security that guarantees the development process. (Figure 3).
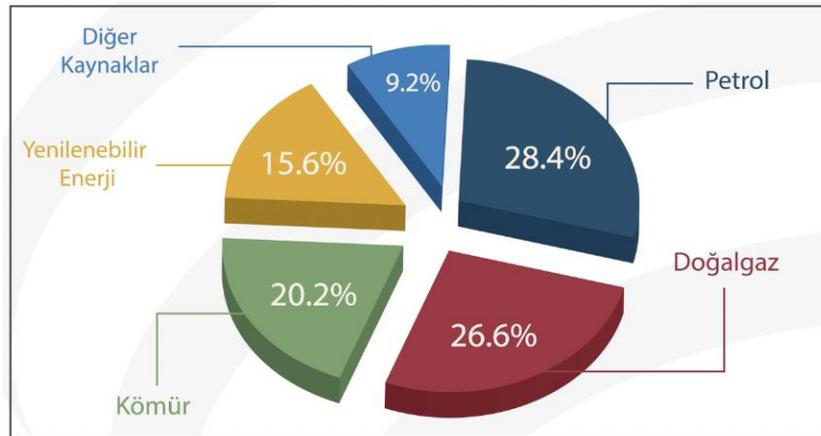
Figure 3 - Energy resources consumed in Turkey in 2019

Table 6 - EU biodiesel production data for 2019

(Million liters)	Biodiesel
Production	14 170
HVO* production	3 030
Consumption	17 380
Number of biodiesel refineries	188
Capacity Use (%)	53
Number of HVO refineries*	14
Capacity use (%)	60
Feedstock use for bioethanol	(1 000 MT)
Rapeseed oil	5 000
UCO	2 750
Palm oil	2 640
Soybean oil	1 100
Animal fats	800
Sunflower oil	190
Other, pine/tall oils, fatty acids	700

*HVO: Hydrotreated vegetable oil

Average oil consumption in Turkey constitutes 30 percent of total energy consumption. Turkey's crude oil production is approximately 2.5 million tons per year, its oil reserves are 324 million barrels and 47.9 million tons of oil has been imported. According to EMRA (Energy Market Regulatory Authority) data, diesel consumption is 28 million m³ and gasoline consumption is 3

million m³ in 2019. In case it is mandatory within the framework of EU harmonization, it needs 60 000 m³ of bioethanol and 560 000 m³ of biodiesel at a mixture ratio of 2% (Table 7). Considering that approximately 1.1 t of biodiesel is obtained from 1 t of oil, 510 000 m³ of oil is needed for 560 000 m³ of biodiesel. Considering that 150 000 m³ of waste vegetable and animal oil is used in biodiesel production in Turkey, this amount will decrease to 360 000 m³.

Table 7 - Turkey's biofuel needs according to different mixing ratios (m³)

Mixture rate	%2	%5	%10
Bioethanol	60 000	150 000	300 000
Biodiesel	560 000	1 400 000	2 800 000

The most planted oilseed plant in Turkey is sunflower. 50% of our vegetable oil production is obtained from sunflower, 35% from cotton and 15% from other oil plants. Our production of canola, safflower, soybean and other oil crops is insufficient. Although sunflower, cotton seed, soybean, canola, safflower, sesame, peanut, poppy, hazelnut and olive are oily plants, they are not included in the scope of oilseeds in world trade. It is not possible to increase the production in a short time due to the fact that peanuts and sesame are produced for food purposes, seeds and corn germ are by-products, and olive is perennial (Arıoğlu, 2016). The area devoted to oilseed production in Turkey constitutes only 4% of the total arable land. For this reason, the amount of oil seeds obtained from domestic production cannot meet the country's requirements. In this case, in order to increase the production of oilseeds in Turkey, the development of solutions that can increase the production of plants such as sunflower, soybean, rapeseed and safflower emerges as a solution. However, considering the climatic demands of the plants, soybean can grow in irrigable areas, sunflower in irrigable or semi-arid areas, rapeseed in partially insufficient precipitation and safflower in arid areas (Arıoğlu, 2016). In this respect, it can be said that the most suitable products for biodiesel production are safflower and rapeseed. Oil ratios according to the products are given in Table 8. According to the values given, a total of 900 000 t rapeseed and safflower production is needed for the production of 560 000 m³ of biodiesel. Considering that the rapeseed yield in Turkey is 3.6 t ha^{-1} and the safflower yield is 1.8 t ha^{-1} (Kadakoğlu et. al., 2019) and the oil requirement will be obtained in equal amounts for both crops, 354 000 ha of rapeseed and 707 000 ha of safflower cultivation area is needed. According to the 2018 TUIK data, there is 15.5 million hectares of grain and 3.4 million hectares of fallow land in Turkey, corresponding to a total agricultural area of 37.8 million hectares (TUIK, 2021), and fallow fields have the potential to realize the required production.

Table 8 - Oil ratios of oilseeds

Crop	Oil rate (%)
Sunflower	35-45
Cotton seed	18-20
Soy	18-20
Canola	38-42
Safflower	35-40
Peanut	45-50
Hazelnut	55-60
Sweet corn	18-20
Olive fruit	25-30

Since Turkey was not yet a party to the convention when the Kyoto Protocol was adopted in 1997, no digitized emission limitation or reduction specific to Turkey was determined within the scope of the Kyoto Protocol. Pursuant to the decision numbered 26/CP/7 adopted in 2001, it was

entitled to be included in the Annex-1 of the convention, in a different position from other countries, and joined the Convention in 2004. Turkey does not have any obligations as it is in the Annex-1 list of the convention but not in the Annex-B list of the protocol.

Oils used in frying processes are generally easily oxidized at high temperatures. In our country, in accordance with the Regulation on the Control of Hazardous Wastes, which was published in the Official Gazette dated 27 August 1995 and numbered 22387, the use of waste vegetable oils was limited and it was made compulsory to collect, transport, dispose and/or recover by licensed institutions.

The "Regulation on Control of Waste Vegetable and Animal Oils", which aims to collect waste vegetable oils (used frying oils, etc.), which is one of the raw materials of biodiesel, with an organized collection system and direct them to biodiesel production, entered into force after being published in the official newspaper dated 06.06.2015 and numbered 29378. According to the regulation, it is stated that "vegetable and animal waste oils can only be used in biodiesel and biogas production in accordance with technical regulations". It is aimed to reduce the amount of foreign exchange paid for oil abroad by including approximately 150 000 tons/year of vegetable waste oil in biodiesel production in Turkey. The waste oil, which is approximately 150 000 000 kg, is not poured into the sewer and is recovered, thus contributing to the economy by producing 150 000 000 kg of biodiesel and 15 000 000 kg of glycerin per year (Öztürk, 2018). However, according to 2017 data, only 35 000 tons of this amount of waste oil can be collected (BSD, 2019) (Table 9). With the recycling of vegetable and animal waste oils, domestic wastewater will be 25% less polluted. By mixing biodiesel containing 11% oxygen in its structure, the toxic gases released during combustion in the engine and especially carbon monoxide (3%) decrease by three tons of carbon dioxide emissions for each ton of biodiesel used (Figure 4). If 150 000 tons of animal and vegetable waste oil produced in Turkey were recovered and used in biodiesel production, the greenhouse gas carbon dioxide released into the atmosphere would decrease by 450.000 tons compared to diesel fuel. There are 6 biodiesel conversion facilities from vegetable and animal oils (including waste oils) with an annual capacity of 115 000 tons in Turkey (Öztürk, 2018).

Table 9 - Amount of waste vegetable oil collected in Europe in 2017

Country	Amount (ton)	Population (million)
Germany	140 000	82.2
Britain	100 000	60.6
Spain	65 000	47.1
Holland	60 000	16.4
Italy	59 000	59.3
France	44 000	63.8
Turkey	**35 000**	**74.9**
Poland	32 000	38.1
Belgium	29 000	10.5
Greece	13 000	11.1
Sweden	8 000	9.1
Czech Rep.	7 000	10.3
Denmark	5 000	5.4
Finland	4 000	5.3
Norway	4 000	5.2
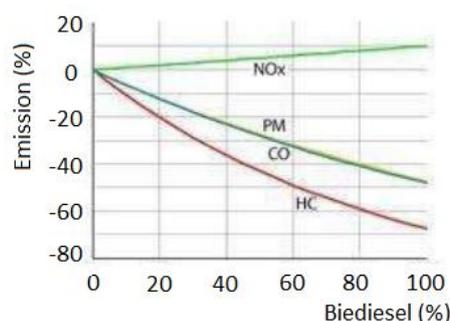
Figure 4 - Change in emission rate if biodiesel is used instead of diesel oil.

Turkey's oil crops production potential

The world's total oilseed production in 2017 was 575 Mt, and crude oil production was 194 Mt. In the same period, 3.8 Mt of oil seeds and 0.9 Mt of crude oil were produced in Turkey (TUIK, 2021a) (Table 10). Due to insufficient production, Turkey mostly imports oilseeds, crude oil and oilseed meal. (Küçük et. al., 2022).

Table 10 - Turkey's oil seed production between 2014 - 2020 (1000 tons)

Yıllar	Soybean	Peanut	Sunflower	Sesame	Safflower	Canola	Cottonseed	Total
2015	161.0	147.5	1680.7	18.5	70.0	120.0	1213.6	3442.1
2016	165.0	164.2	1670.7	19.5	58.0	125.0	1260.0	3480.6
2017	140.0	165.3	1964.4	18.4	50.0	60.0	1470.0	3883.4
2018	140.0	173.8	1949.2	17.4	35.0	125.0	1542.0	4009.5
2019	150.0	169.3	2100.0	16.9	21.9	180.0	1320.0	3985.4
2020	155.2	215.9	2067.0	18.6	21.3	121.5	1064.2	3684.7
Rate	4.2	5.9	56.1	0.5	0.6	3.3	28.9	100.0

Table 11 - Turkey's self-sufficiency rates in oilseeds (%)

Years	Sunflower	Cottonseed	Soybean	Canola
Rate	60.1	101.0	7.1	76.7

In Turkey, it is seen that oil seeds are not sufficient in terms of self-sufficiency except cottonseeds. According to 2017 data, the self-sufficiency rate is 76.7% in canola and 60.1% in sunflower (Agriculture-Forest, 2020c) (Table 11). In 2016, 2 million 940 thousand tons of oilseeds were imported in Turkey, corresponding to 239 thousand tons of oilseed exports. The largest share of imports belongs to soybean with 74%. The share of sunflower in oil seeds import is 13%. On the other hand, in Turkey's oilseed exports, respectively; sunflower (48.8%), soy (43.9%) and sesame (5.5%) have a significant share. (Kadakoğlu et. al., 2019).

Cost analysis

Depending on the nature of the raw materials used in production, less than 5% wastage is possible, but 1100 liters of biodiesel is produced from 1 t of oil. For 1000 kg of oil, the raw material ratios and product quantities used in production are as follows:

Raw Material   Processed Product

    Oil, 1 t

    Methyl alcohol, 170 kg,   Biodiesel, 1100 l + Crude glycerin, 200 kg.

     Caustic, 50 kg.
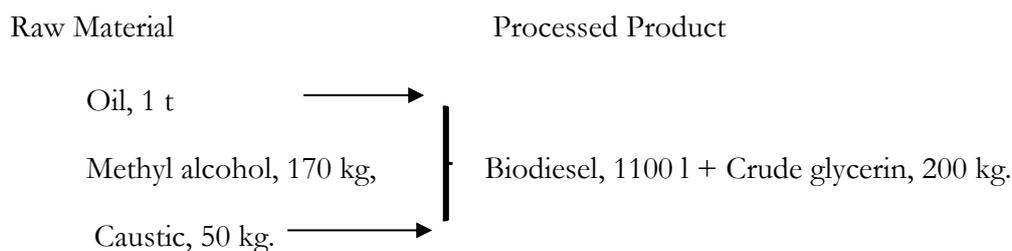
Diesel fuel has a density of 0.830. Average oil prices are 687 - 775 $/ton; the price of methyl alcohol is $1000-1300/ton, and an average production cost of $25 is made for the processing of one ton of oil. The crude glycerin obtained is sold at a price of $500/ton. With these data, when 1 ton of oil is processed and 1 ton of biodiesel is produced, the cost is calculated as follows;

$775 + 1300 \times 0.17 + 25 - (500 \times 0.20) = 921$ $/ton.

Current state

In 2020, an average of 62 thousand v/g crude oil was produced daily in Turkey; 590 thousand b/g of crude oil was imported. While the ratio of domestic crude oil production to total oil supply was 6.3% in 2019, this ratio was 7.1% in 2020. In other words, our country's dependence on oil imports was 92.9% in 2020 (TPAO, 2020). Oil prices, which have been increasing and continuing to increase, have a very high cost to the country's economy. The need for a solution to reduce the oil bill is clear. Diesel is one of the biggest inputs of agricultural production. High-priced diesel fuel also increases production costs. Biofuels may seem like the solution to this problem! Although our country has a high potential in agriculture, it imports about 3 million tons of oil every year. Turkey essentially has a significant canola production capacity. In particular, the utilization of barren lands that are not suitable for agriculture can meet the need for oilseeds without affecting the production of other agricultural products. In addition, the contribution of its by-products to animal husbandry should also be considered.

Turkey is among the world's leading soap and glycerin producers. The raw material of soap and glycerin is various oils. The increase in oilseed production will increase the potential of this industry and lead to more income for the country's economy. With the proper processing of the glycerin obtained as a by-product, an additional external income door will be opened.

There is an advanced oil technology and many oil factories in our country. Some of these facilities are inactive and some of them are operating at low capacity due to both excess capacity and old and/or deficient technology. On the other hand, the operating facilities are mostly imported soybean and so on. They process oilseeds. Increasing oilseed production in our country has the potential to bring these facilities back to the economy.

Renewable energy consumption has changed significantly over the last decade (Figure 5). In total, renewable energy consumption rose 36% in ten years to 11.7 Mtoe in 2018. The transition from traditional methods to the use of modern heating and cooking technologies in domestic use has reduced the bioenergy consumption in the residential sector by half. Despite the growth in total renewable energy consumption, the share of renewable resources in TFEC (total final energy consumption) still seems somewhat low. The situation of 11.9% renewable share in TFEC in 2018 with IEA (international energy agency) member countries is given in Figure 6 (IEA, 2021).

Figure 5 - Share of renewable energy consumption in total final energy consumption in Turkey.
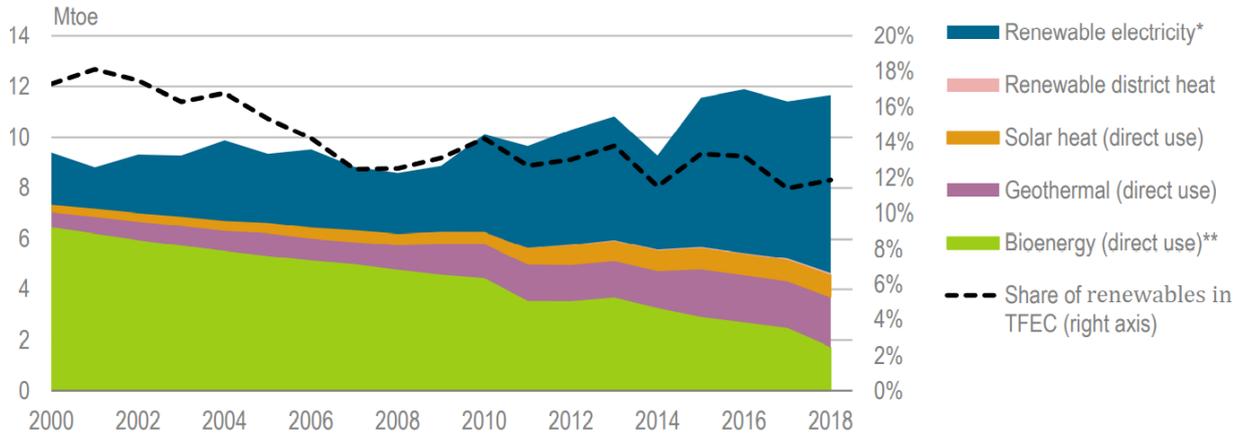
Figure 6 - Share of renewable energy in total final energy consumption in IEA member countries in 2018.
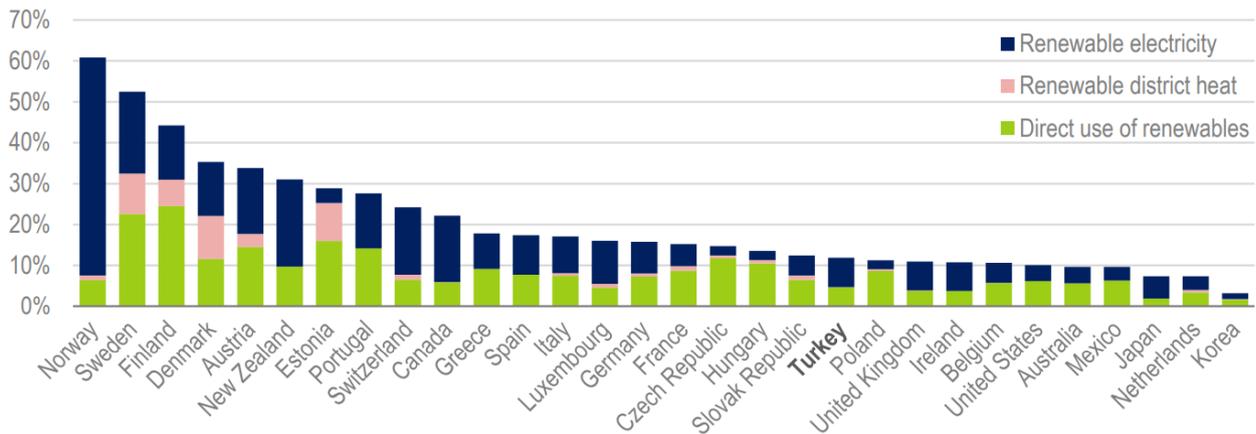
CONCLUSION

The way to save foreign currency in crude oil and crude oil, which are the biggest items of our imports, is to increase the rate of domestic production. If Turkey applies the 2% mixing ratio, it needs 60.000 m³ of bioethanol annually. Currently, the installed bioethanol capacity in Turkey is 210 thousand m³. It has the potential to produce alcohol, which is needed for both the chemical and pharmaceutical industries and for gasoline mixtures, originating only from molasses, which is a by-product of sugar beet.

On the other hand, it does not seem possible to say the same for biodiesel. 560,000 m³ of biodiesel is needed for a 2% mixture. Although Turkey is self-sufficient in the production of many agricultural products, it is not self-sufficient in oilseed and vegetable oil production. Among the oilseed plants cultivated in Turkey, sunflower takes the first place in terms of cultivation area and production, with a rate of 60.1% (Agriculture-Orman, 2020c). Sunflower production alone is not enough for consumption. According to the November Product Tables Sunflower Report of the Ministry of Agriculture and Forestry, Turkey is the country that imports the most with a 37% share in world sunflower imports.

In addition to sunflower production, the share of soybean and canola, which are the most produced oil seeds in the world, in Turkey's production is low. Although Turkey is suitable for soybean and canola production in terms of its climate characteristics, the desired levels have not yet been reached in the production of these two products. The feed and vegetable oil industry data show that the only way to reduce imports in both energy and agricultural production, which Turkey is heavily dependent on, is to increase production. Increasing the production of oilseeds will contribute not only to the need for oil, but also to the feed sector, which is one of the main raw materials of the livestock sector. There is a potential to utilize approximately 3.5 million fallow land in Turkey every year. It is clear that opening the fallow areas to agriculture and making room for products that will meet the oil needs, especially canola, is not a solution in terms of biodiesel production. The main reason for this is Turkey's high crude oil deficit.

While people are starving in many countries and many agricultural and food products are imported, the question of how right it is to produce energy from agricultural products is always questioned. Although the issue has a humanitarian, economic and legal dimension, it can be offered as a solution to meet the need by planting oily plants such as canola, safflower and flax, which are not consumed by humans, in fallow areas. On the other hand, it should be questioned that the use of fallow lands in sunflower production would be a priority, since Turkey is dependent on foreign sources for a product such as sunflower by around 30%. While determining agricultural policies, it should not be overlooked that the choice to be made in this regard is an important decision for the future of the country.

It would not be a logical approach to use vegetable oil to be produced for food purposes as a fuel mixture for industrial purposes, since the vegetable oil deficit is high and the need increases every year due to the increasing population. First of all, Turkey should fully recycle waste oils of vegetable and animal origin and meet some of the amount it needs for the biodiesel blend. The rest can be obtained by encouraging the use of electric vehicles and reducing vehicle-related emissions. Thus, it will have taken an important step towards meeting the agricultural oil need it needs.

Apart from these, what needs to be done can be summarized as follows:
• All alternative energy sources that will reduce foreign dependency should be evaluated.
• More investment should be made in the collection of waste oil generated at home.
• Additional incentives should be given to licensed recovery facilities for waste oils to reach biodiesel facilities.
• Biodiesel production and use should continue to be encouraged.
• Making the use of biodiesel compulsory for public use at a certain rate will set a good example.
• A more effective environmental control system should be established.

REFERENCES

Adıgüzel, A.O., (2013). General characteristics and necessary feedstock sources for the production of bioethanol. BEU Journal of Science 2(2): 204-220.

Arıoğlu, H. (2016). Oil Seeds and Crude Oil Production in Turkey, Problems and Solutions. Tarla Bitkileri Merkez Araştırma Enstitüsü Dergisi, 2016, 25 (2): 357-368.

Ayçiçek Raporu. (2020). 2019 yılı ayçiçeği raporu. T.C. Ticaret Bakanlığı Esnaf, Sanatkârlar ve Kooperatifçilik Genel Müdürlüğü.

https://esnafkoop.ticaret.gov.tr/data/5d44168e13b876433065544f/2019%20Ay%C3%A7i%C3%A7e%C4%9Fi%20Raporu.pdf (Erişim Tarihi: 15.03.2022).

BSD. (2019). Biodiesel industry report. Biodiesel Industry Association. İzmir, Turkey. http://www.biyodizel.org.tr/asset/pdf/biyodizel.pdf (Erişim Tarihi: 15.03.2022).

Crop report. (2020a). Şeker pancarı ürün raporu. T.C. Tarım ve Orman Bakanlığı. Tarımsal Ekonomi ve Politika Geliştirme Enstitüsü (TEPGE).

https://arastirma.tarimorman.gov.tr/tepge/Belgeler/PDF%20%C3%9Cr%C3%BCn%20Raporlar%C4%B1/2020%20%C3%9Cr%C3%BCn%20Raporlar%C4%B1/%C5%9Eeker%20Pancar%C4%B1%20%C3%9Cr%C3%BCn%20Raporu%202020-328%20TEPGE.pdf (Erişim Tarihi:15.03.2022).

Crop report. (2020b). Patates ürün raporu. T.C. Tarım ve Orman Bakanlığı. Tarımsal Ekonomi ve Politika Geliştirme Enstitüsü (TEPGE).

https://arastirma.tarimorman.gov.tr/tepge/Belgeler/PDF%20Tar%C4%B1m%20%C3%9Cr%C3%BCnleri%20Piyasalar%C4%B1/2020-Temmuz%20Tar%C4%B1m%20%C3%9Cr%C3%BCnleri%20Raporu/Patates,%20Temmuz-2020,%20Tar%C4%B1m%20%C3%9Cr%C3%BCnleri%20Piyasa%20Raporu.pdf

GAIN. (2019). EU Biofuels Annual. GAIN Report Number:NL9022. https://apps.fas.usda.gov/newgainapi/api/report/downloadreportbyfilename?filename=Biofuels%20Annual_The%20Hague_EU-28_7-15-2019.pdf (Erişim Tarihi: 15.03.2022).

Horuz, A., Korkmaz, A., Akınoğlu G. (2015). Biofuel plants and technology. Journal of Soil Science and Plant Nutrition. 3(2): 69-81.

IEA. (2021). Energy policy review, Turkey 2021. International Energy Agency. https://iea.blob.core.windows.net/assets/cc499a7b-b72a-466c-88de-d792a9daff44/Turkey_2021_Energy_Policy_Review.pdf (Erişim Tarihi: 17.03.2022).

İçöz, E., Tuğrul, K. M., Saral, A., İçöz, E. (2009). Research on ethanol production and use from sugar beet in Turkey. Biomass and Bioenergy 33 (2009):1-7. DOI:10.1016/j.biombioe.2008.05.005

Kadakoğlu, B., KARLI, B. (2019). Oilseeds Production and Foreign Trade in Turkey. The Journal of Academic Social Science 96(7): 324-341.

Kampman, B., Verbeek, R., van Grinsven, A., van Mensch, Pim., Croezen, H., Patuleia A. (2013). Options to increase EU biofuels volumes beyond the current blending limits. Delft, CE Delft. The European Commission, DG Energy. https://ec.europa.eu/ energy/sites/ener/files /documents/2013_11_bringing_biofuels_on_the_market.pdf (Erişim Tarihi: 15.03.2022).

Küçük, N., Aydoğdu, M.H. ve Şahin, Z. (2022). Yağlı Tohum Piyasalarındaki Gelişmeler ve Türkiye Kolza Piyasası Trend Analizi. Fırat Üniversitesi Sosyal Bilimler Dergisi, 32, 1(215-227).

Melikoğlu, M., Albostan, A. (2011). Bioethanol production and potential of Turkey. J. Fac. Eng. Arch. Gazi Univ. 26(1): 151-160.

Öztürk, M. (2018). Bitkisel ve hayvansal atık yağlardan biyodizel üretimi. Çevre ve Şehircilik Bakanlığı. Ankara, Turkey. http://www.cevresehirkutuphanesi.com/assets/files/slider_pdf/ QnZyyphkC9xp.pdf (Erişim Tarihi: 15.03.2022)

Songstad, D.D., Lakshmanan, P., Chen, J., Gibbons, W,. Hughes, S., Nelson, R. (2009). Historical perspective of biofuels: learning from the past to rediscover the future. In Vitro Cellular & Developmental Biology. Plant, Biofuels, 45(3):189-192. DOI 10.1007/s 11627-009-9218-6 (Erişim Tarihi: 15.03.2022)

Tarım-Orman. (2019). Ürün masaları ayçiçeği bülteni. T.C. Tarım ve Orman Bakanlığı Bitkisel Üretim Genel Müdürlüğü Tarım Havzaları Daire Başkanlığı yayınları, Ankara, Turkey.

https://www.tarimorman.gov.tr/BUGEM/Belgeler/M%C4%B0LL%C4%B0%20TARIM /AY%C3%87%C4%B0%C3%87E%C4%9E%C4%B0%20KASIM%20B%C3%9CLTEN%C4 %B0.pdf (Erişim Tarihi: 15.03.2022).

Tarım-Orman. (2020a). Ürün masaları mısır bülteni. T.C. Tarım ve Orman Bakanlığı Bitkisel Üretim Genel Müdürlüğü Tarım Havzaları Daire Başkanlığı yayınları, Ankara, Turkey. https://www.tarimorman.gov.tr/BUGEM/Belgeler/M%C4%B0LL%C4%B0%20TARIM/%C3 %9Cr%C3%BCn%20Masalar%C4%B1%20Eyl%C3%BCl%20Ay%C4%B1%20B%C3%BCltenle ri/M%C4%B1s%C4%B1r%20Eyl%C3%BCl%20B%C3%BClteni.pdf (Erişim Tarihi: 15.03.2022).

Tarım-Orman. (2020b). Ürün masaları buğday bülteni. T.C. Tarım ve Orman Bakanlığı Bitkisel Üretim Genel Müdürlüğü Tarım Havzaları Daire Başkanlığı yayınları, Ankara, Turkey. https://www.tarimorman.gov.tr/BUGEM/Belgeler/B%C3%BCltenler/HAZIRAN%202021/B u%C4%9Fday%20Haziran%20B%C3%BClteni.pdf. (Erişim Tarihi: 15.03.2022).

Tarım-Orman. (2020c). Ürün masaları ayçiçeği bülteni. T.C. Tarım ve Orman Bakanlığı Bitkisel Üretim Genel Müdürlüğü Tarım Havzaları Daire Başkanlığı yayınları, Ankara, Turkey. https://www.tarimorman.gov.tr/BUGEM/Belgeler/B%C3%BCltenler/HAZIRAN%202021/A y%C3%A7i%C3%A7e%C4%9Fi%20Haziran%20B%C3%BClteni.pdf

TPAO. (2020). Petrol ve doğal gaz sektör raporu. Turkey Petrolleri A.O., Ankara, Turkey. https://www.tpao.gov.tr/file/2106/2020-petrol-ve-dogal-gaz-sektor-raporu-47460b743c70c609.pdf (Erişim Tarihi: 15.03.2022).

TUIK. (2020). Turkish Statistical Institute, Ankara, Turkey. https://www.tuik.gov.tr/ (Erişim Tarihi: 15.03.2022).

TUIK. (2021). https://data.tuik.gov.tr/Bulten/Index?p=Bitkisel-Uretim-Istatistikleri-2021-37249 (Erişim Tarihi: 15.03.2022).

USDA. (2020a). https://apps.fas.usda.gov/psdonline. (Erişim Tarihi: 15.03.2022).

USDA. (2020b).Ethanol 2020 Export Highlights. https://www.fas.usda.gov/ethanol-2020-export-highlights (Erişim Tarihi: 15.03.2022).

Identification of at Distance Materials Using Laser Signals and Deep Learning

Nevzat OLGUN[1]
İbrahim TÜRKOĞLU[2]

1.Introduction

Objects that we frequently use in our environment consist of various materials such as glass, metal, wood, plastic and stone. When we know what materials the objects around us are made of, we can interact more accurately with our environment. Similarly, it is important to define the materials correctly for computer aided systems. For example, an autonomous robot should use power according to the type of material from which the cup is made to grasp a cup made of glass, plastic, metal, or cardboard. Similarly, an autonomous robot or a vehicle should be aware that it is moving on concrete, metal, glass-like materials when performing its task, and it should reposition itself according to the roughness or slipperiness of the road. In a similar way, it is also important to identify materials contactless and remotely in very dangerous places or on space missions beyond the reach of humans. New generation cleaning robots should detect parquet, marble or carpet-like surfaces and perform cleaning scenarios suitable for the surface.

Although material classification is popular in the fields of computer vision and machine vision, it is still a challenging task. Traditionally, the material identification process is carried out using the color, texture and shape information in the camera images(Bian et al., 2018). The main disadvantage of these methods is that there are different materials with the same appearance. For example, a chair with the same appearance may be made of metal, plastic or wood. Another disadvantage is that the cameras do not work well in high or low light conditions, and they can display the same material differently depending on the environmental conditions in which they are located. In the dark, they do not work at all. This situation causes difficulties in identifying material from the image.

In addition to cameras, various sensors such as temperature, vibration, tactile, force and spectroscopy are used in material identification. Most of these methods require close contact and special environments.

Cameras used in material classification studies are sensitive to ambient light and fail when color, texture and geometry information cannot be obtained from the images. Other sensors require close contact or may have cumbersome structures. In material identification applications where RGB image is used, the system can be easily misled by giving the printed image of the material to the system instead of a real material. This can lead to security vulnerabilities in real-world applications and application downtime.

---

[1] Lecturer, Zonguldak Bulent Ecevit University, Department of Software Technologies, Orcid: 0000-0003-2461-4923
[2] Prof. Dr., Firat University, Department of Software Engineering, Orcid: 0000-0003-2461-4923

In this study, instead of using a camera due to the difficulties mentioned above, the way light temporarily interacts with the material is utilized. For example, when a light interacts with a material through reflection and subsurface scattering, it will have a descriptive reflection value of that material. From this point of view, in the study, laser light is reflected on the material and the laser signals reflected from the material are recorded with a simple electro-optical sensor circuit. Laser signals are trained with a deep learning network structure created with Neural Circuit Policies (NCP) and material identification is performed.

The main contributions of the study can be summarized as follows:

1. 10 different materials were successfully classified with an average rate of 92.66% using a single laser measurement signal.

2. The classification process is made with a deep learning architecture designed with NCP and consisting of only 29 neurons and 113 connections. With this architecture, the processing cost and the computation time are reduced.

3. Ambient light plays an important role in material identification studies with a camera, which is a passive measurement technique. Excessively illuminated environments and dark environments reduce the performance of the work done with the camera. Laser lights, which are active measurement techniques, have less potential to be affected by ambient light.

4. Instead of raw laser signals, the use of laser signals reduced in size by the Welch method gives faster and more accurate results.

In the second chapter of the study, a brief literature review on material identification studies, the structure of the NCP model, the theoretical foundations of reflection and the Welch PSD method are given. In chapter 3, the experimental setup and studies for the laser light source/sensor system, the data acquisition processes used to test the classifier are explained. In the following, the data preparation steps and the architecture of the deep learning model used in this study are explained. In chapter 4, the results obtained from the experimental studies are explained and the study is evaluated. In Chapter 5, the limitations of the current study and information about future studies are given. In Chapter 6, the conclusions are given.

2. Related Works

A Review of the Literature

Identification of the materials that make up the objects with computer or machine vision is one of the important fields of study. The objects we use in our daily lives consist of different materials such as fabric, metal, glass, wood. Each material that makes up the objects gives different properties to the object. For example, a glass cup is hard and fragile, a plastic cup is flexible, and a metal cup is hard and strong. People use objects according to these specified characteristics of materials. This is also the case in robotics and in industry.

There are early studies on material identification with different perspectives. Some of these methods require close contact, while others are contactless and from a distance. One of the methods used in material identification is to extract the properties of the material surface using tactile sensors and classify the material. Inspired by the human touch, these sensors are usually placed on the tips of a robotic hand. By moving these sensors along the material surface, the friction

coefficient of the material surface, the texture and the roughness coefficients are obtained and the material identification process is performed (Bhattacharjee et al., 2018; Gao et al., 2021; Lam et al., 2014; Sonoda et al., 2009; Xie et al., 2019). In the material identification study, which was carried out with reference to the vibration and force sensing properties of the human hand, different fabric types were determined (Chathuranga et al., 2013). Ryu et al. categorized 10 types of materials using the deep learning method, using the sound of the material by striking a blow on the material (Ryu & Kim, 2020). There are also studies using force (Baghaei Naeini et al., 2020; Baglio et al., 2015; Fernando & Marshall, 2020) and temperature modality (Kerr et al., 2018) from tactile sensors that require close contact. Such tactile sensors require close contact and they can also have a cumbersome feature due to their structure (Baglio et al., 2015). In studies conducted using the thermal conductivity of materials, the materials that want to be detected are first heated by an external heat source, and then the propagation of heat on the material is detected and the material is identified (Aujeszky et al., 2019; Bai et al., 2018; Bhattacharjee et al., n.d.; Emenike et al., 2021). These methods, which use the thermal conductivity of materials, are not safe because they require an external heat source, and their implementation seems impractical (Bai et al., 2018).

Radar signals are also used for non-contact and long-distance material identification. For these purposes, radar signals are sent towards the material and the reflected signals are processed to identify the material (Ni et al., 2020; Yeo et al., 2016).

One of the popular and powerful tools used for material identification is RGB cameras. Extensive studies have been conducted on identifying material from images (Bell et al., 2015; Dimitrov & Golparvar-Fard, 2014; Han & Golparvar-Fard, 2015; Hoskere et al., 2020; Kumar et al., 2021; Li et al., 2021; Liu et al., 2010; Rashidi et al., 2015; Son et al., 2014; Varma & Zisserman, 2009). In these studies, material identification is performed using properties such as texture, color, reflection properties from images in general. The main problem in these studies is that there may be different materials with the same texture and color (Liu et al., 2010). Another problem is that the material surface colors can change according to the appearance, direction and intensity of the lighting (Son et al., 2014). In addition, there are also deep learning-based material identification studies that do not require any feature extraction (Bian et al., 2018; Bunrit et al., 2020; Ilehag et al., 2020; Xu et al., 2018). The use of cameras in private living areas can cause privacy problems.

There has been an increase in the use of terrestrial laser scanners (TLS) in material identification studies in recent years. By using TLS, the distance of the target material, the intensity value of the laser signal reflected from the material and the color values can be recorded with the built-in RGB camera.

Hess et al. classified building materials to form knowledge models of cultural heritage structures. In addition to the color and laser intensity values from the laser scanning data, they also determined the mortars on the walls using surface geometry (Hess et al., 2017). Yuan et al. studied the classification of 10 different materials that are frequently used in construction materials (Yuan et al., 2020a). As far as we know, only a part of the study conducted by Yuan et al. has similar features to our study. In their work, they used laser intensity values, HSV color values and surface roughness values reflected from materials, as well as RGB images. In the material identification study, where they only used laser intensity values, they achieved the highest classification accuracy of 40.4% between 2-4 m. In the material identification study between 4-10 m, they obtained the highest accurate classification rate of 77.5% by using the material reflectance value corrected for distance. Zahiri et al. used TLS and multispectral camera data to classify concrete, brick and mortar. Its highest performance rate was 83.07% (Zahiri et al., 2021). Zivec et al. studied the distinguishability of sandstone, marlstone and claystone in the quarry using TLS intensity data (Živec et al., 2018).

When the literature is examined, Time of Flight (TOF) cameras are used in material identification studies. In such cameras, laser light is reflected to the target in continuous or pulsed mode, and RGB image, intensity and depth values of the target are obtained. In the study by Martino et al., an accuracy of about 80% was achieved by using 3D depth values and intensity information of 4 different materials at a distance of 1 m (Martino et al., 2016). For a robotic plastering process, Frangez et al. classified plaster surfaces with 4 different roughnesses in their experimental study with TOF camera. In their study, they achieved a classification accuracy of 97% (Frangez et al., 2021). They used color information obtained from color images and 3D laser range features in their studies. Galdames et al. performed lithological classification using a 3D laser rangefinder. In their studies, they used color information obtained from color images and 3D laser range features. They obtained an accurate classification rate of 99.24% with support vector machines (Galdames et al., 2017).

In our previous study, 10 different types of materials were classified using a single laser measurement signal with the LSTM deep learning model (Olgun & Türkoğlu, 2022).

Although image-based material classification techniques are frequently used in the literature, factors such as variable lighting conditions in real world conditions and not working at all in the dark are the difficulties of this technique. Other sensors, on the other hand, require contact and usually have cumbersome structures. Material identification studies based on active measurement techniques with TLS, TOF camera and similar lasers are independent of lighting conditions. Studies based on the active measurement technique with laser are generally supported by camera images. In the methods using only laser signals, a few materials have been classified. In this study, 10 types of materials were classified with only one laser signal, using the NCP deep learning model, which contains few neurons and connections, unlike previous studies.

Neural Circuit Policies

Artificial neural networks (ANNs), which form the basis of deep learning algorithms, are a machine learning algorithm based on brain cells. An artificial neural cell has input values, weight values that allow to adjust the effect of input values on output, a transfer function that calculates the output of values entering a cell, an activation function that decides at what rate the output of the cell will be transferred to the next cell. Single layer ANN models cannot be used to solve nonlinear problems. As a result of the increase in the computational capacity of graphics processors in parallel with the development of technology, ANN models with multiple layers and different architectures have been developed. Deep learning architectures are basically artificial neural networks consisting of more than one nonlinear layer. Deep learning architectures can be grouped into three main groups according to the characteristics of the input data and the type of problem to be solved. These are deep neural networks (DNN), convolutional neural networks (CNN), and recurrent neural networks (RNN). According to the design architecture used in deep learning, usually all artificial neurons are interconnected. According to the designed deep learning architecture, millions of trainable parameters can emerge, and in this case, the processing cost for training the network increases.

NCP is a new neural network architecture inspired by the nervous system of the C.Elagans (Corsi et al., 2015) nematode and created by connecting a very small number of neurons compared to classical deep learning architectures (Lechner et al., 2020). Unlike classical deep learning architectures, not all neurons are interconnected in NCP, which means that the computational cost of the network is greatly reduced, but it can provide as much performance as a fully connected deep learning architecture of a similar structure. NCP architecture, which consists of a sparse neural

network, has a 4-layer structure consisting of sensory neurons, inter-neurons, command neurons and motor neurons, as can be seen in Figure 1. Sensory neurons are used as the input layer. According to the problem to be solved, the features extracted from the data should be presented to the sensory neurons as input data. In deep learning architectures, feature extraction is usually done using CNN. The input data in the sensory neurons is transmitted to the inter-neurons located in the hidden layer using a feed-forward connection with a sparse connection structure. Inter-neurons are sparsely connected by feedforward connections to motor neurons in the next layer, which consists of recurrent neural cells according to the configuration of the network. RNN cells in motor neurons have a memory and these cells can also work successfully with noisy data (Lechner et al., 2020). Motor neurons can also make connections between themselves. The command neurons are connected to the motor neurons in the last layer with a feed-forward connection, and the motor neurons produce an output value.
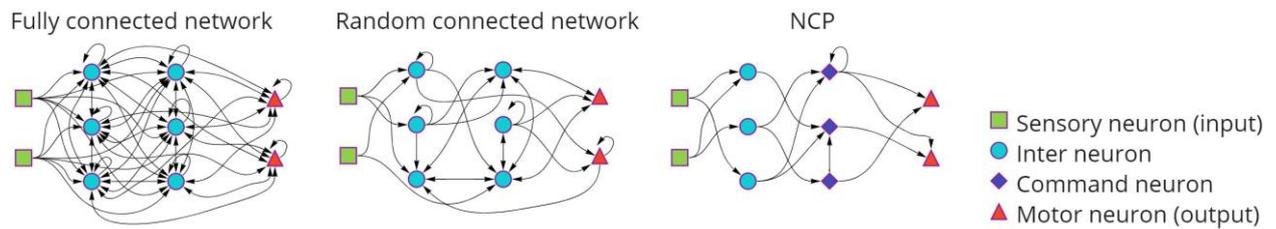

Figure 1. Full connected network, rabdom connected network and NCP

The 4-layer NCP architecture, which is in a sparse structure, can consist of 90% fewer neurons than other deep learning architectures (Yan et al., 2017). NCPs have a non-linear network structure with high performance on time series data. The basic neural building blocks of NCPs are called liquid time constant (LTC) networks (Hasani et al., 2020). The small size of the network architecture created with NCP allows the examination and interpretation of the relationships developed by each cell. At the stage of creating the network architecture with NCP, the number of inter-neuron and command neuron in the network, the number of random connections between the layers and the number of RNN cells in the motor neurons can be selected.

Theoretical Basics of Laser Measurements

In a laser detection system, a laser light is reflected to the target continuously or pulsed, and the laser signals reflected from the target are recorded. In this study, laser light is reflected to the target in a continuous mode. Laser signals are a numerical representation of the signal power backscattered from the target. The signal power reflected from the target depends on the type of material, the environmental conditions, the design electronics of the device, the wavelength of the laser light, and the distance between the target and the laser system.

When laser light is directed at a material, it is reflected diffusely or specularly, depending on the surface roughness of the material. When the size of the surface particles in the material is larger than the wavelength of the laser light which directed on the surface of the material, diffuse reflection occurs. When the surface particles are smaller than the wavelength of the laser, specular reflection occurs. In cases of specular reflection, the angle of the light reflected from the material is equal to the angle of the incident laser light. Where there is diffuse reflection, the laser lights will scatter in all directions. In diffuse reflection, the power of the laser beams scattered from the target reaching the receiver depends on the angle between the receiver and the normal of target (Carrea et al., 2016). When there is diffuse reflection, it can be in sub-surface scattering. In Figure 2, specular and diffuse reflection on the surface of the material can be seen.
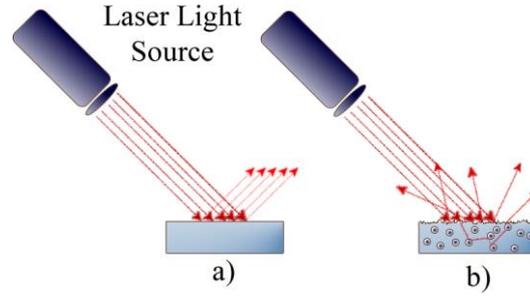
Figure 2. Laser beams and reflection types a) Specular reflection from a smooth surface b) Diffuse reflection and subsurface scattering from a rough surface

In real-world conditions, most materials reflect as a combination of specular and diffuse reflection due to micro-roughnesses on their surface. Due to the different surface and micro characteristics of the materials, laser beams will cause different reflection intensities in different materials (Olgun & Türkoğlu, 2022).

The relationship between the signal power transmitted to the target and the received signal power from the target is explained in Equation 1 (Jelalian, 1992; Suchocki et al., 2020; Suchocki & Katzer, 2018a). This equation is valid when the laser signal is projected onto a rough surface and the laser beam radius is smaller than the target (Suchocki & Katzer, 2018b).

$$P_R = \frac{\pi P_T \rho}{4R^2} \eta_{Atm} \eta_{Sys} cos\,(\alpha)\;(1)$$

According to Equation 1, the parameters affecting the power of the laser beams reflected from the target can be considered in 3 groups. In the first group, the parameters η_{Atm} and η_{Sys}, which can be fixed in the short measurement range. Small changes in these parameters can be ignored during the measurement. The α and R parameters in the second group are the values that can be controlled by standardization techniques provided at the time of measurement or correction techniques after measurement. In the third group, ρ is the reflection coefficient that changes according to the type, colour, roughness and wavelength of the target material (Carrea et al., 2016; Yuan et al., 2020a).

When the distance between the target and the laser sensor system is short, the η_{Atm} value in the environment where the laser signal reflected from the target and the target is recorded can be accepted as a fixed value. If the same device is used during the laser signal recording process, the value of η_{Sys} and P_T can also be accepted as a fixed value. In this case, if these values are expressed with a constant K coefficient as in Equation 2, the laser power obtained from the target can be expressed as in Equation 3.

$$K = \frac{\pi P_T}{4} \eta_{Atm} \eta_{Sys} (2)$$

$$P_R = \rho K \frac{cos\,(\alpha)}{R^2} (3)$$

According to Equation 3, the power of the laser reflected from the target depends on the reflection coefficient of the target, the angle of the laser beam reflected on the target and the distance between the target and the laser receiver / transmitter device.

According to the study of Yuan et al.; since corrections can be made for different laser beam and receiver devices, it has been reported that the measured laser power expressed in Eq. 8 may

not be completely linear with distance and angle (Yuan et al., 2020b). Accordingly, the laser power obtained from the target can be defined as in Equation 4. In Equation 4, b is a fixed term that can vary according to the device.

$$P_R = \rho K \frac{\cos{(\alpha)}}{R^2} + b \quad (4)$$

Welch Method

The Periodogram method calculates the spectral power density estimate of a signal using the Discrete Fourier Transform (Zhao & He, 2013). In this method, the power of each frequency that makes up a signal is calculated, and the signal in the time domain is converted into the frequency domain. In the Bartlett method, periodograms are calculated by dividing the signal into windows that do not overlap each other, and power spectrums are found by averaging them.

The Welch method is an improved version of the Bartlett method. In the Welch method, the signal is divided into windows so that they overlap each other at a certain rate. The spectral power density is calculated by averaging the periodograms of each window. The process of segmentation of the signal can be calculated as given in equation 5 (Gupta & Mehra, 2013; Kumar Rahi et al., 2014; Rao & Swamy, 2018).

$$x_i(t) = \begin{cases} x(iD + t), & t = 0,1,2, \dots . M - 1 \\ & i = 0,1,2, \dots . L - 1 \end{cases} \quad (5)$$

In the equation, the ith part of the signal, which is formed as a result of segmentation, is denoted by x_i. The length of the segmented signal is denoted by M. The starting point of the ith part is indicated by iD. The total number of sections is indicated by L. If the value of D is chosen equal to the value of M, the segmented signals do not overlap each other. In order for the successive signals to overlap each other by 50%, the value of D should be chosen as much as the value of $M/2$. The spectral power density of each segmented signal is calculated as in Equation 6.

$$\breve{P}_i(f) = \frac{1}{MK} \left| \sum_{t=0}^{M-1} x_i(t)w(t)e^{-j2\pi ft} \right|^2 \quad (6)$$

In the equation, $w(t)$ represents the windowing function, f represents the normalized frequency variable and K represents the normalized constant. K is expressed as shown in Equation 7. The Welch PSD obtained by averaging the power densities of the windowed signals can be calculated as in Equation 8.

$$K = \frac{1}{M} \sum_{t=0}^{M-1} w^2(t) \quad (7)$$

$$P_w = \frac{1}{L} \sum_{i=0}^{L-1} \breve{P}_i(f) \quad (8)$$

In the Welch method, since the peridiograms of the overlapping small-sized windows are averaged, the variance of the original-length signal relative to the peridogram decreases. Using the Welch method for noisy signals gives better results than the classical peridiogram. The length of the new signal to be generated with Welch PSD can be calculated as expressed in Equation 9. In the equation, the $nfft$ value indicates the number of discrete Fourrier transform points to be used in the spectral power density.

$$N = \frac{nfft}{2} + 1 \quad (9)$$

3. 3.Materials and Methods

The method proposed in this study is based on the use of only one laser signal for each material identification process. A large amount of data is needed to train deep learning networks effectively. A large number of laser signal samples can be taken from different points of the target material with the help of the cartesian robot arm in the experimental setup designed for this purpose. In this way, sufficient number of laser signal samples for each material type can be obtained and the deep learning model can be trained effectively.

The proposed method consists of two steps. In the first step, an unmodulated continuous mode laser light is briefly projected onto a material at a distance, and the raw laser signals reflected from the material are recorded. In the second step, the laser signal is trained in the deep learning model created with NCP for material identification after the data preparation steps. The processes of the proposed method are given in Figure 3.
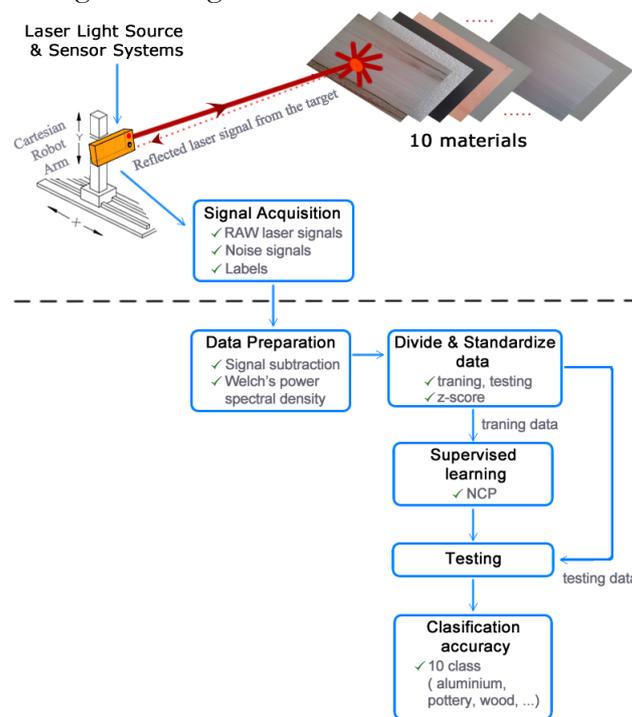
Figure 3. Block diagram of the study

Laser Beam Source and Detecting System Design

The laser light source and signal recording system used in material identification were obtained by revising the equipment of a laser meter (Olgun & Türkoğlu, 2018, 2022). The laser meter module has been reprogrammed so that the laser light can be turned on/off when desired, and the reflected laser signals can be recorded as raw data. A USB serial converter module has been added to the laser meter module in order to transfer the obtained signals to the computer system. The device has a red laser light with a wavelength of 650 nm. The device is capable of delivering 1mW of output power and is located at the Class II safety level. The reprogrammed laser module can transfer 3000 raw data to the computer system with a sampling frequency of 50 kHz in one measurement. The voltage gain of the avalanche photodiode in the device can be adjusted with the software and the gain was kept constant during this study. Figure 4 shows the laser beam source

and sensor system which is used in the study. The STM32 microcontroller on the laser module has a 12-bit resolution analog-to-digital converter and the measurement value ranges from 0 to 4095.
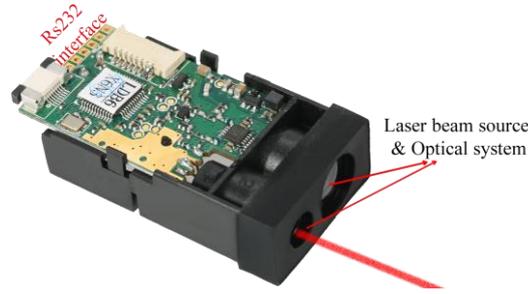
Figure 4. Laser beam source and sensor system

Material Types

As shown in Table 1, 10 types of materials consisting of 6 main material groups were used in experimental studies.

Table 1. Materials used in the study

Group	Material name
Plastic	Polyethylene
Metal	Aluminum, magnet
Fabric	Black fabric
Wood	Linden
Glass	Frosted glass, glass
Building material	Granite, artificial marble, pottery

In order to ensure balance between the material classes and to obtain an equal amount of sample data in the training of the deep learning model, the material dimensions were kept equal. For this purpose, each material was cut into a rectangular shape with a width of 10 cm and a length of 15 cm. The materials used in the study and the laser light on the material at the signal receiving stage can be seen in Figure 5.

Figure 5. Materials used in experimental studies and sample laser beam on the material(Olgun & Türkoğlu, 2022)

Data Collection Procedure

A data set was created in the laboratory environment for material identification with laser marks. The laboratory where the studies are carried out does not receive direct sunlight. Daytime hours when the weather is clear were preferred for data collection from the materials. In order for deep learning architectures to produce successful results, a large amount of data is needed in the education process. In the experimental setup set up for this purpose, the laser module was placed on a Cartesian robot arm. In order to ensure standardization during the data acquisition process, the distance between the material and the laser module was chosen as 2 m. Data acquisition processes were carried out with the help of a Cartesian robot, starting from the bottom right of the material, from right to left, and then from left to right, at approximately 5 mm intervals. Figure 6 shows the experimental setup and the pattern layout of the cartesian robot.
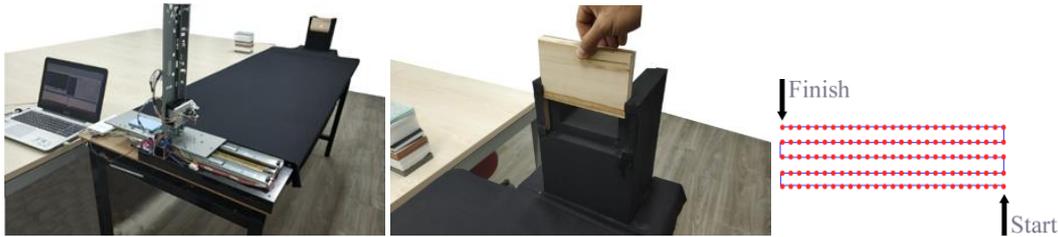

Figure 6. Experimental setup and the motion pattern of the Cartesian robot used for measuring

Laser signals can be noisy due to the dark current effect of the laser module and the effect of ambient lights. For this purpose, the laser light source was turned off at each position of the cartesian robot during the measurements, and the noisy signals generated by the device/ambient lights were also recorded. After this process, laser light was turned on at the same position of the cartesian robot and the laser signals reflected from the material were recorded. Small vibrations may occur during the movement of the Cartesian robot. In order to avoid the effects of vibrations, measurements were started 3 seconds after the movement of the robot arm. During the measurements, a matte black material was placed behind the objects as a fixed background, and a stable background was provided for the transparent glass and semi-transparent frosted glass due to the light transmittance. During the measurement, a reference point measurement was made from the background to measure the possible reflections of the matte black background, and then the measurement was started from the material. During data preparation processes, these reference signals were subtracted from the raw laser signals of the materials.

Data saving operations were performed with a desktop program prepared in the c# programming language for the laser module. In the study, 391 device/ambient light noise signals and 391 laser signals were measured for each material and the signals were recorded in CSV file format. The data in the CSV files were combined into a single file in the MATLAB programming environment. Data preparation and classification processes were done using the Python programming language. All experimental studies were performed on a computer with an Intel Core i7-5500U 2.40 GHz CPU, 8 GB memory and 2 GB NVIDIA GeForce 840M graphics card.

Data Preparation Steps

After measurements taken at different days and hours for the material identification process, the average energy of each signal was calculated as given in Equation 10 so that the characteristic

features of noisy raw laser signals can be examined. In the equation, $s_i(n)$ represents i^{th} of the raw laser signal and N represents the signal length (Chaparro & Akan, 2019).

$$e_i = \frac{1}{N}\sum_{n=1}^{n=N}|s_i(n)|^2 \text{ (10)}$$

In Figure 7, a boxplot showing the minimum, maximum, first quarter, third quarter and outlier values of noisy raw laser signals for each material can be seen. The boxplot is an effective method for examining univariate data. The box plot shows the average energy distributions of the 391 raw laser signals measured from each material.
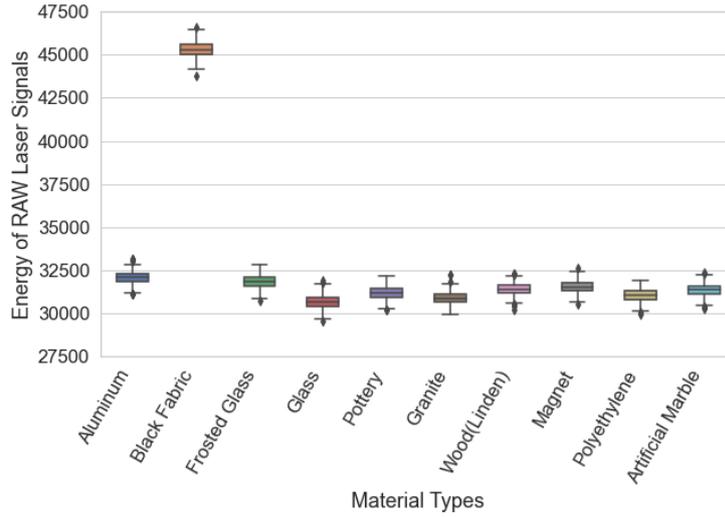

Figure 7. Box plot showing the average energy distributions of the noisy laser signals for each material

When the boxplot in Figure 7 is examined, it is seen that the average energy of the noisy laser signals recorded for each material at different days and times is generally in the same range. In order to detect the noise caused by the dark current effect of the laser module and ambient light and then to remove the noise from the signals, measurements were made by turning off the laser light at each measurement point made while the laser light was on. The noise in the signals can be reduced by subtracting the device/ambient lights noise signals from the raw laser signals. For this purpose, subtraction was performed as described in Equation 11. After the subtraction, the reference signals (background reflection signals) recorded during the measurements were subtracted from the laser signals obtained for glass and frosted glass. The purpose of this process is to minimize the effect of the background placed behind the glass and frosted glass on the laser signals obtained from these materials. The noise signal measured when the laser light is off is also subtracted from the reflection signal of the background (Olgun & Türkoğlu, 2022).

$$x(n) = s(n) - d(n) \text{ (11)}$$

In the equation 11, $x(n)$ represents the laser signal cleared of noise, $s(n)$ represents the noisy laser signal reflected from the material, and $d(n)$ represents the noise signal caused by the device/ambient lights. Figure 8 shows an example of noisy laser signals reflected from 10 different materials, device/ambient lights noise signals, and signals obtained as a result of subtraction process.
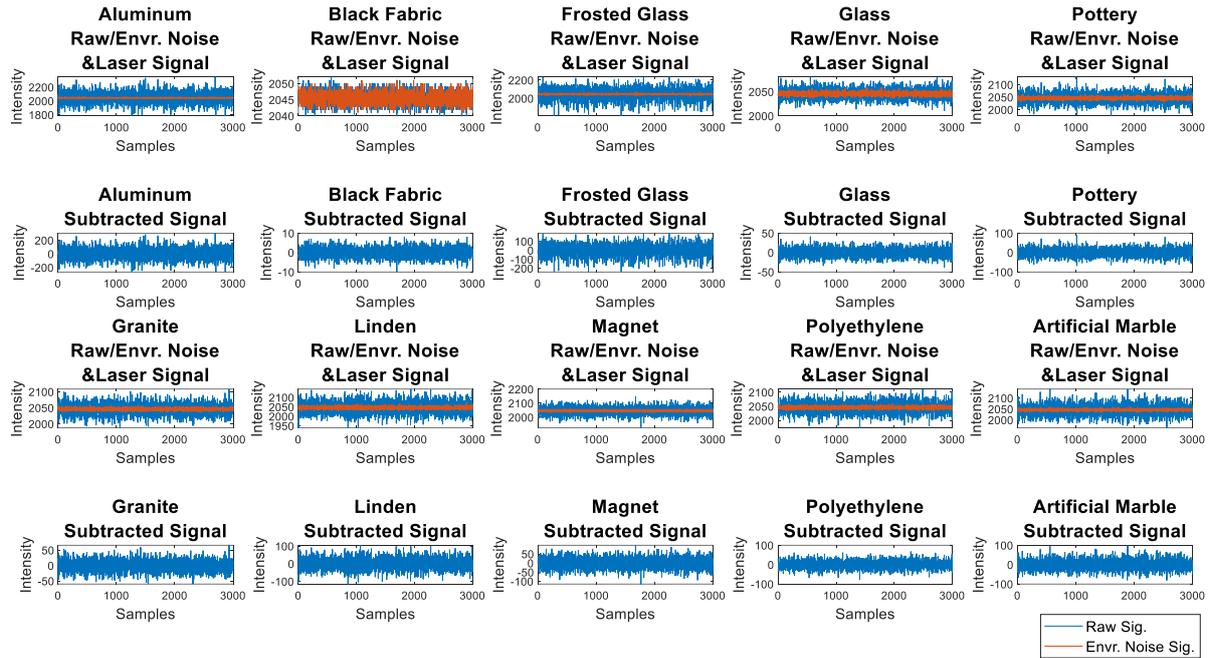
Figure 8. An example of noisy laser signals reflected from 10 different materials, device/ambient lights noise signals, and signals obtained as a result of subtraction process.

When the average energy distributions of the laser signals formed as a result of the subtraction process are examined according to the material classes, it can be seen that there are more distinct separations in the energy distributions compared to the classes. In Figure 9, the boxplot showing the distribution of the average energies and outliers of the laser signals generated as a result of the subtraction for each material class can be seen.
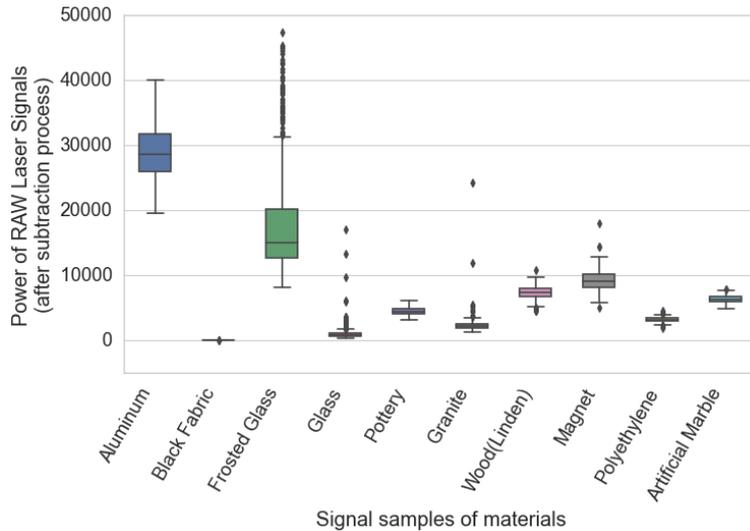
Figure 9. A box graph showing the average energy distributions and outliers of laser signals for each material after subtraction process

In the study, spectral power density of each signal was calculated according to the Welch method after the subtraction to reduce the effect of device/ambient lights noise. The length of the noise-free laser signal consisting of 3000 points was reduced to 32 points after Welch spectral power density conversion. After the extraction process, the signal samples formed when the power

spectral density is calculated according to the Welch method using the laser signals of each material sample is shown in Figure 10. As can be seen from the figure, the size of the laser signals decreases from 3000 to 32 in the normalized Welch power spectral density where the $nfft$ value is selected as 62.
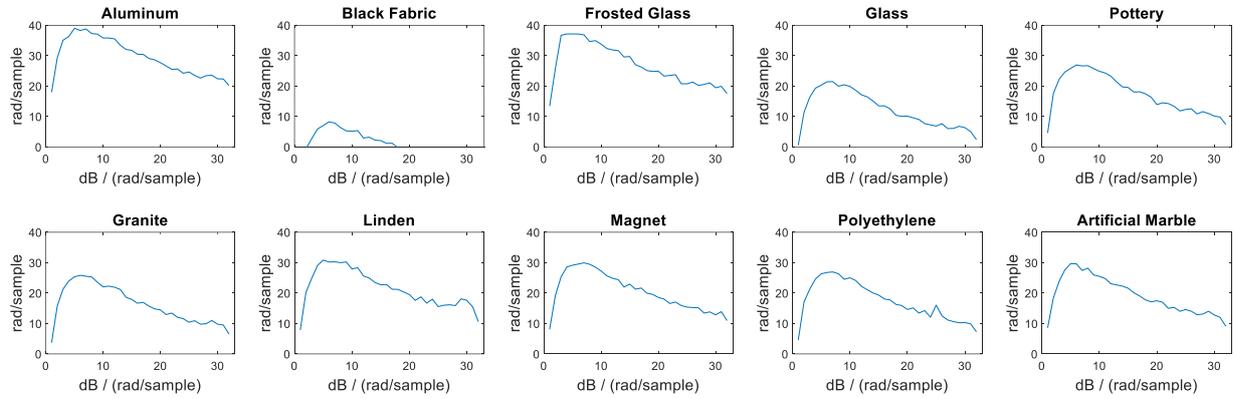
Figure 10. An example of power spectral density estimates calculated according to the Welch method after subtraction process for 10 different materials

Design of Deep Learning Architecture and Training the Network

In this study, a sparse deep learning architecture based on NCP was used for material classification with laser signals. After the data preparation steps, a 32-point laser signals were applied as an input to the NCP deep learning network. The parameters of the NCP deep learning architecture proposed for the classification process are shown in Figure 11. In this study, the number of inter-neurons, the number of command neurons, the number of command neurons in the RNN cell structure, the number of connections between each layer were selected by trial and error method.
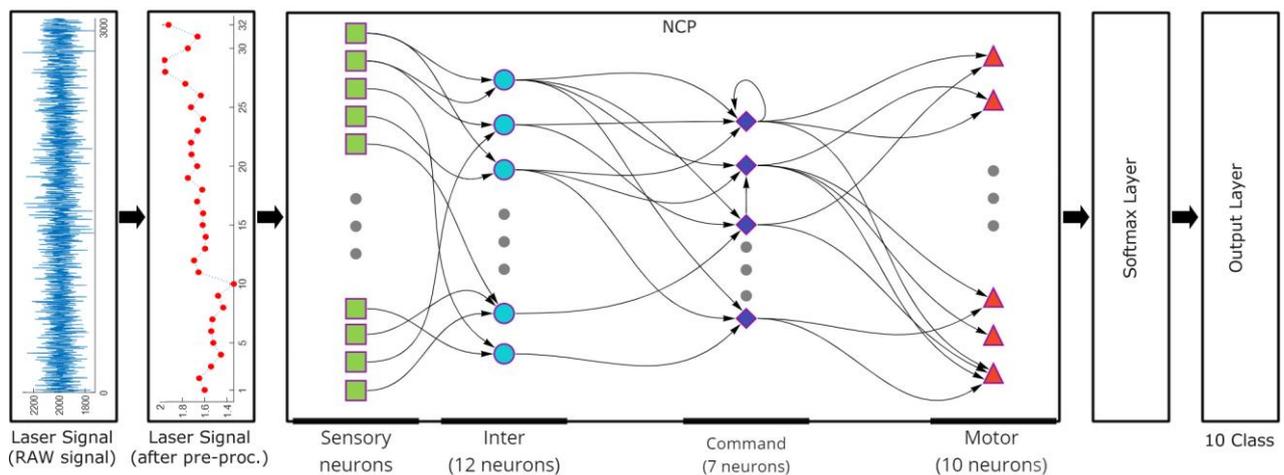
Figure. 11. The structure of the NCP model and the method of entering the laser signals into the network after data preparation processes.

The number of sensor neurons varies depending on the size of the input data. The Softmax layer, which is frequently used in classification problems, evaluates the inputs in the motor neuron layer and calculates the probability of which class the output may belong to. The total value of the

probabilities obtained in this layer is equal to 1 and the output value with the highest probability value determines the class.

Performance Evaluation

In this study, 10-fold cross validation method was used for classification performance evaluation of deep learning architecture designed with NCP. In this method, 90% of the data was used for training and 10% for testing. The data set consisting of 3910 samples is randomly divided into 10 equal parts, 9 of each part is used for training and one part is used for testing. With this technique, the average of the performance evaluations obtained by performing the training and testing process 10 times using different parts of the dataset. In this way, it is possible to prevent the validation results from producing biased results. Before starting the training process, z-scores were calculated for the training and test data.

In the literature, classification accuracy is generally used for performance evaluation in studies. It is a reasonable criterion to use classification accuracy when the data set is balanced. In this study, classification accuracy evaluation criterion was used to make comparisons with other studies. The classification accuracy is given in Equation 12.

$$Accuracy = \frac{TP+TN}{TP+TN+FP+FN} \quad (12)$$

In the accuracy performance measure calculation in Equation 12, *TP* is the number of true positives, *TN* is the number of true negatives, *FP* is the number of false positives, and *FN* is the number of false negatives. For example, if an aluminum material was correctly classified as aluminum, it would be *TP*. If a granite material is misclassified as artificial marble, this will be *FP* for the artificial marble class. When an aluminum material is not correctly classified as aluminum, it will be *FN* for that aluminum class. Similarly, if a material is not aluminum and is classified as a different material other than aluminum, it will be *TN*.

In this study, the confusion matrix was also used to examine the classification accuracy of each material in more detail. In the confusion matrix, TP, TN, FP, FN numbers can be examined for each material class. In addition, the classes in which the materials are classified correctly or incorrectly can also be examined.

4. 4.Experimental Results and Discussion

In experimental studies, different numbers of neurons in the intermediate layer and different numbers of connections between neurons were tested using the NCP architecture. In the Welch PSD method, laser signals of different sizes, which are formed as a result of changing the number of parameters, are used as input signals in the NCP network. In addition, the results of the previous study were compared with the new results (Olgun & Türkoğlu, 2022). In the NCP model with the highest performance in this study, the number of neurons and connection configuration information can be seen in Table 2. In Table 2, s_n represents the number of synapses connected from each sensor neuron to neurons in the interlayer, I_n represents the number of synapses connected from each interneuron to the command neuron layer, R_n is the number of command neurons that are RNNs, and M_n is how many synapses are connected to each motor neuron from the previous layer.

Table 2. NCP deep learning architecture parameters

Parameters	Values
Number of inter neurons	12
Number of command neurons	7
Number of motor neurons	10
Sn	8
In	6
Rn	1
Mn	4
Total neurons number	29
Total synapses number	113

As can be seen in Table 2, since the number of connections between the middle layers is limited, the computational cost of the network is greatly reduced compared to a fully connected network architecture with a similar structure. In order to calculate the classification probabilities in the material identification study consisting of 10 classes, the Softmax layer was added to the last layer of the NCP architecture. Because of its structure, the layer before the Softmax layer should consist of as many neurons as the number of classes, the number of motor neurons in the NCP network was selected as 10 layers. In the hyper-parameters used in the training conducted with the deep learning architecture designed with NCP, the maximum number of epochs was chosen as 1500, the learning coefficient was 0.001, the optimization algorithm was Adam, and the mini-batch size was 512.

In order to compare with previous studies, 2 new signal types with much lower size (32 and 63 points) and different characteristics, whose power spectral densities were calculated according to the Welch and Yule-Walker AR method (Olgun & Türkoğlu, 2022), were trained using different combinations. The results obtained are given in Table 3.

When Table 3 is examined, the use of 32-point Welch power density signals in the deep learning architecture designed with NCP produces more successful results than the use of signals with other possibilities. The use of a sparse network with the NCP model combined with the use of a low-size signal significantly reduces the computational cost. Such a signal conversion removes the noise effect of the 3000-dimensional noisy raw laser signals and significantly reduces the size of the signal (Olgun & Türkoğlu, 2022). It can be seen that the NCP architecture fails in training the signals whose PSD values are calculated according to the Yule-Walker AR method.

Table 3. Average classification results of laser signals with reduced dimensions.

Study	Signal type	Signal size (points)	Deep Learning model	Epoch size	Accuracy (%)
Olgun et al.(Olgun & Türkoğlu, 2022)	Welch PSD estimate	63	LSTM	1500	93.07 ± 1.11
	Yule-Walker PSD estimate	63	LSTM	1500	93.43 ± 1.47
	Welch PSD estimate + Yule-Walker PSD estimate	2 x 63	LSTM	1500	**93.63 ± 1.56**
The proposed model	Welch PSD estimate	63	NCP	400	91.23 ± 1.32
		32	NCP	400	**92.66 ± 1.50**
	Yule-Walker PSD estimate	63	NCP	400	22.23 ± 1.12
		32	NCP	400	21.41 ± 1.18
	Welch PSD estimate + Yule-Walker PSD estimate	2 x 63	NCP	400	90.66 ± 1.83
		2 x 32	NCP	400	91.51 ± 1.41

In experimental studies with laser signals reduced to 32 dimensions by the Pwelch method, the loss graph and the accuracy graph for one of the cross-validation steps with the highest classification accuracy in the NCP model can be seen in Figure 12.

(a)   (b)
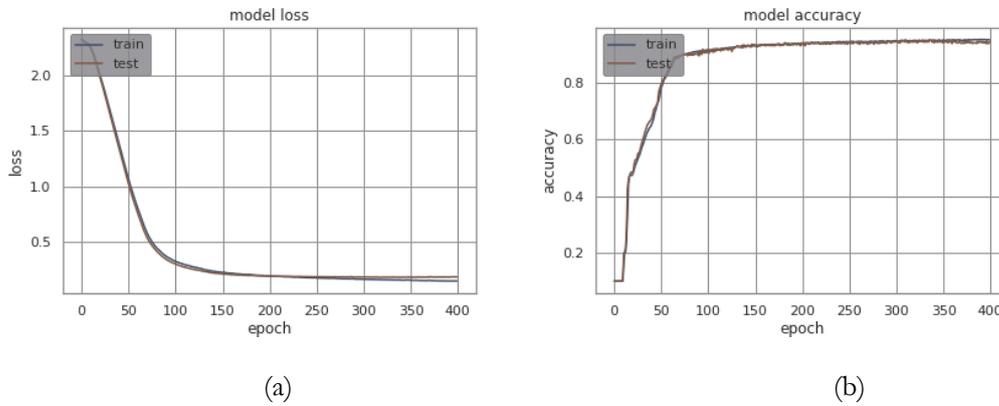
Fig. 12. Loss and Accuracy graphs of size-reduced laser signals with Pwelch PSD, in NCP model a) Loss graph for NCP model. b) Accuracy graph for NCP model.

In the study, a confusion matrix was used to better understand the classification accuracy of the proposed model using test data. The confusion matrix with the highest accuracy performance in the test data set is given in Figure 13.
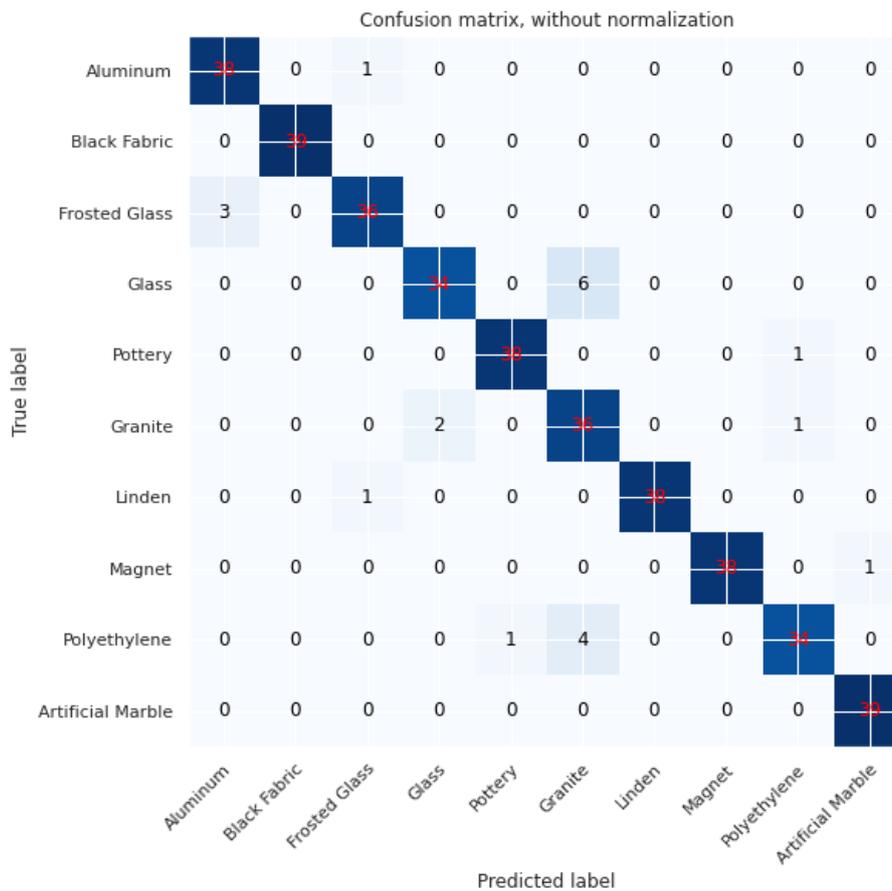
Fig. 13. Confusion matrix with best validation value for test data at 10-fold cross validation steps.

When the prediction results in cross-validation steps are examined, it is seen that the highest result is 94.63%. In the confusion matrix, each row shows the number TP and FN of the corresponding material. Similar to the previous study, when the confusion matrix containing 391 test data is examined, it is seen that black fabric, linden and artificial marble can be completely separated from the others. It can be seen that the data of 3 frosted glass materials are incorrectly classified as aluminum, 6 data of the glass material and 4 data of the polyethylene material are incorrectly classified as granite. In the prediction results, the lowest accuracy rate was 89.51%. The confusion matrix of the test dataset with the lowest accuracy can be seen in Figure 14. Examining the confusion matrix in the figure, it is seen that aluminum/frosted glass, granite/glass, granite/polyethylene materials are predicted interchangeably.
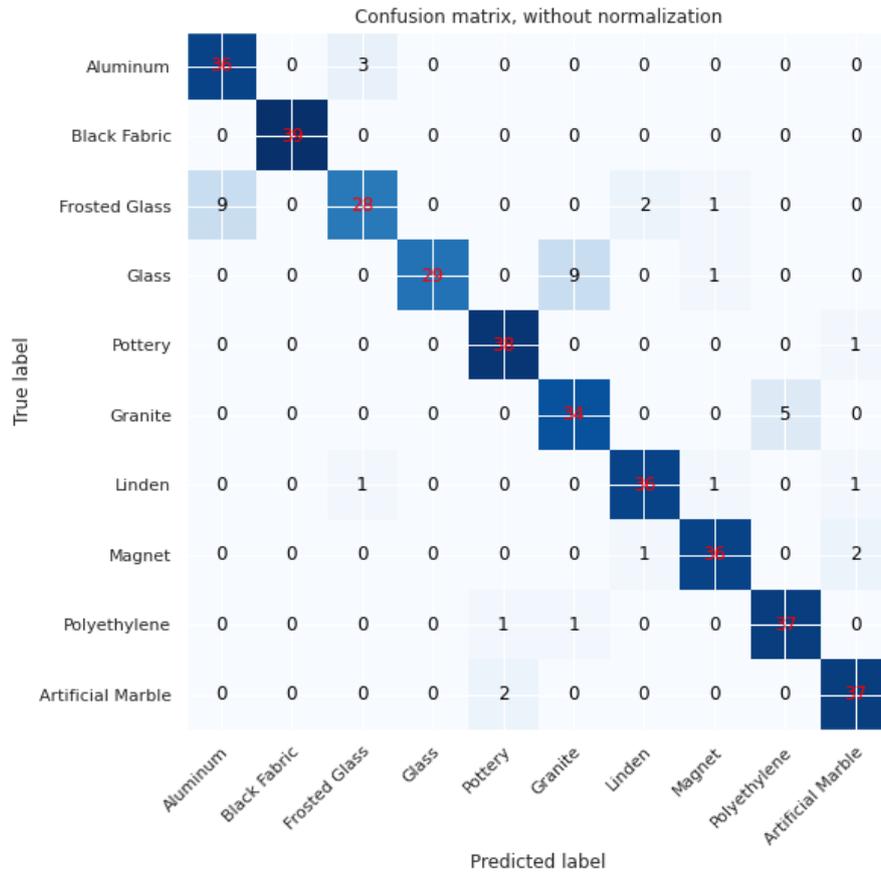
Fig. 14. Confusion matrix for test data with the lowest accuracy rate in 10-fold cross-validation.

5. 5.Limitations and future works

In material identification studies with laser signals, a database containing material reflection values is created. When a material is wanted to be defined, it is compared with the previous known materials in the database and this material is accepted into the class of materials that is closest to it. This study was conducted to identify 10 types of materials that are often used in our environment. For this reason, only these 10 materials can be defined in the material classification. In the future, it is necessary to collect data from more materials so that more materials can be classified with laser signals. In this study, a matte black material with low reflectivity was placed on the background to identify transparent glass and translucent frosted glass. In future studies, algorithms that can identify transparent materials more efficiently are needed.

Moisture on material surfaces, humidity in the air, fog and sunlight have negative effects on material identification. There may be distortions in the laser signals reflected from highly humid surfaces and this may adversely affect the classification performance. For this purpose, studies are needed that take into account surface moisture and air humidity. Similarly, other atmospheric conditions can affect the measurement accuracy. In the future, more studies can be made on the performance of the system in night, day, cloudy and sunny environments.

It is known that laser marks vary according to the distance between the material and the device, the internal hardware and software of the device, the normal of the material and the angle of the laser. The angle between the normal of the material and the laser device will cause differences in the reflected intensity values, and in such a case, the classification performance may be adversely affected. There is also a need for studies that take into account the distance and angle between the laser device and the material.

6. 6.Conclusion

In this study, a deep learning architecture was designed with NCP for the classification of long-distance materials using a basic level laser module and the performance of this classifier was verified. In the proposed method, the 3000-dimensional laser signals obtained depending on the laser light intensity reflected from the materials were converted into 32-dimensional signals by Welch PSD and Yule Walker AR signal conversion, immediately after noise removal. With this data preparation method, the computational cost of deep learning architecture is greatly reduced. In addition, thanks to the proposed NCP model, contactless and remote material classification can be made with a high degree of accuracy with the connection between a small number of neurons and a small number of neurons. Unlike systems that are easily affected by light, such as cameras, classification can be made with a single laser light, which is not affected by ambient light. Due to its low computational cost, the proposed system can be easily adapted to any embedded system.

In the 4-layer NCP model developed inspired by the Elegans nematode, there are sensory neurons in the input layer, inter and command neurons in the intermediate layer, and motor neurons in the last output layer. With the NCP model, the number of synapses between the layers can be adjusted. According to the determined number of connections, the synapses are connected to the neurons in the next layer in a random order. In addition, the number of RNN cells in command neurons can be selected. The architecture in the sparse structure, which is created by the specified number of neurons and the number of connections configuration, can perform as well as the architecture in the fully connected structure.

Experimental studies were carried out in the laboratory environment at different times of the day and the amount of light in the working environment could vary. In the experimental setup, signals were received from polyethylene, aluminum, magnet, black fabric, linden, frosted glass, glass, granite, artificial marble, pottery, which are at a certain distance and are frequently used in daily life. During the process of receiving the signal from the materials, the laser light was turned off first and the noisy signal caused by the device/ambient lights was recorded. Then, while the laser device was in the same position, the laser light was turned on and the laser intensity values reflected from the material were recorded. With this measurement method, the system can be more resistant to noises caused by the device and ambient lights. At the end of the measurements, 391 raw and noisy laser signals were obtained from each material. In the classification studies performed with the 10-fold cross-validation technique, the average classification success was 92.66% with the 32-dimensional laser signals obtained by using the Welch PSD method. To the best of our

knowledge, this study is the first to identify material using the laser signal measured from a single point of the material and the NCP model.

In a robotic gripping system that makes material classification with laser, it will be possible to position the robot in accordance with the material. Similarly, in autonomous vehicles, safer driving will be possible by detecting the road type (asphalt, soil, pebbles, etc.) signals or detecting the icing of the road by using laser signals.

References

Aujeszky, T., Korres, G., Eid, M., & Khorrami, F. (2019). An Approach to Estimate Emissivity for Thermography-based Material Recognition. *2019 IEEE International Conference on Computational Intelligence and Virtual Environments for Measurement Systems and Applications, CIVEMSA 2019 - Proceedings.* https://doi.org/10.1109/CIVEMSA45640.2019.9071626

Baghaei Naeini, F., Alali, A. M., Al-Husari, R., Rigi, A., Al-Sharman, M. K., Makris, Dı., & Zweiri, Y. (2020). A Novel Dynamic-Vision-Based Approach for Tactile Sensing Applications. *IEEE Transactions on Instrumentation and Measurement*, *69*(5), 1881–1893. https://doi.org/10.1109/TIM.2019.2919354

Baglio, S., Cantelli, L., Giusa, F., & Muscato, G. (2015). Intelligent prodder: Implementation of measurement methodologies for material recognition and classification with humanitarian demining applications. *IEEE Transactions on Instrumentation and Measurement*, *64*(8), 2217–2226. https://doi.org/10.1109/TIM.2014.2386917

Bai, H., Bhattacharjee, T., Chen, H., Kapusta, A., & Kemp, C. C. (2018). Towards Material Classification of Scenes Using Active Thermography. *IEEE International Conference on Intelligent Robots and Systems*, 4262–4269. https://doi.org/10.1109/IROS.2018.8594469

Bell, S., Upchurch, P., Snavely, N., & Bala, K. (2015). Material recognition in the wild with the Materials in Context Database. *Proceedings of the IEEE Computer Society Conference on Computer Vision and Pattern Recognition*, *07-12-June-2015*, 3479–3487. https://doi.org/10.1109/CVPR.2015.7298970

Bhattacharjee, T., Clever, H. M., Wade, J., & Kemp, C. C. (2018). Multimodal Tactile Perception of Objects in a Real Home. *IEEE Robotics and Automation Letters*, *3*(3), 2523–2530. https://doi.org/10.1109/LRA.2018.2810956

Bhattacharjee, T., Wade, J., & Kemp, C. C. (n.d.). *Material Recognition from Heat Transfer given Varying Initial Conditions and Short-Duration Contact.*

Bian, P., Li, W., Jin, Y., & Zhi, R. (2018). Ensemble feature learning for material recognition with convolutional neural networks. *Eurasip Journal on Image and Video Processing*, *2018*(1), 1–11. https://doi.org/10.1186/s13640-018-0300-z

Bunrit, S., Kerdprasop, N., & Kerdprasop, K. (2020). *Improving the Representation of CNN Based Features by Autoencoder for a Task of Construction Material Image Classification.* https://doi.org/10.12720/jait.11.4.192-199

Carrea, D., Abellan, A., Humair, F., Matasci, B., Derron, M.-H., & Jaboyedoff, M. (2016). Correction of terrestrial LiDAR intensity channel using Oren–Nayar reflectance model: An application to lithological differentiation. *ISPRS Journal of Photogrammetry and Remote Sensing*, *113*, 17–29. https://doi.org/10.1016/j.isprsjprs.2015.12.004

Chaparro, L. F., & Akan, A. (2019). Discrete-Time Signals and Systems. In *Signals and Systems Using MATLAB* (3rd ed., pp. 487–557). Academic Press. https://doi.org/10.1016/b978-0-12-814204-2.00020-x

Chathuranga, D. S., Ho, V. A., & Hirai, S. (2013). Investigation of a biomimetic fingertip's ability to discriminate fabrics based on surface textures. *2013 IEEE/ASME International Conference on Advanced Intelligent Mechatronics: Mechatronics for Human Wellbeing, AIM 2013*, 1667–1674. https://doi.org/10.1109/AIM.2013.6584336

Corsi, A. K., Wightman, B., & Chalfie, M. (2015). A Transparent window into biology: A primer on Caenorhabditis elegans. In *WormBook : the online review of C. elegans biology* (pp. 1–31). WormBook. https://doi.org/10.1895/WORMBOOK.1.177.1

Dimitrov, A., & Golparvar-Fard, M. (2014). Vision-based material recognition for automated monitoring of construction progress and generating building information modeling from unordered site image collections. *Advanced Engineering Informatics*, *28*(1), 37–49. https://doi.org/10.1016/j.aei.2013.11.002

Emenike, H., Dar, F., Liyanage, M., Sharma, R., Zuniga, A., Hoque, M. A., Radeta, M., Nurmi, P., & Flores, H. (2021). Characterizing Everyday Objects using Human Touch: Thermal Dissipation as a Sensing Modality. *2021 IEEE International Conference on Pervasive Computing and Communications (PerCom)*, 1–8. https://doi.org/10.1109/PERCOM50583.2021.9439120

Fernando, H., & Marshall, J. (2020). What lies beneath: Material classification for autonomous excavators using proprioceptive force sensing and machine learning. *Automation in Construction*, *119*, 103374. https://doi.org/10.1016/j.autcon.2020.103374

Frangez, V., Salido-Monzú, D., & Wieser, A. (2021). Surface finish classification using depth camera data. *Automation in Construction*, *129*, 103799. https://doi.org/10.1016/J.AUTCON.2021.103799

Galdames, F. J., Perez, C. A., Estévez, P. A., & Adams, M. (2017). Classification of rock lithology by laser range 3D and color images. *International Journal of Mineral Processing*, *160*, 47–57. https://doi.org/10.1016/J.MINPRO.2017.01.008

Gao, S., Weng, L., Deng, Z., Wang, B., & Huang, W. (2021). Biomimetic Tactile Sensor Array based on Magnetostrictive Materials. *IEEE Sensors Journal*. https://doi.org/10.1109/JSEN.2021.3068160

Gupta, H. R., & Mehra, R. (2013). Power Spectrum Estimation using Welch Method for various Window Techniques. *International Journal of Scientific Research Engineering & Technology*, *2*(6), 389–392.

Han, K. K., & Golparvar-Fard, M. (2015). Appearance-based material classification for monitoring of operation-level construction progress using 4D BIM and site photologs. *Automation in Construction*, *53*, 44–57. https://doi.org/10.1016/j.autcon.2015.02.007

Hasani, R., Lechner, M., Amini, A., Rus, D., & Grosu, R. (2020). *Liquid Time-constant Networks*. https://doi.org/10.48550/arxiv.2006.04439

Hess, M. R., Petrovic, V., & Kuester, F. (2017). Interactive classification of construction materials: Feedback driven framework for annotation and analysis of 3D point clouds. *International Archives of the Photogrammetry, Remote Sensing and Spatial Information Sciences - ISPRS Archives*, *42*(2W5), 343–347. https://doi.org/10.5194/ISPRS-ARCHIVES-XLII-2-W5-343-2017

Hoskere, V., Narazaki, Y., Hoang, T. A., & Jr., B. F. S. (2020). MaDnet: multi-task semantic segmentation of multiple types of structural materials and damage in images of civil infrastructure. *Journal of Civil Structural Health Monitoring 2020 10:5*, *10*(5), 757–773. https://doi.org/10.1007/S13349-020-00409-0

Ilehag, R., Leitloff, J., Weinmann, M., & Schenk, A. (2020). Urban Material Classification Using Spectral and Textural Features Retrieved from Autoencoders. *ISPRS Annals of the Photogrammetry, Remote Sensing and Spatial Information Sciences, Volume V-1-2020, 2020, XXIV ISPRS Congress (2020 Edition). Ed.: N. Paparoditis*, *5*(1), 25. https://doi.org/10.5194/ISPRS-ANNALS-V-1-2020-25-2020

Jelalian, A. V. (1992). LASER RADAR SYSTEMS. In *Conference Record - Electro*. Artech House.

Kerr, E., McGinnity, T. M., & Coleman, S. (2018). Material recognition using tactile sensing. *Expert Systems with Applications*, *94*, 94–111. https://doi.org/10.1016/J.ESWA.2017.10.045

Kumar, R., Amrita, & Kumar Mishra, P. (2021). An intelligent computing system to detect material. *Materials Today: Proceedings*, *34*, 679–683. https://doi.org/10.1016/j.matpr.2020.03.332

Kumar Rahi, P., Mehra, R., Scholar, M., & Professor, A. (2014). Analysis of Power Spectrum Estimation Using Welch Method for Various Window Techniques. *International Journal of Emerging Technologies and Engineering*, *2*(6), 106–109.

Lam, H. K., Ekong, U., Liu, H., Xiao, B., Araujo, H., Ling, S. H., & Chan, K. Y. (2014). A study of neural-network-based classifiers for material classification. *Neurocomputing*, *144*, 367–377. https://doi.org/10.1016/j.neucom.2014.05.019

Lechner, M., Hasani, R., Amini, A., Henzinger, T. A., Rus, D., & Grosu, R. (2020). Neural circuit policies enabling auditable autonomy. *Nature Machine Intelligence 2020 2:10*, *2*(10), 642–652. https://doi.org/10.1038/s42256-020-00237-3

Li, Y., Lu, Y., & Chen, J. (2021). A deep learning approach for real-time rebar counting on the construction site based on YOLOv3 detector. *Automation in Construction*, *124*, 103602. https://doi.org/10.1016/j.autcon.2021.103602

Liu, C., Sharan, L., Adelson, E. H., & Rosenholtz, R. (2010). Exploring features in a Bayesian framework for material recognition. *Proceedings of the IEEE Computer Society Conference on Computer Vision and Pattern Recognition*, 239–246. https://doi.org/10.1109/CVPR.2010.5540207

Martino, F., Patruno, C., Mosca, N., & Stella, E. (2016). Material recognition by feature classification using time-of-flight camera. *Journal of Electronic Imaging*, *25*(6), 061412. https://doi.org/10.1117/1.jei.25.6.061412

Ni, P., Miao, C., Tang, H., Jiang, M., & Wu, W. (2020). Small Foreign Object Debris Detection for Millimeter-Wave Radar Based on Power Spectrum Features. *Sensors 2020, Vol. 20, Page 2316*, *20*(8), 2316. https://doi.org/10.3390/S20082316

Olgun, N., & Türkoğlu, İ. (2018). Lazer İşaretleri ile Otomatik Hedef Tanıma. *Sakarya University Journal of Computer and Information Sciences*, *1*(3), 1–10.

Olgun, N., & Türkoğlu, İ. (2022). Defining materials using laser signals from long distance via deep learning. *Ain Shams Engineering Journal*, *13*(3), 101603. https://doi.org/10.1016/J.ASEJ.2021.10.001

Rao, K. D., & Swamy, M. N. S. (2018). Spectral Analysis of Signals. In *Digital Signal Processing* (pp. 721–751). Springer Singapore. https://doi.org/10.1007/978-981-10-8081-4_12

Rashidi, A., Sigari, M. H., Maghiar, M., & Citrin, D. (2015). An analogy between various machine-learning techniques for detecting construction materials in digital images. *KSCE Journal of Civil Engineering 2016 20:4*, *20*(4), 1178–1188. https://doi.org/10.1007/S12205-015-0726-0

Ryu, S., & Kim, S.-C. (2020). Knocking and Listening: Learning Mechanical Impulse Response for Understanding Surface Characteristics. *Sensors 2020, Vol. 20, Page 369*, *20*(2), 369. https://doi.org/10.3390/S20020369

Son, H., Kim, C., Hwang, N., Kim, C., & Kang, Y. (2014). Classification of major construction materials in construction environments using ensemble classifiers. *Advanced Engineering Informatics*, *28*(1), 1–10. https://doi.org/10.1016/j.aei.2013.10.001

Sonoda, C., Miki, T., & Tateishi, Y. (2009). Fuzzy inference based subjective material-recognition system employing a multi-modal tactile sensor. *IEEE International Conference on Fuzzy Systems*, 245–250. https://doi.org/10.1109/FUZZY.2009.5277178

Suchocki, C., Damięcka-Suchocka, M., Katzer, J., Janicka, J., Rapiński, J., & Stałowska, P. (2020). Remote Detection of Moisture and Bio-Deterioration of Building Walls by Time-Of-Flight and Phase-Shift Terrestrial Laser Scanners. *Remote Sensing*, *12*(11), 1708. https://doi.org/10.3390/rs12111708

Suchocki, C., & Katzer, J. (2018a). Terrestrial laser scanning harnessed for moisture detection in building materials – Problems and limitations. *Automation in Construction*, *94*, 127–134. https://doi.org/10.1016/j.autcon.2018.06.010

Suchocki, C., & Katzer, J. (2018b). Terrestrial laser scanning harnessed for moisture detection in building materials – Problems and limitations. *Automation in Construction*, *94*, 127–134. https://doi.org/10.1016/j.autcon.2018.06.010

Varma, M., & Zisserman, A. (2009). A Statistical Approach to Material Classification Using Image Patch Exemplars. *IEEE Transactions on Pattern Analysis and Machine Intelligence*, *31*(11), 2032–2047. https://doi.org/10.1109/TPAMI.2008.182

Xie, Y., Chen, C., Wu, D., Xi, W., & Liu, H. (2019). Human-Touch-Inspired Material Recognition for Robotic Tactile Sensing. *Applied Sciences 2019, Vol. 9, Page 2537*, *9*(12), 2537. https://doi.org/10.3390/APP9122537

Xu, H., Han, Z., Feng, S., Zhou, H., & Fang, Y. (2018). Foreign object debris material recognition based on convolutional neural networks. *EURASIP Journal on Image and Video Processing 2018 2018:1*, *2018*(1), 1–10. https://doi.org/10.1186/S13640-018-0261-2

Yan, G., Vértes, P. E., Towlson, E. K., Chew, Y. L., Walker, D. S., Schafer, W. R., & Barabási, A. L. (2017). Network control principles predict neuron function in the Caenorhabditis elegans connectome. *Nature 2017 550:7677*, *550*(7677), 519–523. https://doi.org/10.1038/nature24056

Yeo, H. S., Flamich, G., Schrempf, P., Harris-Birtill, D., & Quigley, A. (2016). RadarCat: Radar categorization for input & interaction. *UIST 2016 - Proceedings of the 29th Annual Symposium on User Interface Software and Technology*, 833–841. https://doi.org/10.1145/2984511.2984515

Yuan, L., Guo, J., & Wang, Q. (2020a). Automatic classification of common building materials from 3D terrestrial laser scan data. *Automation in Construction*, *110*, 103017. https://doi.org/10.1016/j.autcon.2019.103017

Yuan, L., Guo, J., & Wang, Q. (2020b). Automatic classification of common building materials from 3D terrestrial laser scan data. *Automation in Construction*, *110*, 103017. https://doi.org/10.1016/j.autcon.2019.103017

Zahiri, Z., Laefer, D. F., & Gowen, A. (2021). Characterizing building materials using multispectral imagery and LiDAR intensity data. *Journal of Building Engineering*, *44*, 102603. https://doi.org/10.1016/J.JOBE.2021.102603

Zhao, L., & He, Y. (2013). Power Spectrum Estimation of the Welch Method Based on Imagery EEG. *Applied Mechanics and Materials*, *278–280*, 1260–1264. https://doi.org/10.4028/WWW.SCIENTIFIC.NET/AMM.278-280.1260

Živec, T., Anžur, A., & Verbovšek, T. (2018). Determination of rock type and moisture content in flysch using TLS intensity in the Elerji quarry (south-west Slovenia). *Bulletin of Engineering Geology and the Environment 2018 78:3*, *78*(3), 1631–1643. https://doi.org/10.1007/S10064-018-1245-2

Predicting Tuberculosis from X-Rays By Using Deep Learning

Ömer SEVİNÇ[1]
Mehrube MEHRUBEOĞLU [2]
Mehmet KARA [3]
M Serdar GÜZEL [4]
İman ASKERZADE [5]

Introduction

Tuberculosis (TB) is a significant health issue for most countries across the world. According to Pasa, Golkov, Pfeiffer, Cremers, & Pfeiffer (2019), tuberculosis is the fifth leading cause of death across the globe, with 1.5 million annual deaths and 10 million new cases reported every year. Notably, it can be easily treated; therefore, the World Health Organization recommends broad and systematic screening to facilitate the management of the disease. The normal and tuberculosis chest X-ray samples can be seen in Figure-1 and Figure-2. The most common measure used for monitoring and diagnosing lung diseases such as tuberculosis is the chest X-ray (CXR), as they are affordable and easily accessible (Stirenko et al., 2018). The development and evolution of modern technologies such as deep learning modalities allow scientists to automatically detect the lung diseases from CXR images even for radiologists without certified expert knowledge on radiography. Deep learning is a branch of artificial intelligence with a network capable of learning unlabeled, unstructured, and unsupervised data. The NIH Chest X-rays images and text data can incorporate deep learning methods like Convolutional Neural Networks (CNN) and Recurrent Neural Network (RNN) to predict tuberculosis and thus enhance management and reduce deaths. This paper proposes a deep learning technique which is CNN and efficacy of using it in predicting tuberculosis using the National Institution of Health (NIH) chest X-ray images. The proposed model achieved %98 validation accuracy scores which is over state-of-art models.

[1] Lecturer, Ondokuz Mayis University, Computer Programming, Orcıd:
[2] Prof. Dr., Texas A&M University Corpus Christi, Computer Science, Orcıd:
[3] Developer, Ankara University, Computer Engineering, Orcıd:
[4] Assoc. Prof., Ankara University, Computer Engineering, Orcıd:
[5] Prof. Dr., Ankara University, Computer Engineering, Orcıd:

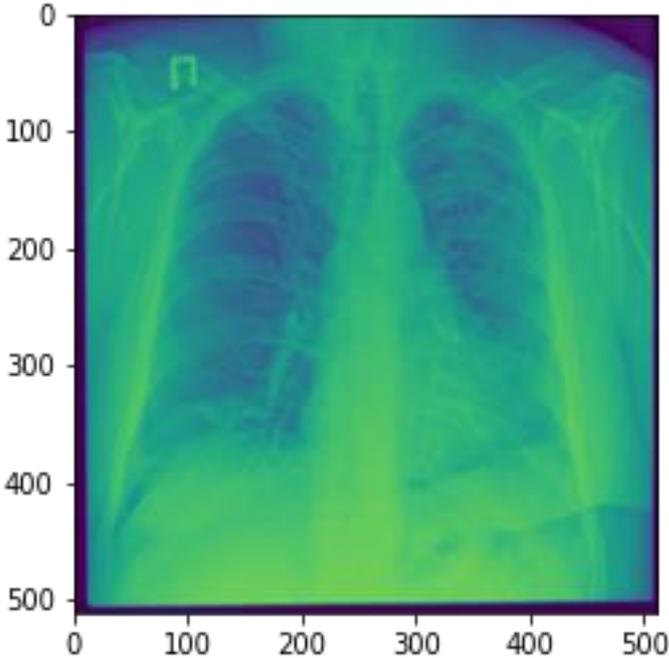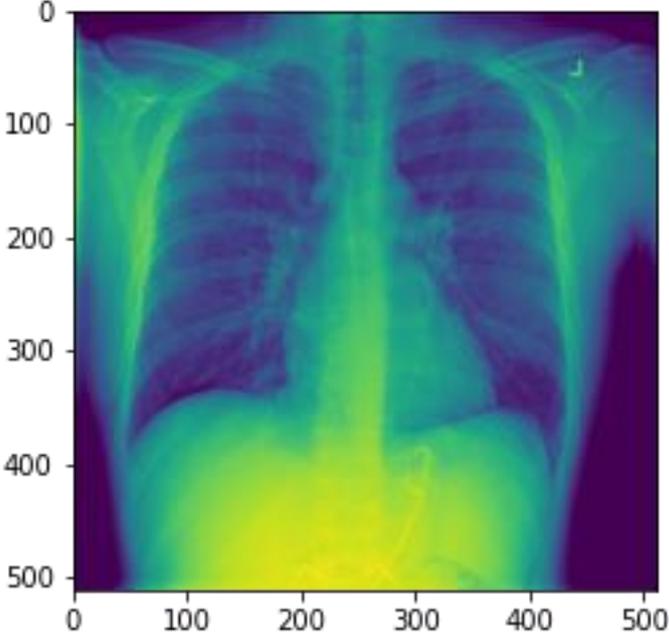**Figure-1** Tuberculosis chest X-ray sample

Figure-2 Normal chest X-ray sample

Significance of Deep Learning Techniques

The most common measure used in the screening of tuberculosis is CXR. However, the uses involve a long, complicated process. They require expert radiologists, yet most affected developing countries do not have enough radiologists with sufficient skills in interpreting results from the CXR (Stirenko et al., 2018). Similarly, Lakhani & Sundaram (2017) say that there is a lack of radiology expertise necessary for interpreting tuberculosis in many regions across the world, which consequently impairs work-up efforts and screening efforts. Deep learning technology describes artificial intelligence where computers can help human beings to perform tasks such as using existing data to examine relationships. Deep learning techniques thus provide an effective intervention as they increase accuracy in prediction tuberculosis.

Furthermore, identification of people with high risks of developing tuberculosis is a critical consideration of a need for imaging techniques that easy to use and accurate in making a prediction. Imaging is mainly a key screening measure for people suspected to have pulmonary tuberculosis among work-up patients (Lakhani & Sundaram, 2017). Therefore, deep learning techniques, which are cost-effective and efficacious automated methods, can help and facilitate screening and earlier detection of tuberculosis.

Convolutional Neural Networks (CNN)

According to Lopez-Garnier, Sheen, & Zimic (2019), CNNs, along with increasingly high medical datasets, have increased classification and detection capabilities. The CNNS are biologically inspired and use hierarchical methods to make assumptions about the location of images using pixels learned through information hierarchies. The layers are used to detect layers where the higher layers help in detecting sophisticated features. (World Health Organization, 2011) suggest that CNNs have abilities to outperform human experts in classification, recognition, and processing of images and texts, among other tasks. Lopez-Garnier, Sheen, & Zimic, (2019) designed and developed a trained CNN with abilities to identify *M. Tuberculosis* in a Microscopic Observed Drug Susceptibility (MODS) culture. CNN was trained on the 12510 MODS dataset and showed an accuracy of between 91% and 99% hence the efficacy of using deep learning in predicting tuberculosis using the NIH data.

DCNN (Deep CNN) is one supervised type of deep learning technology that incorporates multiple layers and has been successful in the classification of images (LeCun, Bengio, & Hinton, 2015). The abilities to present datasets like images at multiple levels are one significant advantage of deep learning. For instance, DCNN can whole objects in higher levels, parts of objects in intermediate level, and pixels with blobs, values, and edges at lower levels. The multiple layers make data analysis easy and increase the abilities to produce accurate results.

Deep learning techniques rely on big data sets to produce accurate and reliable results. Unfortunately, Wang, Peng, Lu, Lu, Bagheri, & Summers (2017), acknowledges that the incorporation of machine learning in CXR continues to be a challenge because of a lack of techniques that mimic high reasoning of human beings as well as a shortage of large-scale machine learning datasets.

Furthermore, the chest X-ray data set released by the National Institution of Health (NIH) with 100,000 anonymized CXR images form 32000 patients could be mislabeled as usual when they are not specific to TB (Wang et al., 2017). Additionally, Stirenko et al. (2018) assert that there is an increased belief that deep learning modalities are only valid when used with more massive datasets

with more than 10,000 images and ineffective with smaller data sets of less than 1000 images as they are associated with lower accuracies and weak predictions. The small data on tuberculosis from NIH thus creates efficacy issues surrounding the use of deep learning in predicting tuberculosis. However, the embedding of texts and images, the use of pre-learning tools, augmentation of datasets, and ensembles help in countering the issues of small tuberculosis chest images available in NIH.

Most chest pathologies have large datasets that make a diagnosis using deep learning feasible. However, the use of deep learning in the diagnosis for some chest pathologies such as tuberculosis remains a challenge because of the available small dataset. For this reason, Lakhani & Sundaram (2017); Sivaramakrishnan et al. (2018) demonstrated that pre-trained architectures like ImageNet could effectively produce diagnosis results and detection of TB on small datasets. According to Lakhani & Sundaram (2017), training of ImageNet used in deep convolutional neural networks (DCNN) augments processing techniques, which consequently leads to increased accuracy in prediction of tuberculosis as opposed to the incorporation of untrained ImageNet. The pre-training ImageNet feature enables the DCNN to make accurate predictions even with small datasets. Besides, datasets can also be augmented by contrasting or rotating images. The augmentation features are essential to improving the performance of the deep learning technique.

Gozes & Greenspan (2019) found that deep learning modalities can be enhanced by incorporating learning image features that are specific to CXR using hospital scale datasets with metadata and pathology labels. Gozes & Greenspan (2019) proposed pre-training features, NIH Chest Xray14, and stated that metadata is an accurate and objective label for the element as it helps in countering the noise in the dataset. According to Gozes & Greenspan (2019), the MetachexNet feature is better than ImageNet in terms of predicting tuberculosis and the generalizability of results. Lakhani & Sundaram (2017); Sivaramakrishnan et al. (2018); Gozes & Greenspan (2019) all agree that deep learning can lead to the attainment of accurate results in predicting tuberculosis using CXR by adding learning features to the machine learning architecture. Small datasets are, therefore, not a limitation to the uses of deep learning for predicting tuberculosis.

The feature reduction is also an important part of deep learning models due to process time and eliminate overfitting. So there some approaches like principal component analysis, auto encoders to reduce features (Karim, A. M et al, 2019). However, auto encoder can be used as a model to data augmentation, reduction, and mapping input features to output features to reconstruct the image again (Karim, A. M et al, 2020).

The pertaining feature incorporation in deep learning architecture allows for random initialization so that the machine learning technology can relearn from the medical images provided. Another challenge with the use of deep learning is over-fitting, which occurs when trained models fit that dataset well but do not generalize unseen cases. However, measures such as model regularization or dropout can be used to overcome the challenge of over-fitting. In our model regularization and dropout parameters are used to fine tune the model.

Machine learning technologies in neural networks are nonlinear and can scale depending on the training data available. The stochastic training algorithm in deep leaning implies that they are specific to the different types of training, and the associated weights may give different predictions whenever the algorithm is run (Brownlee, 2019).

Method & Results

In the proposed model a custom CNN model is used to train and test NIH Chest X-ray dataset to predict an input image either indicates the tuberculosis or not. The dataset from Kaggle includes 4200 images consists of 3500 is normal and 700 tuberculosis. The test size is specified as 0.2 to train the model with 80% and test with 20% of the dataset. Images are resized to an 250x250 array. The convolution filters are used amount of 32, 64, 128 (3x3) and at the flattening layer 28800 features are handled. On the flatten layer the dense layers are added to reduce the features 128 and then the output layer gives the 2 values to classify the images is tuberculosis sample or not. Totally 6 convolutional, 2 dense and 4 maxpool layers are used to build the model. The optimizer has chosen as 'Adam' where the activation functions are set as 'relu' and at the output layer is used as 'softmax' to have best classification results. The batch value is provided as 32 and the epoch is 20 that gives the maximum accuracy value and does not improve after 20th epoch. After the model successfully trained the test accuracy results for the classification hit the result over 98%. The confusion matrix, train and test accuracy and loss graphs can be seen in Figure-3, Figure-4 and Figure-5. The model evaluation is made on precision, recall, f-score values and the details are shown in the Table-1.

Figure-3 Loss graph for training and the test

Figure-4 Accuracy graph for training and test
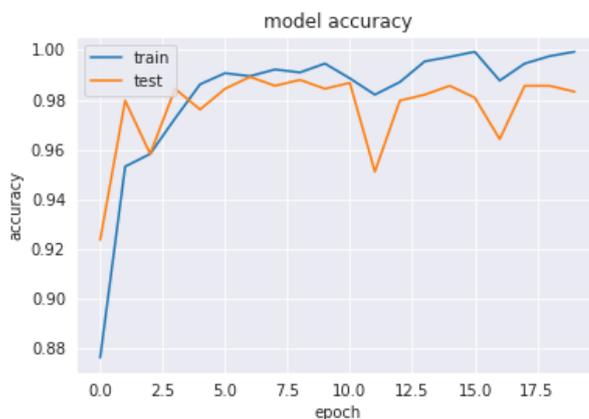
Figure-4 Confusion matrix for validation

Table-1 The scores of model evaluation

	precision	recall	f1-score	support
Normal	0.993	0.996	0.994	679
Tuberculosis	0.981	0.969	0.975	161
Accuracy	0.990	0.990	0.990	0.990476
Macro Avg	0.987	0.982	0.985	840
Weighted Avg	0.990	0.990	0.990	840

Conclusion

There are wide ranges of deep learning technologies such as neural networks, CNN that can be used in predicting tuberculosis in chest x-ray images provided by NIH. With deep learning technologies, users can accurately predict the presence of tuberculosis, even with minimal expert knowledge. Therefore, deep learning has more advantages than the standard modality that involves the use of chest x-ray images that require significant specialist knowledge. As a result, clinicians will be better placed to reduce deaths and new cases of tuberculosis across the world. The tuberculosis datasets available are small, which undermines the use of machine learning technologies that rely on large amounts of data to make an accurate prediction.

Additionally, tuberculosis datasets are limited to the use of strategies such as crowd sourcing, as the data requires expert knowledge. However, the limitation of small data set can be countered by using pre-training learning features, augmentation of datasets. The training of images increases the abilities of the deep learning tools to make accurate predictions of the presence of tuberculosis. In the proposed model CNN architecture successfully helps to classify tuberculosis over chest X-ray image dataset which gives over 98% validation accuracy scores. The regularization parameters

and dropout improve the model success and provide better classification results. For further improvements an optimization algorithm can be implement to find optimum parameters itself.

References

Brownlee, J. (2018). Ensemble learning methods for deep learning neural networks. Machine Learning Mastery. https://machinelearningmastery.com/ensemble-methods-for-deep-learning-neural-networks/

Gozes, O., & Greenspan, H. (2019, July). Deep Feature learning from a hospital-scale chest X-ray dataset with application to TB detection on a small-scale dataset. In *2019 41st Annual International Conference of the IEEE Engineering in Medicine and Biology Society (EMBC)* (pp. 4076-4079). IEEE.

Hsu, T. M. H., Weng, W. H., Boag, W., McDermott, M., & Szolovits, P. (2018). Unsupervised multimodal representation learning across medical images and reports. *arXiv preprint arXiv:1811.08615*.

Karim, A. M., Kaya, H., Güzel, M. S., Tolun, M. R., Çelebi, F. V., & Mishra, A. (2020). A novel framework using deep auto-encoders based linear model for data classification. Sensors, 20(21), 6378.

Karim, A. M., Güzel, M. S., Tolun, M. R., Kaya, H., & Çelebi, F. V. (2019). A new framework using deep auto-encoder and energy spectral density for medical waveform data classification and processing. Biocybernetics and Biomedical Engineering, 39(1), 148-159.

Lakhani, P., & Sundaram, B. (2017). Deep learning at chest radiography: Automated classification of pulmonary tuberculosis by using convolutional neural networks. *Radiology*, *284*(2), 574-582.

Lopez-Garnier, S., Sheen, P., & Zimic, M. (2019). Automatic diagnostics of tuberculosis using convolutional neural networks analysis of MODS digital images. *PloS one*, *14*(2), e0212094. doi:10.1371/journal.pone.0212094

LeCun, Y., Bengio, Y., & Hinton, G. (2015). Deep learning. *Nature*, *521*(7553), 436-444.

Pasa, F., Golkov, V., Pfeiffer, F., Cremers, D., & Pfeiffer, D. (2019). Efficient deep network architectures for fast chest X-ray tuberculosis screening and visualization. *Scientific Reports*, *9*(1), 6268. doi:10.1038/s41598-019-42557-4

Sivaramakrishnan, R., Antani, S., Candemir, S., Xue, Z., Abuya, J., Kohli, M., ... & Thoma, G. (2018, February). Comparing deep learning models for population screening using chest radiography. In *Medical Imaging 2018: Computer-Aided Diagnosis* (Vol. 10575, p. 105751E). International Society for Optics and Photonics.

Stirenko, S., Kochura, Y., Alienin, O., Rokovyi, O., Gordienko, Y., Gang, P., & Zeng, W. (2018, April). Chest X-ray analysis of tuberculosis by deep learning with segmentation and augmentation. In *2018 IEEE 38th International Conference on Electronics and Nanotechnology (ELNANO)* (pp. 422-428). IEEE.

Sathitratanacheewin, S., & Pongpirul, K. (2018). Deep learning for automated classification of tuberculosis-related chest X-ray: Dataset specificity limits diagnostic performance generalizability. *arXiv preprint arXiv:1811.07985*.

Singh, J., Jain, A., Dhyani, T., & Agrawal, P. (2018). Using deep learning for forecasting tuberculosis morbidity rate.

Wang, X., Peng, Y., Lu, L., Lu, Z., Bagheri, M., & Summers, R. M. (2017). Chestx-ray8: Hospital-scale chest X-ray database and benchmarks on weakly-supervised classification and localization of common thorax diseases. In *Proceedings of the IEEE conference on computer vision and pattern recognition* (pp. 2097-2106).

World Health Organization. (2011). *Noncommercial culture and drug-susceptibility testing methods for screening patients at risk for multidrug-resistant tuberculosis: Policy statement* (No. WHO/HTM/TB/2011.9). World Health Organization.

Numerical and Experimental Validation of Water-Sucrose Solution Freezing Inside a Cavity

Ömer Alp ATICI[1]

Introduction

The freezing point depression of various sugars has been studied in the literature and most of the work on this has been done experimentally. It is also clear from the literature that these experimental results have been defined with some correlations to predict values not found experimentally. According to Leighton's studies, the water depression point was calculated taking into account the types of sugar and the amount of salt in the water (Leighton, 1927:300-308). Table 1 shows that the water depression point depends on the amount of sugar cane in the water.

Table 1. Water Freezing Point Depression According to Sugar Cane Amount Inside Water

Dissolved Sugar Cane Amount Inside 100 g Water (g)	Sugar Cane Amount (%)	Water Freezing Point Depression (°C)
3.59	3.47	0.21
6.85	6.41	0.40
10.84	9.78	0.65
15.83	13.67	0.95
19.80	16.53	1.23
22.58	18.42	1.37
25.64	20.41	1.58
28.51	22.19	1.77
32.22	24.37	1.99
35.14	26.00	2.15
37.86	27.46	2.33
43.72	30.42	2.71
45.62	31.33	2.82
50.02	33.35	3.13

Sugar cane is not studied in this work and the amount of sucrose solution is the important parameter for the freezing point depression of water. Cogne and friends have determined the water freezing points of sucrose solutions, and these values can be seen in Table 2 (Cogne et. al., 2003:1129-1135).

---

[1] PhD(c), Yildiz Technical University, Mechanical Engineering Heat and Process Programme, Orcıd: 0000-0002-9494-8032

Table 2. Sucrose Solutions Water Freezing Points

Dissolved Sucrose Amount Inside 100 g Water (g)	Water Freezing Point (°C)
3	0.18
6	0.35
9	0.53
12	0.72
15	0.90
18	1.10
21	1.29
24	1.47
27	1.67
30	1.86
33	2.03
36	2.21
39	2.40
42	2.60
45	2.78
48	2.99
51	3.20

In order to determine the freezing curve, the thermal properties of the water-sucrose solution must be determined. The dry matter content of the water-sucrose solution is %21.1. The density is 1050 kg/m3. The value of the thermal conductivity of the sucrose solution was calculated according to Choi's study (Choi, 1986).

First of all continues phase thermal conductivity value found according to equation 1.1.

$$\lambda_c^{para} = \sum_j \varepsilon_j \lambda_j \qquad 1.1$$

"c" subscript represents the continues phase. "j" represents the number of ingredients.

$$\varepsilon_j = X_j \frac{\rho_c}{\rho_j} \qquad 1.2$$

$$\rho_c = \frac{1}{\sum_j \frac{X_j}{\rho_j}} \qquad 1.3$$

"X" represents the ingredient type. At this study, water and sucrose are the only ingredients. "ε" represents the amount of ingredient in the solution. Total mix thermal conductivity can be found as shown in the equation 1.4 and 1.5.

$$\lambda_{mix} = \lambda_c^{para} \frac{1 - \varepsilon_{ice} + \varepsilon_{ice} F \frac{\lambda_{ice}}{\lambda_c^{para}}}{1 - \varepsilon_{ice} + \varepsilon_{ice} F} \qquad 1.4$$

$$F = \frac{1}{3} \sum_{i=1}^{3} [1 + \left(\frac{\lambda_{ice}}{\lambda_c^{para}} - 1\right) g_i]^{-1} \qquad 1.5$$

163

After defining thermal conductivity, heat capacity values must be defined. Two main heat capacity correlations were investigated in this study and these correlations displayed below. First of all, Schwartzberg model is displayed below equation 1.6. (Schwartzberg, 1976:152-156).

$$if \ T > T_f$$
$$C_p = X_s C_{ps} + X_w C_{pw}$$
$$if \ T < T_f$$
$$C_p(T) = X_s C_{ps} + X_w C_{pw} + (X_b - X_w)(C_{pw} - C_{pice})$$
$$+ \frac{M_w}{M_s} X_s [\frac{RT_0^2}{M_w(T_0 - T)^2} - (C_{pw} - C_{pice})]$$

1.6

Other thermal heat capacity correlation is the Chen et. al.'s correlation. This correlation is showed at the equation 1.7.

$$if \ T > T_f$$
$$C_p = 4180 - 2299X_s - 627X_s^3$$
$$if \ T < T_f$$
$$C_p(T) = 1547 + 1254X_s + \frac{X_s}{M_s} \frac{RT_0^2}{(T - T_0)^2}$$

1.7

EXPERIMENTAL SETUP

As mentioned in the previous section, the water-sugar solution was frozen in the mould. The moulds were placed in the CaCl2 solution to simulate the freezing process, as the temperature of the CaCl2 solution was -31 °C. The midpoint of the water-sucrose solution was recorded with a PT100 temperature probe with an accuracy of ± 0.005 °C. The experimental setup can be seen in Figure 1.
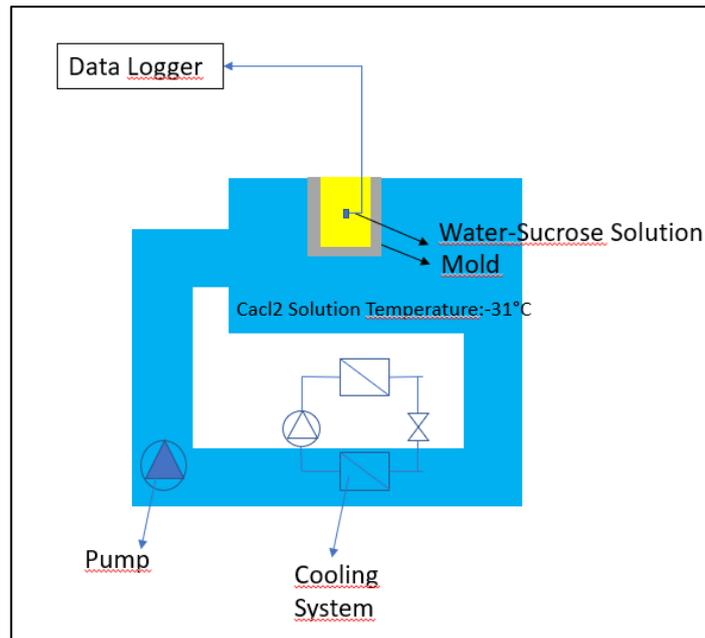
Figure 1. Experimental setup.

RESULTS AND CONCLUSION

In this study, samples of a water-sugar solution were examined. Their dry matter content was 16.6, 19.17 and 21.1% respectively. As shown in Figure 2, the freezing point temperature decreases with increasing sucrose content in the water.

It can also be observed that increasing the amount of sucrose in the water decreases the freezing rate.
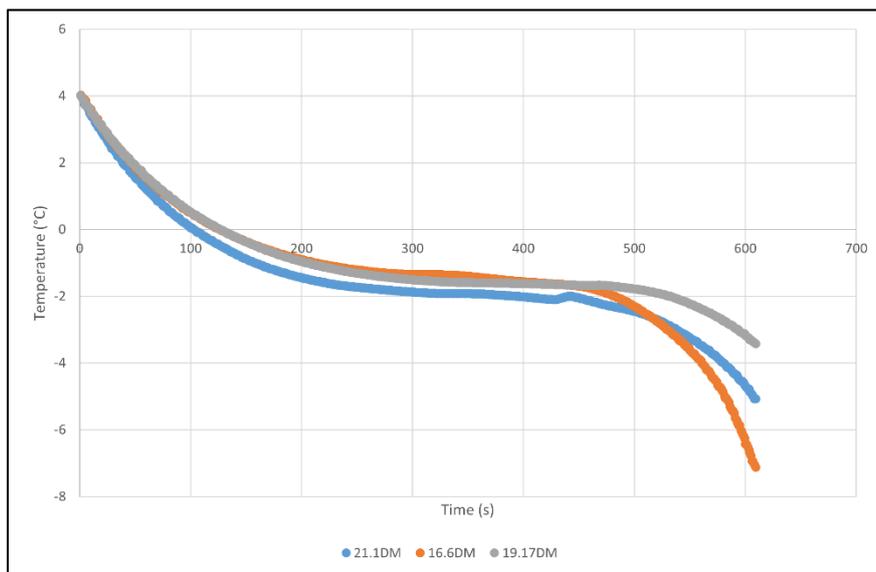
Figure 2. Experimental freezing rate comparison.

Following the experimental studies, numerical analysis was performed using the commercial finite element solver software Ansys with Transient Thermal Toolbox. Unlike many other studies in the literature, a new tool was used for the simulations rather than Fluent.
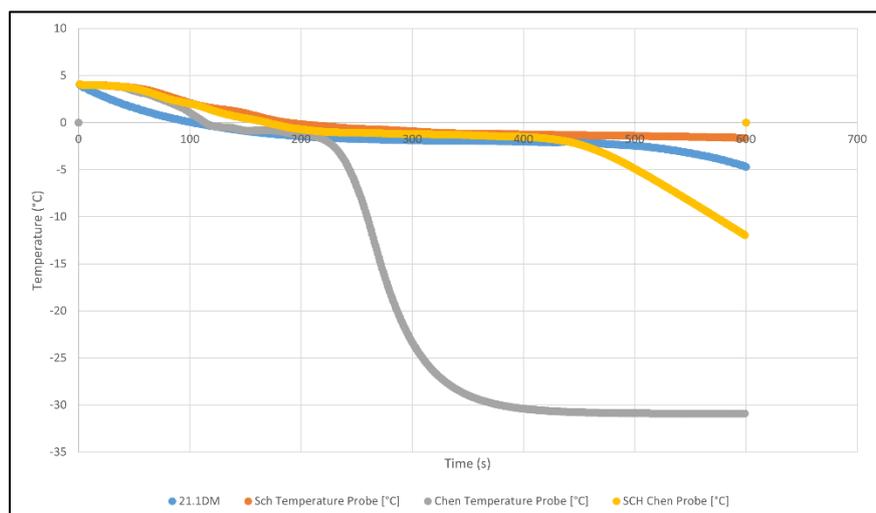
Figure 3. Numerical results comparison with experimental results.

As you can see from Figure 3, Chen's correlation is not good enough to simulate the freezing process of a water-sugar solution. On the other hand, the Schwartzberg correlation did not fit the experimental results either.

For all these reasons, it is decided to propose a new correlation to simulate the freezing process. The mean values of Chen's heat capacity and Schwartzberg's heat capacity results were implemented in numerical simulations and it was found that the freezing point of the experimental result was found with this new correlation.

However, it is found that the freezing rates after the end of phase transformation are different compared to the experimental results.

For further studies, new correlations need to be tried to simulate the experimental results and the mesh quality needs to be improved to obtain more correct results.

REFERENCES

C. Chen, "Thermodynamic analysis of the freezing and thawing of foods: Enthalpy and apparent specific heat," *Journal of food science*, vol. 50, no. 4, pp. 1158–1162, 1985.

Y. Choi, "Effects of temperature and composition on the thermal properties of foods," *Transport phenomena*, 1986.

A. Leighton, "On the calculation of the freezing point of ice-cream mixes and of the quantities of ice separated during the freezing process," *Journal of Dairy Science*, vol. 10, no. 4, pp. 300–308, 1927.

H. G. SCHWARTZBERG, "Effective heat capacities for the freezing and thawing of food," *Journal of Food Science*, vol. 41, no. 1, pp. 152–156, 1976.

Investigation of the Effect of Process Parameters on the Compressive Strength of Al6061/GNP/MWCNT Composites

Türker TÜRKOĞLU[1]
Sare ÇELİK[2]

Introduction

Compared with monolithic pure metals and alloys, composites with metal matrix have properties such as high specific strength, hardness, wear, and corrosion resistance. Thanks to these features; It has a high usage area in key industrial areas such as aerospace, aviation, and automotive. In addition to the lightness feature of aluminum and alloy groups, it also has some drawbacks such as low strength and high wear rate. These reservations are overcome by nano-sized reinforcements added to the metal matrix, which is defined as the matrix phase. The new generation material groups called nano composites have many exceptional properties such as high ductility, and good thermal and electrical properties (Mondal, 2021: 2189). The exceptional in-plane elastic modulus of graphene is due to the sp2 hybrid bonding of carbon atoms. Graphene's 2D structure makes it ideal for usage in metal and ceramic composites, where high pressures are frequently used in processing (Nieto, Bisht, Lahiri, Zhang, & Agarwal, 2017: 241). Carbon nanotubes are one of the nano reinforcement groups that have attracted great interest recently. Carbon nanotubes are used in three forms: i) multiwall CNT (MWCNT), ii) double wall CNT (DWCNT), and single wall CNT (SWCNT). With a tensile strength value 60 times higher than that of steel ($\sim$60 GPa), carbon nanotubes are used in many applications requiring high strength (Soni, Thomas, & Kar, 2020: 2).

The use of carbon-based nano-reinforcements in the field of metal matrix composites has attracted increasing interest in the literature. Different production types have been used for composite production. In the study of reinforcing pure aluminum with GNP, composites were produced by the stir casting method at 0.5-2% weight ratios. It has been reported that the mechanical properties are significantly increased compared to the pure metal and the presence of agglomeration under certain conditions (Subbaiah & Palampalle, 2019). In the study in which Al/CNT composites containing 3% CNT by volume were produced by powder metallurgy method, slurry-based dispersion process and high energy ball milling process were determined as a mixing process. As a result of the mechanical tests of the produced Al/CNT composites, a 67.5% improvement in tensile strength was reported (Fan et al., 2018). In this study, the focus is on improving the compressive strength of the Al6061 alloy composite by hybridization of nano-sized GNP and MWCNT reinforcements in the matrix phase. At the same time, the optimum production conditions were determined by analyzing the production parameters with the Taguchi method.

Materials and method

Al6061 aluminum alloy with 99.5% purity was used as matrix material in the study. GNP and MWCNT carbon-based nanomaterials were chosen as reinforcement materials. The average

---

[1] Türker Türkoğlu, Res. Asst, Balıkesir University, Department of Mechanical Engineering, ORCID:0000-0002-0499-9363

[2] Sare Çelik, Prof. Dr., Balıkesir University, Department of Mechanical Engineering, ORCID:0000-0001-8240-5447

particle size of Al6061 material is 10 µm, while the average particle size of GNP and MWCNT is 50 nm and 200 nm, respectively. Scanning electron microscopy (SEM) views of the powders used in the study are given in Figure 1. The powder metallurgy method was chosen as the consolidation method in the study. In this method, the mixed powders were shaped under a certain temperature and pressure. The production parameters and levels of the composites are given in Table 1. It is known that micron and nano-sized powders are difficult to mix with each other, so two different mixing methods were used together in the study. First, the micron and nano powder groups Al6061, GNP and MWCNT were separately poured into ethyl alcohol, then the mixed powders were subjected to ultrasonication. Ethyl alcohol was removed in an oven at 70 °C for 12 hours. The dried composite mixture powders were conducted to mechanical alloying for 1 hour at a rotational speed of 250 rpm. In order to minimize the cold welding situation during mechanical alloying, zinc stearate was added to the mixture powder. After mixing processes, composite powders were produced in a hot press device using a stainless steel mold. Produced composites are cylindrical and have a diameter of 15 mm and a length of 10 mm.
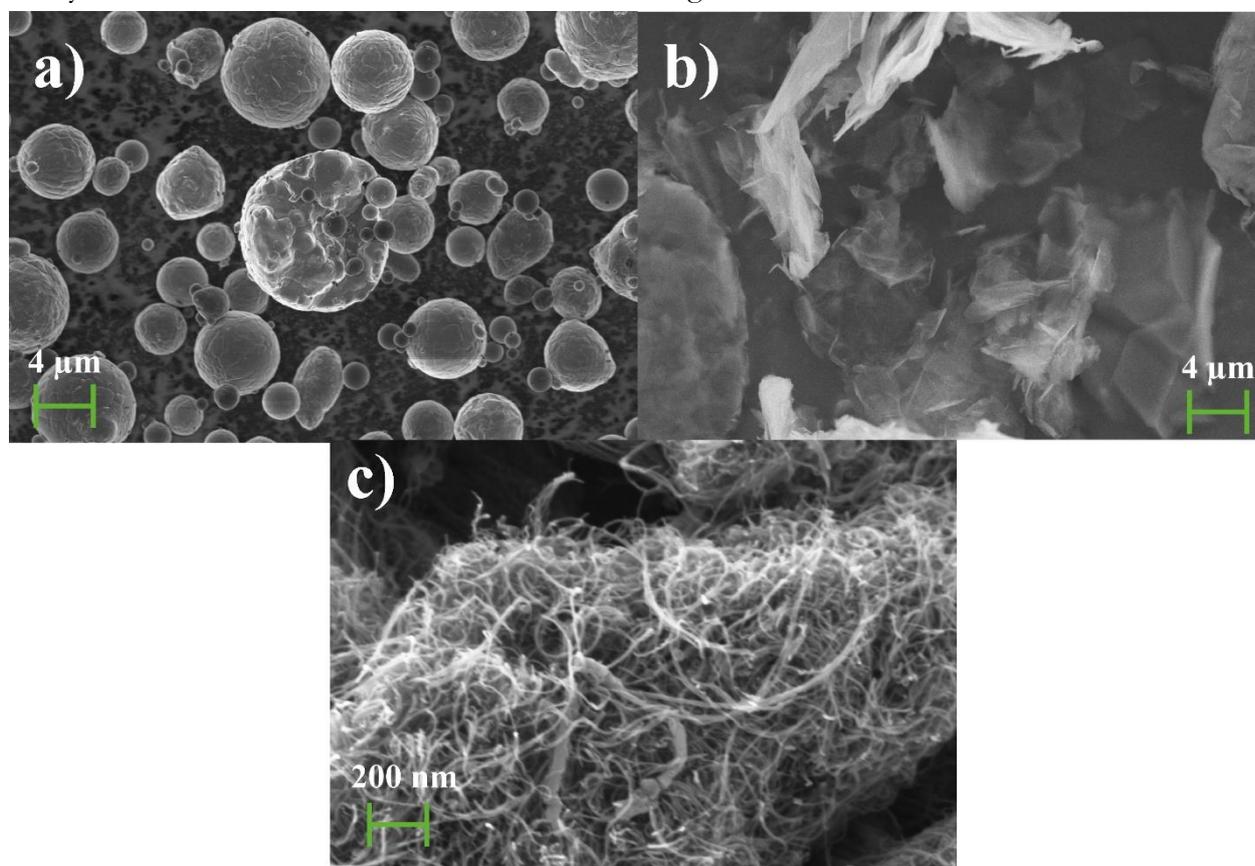
Figure 1. Matrix and reinforcement powders a) Al6061 b) GNP c) MWCNT

Table 1. Processing conditions for composites

	wt% GNP	wt% MWCNT	Sintering temp. (°C)	Sintering duration (min)	Processing pressure (MPa)
Level 1	0,5	0,5	450	15	50
Level 2	1,5	1,5	550	45	150

Densities of the produced composites were determined according to the Archimedes principle. Equations used in calculating density and porosity values are given in Equation 1, Equation 2, and Equation 3.

$$\rho_t = (\rho_m \times w\%) + (\rho_r \times w\%) \tag{1}$$

In Equation 1; While the theoretical density of the composite is expressed as ρ_t, the density of the matrix is expressed as ρ_m, the density of the reinforcement is represented by ρ_r and the percent by weight is represented by w%.

$$\rho_{ex} = \frac{m_a}{m_a - m_w} x1 \tag{2}$$

The experimental density values (ρ_{ex}) of the produced composites were determined by using Equation 2. The dry weight of the composite measured in air is defined as m_a and its suspended weight in water is defined as m_w. The relative density values, which give information about the density of the composites and the porosity, were determined by Equation 3.

$$\rho_{rel} = \frac{\rho_{den}}{\rho_{teo}} x100 \tag{3}$$

Compression tests of the composites were carried out in Zwick/Roell brand compression tester according to the ASTM E9-09 standard. The processing speed was determined as 0.5 mm/min. During the test, the compression strength and % elongation values were automatically graphed.

Results and discussion

The densities and porosity results of the produced composites are shown in Figure 2. Relative density values of hybrid composites consolidated under production parameters were determined to vary between 89-93 %. It was determined that the maximum relative density value was obtained from sample S2 with 93 % (wt% GNP: 0.5-wt% MWCNT:0.5-Sintering temp.: 450 °C- Sintering duration: 45 min-Processing pressure: 150 MPa) The porosity value calculated for the S2 sample is 7 %. It was determined that the minimum relative density value was obtained from sample S7 with 89 % (wt% GNP: 1,5-wt% MWCNT:1,5-Sintering temp.: 450 °C- Sintering duration: 15 min-Processing pressure: 150 MPa). In addition to this situation, the maximum porosity value of 11 % was obtained from sample number S7. While high-density values were obtained at low nano reinforcement ratios, lower densities at high nano reinforcement ratios were attributed to the agglomeration formation seen at high reinforcement ratios. In addition, it is thought that the improvement of the matrix reinforcement interface in high-density composites increases the density.
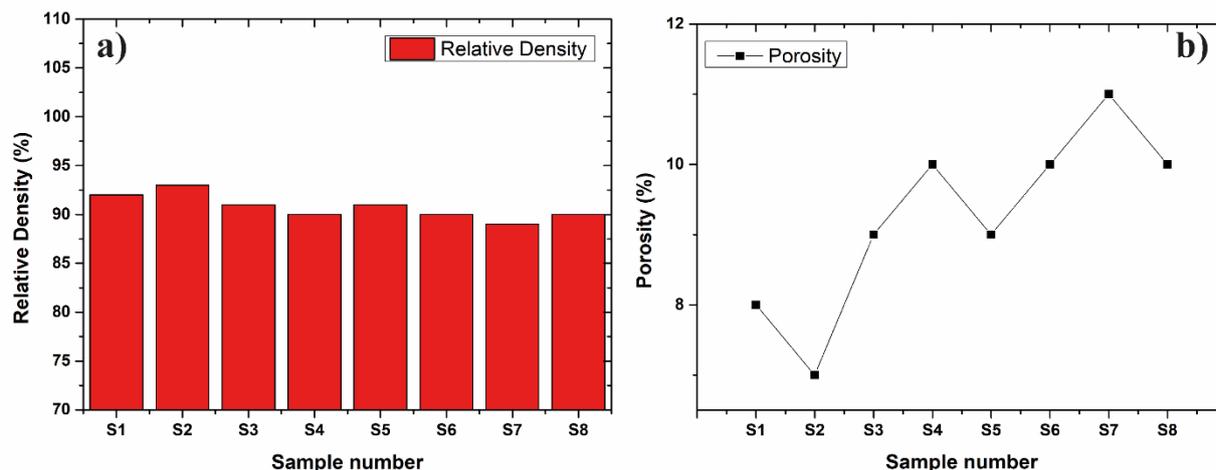
Figure 2. Relative density and porosity values of composites a) Relative density b) Porosity

Table 2 shows the compressive strength of Al6061/GNP/MWCNT composites depending on the production parameters. It was determined that the compressive strength changes of hybrid composites ranged between 69,595 MPa and 321,597 MPa. This wide-scale variation showed that the production parameters were very effective on the compressive strength. In the study, the maximum compressive strength was obtained from the sample number S2 as 321,597 MPa. A 286 % improvement was reported with hybridization compared to the unfortified Al6061 reference sample (83 MPa).

Table 2. Compressive strength of composites

Sample number	wt% GNP	wt% MWCNT	Sintering temp. (°C)	Sintering duration (min)	Processing pressure (MPa)	Compressive strength (MPa)
S1	0,5	0,5	450	15	50	308,592
S2	0,5	0,5	450	45	150	321,597
S3	0,5	1,5	550	15	50	202,279
S4	0,5	1,5	550	45	150	210,116
S5	1,5	0,5	550	15	150	112,349
S6	1,5	0,5	550	45	50	108,446
S7	1,5	1,5	450	15	150	92,395
S8	1,5	1,5	450	45	50	69,595

In addition to this situation, it was determined that the compressive strength decreased sharply in the 1.5 GNP and MWCNT reinforcements added to the matrix structure. This situation is based on the fact that nano reinforcements with high Van der Waals bond strengths show agglomeration due to their affinity with each other, and this agglomeration accelerates the formation and propagation of micro-voids in the composite structure.

The experimental results obtained from the compression test were used to determine the quality of the design, using the S/N ratios used in the Taguchi approach. The larger the better attitude was targeted. The effects of production parameters on compressive strength were found by interpreting the delta values given in Table 3. High delta values indicate that the parameter has a high effect on the result. In this study, the order of the parameters affecting the compressive strength is as follows; wt% GNP, wt% MWCNT, sintering temperature, processing pressure, and sintering duration. it is known that the consolidation process of the powders is done by hot

pressing, it has been reported that temperature and pressure are expected to be effective parameters since the sintering process is diffusion-based. It was also reported that as a result of the determination of the optimum production parameters thanks to the Taguchi analysis, situations that may negatively affect the mechanical properties such as grain growth seen in the sintering process at high temperatures are prevented.

Table 3. Response table for means values

Level	wt% GNP	wt% MWCNT	Sintering temp. (°C)	Sintering duration (min)	Processing pressure (MPa)
1	260,65	212,75	198,04	178,9	172,23
2	95,7	143,6	158,3	177,44	184,11
Delta	164,95	69,15	39,75	1,47	11,89
Rank	1	2	3	5	4
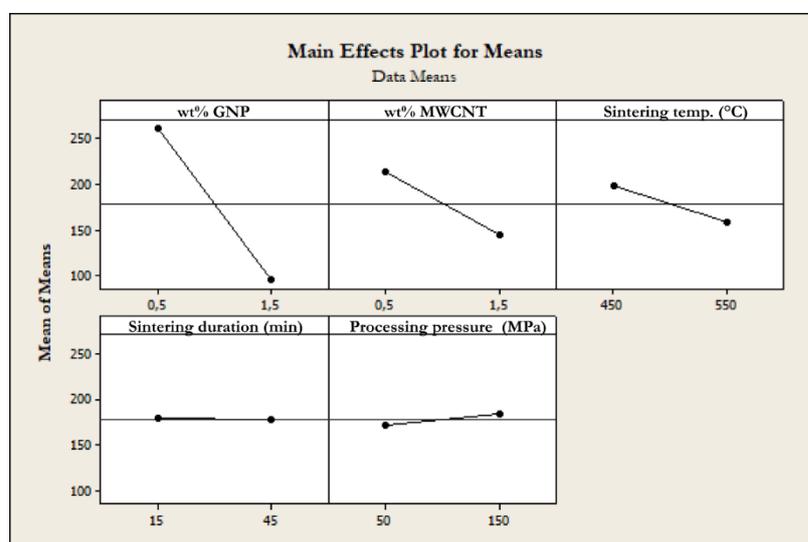
Figure 3. Main effects plot for means values

Figure 3 proved that under optimum fabrication parameters for maximizing compressive strength, favorable conditions for compressive strength of Al6061/GNP/MWCNT hybrid composites; 0.5 wt% GNP, 0.5 wt% MWCNT, 450 °C sintering temperature, 15 min sintering duration, 150 MPa processing pressure.

Conclusions

Al6061/GNP/MWCNT hybrid composites were successfully produced under the specified production parameters.

The maximum relative density value obtained from Al6061/GNP/MWCNT hybrid composites was 93%, and this value was obtained from composite number S2.

Low porosity values were determined at low nano reinforcement ratios in hybrid composites.

Compared to the non-reinforced Al6061 material, a 3.86-fold improvement in compressive strength was achieved in the hybrid composite obtained as a result of hybridization.

After analyzing the production parameters by Taguchi method, optimum production parameters were found as 0.5 wt% GNP, 0.5 wt% MWCNT, 450 °C sintering temperature, 15 min sintering duration, and 150 MPa processing pressure.

References

Mondal, S. (2021). Aluminum or Its Alloy Matrix Hybrid Nanocomposites. *Metals and Materials International*, 27(7), 2188–2204. Retrieved from https://doi.org/10.1007/s12540-020-00750-5

Nieto, A., Bisht, A., Lahiri, D., Zhang, C., & Agarwal, A. (2017). Graphene reinforced metal and ceramic matrix composites: a review. *International Materials Reviews*, 62(5), 241–302. Retrieved from https://doi.org/10.1080/09506608.2016.1219481

Soni, S. K., Thomas, B., & Kar, V. R. (2020). A Comprehensive Review on CNTs and CNT-Reinforced Composites: Syntheses, Characteristics and Applications. *Materials Today Communications*, 25(June), 101546. Retrieved from https://doi.org/10.1016/j.mtcomm.2020.101546

Subbaiah, V., & Palampalle, B. (2019). Microstructural Analysis and Mechanical Properties of Pure Al – GNPs Composites by Stir Casting Method. *Journal of The Institution of Engineers (India): Series C*, 100(3), 493–500. Retrieved from https://doi.org/10.1007/s40032-018-0491-1

Fan, G., Jiang, Y., Tan, Z., Guo, Q., Xiong, D. bang, Su, Y., … Zhang, D. (2018). Enhanced interfacial bonding and mechanical properties in CNT/Al composites fabricated by flake powder metallurgy. *Carbon*, 130, 333–339. Retrieved from https://doi.org/10.1016/j.carbon.2018.01.037

Fibonacci Sequences in Finite Groups

ENGİN ÖZKAN[1]

1. INTRODUCTION

The first application of Fibonacci sequences in groups, in cyclic groups, begins with Wall's article published in 1960. [25]

In the mid-eighties, Then Wilcox expanded Wall's work to abelian groups. [26] Campbell et al. applied this theory to some finite simple groups. [5] Aydın et al. showed that the lengths of ordinary 2-step Fibonacci recurrences in finite nilpotent groups of nilpotency class 4 and a prime exponent are equal to the lengths of ordinary 2-step Fibonacci sequences. [1] The theory has been generalized in [16] to the ordinary 3-step Fibonacci sequences. Özkan proved that the length of the fundamental period of the 2-step general recurrence constructed by two generating elements is equal to the period of the 2-step general Fibonacci sequence [17]. In [20], the theory expanded to the *3*-step general Fibonacci recurrence.

In this paper, I give the applications of Fibonacci numbers in finite groups.

2. DEFINITIONS

Definition 2.1: (2-step Fibonacci sequence)

Let $s = (s_i)$ show the 2-step Fibonacci sequence in *GF(p)* defined by $s_{i+2} = s_i + s_{i+1}$ and the initial data $s_0 = 0$ and $s_1 = 1$.

Definition 2.2: (3-step Fibonacci sequence)

Let $s = (s_i)$ show the 3-step Fibonacci sequence in *GF(p)* defined by the recurrence $s_{i+3} = s_i + s_{i+1} + s_{i+2}$ with $s_0 = 0, s_1 = 0$ and $s_2 = 1$.

Definition 2.3: (Simply Periodic Sequence)

A sequence is simply periodic with a period k if the first element in the sequence forms a repeating subsequence.

[1] Department of Mathematics, Faculty of Arts And Sciences, Erzincan Binali Yıldırım University, Erzincan- Turkiye

Let's use *k(p)* or *k* to show the fundamental period that is the shortest period of that sequence taken modula a distinguished prime *p*.

We sometimes call it Wall's number.

Example 1: $x_1, x_2, x_3, x_4, x_5, x_1, x_2, x_3, x_4, x_5,..$ is simply periodic with period 5.

Example 2: 0,1,1,2,3,5,8,13,21,…

This sequence is a 2-step Fibonacci sequence or known Fibonacci sequence.

If we take modulo a prime 3, we have

0,1,1,2,0,2,2,1,0,1,….

So, we obtain *k(3)=8*.

Definition 2.4: (General 2-step Fibonacci Sequence)

Let (s_i) show the 2-step general recurrence defined by $s_i = ls_{i-1} + ms_{i-2}$ for som $l, m \in \mathbb{N}$. If p does not divide n then we have the 2-step general Fibonacci sequence as $(0, 1, l, l^2 + m, l(l^2 + m) + m, \ldots)$.

If p divides m then the sequence would be ultimately periodic, but would never return to the 0,1.

Example 3: For $p = 2, l = 3, m = 4$, we have

0,1,1,1,1,1,…

If p were not permitted to divide m then this sequence or loop must be periodic. Obviously, *k* depends on *p*.

Example 4: For $p = 2, l = 3, m = 5$, we have

0,1,0,1,0,1,….So, *k(2)=2*.

Definition 2.5: (General 3-step Fibonacci Sequence)

Let (s_i) show the 3-step general recurrence defined by $s_i = ls_{i-1} + ms_{i-2} + ns_{i-3}$ for some $l, m, n \in \mathbb{N}$. If p does not divide n then we have the 3-step general Fibonacci sequence as $(0, 0, 1, l, l^2 + m, l(l^2 + m) + lm + n, \ldots)$. If p divides n then the sequence would be ultimately periodic, but would never return to the 0,0,1.

3. 2 and 3-Step Fibonacci Series Modulo m

Theorem 3: Let f_n be a 2-step Fibonacci sequence. Then $f_n(\mathrm{mod}\,m)$ forms a simply periodic series. That is, the series is periodic and repeats by returning to its starting values.[25]

Theorem 2(D. D. Wall [25]): In $\mathbb{Z}_m,$ we have

1. If p is a prime and $p = 10x \pm 1$ then $k\,|\,(p-1)$.

2. If p is a prime and $p = 10x \pm 3$ then $k\,|\,(2p+2)$.

3. If p is a prime and $p = 10x \pm 3$ then $h(p^e) = k(p^e)$.

Corollary (D. D. Wall [25]): If $p = 10x \pm 3$ then $k \equiv 0(\mathrm{mod}\,4)$.

Theorem 3: Let f_n be a 3-step Fibonacci sequence. Then $f_n(\mathrm{mod}\,m)$ forms a simply periodic series. That is, the series is periodic and repeats by returning to its starting values. [19]

Conjecture 1: If p is a prime and $k < p$ then $k\,|\,(p-1)$.[19]

Conjecture 2: If p is a prime and $k \equiv 0(\mathrm{mod}\,2)$ then $(p \pm 1)\,|\,k$.[19]

Conjecture 3: If p is a prime and $k \equiv 1(\mathrm{mod}\,2)$ then $(p \pm 1)\,|\,(k-1)$ or $p\,|\,(k-1)$.[19]

We have Wall's number for all primes less than 5.10^5. But, we give some prime numbers in Table 1 for which those conjectures are not satisfied.

p	k
83	287
101	680
571	40755
593	3256
613	46971
1531	58599
1913	304964

Table 1.

In Table 2, we give some of the values that provide the conjectures.

p	k	Results
5	31	$p \mid (k-1)$
13	168	$(p-1) \mid k$
23	553	$p \mid (k-1)$
389	151711	$p \mid (k-1)$
557	103416	$(p-1) \mid k$
839	704761	$p \mid (k-1)$
1447	2093808	$(p-1) \mid k$
3347	11205760	$p \mid (k-1)$
4831	11669280	$(p-1) \mid k$
17207	17206	$(p-1) \mid k$
18047	1696324	$(p-1) \mid k$

Table 2.

Conjecture 4: Let's $p > 2$ a prime number and k be the Wall number of n-step Fibonacci sequence such that n is an even number , then k is an even number. [19]

Conjecture 5: Let k be Wall number of n-step Fibonacci sequence such that $n = 2t$ and $t > 1$. Then $(p \pm 1) \mid k$, except for some primes. [19]

We have seen that the last two conjectures are satisfied for $p < 5.10^5$. Also, we have many data for various values of p. In Table 3, we give some values that provide Conjunction 5.

p	k	Results
3	26	$(p-1)\,|\,k$
67	100254	$(p-1)\,|\,k$
151	533256	$(p+1)\,|\,k$
211	9393930	$(p-1)\,|\,k$
433	92880	$(p-1)\,|\,k$
907	822648	$(p-1)\,|\,k$
1277	1630728	$(p-1)\,|\,k$
2593	1680912	$(p+1)\,|\,k$
3733	23225448	$(p+1)\,|\,k$
4253	6029336	$(p-1)\,|\,k$

Table 3.

4. FIBONACCI SEQUENCE IN FINITE GROUP

Let G be finite group. We define a family of recurrences, parameterized by natural numbers n, via equations

$$x_i = x_{i-1}x_{i-2}...x_{i-n} \qquad\qquad (R_n)$$

We fix $n > 1$. We may 'start' the recurrence with any inital data $g_0, g_1,..., g_{n-1}$ and then the recurrence will define a periodic bi-infinite sequence (g_i) indexed by the integers. We use the loop to describe a bi-infinite sequence satisfying the recurrence.

4.1. General Recurrences in Modular Groups

2-step Fibonacci sequence in group is defined by $f_n = f_{n-1} + f_{n-2}$, $n \geq 2$ which is constructed by two generating elements of the group. Since we work on modulo p, this sequence would ultimately be periodic and let's $k(G)$ denotes the shortest period of this sequence.

The set of all Möbius transformations of the form

$$\tau' = \frac{a\tau + b}{c\tau + d}$$

where a, b, c, d are integers with *ad-bc*=1, is called the modular group under the composition of transformations.

This group can be represented by 2x2 integer matrices as $\begin{pmatrix} a & b \\ c & d \end{pmatrix}$ with *detA*=1 such that each matrix with its negative, since A and $-A$ represent the same transformation.

THEOREM 4.1.1: The modular group Γ is generated by two matrices

$$T = \begin{pmatrix} 1 & 1 \\ 0 & 1 \end{pmatrix} \text{ and } S = \begin{pmatrix} 0 & -1 \\ 1 & 0 \end{pmatrix}.$$

That is every A in Γ can be expressed in the form $A = T^{n_1} S T^{n_2} \ldots S T^{n_k}$ where the n_i are integers. This representation is not unique [10].

We now express the first theorem concerning the Fibonacci sequences in modular group.

THEOREM 4.1.2: Let Γ be a modular group generated by $S = \begin{pmatrix} 0 & -1 \\ 1 & 0 \end{pmatrix}$ and $T = \begin{pmatrix} 1 & 1 \\ 0 & 1 \end{pmatrix}$. Then $k(\Gamma) \neq k(p)$.[10]

PROOF: The group Γ is a finitely generated infinite group. Take the generators $S, T \in \Gamma$. We shall construct the 2-step Fibonacci sequence starting with this generating pair, where the product is to be understood as matrix multiplication. It can also be considered the composition of functions when the matrices are thought as functions. Thus, we have the sequence

$$S, T, ST, TST, ST^2ST,\ldots \qquad (1)$$

We first of all, demonstrate some data about Wall number of ordinary -step Fibonacci sequence for various primes p. This is,

p	*k(p)*
2	3
3	8

Figure 1

There is a direct connection between p and k(p) in the case of cyclic groups. k(p) stands for k(G). Wall distinguishes this connection in [1] and append a list of p and k(p) where 5<p<2000. We have used a computer code to calculate the next term of (1). We have more data but for the hospitality of the journal a small part of it is given. This is,

p	**k(p)+1 th element of (1)**	**expected value**
2	$\begin{pmatrix} 1 & 0 \\ 1 & 1 \end{pmatrix}$	$\begin{pmatrix} 0 & -1 \\ 1 & 0 \end{pmatrix}$
3	$\begin{pmatrix} 0 & 1 \\ -1 & 0 \end{pmatrix}$	$\begin{pmatrix} 0 & -1 \\ 1 & 0 \end{pmatrix}$

Figure 2

It tells us that the fundamental period of the sequence made by two generating elements of modular group is different from that of cyclic groups.

The 2-step general Fibonacci sequence constructed by any two generating pair is defined by

$$S, T, S^m T^l, T^m (S^m T^l)^l, (S^m T^l)^m (T^m (S^m T^l)^l)^l, \ldots \qquad (2)$$

where $l, m \in Z$. We now prove the second original theorem of this document.

THEOREM 4.1.3: Let Γ be a modular group generated by $T = \begin{pmatrix} 1 & 1 \\ 0 & 1 \end{pmatrix}$ and $S = \begin{pmatrix} 0 & -1 \\ 1 & 0 \end{pmatrix}$. The series constructed by this generating pair in a sense of (2) is periodic and ultimately returns to its starting values.[19]

4.2. 3-step General Fibonacci Recurrence in Nilpotent Groups of Class 2

Let G be a 3-generator relatively free group in the variety of nilpotent groups of class 2 and exponent p. Thus, G is free on a set of generators $\{x, y, z\}$.
$$G = < x, y, z, t, u, v : (y, x) = t, (z, x) = u, (z, y) = v >$$

The group G has order p^6. The subgroup $< t, u, v >$ has order p^3 and is both the center and derived group of G. Every element of G has a unique representation as
$$x^a y^b z^c t^d u^e v^f$$

where the exponents are elements of $GF(p)$. We need an explicit formula for the element $\left(x^a y^b z^c t^d u^e v^f \right)^n$ which is clearly

$$\left(x^a y^b z^c t^d u^e v^f \right)^n = \left(x^{na} y^{nb} z^{nc} t^{nd+\binom{n}{2}ab} u^{ne+\binom{n}{2}ac} v^{nf+\binom{n}{2}bc} \right) \qquad (1)$$

This could be proved by induction on n using the group relations. We assume that $\left(x^{a_0} y^{b_0} z^{c_0} t^{d_0} u^{e_0} v^{f_0}\right), \left(x^{a_1} y^{b_1} z^{c_1} t^{d_1} u^{e_1} v^{f_1}\right), \left(x^{a_2} y^{b_2} z^{c_2} t^{d_2} u^{e_2} v^{f_2}\right)$ be three elements of G. For our purpose, we need a formula to describe how to be the next term of the sequence. Therefore using by (1) and the group relations we can write $(x^{a_0} y^{b_0} z^{c_0} t^{d_0} u^{e_0} v^{f_0})^n . (x^{a_1} y^{b_1} z^{c_1} t^{d_1} u^{e_1} v^{f_1})^m . (x^{a_2} y^{b_2} z^{c_2} t^{d_2} u^{e_2} v^{f_2})^l = x^{a_3} y^{b_3} z^{c_3} t^{d_3} u^{e_3} v^{f_3}$ where,

$$a_3 = na_0 + ma_1 + la_2,$$

$$b_3 = nb_0 + mb_1 + lb_2,$$

$$c_3 = nc_0 + mc_1 + lc_2,$$

$$d_3 = nd_0 + md_1 + ld_2 + \binom{n}{2}a_0 b_o + \binom{m}{2}a_1 b_1 + \binom{l}{2}a_2 b_2 + mna_1 b_0 + la_2(nb_0 + mb_1),$$

$$e_3 = ne_0 + me_1 + le_2 + \binom{n}{2}a_0 c_o + \binom{m}{2}a_1 c_1 + \binom{l}{2}a_2 c_2 + mna_1 c_0 + la_2(nc_0 + mc_1)$$

and

$$f_3 = nf_0 + mf_1 + lf_2 + \binom{n}{2}b_0 c_o + \binom{m}{2}b_1 c_1 + \binom{l}{2}b_2 c_2 + mnb_1 c_0 + lb_2(nc_0 + mc_1).$$

A straightforward induction yields that for $\alpha \geq 0$

$$d_k = \binom{n}{2}\sum_{i=0}^{k-1} s_{k-i-1} u_i t_i + \binom{m}{2}\sum_{i=0}^{k-1} s_{k-i-1} u_{i+1} t_{i+1} + \binom{l}{2}\sum_{i=0}^{k-1} s_{k-i-1} u_{i+2} t_{i+2} + mn\sum_{i=0}^{k-1} s_{k-i-1} u_{i+1} t_i$$
$$+ \ln \sum_{i=0}^{k-1} s_{k-i-1} u_{i+2} t_i + lm\sum_{i=0}^{k-1} s_{k-i-1} u_{i+2} t_{i+1},$$

$$e_k = \binom{n}{2}\sum_{i=0}^{k-1} s_{k-i-1} s_i u_i + \binom{m}{2}\sum_{i=0}^{k-1} s_{k-i-1} s_{i+1} u_{i+1} + \binom{l}{2}\sum_{i=0}^{k-1} s_{k-i-1} s_{i+2} u_{i+2} + mn\sum_{i=0}^{k-1} s_{k-i-1} s_i u_{i+1}$$
$$+ \ln \sum_{i=0}^{k-1} s_{k-i-1} s_i u_{i+2} + lm\sum_{i=0}^{k-1} s_{k-i-1} s_{i+1} u_{i+2},$$

and

$$f_k = \binom{n}{2}\sum_{i=0}^{k-1} s_{k-i-1} s_i t_i + \binom{m}{2}\sum_{i=0}^{k-1} s_{k-i-1} s_{i+1} t_{i+1} + \binom{l}{2}\sum_{i=0}^{k-1} s_{k-i-1} s_{i+2} t_{i+2} + mn\sum_{i=0}^{k-1} s_{k-i-1} s_i t_{i+1}$$
$$+ \ln \sum_{i=0}^{k-1} s_{k-i-1} s_i t_{i+2} + lm\sum_{i=0}^{k-1} s_{k-i-1} s_{i+1} t_{i+2}.$$

THEOREM 4.2.3: Let G be a non-trivial finite p-group of exponent p and nilpotency class 2. Then $k(G) = k(p)$ [12].

4.3. 3-step General Fibonacci Recurrence in Nilpotent Groups of Class 4

Let G be a nilpotent group with nilpotency class 4 and exponent p for a prime number $p>3$. G has two generators x and y. A presentation of G is

$$G =< x, y, z, t, u : (y, x) = z, (z, x) = t, (t, x) = u >$$

where pairs of generators with unspecified commutator are implicitly deemed to commute. The subgroup $<y,z,t,u>$ is abelian and u is in the centre of G. Every element of G has a unique representation as

$$x^a y^b z^c t^d u^e$$

where the exponents are elements of $GF(p)$. Having distinguished this way of writing elements we can even think of groups elements as vectors of dimension 5 over $GF(p)$, i.e. as (a,b,c,d,e). So, triple multiplication is determined by the following rules;

$$(x^{a_0} y^{b_0} z^{c_0} t^{d_0} u^{e_0})(x^{a_1} y^{b_1} z^{c_1} t^{d_1} u^{e_1})(x^{a_2} y^{b_2} z^{c_2} t^{d_2} u^{e_2}) = (x^{a_3} y^{b_3} z^{c_3} t^{d_3} u^{e_3})$$

$$= (x^{a_0} y^{b_0} z^{c_0} x^{a_1} y^{b_1} z^{c_1} t^{d_0+d_1} u^{e_0+e_1+d_0 a_1})(x^{a_2} y^{b_2} z^{c_2} t^{d_2} u^{e_2})$$

$$= (x^{a_0} y^{b_0} x^{a_1} y^{b_1} z^{c_0+c_1} t^{d_0+d_1+c_0 a_1} u^{e_0+e_1+d_0 a_1 + c_0 \binom{a_1}{2}})(x^{a_2} y^{b_2} z^{c_2} t^{d_2} u^{e_2})$$

$$= (x^{a_0+a_1} y^{b_0+b_1} z^{c_0+c_1+b_0 a_1} t^{d_0+d_1+c_0 a_1 + b_0\binom{a_1}{2}} u^{e_0+e_1+d_0 a_1 + c_0\binom{a_1}{2}+b_0\binom{a_1}{3}})(x^{a_2} y^{b_2} z^{c_2} t^{d_2} u^{e_2})$$

$$= x^{a_0+a_1+a_2} y^{b_0+b_1+b_2} z^{c_0+c_1+c_2+b_0 a_1 + (b_0+b_1)a_2} t^{d_0+d_1+d_2+c_0 a_1 + b_0\binom{a_1}{2} + a_2(c_0+c_1+b_0 a_1) + (b_0+b_1)\binom{a_2}{2}}$$
$$u^{e_0+e_1+e_3+d_0 a_1 + c_0\binom{a_1}{2}+b_0\binom{a_1}{3} + a_2(d_0+d_1+c_0 a_1 + b_0\binom{a_1}{2}) + (c_0+c_1+b_0 a_1)\binom{a_2}{2}+(b_0+b_1)\binom{a_2}{3}}.$$

That is, $(a_0,b_0,c_0,d_0,e_0)(a_1,b_1,c_1,d_1,e_3)(a_2,b_2,c_2,d_2,e_3) = (a_3,b_3,c_3,d_3,e_3)$

where

$$a_3 = a_0 + a_1 + a_2$$
$$b_3 = b_0 + b_1 + b_2$$
$$c_3 = c_0 + c_1 + c_2 + b_0 a_1 + (b_0 + b_1)a_2$$
$$d_3 = d_0 + d_1 + d_2 + c_0 a_1 + b_0 \binom{a_1}{2} + a_2(c_0 + c_1 + b_0 a_1) + \binom{a_2}{2}(b_0 + b_1)$$

and finally

$$e_3 = e_0 + e_1 + e_2 + d_0 a_1 + c_0 \binom{a_1}{2} + b_0 \binom{a_1}{3} + a_2(d_0 + d_1 + c_0 a_1 + b_0 \binom{a_1}{2})$$

$$+ \binom{a_2}{2}(c_0 + c_1 + b_0 a_1) + \binom{a_2}{3}(b_0 + b_1)$$

Theorem 4.3.1. [18,20] Let $p > 3$ be a prime number, then if G is a non-trivial finite p-group of exponent p and nilpotency class 4 then $k(G) = k$, except for finitely bad primes.

Of course, if G is the trivial group then $k(G) = 1$.

Theorem 4.3.2. [18,20] Let $p > 3$ be a prime number, then if G is a non-trivial finite p-group of exponent p and nilpotency class 4 then $k(G) = kp$ for all primes.

4.4. 3-step Fibonacci Recurrence in Nilpotent Groups of Class n

Now, we have constituted 3-step Fibonacci sequences by the three generating elements of a group of exponent p (p is prime) and nilpotency class n and we have given a formula for α. term of the sequence.

Theorem 4.4.1. [16,17]: If G is a group of exponent p , nilpotency class n and with the presentation

$$G =< x_1, x_2,...,x_n, x_{n+1} :[x_2,x_1] = x_3,[x_3,x_1] = x_4,...,[x_n,x_1] = x_{n+1} >$$

then entries of the 3-step Fibonacci sequences formed by three elements of G have the following form.

$$a_\alpha = \sum_{i=0}^{\alpha-1} t_i = \sum_{i=0}^{\alpha-1}(s_{i+1} - s_i)$$

$$b_\alpha = \sum_{i=0}^{\alpha-1} s_i$$

$$c_\alpha = \sum_{i=0}^{\alpha-1} s_{\alpha-i-1}(s_i t_{i+1} + t_{i+2}(s_i + s_{i+1}))$$

$$d_\alpha = \sum_{i=0}^{\alpha-1} s_{\alpha-i-1} t_{i+1} c_i + \sum_{i=0}^{\alpha-1} s_{\alpha-i-1} s_i \binom{t_{i+1}}{2} + \sum_{i=0}^{\alpha-1} s_{\alpha-i-1} t_{i+2}(c_i + c_{i+1} + s_i t_{i+1})$$

$$+ \sum_{i=0}^{\alpha-1} s_{\alpha-i-1} \binom{t_{i+2}}{2}(s_i + s_{i+1})$$

$$y_\alpha = \sum_{i=0}^{\alpha-1} s_{\alpha-i-1} v_i \begin{pmatrix} t_{i+1} \\ 1 \end{pmatrix} + \sum_{i=0}^{\alpha-1} s_{\alpha-i-1} u_i \begin{pmatrix} t_{i+1} \\ 2 \end{pmatrix} + \ldots + \sum_{i=0}^{\alpha-1} s_{\alpha-i-1} c_i \begin{pmatrix} t_{i+1} \\ n-3 \end{pmatrix} + \sum_{i=0}^{\alpha-1} s_{\alpha-i-1} s_i \begin{pmatrix} t_{i+1} \\ n-2 \end{pmatrix}$$

$$+ \sum_{i=0}^{\alpha-1} s_{\alpha-i-1} \begin{pmatrix} t_{i+2} \\ 1 \end{pmatrix} \left[v_i + v_{i+1} + u_i \begin{pmatrix} t_{i+1} \\ 1 \end{pmatrix} + r_i \begin{pmatrix} t_{i+1} \\ 2 \end{pmatrix} + \ldots + c_i \begin{pmatrix} t_{i+1} \\ n-4 \end{pmatrix} + s_i \begin{pmatrix} t_{i+1} \\ n-3 \end{pmatrix} \right]$$

$$. \quad + \sum_{i=0}^{\alpha-1} s_{\alpha-i-1} \begin{pmatrix} t_{i+2} \\ 2 \end{pmatrix} \left[u_i + u_{i+1} + r_i \begin{pmatrix} t_{i+1} \\ 1 \end{pmatrix} + \ldots + c_i \begin{pmatrix} t_{i+1} \\ n-5 \end{pmatrix} + s_i \begin{pmatrix} t_{i+1} \\ n-4 \end{pmatrix} \right] + \ldots$$

$$+ \sum_{i=0}^{\alpha-1} s_{\alpha-i-1} \begin{pmatrix} t_{i+2} \\ n-4 \end{pmatrix} \left[d_i + d_{i+1} + c_i \begin{pmatrix} t_{i+1} \\ 1 \end{pmatrix} + s_i \begin{pmatrix} t_{i+1} \\ 2 \end{pmatrix} \right] + \sum_{i=0}^{\alpha-1} s_{\alpha-i-1} \begin{pmatrix} t_{i+2} \\ n-3 \end{pmatrix} \left[c_i + c_{i+1} + s_i \begin{pmatrix} t_{i+1} \\ 1 \end{pmatrix} \right]$$

$$+ \sum_{i=0}^{\alpha-1} s_{\alpha-i-1} \begin{pmatrix} t_{i+2} \\ n-2 \end{pmatrix} (s_i + s_{i+1})$$

and

$$z_\alpha = \sum_{i=0}^{\alpha-1} s_{\alpha-i-1} y_i \begin{pmatrix} t_{i+1} \\ 1 \end{pmatrix} + \sum_{i=0}^{\alpha-1} s_{\alpha-i-1} v_i \begin{pmatrix} t_{i+1} \\ 2 \end{pmatrix} + \ldots + \sum_{i=0}^{\alpha-1} s_{\alpha-i-1} c_i \begin{pmatrix} t_{i+1} \\ n-2 \end{pmatrix} + \sum_{i=0}^{\alpha-1} s_{\alpha-i-1} s_i \begin{pmatrix} t_{i+1} \\ n-1 \end{pmatrix}$$

$$+ \sum_{i=0}^{\alpha-1} s_{\alpha-i-1} \begin{pmatrix} t_{i+2} \\ 1 \end{pmatrix} \left[y_i + y_{i+1} + v_i \begin{pmatrix} t_{i+1} \\ 1 \end{pmatrix} + u_i \begin{pmatrix} t_{i+1} \\ 2 \end{pmatrix} + \ldots + c_i \begin{pmatrix} t_{i+1} \\ n-3 \end{pmatrix} + s_i \begin{pmatrix} t_{i+1} \\ n-2 \end{pmatrix} \right]$$

$$+ \sum_{i=0}^{\alpha-1} s_{\alpha-i-1} \begin{pmatrix} t_{i+2} \\ 2 \end{pmatrix} \left[v_i + v_{i+1} + u_i \begin{pmatrix} t_{i+1} \\ 1 \end{pmatrix} + r_i \begin{pmatrix} t_{i+1} \\ 2 \end{pmatrix} \ldots + c_i \begin{pmatrix} t_{i+1} \\ n-4 \end{pmatrix} + s_i \begin{pmatrix} t_{i+1} \\ n-3 \end{pmatrix} \right] + \ldots$$

$$+ \sum_{i=0}^{\alpha-1} s_{\alpha-i-1} \begin{pmatrix} t_{i+2} \\ n-3 \end{pmatrix} \left[d_i + d_{i+1} + c_i \begin{pmatrix} t_{i+1} \\ 1 \end{pmatrix} + s_i \begin{pmatrix} t_{i+1} \\ 2 \end{pmatrix} \right] + \sum_{i=0}^{\alpha-1} s_{\alpha-i-1} \begin{pmatrix} t_{i+2} \\ n-2 \end{pmatrix} \left[c_i + c_{i+1} + s_i \begin{pmatrix} t_{i+1} \\ 1 \end{pmatrix} \right]$$

$$+ \sum_{i=0}^{\alpha-1} s_{\alpha-i-1} \begin{pmatrix} t_{i+2} \\ n-1 \end{pmatrix} (s_i + s_{i+1})$$

For example, let $n = 4$. The first few terms are as follows

(1,0,0,0,0)

(0,1,0,0,0)

(0,0,1,0,0)

(1,1,1,0,0)

(1,2,3,1,0)

(2,3,6,4,1)

(4,6,17,19,15)

.

REFERENCES

[1] H. Aydın and G. C. Smith, Finite p-Quotient of Some Cyclically Presented Groups. J. London Math. Soc.(2) 49, 83-92, (1994).

[2] H. Aydın and R. Dikici, General Fibonacci sequences in finite groups, The Fibonacci Quarterly 36.3, 216-221(1998).

[3] H. Aydın, R. Dikici and G.C. Smith, Wall and Vinson Revisited. Applications Fibonacci Numbers, Volume 5. Edited by G. E. Bergum et al. Kluwer Academic Publishers, 61-68(1993)

[4] C. M. Campbell and P. P. Campbell, The Fibonacci lenght of certain centro-polyhedral groups, J. Appl. Math. Comput., 2005; 19: 231-240.

[5] C. M. Campbell, H. Doostie and E. F. Robertson, Fibonacci Length of Generating Pairs in Groups. Applications of Fibonacci Numbers, Volume 3.Edited by G. E. Bergum et al. Kluwer Academic Publishers, 27-35(1990).

[6] Ö. Deveci and E. Karaduman, On the basic k-nacci sequences in finite groups, Discrete Dyn. Nat. Soc., 2011; 639476-1-639476-13.

[7] Ö. Deveci and E. Karaduman, The Pell sequences in finite groups, Util. Math., 2015; 96: 263-276.

[8] Ö. Deveci, The Pell-Padovan sequences and Jacobsthal-Padovan sequences in finite groups, Util. Math., 2015; 98: 257-270.

[9] Ö. Deveci and E. Karaduman, The generalized order -k Lucas sequences in finite groups, J. Appl. Math., 2012; DOI: 10.1155/2012/464580.

[10] Dikici, R., Özkan, E., "General Recurrences in Modular Groups", Ege University Journal of The Faculty of Science, 21(2), 1998.

[11] R. Dikici and G.C. Smith, Recurrences in Finite Groups, Turkish J. Math. 19, 321-329(1995).

[12] R. Dikici and E. Özkan, An Application of Fibonacci Sequences in Groups. Applied Mathematics and Computation, **136(2-3)**, 323-331, (2003).

[13] R. Dikici, Applications of Computer Algebra to the Study of Recurrence in p- Groups. Ph. D. Thesis, University of Bath (1992).

[14] R. Dikici and G.C. Smith, Fibonacci Sequances in Finite Nilpotent Groups, Turkish J. Math. 21,133-142(1997). [12] H. Doostie, Fibonacci-type Sequences and Classes of Groups, Ph. D. thesis, University of St Andrews (1988).

[15] S. W. Knox., Fibonacci sequences infinite groups, The Fibonacci Quaterly, 1992; 30, 2: 116-120.

[16] E. Özkan, 3-Step Fibonacci Sequences in Nilpotent Groups, Applied Mathematics and Computation, 144, 517-527, (2003).

[17] E. Özkan, Fibonacci sequences in nilpotent groups with class n, Chiang Mai Journal of Science, 31(3), 205-212, 2004.

[18] E. Özkan, On General Fibonacci Sequences in Groups, Turkish Journal of Mathematics" 27(4), 525 – 537, (2003).

[19] E. Özkan, H. Aydın and R. Dikici, 3-step Fibonacci series modulo m, Appl. Math. Comp., 2003; 143: 165-172.

[20] E. Özkan, H. Aydın and R. Dikici, "Applications of Fibonacci Sequences in a Finite Nilpotent Group", Applied Mathematics and Computation, 141(2-3), 565-578, (2003).

[21] L. Somer, The Divisibility Properties of Primary Lucas Recurrences with Respect to Primes, The Fibonacci Quarterly 18.4, 316-334(1980).

[22] S. Taş, E. Karaduman The Padovan Sequences in Finite Groups, Chiang Mai J. Sci, 2014; 41(2): 456-462.

[23]   R. M. Thomas, The Fibonacci Groups Revisited, Proceedings of Groups St. Andrews 1989, Volume 2 LMS Lecture Note Series 160, CUP. Edited by C.M. Campbell and E.F. Robertson,445-454(1991).

[24]   J. Vinson, The Relations of the Period Modulo m to the Rank of Apparition of m in the Fibonacci Sequence. The Fibonacci Quarterly, 1,37-45(1963).

[25]   D. Wall, Fibonacci Series Modulo m. Amer. Math. Monthly, 67, 525-532, (1960).

[26] H. J. Wilcox, Fibonacci Sequences of Period n in Groups. The Fibonacci Quarterly, 24, 356-361, (1986).

Modeling the theoretical speed curve of a wind turbine using a nonlinear autoregressive exogenous model (NARX) neural network

Mahmut Dirik[1]

Introduction

In recent years, the global decline in conventional energy supply, together with the rapidly growing demand for energy, has been of great concern to the public. The use of renewable and ecologically beneficial wind energy is becoming more and more common and accepted. Among the renewable methods of electricity generation, wind energy is one that helps to keep the cost of electricity generation as low as possible. Wind energy is a renewable type of electricity that is regarded to be environmentally friendly. It is conversion technology is more cost-effective than other forms of energy generation. Continuing research-based programs to increase wind turbine performance can be extremely difficult and costly if trustworthy models are not available. Using established models for wind turbines allows for upfront simulation of turbine-generator unit performance changes and gives operators and engineers in the turbine control center the ability to make timely and personalized decisions based on the data collected [1]–[3]. Due to the increasing use of renewable energy sources in power generation, it was necessary to estimate the amount of energy that will be produced. Designing a controller for any system requires accurate dynamic models of the system. It is possible to evaluate the performance of the controller if a model-based control technique is used. Moreover, we can embed the model into the controller [4]. Modeling wind turbines is a difficult task because their operation depends on physical phenomena such as the rotation of the spinning rotor, the aerodynamics of the blades, and the viscosity of the fluid, as well as random sources such as the wind. Typically, sophisticated fluid dynamics, aerodynamic theory, and blade element approaches are used to study them. Numerous models have been presented to simulate the behavior of wind turbines (WT) that account for all of these complicated processes [4]–[8]. Machine learning approaches have gained popularity in recent years for predicting the performance of power generators [9]–[11]. Models for wind turbine control can be built using neural networks. Long-term memory recurrent neural networks (LSTM) and nonlinear autoregressive neural networks with external inputs (NARX) are two architectural variants of recurrent neural networks that are ideal for representing time series and processes, respectively. Focusing on a simple, control-oriented paradigm, we chose the NARX architecture for its lower computational cost and simplicity. Control-oriented neural network models with low complexity can be easily combined with control techniques [12]–[14]. WT Modeling and control have been explored in the literature using a variety of classical and intelligent methods [15]–[17].

In this research, control-oriented neural network models of the performance of a wind turbine simulated with NARX are developed with a modest degree of complexity. We chose NARX neural networks for this application because they have been shown to be well matched to the output signal and have a relatively low computational cost. A variety of wind speeds and tilt amplitude steps are used to generate the output signals for the wind reference. The validity of the technique is demonstrated by both graphical and numerical results.

[1] Sirnak University, Department of Computer Engineering

The following is how the rest of the article is organized: Section 2 provides a description of the material and the procedure. Here we provide detailed information on the evaluation metrics, a nonlinear autoregressive exogenous model (NARX), and the dataset. Section 3 contains a description of the results and specifics. Section 4 concludes with a conclusion.

1. Materials and Procedures

This section explains how the NARX model is used to predict the wind speed of a wind turbine installation. The output of the system is calculated using the training process of the NARX model based on the time series of the neural network. The main purpose of this section is to show the generation as a function of wind speed. The specifics on how to achieve this are given below.

1.1. Dataset

The data utilized [18] are derived from SCADA systems installed in current wind turbines. Most wind turbines have a SCADA system[19], [20] that allows monitoring and collection of data, so there is no need to implement additional hardware/software for this purpose. The number of record variables (columns) used is 4 and the number of samples (rows) is 50531. The variables included here are: The power generated by the turbine at that time (kW), the wind speed (m/s), the theoretical power values of the turbine at that wind speed (kWh) given by the turbine manufacturer, and the wind direction (°). The target variable is the prediction of the wind speed of the model. The instances used to train and test the system are separated into variable proportions of training, testing, and validation subsets. The calculation of data distributions allows us to check the correctness of the given data and to detect anomalies. The histogram of the samples used as input variables is shown in the following graph.
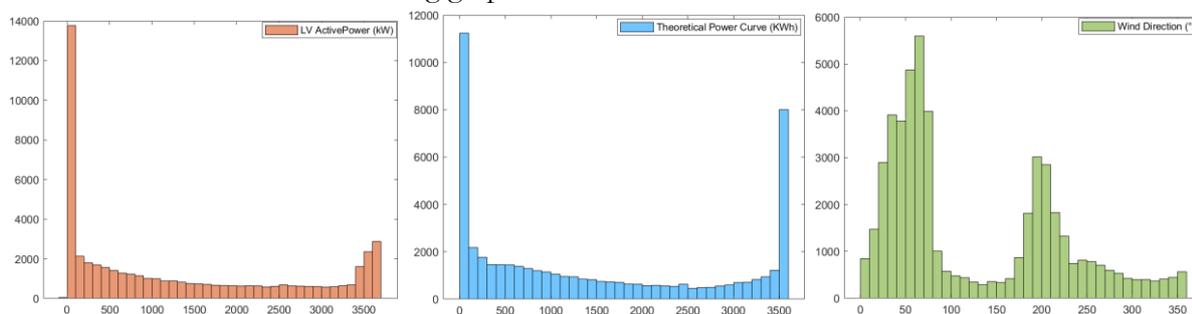

Figure 4. Histogram of the data distribution for the variables used as input.

1.2. Nonlinear Autoregressive Exogenous (NARX)

A subset of dynamic filtering known as prediction is a technique in which future values are predicted based on the values of one or more time series. When applied to nonlinear systems, NARX is a dynamic neural network that can be used for both filtering and prediction. NARX is based on the linear ARX model, also known as recurrent neural networks, which is able to efficiently model time series data sets by using feedback connections at different levels of the network [3], [9], [12], [21]. NARX are referred to as "dynamic network categories" because they have feedback connections that surround the numerous layers of the network [22]–[24]. The main advantages of NARX networks over other ANN approaches are their ability to quickly establish

ideal weights for connections between neurons and input parameters, require less calibration effort, and enable model construction [25], [26]. A NARX network, which is utilized in time series estimation, has the following fundamental equation: Eq (1).

$$y(t) = f\Big((y(t-1), y(t+2), \dots, y(t-n_y), u(t-1), u(t-2), \dots, u(t-n_u)\Big) \tag{1}$$

Here, u(t) and y(t) represent the input and output values at time t, respectively, nu and ny represent the network's input and output layers, and f represents the nonlinear function. As can be seen in Figure 2, the structure of NARX consists of three successive layers.
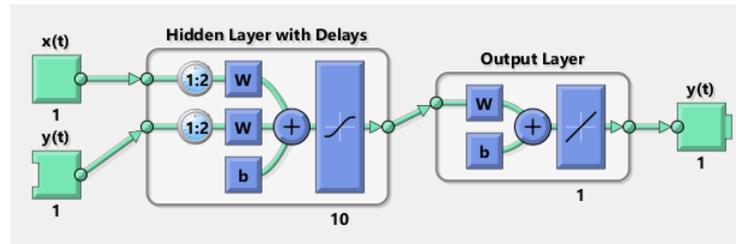

Figure 5. The construction of the NARX model

The open loop (one step) is more efficient compared to the closed loop (multiple steps). A closed-loop configuration (or any other configuration required for the application) can be implemented once the network has been thoroughly trained. The input layer contains the parameters used to train the neural network, the hidden layer contains the computation step performed between the input and output layers, and the output layer contains the predicted value. The proposed model contains three inputs and a single output. In this example, two perceptron layers are used: the first detector layer contains three inputs, the number of neurons in the hidden layer (NHN), and a hyperbolic tangent activation function. The second sensor layer has an NHN input, a single neuron, and a linear activation function. The weight (w) and bias (b) of the NARX model were tuned for the output layer using the "Levenberg-Marquardt [27]," "Bayesian regularization [28]," and "Scaled conjugate gradient [29]" training algorithms. Typically, "Levenberg-Marquardt" consumes more memory but takes less time. "Bayesian regularization" takes longer to complete than other methods, but the results are great when dealing with tough, tiny, or noisy data sets. In line with the adaptive weight reduction (processing) method, training is ended at the end of the session. "Scaled Conjugate Gradient" is less memory intensive. Training is automatically terminated when generalization deteriorates, as evidenced by an increase in the mean square error of the validation samples. The data used were divided in different proportions for training, testing and validation. The most accepted proportion in the literature is 70% for training the network and 30% for testing [25], [30]–[32]. The purpose of this experiment is to investigate the effects of splitting the data into different ratios on the performance of the model with a variable number of neurons as well as the influence of training techniques on the performance of the model.

1.3.Evaluation metrics

In order to evaluate the performance of the model, the obtained results were evaluated using metrics such as the coefficient of determination R^2, which indicates how well the model replicates the observed results and predicts future outcomes, and metrics such as the mean absolute error and the root mean square error, which is the mean magnitude of error for the prediction. The equations for these metrics can be found between (2) and (6). For details, see the corresponding bibliographies.

$R^2 = \left(\dfrac{(\sum_{i=1}^{N}(x_i - \bar{x})(y_i - \bar{y}))^2}{\sum_{i=1}^{N}(x_i - \bar{x})^2 * (y_i - \bar{y})^2} \right)$	[33][34]	*(2)*
$MSE = \dfrac{1}{N}\sum_{i=1}^{N}(x_i - y_i)^2$	[33][34]	*(3)*
$RMSE = \sqrt{\dfrac{1}{N}\sum_{i=1}^{N}(x_i - y_i)^2}$	[35]	*(4)*
$Error\ Mean = \dfrac{1}{N}\sum_{i=1}^{N}(x_i - y_i)$	[34]	*(5)*
$Error\ St.D = \sqrt{\sum_{i=1}^{N}\dfrac{(x_i - \bar{x}_i)^2}{N-1}}$	[36][37]	*(6)*

The proposed model is trained using the mean square error (MSE) and correlation coefficient (R). The trained network is switched to closed-loop mode and restructured to produce sophisticated multilayer predictions. The output y(t) of the network is used as feedback for the input. The trained artificial neural network (ANN) is transformed into a closed loop by establishing a feedback loop between the network output and the network input.
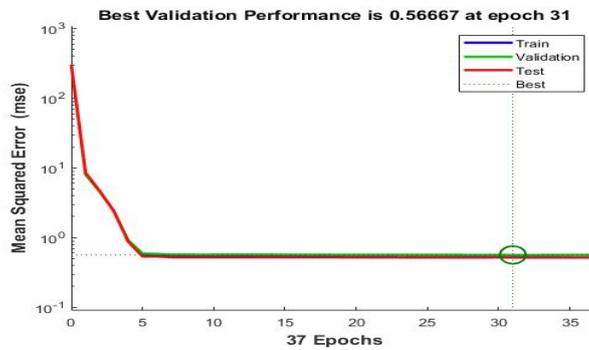

Figure 6. NARX Training Process Performance Chart

The performance, parameters, and explanatory graphs of the network were obtained through regression analysis and examination of the data obtained from the estimating equations using the NARX technique. Fig. 3 illustrates the results of the NARX-based wind speed estimates. In this figure, The number of iterations (37 levels) is shown on the X-axis, and the mean squared error (MSE) for each iteration is represented on the Y-axis in the graphic. The maximum number of learning periods was quite easy to determine experimentally by plotting the performance of the network using the Plot Performance function. After analyzing the learning curve of the network, it was found that the training of the network effectively stopped at iteration 37. The results of the training phase are shown in blue, those of the validation phase in green, and those of the testing phase in red. The point where the lines representing the training, validation, and testing results converge is the point of optimal performance. The training gain is a control parameter of the technique that was used to train the neural network (Mu). The best realization value was calculated

to be 31 and the performance value (Mu) 0.00100. The training, validation, and test values for this value are very close. This result shows that the ability of the network to predict wind speed is high. Figure 4 depicts the change in correlation coefficient between input (1) and error (1) as a function of time.
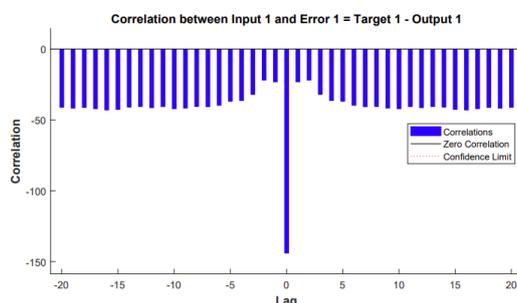

Figure 7. The input-Error Cross correlation

An ANN histogram is a useful tool for determining the frequency of mistakes. The error histogram displays the values of the error value (EV) and the frequency of the errors (EF). Based on the amount and variation of the mistakes, we may categorize the errors. The cumulative instantaneous variance of the training, validation, and testing errors is shown in Figure 5. A vertical line represents the imprecision of the zero points in this graph.
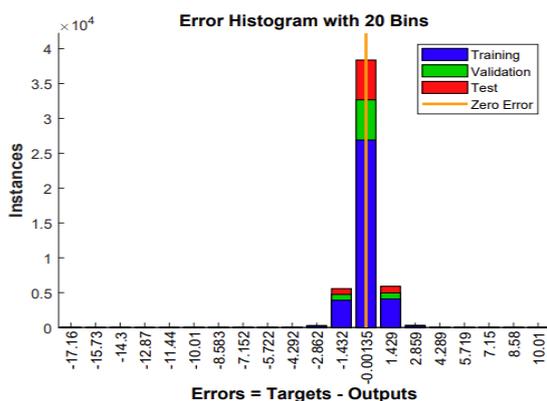
Figure 8. The error histogram of the NARX wind speed prediction model.
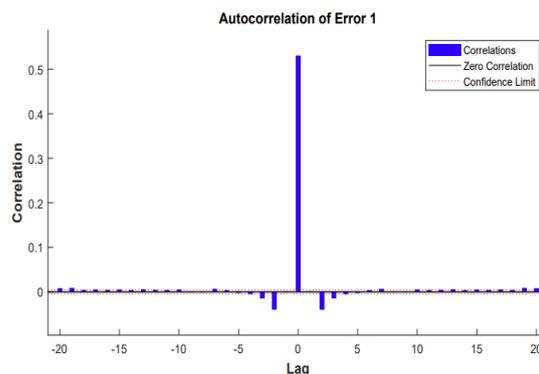
Figure 9. Prediction error plotted using autocorrelation.

The majority of the errors are zero, indicating a fairly strong predictive agreement. Here, the majority of errors (small errors) approaches zero in the training data sets, which account for 70% of all samples, and the test data sets, which account for 15% of all samples. Autocorrelation explains the relationship between prediction errors and time. For an error-free training model, the autocorrelation should be non-zero at zero lags. The autocorrelation function of errors is used to check the network performance in Figure 6. In this case, the autocorrelation of the errors is within the 95 percent confidence intervals.

Figure 10. Regression of all data, including training, validation, and test data

The regression coefficient R shows that there is a significant relationship between the two variables. The values calculated for training, validation, test, and all data are R = 0.98516, R = 0.98382, R = 98582, and R = 98505, respectively. The regression diagram in Figure 7 depicts the training, validation, and testing procedures between the input and target variables.
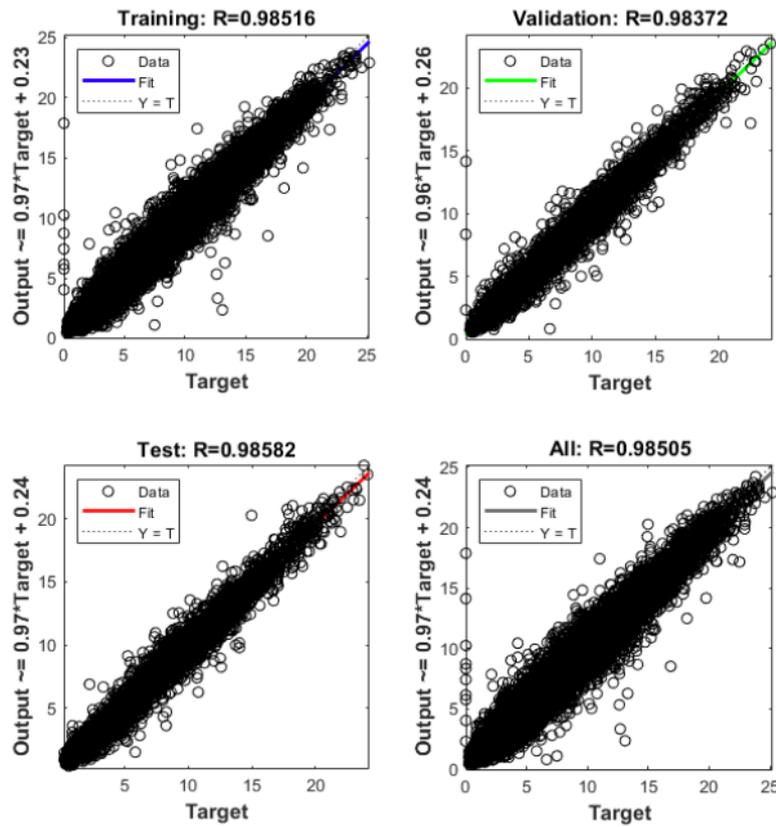
2.Results

Machine learning algorithms, such as artificial neural networks, are more accurate data-driven models that we use to address predicted difficulties. Using NARX, correlation and regression approaches, we can explain the relationships between the factors that influence wind speed. When we use the learning algorithm (LM) to train the wind speed model, we can find that the NARX model performs well in predicting the wind speed. The primary objective of this research is to assess the NARX neural network's efficacy utilizing a variety of different learning techniques and data splits for wind speed forecasting. Using the prediction algorithms from ANN, the average wind speed can be predicted 24 hours in advance. A sufficient wind database coupled with the performance of the NARX model results in an accurate short-term wind speed forecast (see Table 8). The MSE, RMSE, and R statistics all affect the performance of the NARX model. The results of the study show that the performance metrics are within the targeted accuracy range (Table 1).
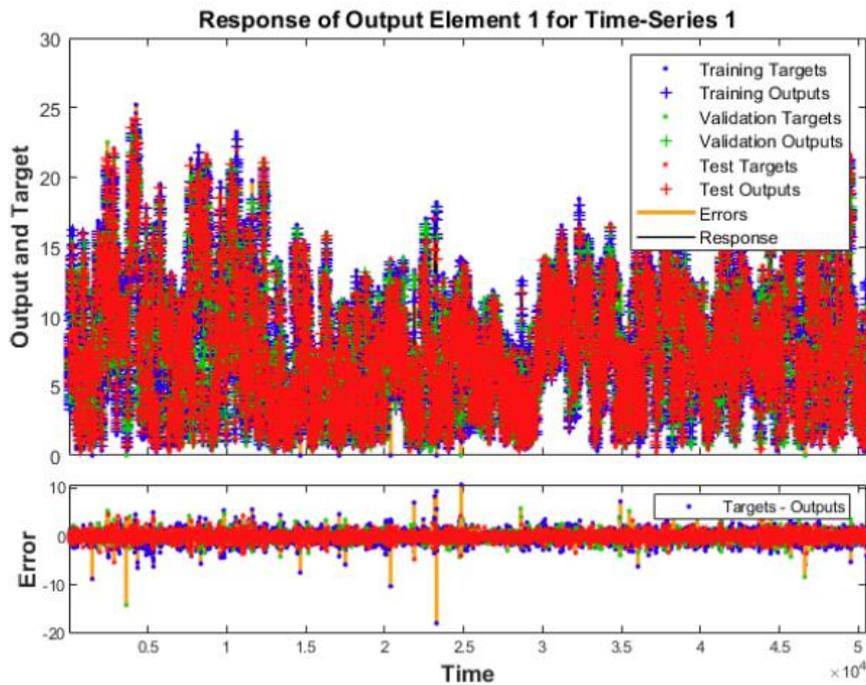
Figure 11. Data on wind speed were used to determine the reaction of the NARX prediction model.

Table 1 contains 11 different results for the performance of the proposed model. When it comes to training, validation, and testing, the second column gives the data separation rates for each of these three categories. The number of neurons in the hidden layer (NHN) is represented by the third column, while the delay time is shown by the fourth column (ND). Columns 5, 6, and 7 show both performance and regression values (R) for training, validation, and testing. Columns 8, 9, 10, and 11 show the metric calculations: Root mean square error (RMSE), mean square error (MSE), error mean (EM), and standard error variation (Error Std.). As the correlation coefficient (R) between -1 and 1, the contrast ratio between the results of the estimated and measured values can be defined as the difference between the two values. The fit coefficient (R) of a regression model indicates how well it fits the data. Each situation results in a large number of predicted and measured values centered around the diagonal line, as expected. Table 1 shows that all R values obtained during the training of the network are greater than 0.90, indicating that the output of the network is extremely close to the target and the model is good. After several trials with three learning algorithms and different architectures, the results showed that the NARX model had a performance training value of less than 0.60 and the results of all models were close to each other.

Table 4. Results obtained using the NARX model

Training Algorithms	NARX Architecture (Training,Validation,Testing)	NHN	ND	Training		Validation		Testing		RMSE	MSE	EM	Error Std
				Performance	*Regression*	*Performance*	*Regression*	*Performance*	*Regression*				
Levenberg-Marquardt	70%:15%:15% (35371: 7580:7580)	5	2	0.5548	0.9843	0.5191	0.9852	0.5329	0.9854	0.7390	0.5462	-0.0013	0.7391
		10	2	0.5283	0.9851	0.5699	0.9839	0.5625	0.9843	0.7346	0.5397	-0.0071	0.7346
		20	2	0.5273	0.9852	0.5253	0.9853	0.5383	0.9846	0.7271	0.5286	0.0266	0.7266
	60%:20%:20% (30319: 10106:10106)	5	2	0.5332	0.9849	0.5712	0.9837	0.5806	0.9838	0.7418	0.5503	0.0046	0.7418
		10	2	0.5459	0.9845	0.5339	0.9847	0.5073	0.9862	0.7319	0.5358	0.0034	0.7319
		20	2	0.5242	0.9853	0.5049	0.9855	0.5604	0.9843	0.7263	0.5276	-0.0235	0.7259
	50%:25%:25% (25265: 12633:12633)	5	2	0.5405	0.9849	0.5243	0.9848	0.5416	0.9848	0.7325	0.5366	-0.0021	0.7326
		10	2	0.5244	0.9851	0.5368	0.9849	0.5545	0.9846	0.7314	0.5350	-0.0159	0.7313
		20	2	0.5241	0.9852	0.5263	0.9853	0.5565	0.9843	0.7299	0.5327	0.0036	0.7299
Bayesian regularization	70%:15%:15% (35371: 7580:7580)	5	2	0.5318	0.985	NaN	NaN	0.5194	0.9855	0.7279	0.5299	0.0006	0.7279
		10	2	0.5269	0.9852	NaN	NaN	0.5292	0.9851	0.7262	0.5273	0.0029	0.7262
		20	2	0.5122	0.9856	NaN	NaN	0.5271	0.9848	0.7172	0.5144	-0.00003	0.7172
	60%:20%:20% (30319: 10106:10106)	5	2	0.5309	0.9850	NaN	NaN	0.5377	0.9846	0.7296	0.5323	0.0011	0.7296
		10	2	0.5269	0.9852	NaN	NaN	0.5154	0.9851	0.7243	0.5246	-0.0019	0.7243
		20	2	0.5093	0.9856	NaN	NaN	0.5526	0.9843	0.7197	0.5180	0.0025	0.7197
	50%:25%:25% (25265: 12633:12633)	5	2	0.5385	0.9848	NaN	NaN	0.5194	0.9852	0.7306	0.5337	-0.0024	0.7306
		10	2	0.5215	0.9852	NaN	NaN	0.5299	0.9851	0.7236	0.5236	0.0019	0.7236
		20	2	0.5076	0.9856	NaN	NaN	0.5392	0.9847	0.7180	0.5155	0.0012	0.7180
Scaled conjugate gradient	70%:15%:15% (35371: 7580:7580)	5	2	0.5903	0.9833	0.5737	0.9838	0.6307	0.9820	0.7706	0.5939	-0.0054	0.7706
		10	2	0.5698	0.9839	0.5231	0.9854	0.5102	0.9855	0.7442	0.5538	0.0009	0.7442
		20	2	0.5756	0.9838	0.5228	0.9851	0.5514	0.9843	0.7510	0.5640	-0.0001	0.7510
	60%:20%:20% (30319: 10106:10106)	5	2	0.5931	0.9832	0.5739	0.9839	0.6135	0.9826	0.7702	0.5933	0.0071	0.7702
		10	2	0.5549	0.9843	0.5907	0.9830	0.5967	0.9835	0.7552	0.5704	-0.0012	0.7552
		20	2	0.5582	0.9843	0.5838	0.9833	0.5385	0.984	0.7479	0.5594	0.0029	0.7479
	50%:25%:25% (25265: 12633:12633)	5	2	0.5480	0.9843	0.5661	0.9842	0.5682	0.9840	0.7467	0.5576	0.0003	0.7467
		10	2	0.5776	0.9836	0.5063	0.9857	0.5740	0.9838	0.7475	0.5588	-0.0041	0.7475
		20	2	0.5753	0.9838	0.5486	0.9845	0.5732	0.9837	0.7537	0.5681	-0.0141	0.7536

3.Conclusion

Wind speed forecasting (WSF) is critical in wind energy production, which is one of the world's fastest increasing renewable energy sources. Accurate wind speed estimate is critical for improving and optimizing wind energy output. Long-term velocity forecasting, in particular, may assist us in extending real-time wind farm operations and managing wind turbine model projections. Predicting the behavior of wind resources can be useful for energy managers, regulators, and power traders, as it can provide them with valuable information. In addition, the prediction data can be used to operate, repair, and replace wind turbines and substations. The results and accuracy of predictions for WSF are of great importance for the performance of learning algorithms and the NARX model. Due to the excellent statistical properties of artificial neural networks, which have been widely used by academics in forecasting and prediction studies in recent years, a WSF model was constructed in this study. In the study, data from 50531 observations covering the period 01/01/2018, 00:00–31/12/2018, 23:50 were analyzed using the MATLAB R2021a program. The number of hidden layers ranges from 5–20, and the network was trained using Levenberg-Marquardt, Bayesian regularization, and Scaled conjugate gradient.

As a result of the study, it was found that when comparing the predicted values generated by artificial neural networks with the real values of WSF, the corresponding values are quite close and the MSE value used as the performance requirement is sufficiently low. These results show that the proposed model is effective in predicting wind speed as it provides robust statistical results. Although many research and development studies have been conducted in this field, the improvement of wind speed estimation using different learning algorithms, datasets, and neuron numbers is considered one of the most important findings of this study. On the other hand, it is believed that this study will help practitioners obtain useful information about the NARX model from the more general conceptual wind speed estimation, and it can be used to predict future daily WSF values.

References

[1]   H. Calik, N. Ak, and I. Guney, "Artificial NARX Neural Network Model of Wind Speed: Case of Istanbul-Avcilar," *Journal of Electrical Engineering and Technology*, vol. 16, no. 5, pp. 2553–2560, Sep. 2021, doi: 10.1007/s42835-021-00763-z.

[2]   M. R. C. Qazani, H. Asadi, C. P. Lim, S. Mohamed, and S. Nahavandi, "Prediction of Motion Simulator Signals Using Time-Series Neural Networks," *IEEE Transactions on Aerospace and Electronic Systems*, vol. 57, no. 5, pp. 3383–3392, Oct. 2021, doi: 10.1109/TAES.2021.3082662.

[3]   R. Sarkar, S. Julai, S. Hossain, W. T. Chong, and M. Rahman, "A comparative study of activation functions of NAR and NARX neural network for long-term wind speed forecasting in Malaysia," *Mathematical Problems in Engineering*, vol. 2019, 2019, doi: 10.1155/2019/6403081.

[4]   I. L. R. Gomes, R. Melicio, V. M. F. Mendes, and H. M. I. Pousinho, "Wind Power with Energy Storage Arbitrage in Day-ahead Market by a Stochastic MILP Approach," *Logic Journal of the IGPL*, vol. 28, no. 4, pp. 570–582, Jul. 2020, doi: 10.1093/JIGPAL/JZZ054.

[5]   I. D. Margaris, S. A. Papathanassiou, N. D. Hatziargyriou, A. D. Hansen, and P. Sorensen, "Frequency Control in Autonomous Power Systems with High Wind Power Penetration," *IEEE Transactions on Sustainable Energy*, vol. 3, no. 2, pp. 189–199, Apr. 2012, doi: 10.1109/TSTE.2011.2174660.

[6]   L. Holdsworth, J. B. Ekanayake, and N. Jenkins, "Power system frequency response from fixed speed and doubly fed induction generator-based wind turbines," *Wind Energy*, vol. 7, no. 1, pp. 21–35, Jan. 2004, doi: 10.1002/WE.105.

[7]   Y. L. Chen, Y. P. Liu, and X. F. Sun, "The Active Frequency Control Strategy of the Wind Power Based on Model Predictive Control," *Complexity*, vol. 2021, 2021, doi: 10.1155/2021/8834234.

[8]   F. Fazelpour, • Negar Tarashkar, and M. A. Rosen, "Short-term wind speed forecasting using artificial neural networks for Tehran, Iran," *International Journal of Energy and Environmental Engineering*, vol. 7, doi: 10.1007/s40095-016-0220-6.

[9]   Y. Raptodimos and I. Lazakis, "Application of NARX neural network for predicting marine engine performance parameters," *https://doi.org/10.1080/17445302.2019.1661619*, vol. 15, no. 4, pp. 443–452, Apr. 2019, doi: 10.1080/17445302.2019.1661619.

[10]   H. Cai, Z. Wu, · Chao Huang, and · Daizheng Huang, "Wind Power Forecasting Based on Ensemble Empirical Mode Decomposition with Generalized Regression Neural Network Based on Cross-Validated Method," *Journal of Electrical Engineering & Technology*, vol. 14, no. 3, pp. 1823–1829, 2019, doi: 10.1007/s42835-019-00186-x.

[11]   L. T. Le, G. Lee, K. S. Park, and H. Kim, "Neural network-based fuel consumption estimation for container ships in Korea," *https://doi.org/10.1080/03088839.2020.1729437*, vol. 47, no. 5, pp. 615–632, Jul. 2020, doi: 10.1080/03088839.2020.1729437.

[12]   Y. Xiu and W. Zhang, "Multivariate Chaotic Time Series Prediction Based on NARX Neural Networks," 2017.

[13]   P. C. Soman, "An Adaptive NARX Neural Network Approach for Financial Time Series Prediction," 2008.

[14]   O. Bektas, J. A. Jones, and warwickacuk JAJones, "NARX Time Series Model for Remaining Useful Life Estimation of Gas Turbine Engines."

[15]   M. Abouheaf, W. Gueaieb, and A. Sharaf, "Model-free adaptive learning control scheme for wind turbines with doubly fed induction generators," *IET Renewable Power Generation*, vol. 12, no. 14, pp. 1675–1686, Oct. 2018, doi: 10.1049/IET-RPG.2018.5353.

[16]   A. B. Asghar and X. Liu, "Adaptive neuro-fuzzy algorithm to estimate effective wind speed and optimal rotor speed for variable-speed wind turbine," *Neurocomputing*, vol. 272, pp. 495–504, Jan. 2018, doi: 10.1016/J.NEUCOM.2017.07.022.

[17]   I. Delgado and M. Fahim, "Wind Turbine Data Analysis and LSTM-Based Prediction in SCADA System," *Energies 2021, Vol. 14, Page 125*, vol. 14, no. 1, p. 125, Dec. 2020, doi: 10.3390/EN14010125.

[18]   "Wind Turbine Scada Dataset | Kaggle." https://www.kaggle.com/datasets/berkerisen/wind-turbine-scada-dataset (accessed Mar. 24, 2022).

[19]   M. Wilkinson, B. Darnell, T. van Delft, and K. Harman, "Comparison of methods for wind turbine condition monitoring with SCADA data," *IET Renewable Power Generation*, vol. 8, no. 4, pp. 390–397, May 2014, doi: 10.1049/IET-RPG.2013.0318.

[20]   P. Marti-Puig, A. Blanco-M, M. Serra-Serra, and J. Solé-Casals, "Wind turbine prognosis models based on scada data and extreme learning machines," *Applied Sciences (Switzerland)*, vol. 11, no. 2, pp. 1–20, Jan. 2021, doi: 10.3390/app11020590.

[21]   Y. Metelkin, Y. Khitskova, and K. Makoviy, "Predicting Load in Datacenters Using NARX Model," 2021. doi: 10.1109/ITNT52450.2021.9649034.

[22]   F. di Nunno, F. Granata, R. Gargano, and G. de Marinis, "Forecasting of extreme storm tide events using NARX neural network-based models," *Atmosphere (Basel)*, vol. 12, no. 4, p. 512, Apr. 2021, doi: 10.3390/atmos12040512.

[23]   F. di Nunno, F. Granata, R. Gargano, and G. de Marinis, "Prediction of spring flows using nonlinear autoregressive exogenous (NARX) neural network models," *Environmental Monitoring and Assessment*, vol. 193, no. 6, pp. 1–17, Jun. 2021, doi: 10.1007/S10661-021-09135-6/TABLES/3.

[24]   S. Kolachalama and H. Malik, "A NARX Model to Predict Cabin Air Temperature to Ameliorate HVAC Functionality," *Vehicles 2021, Vol. 3, Pages 872-889*, vol. 3, no. 4, pp. 872–889, Dec. 2021, doi: 10.3390/VEHICLES3040052.

[25]   S. M. Guzman, J. O. Paz, M. L. M. Tagert, and A. E. Mercer, "Evaluation of Seasonally Classified Inputs for the Prediction of Daily Groundwater Levels: NARX Networks Vs Support Vector Machines," *Environmental Modeling and Assessment*, vol. 24, no. 2, pp. 223–234, Apr. 2019, doi: 10.1007/S10666-018-9639-X/FIGURES/9.

[26]   M. A. A. Desouky and O. Abdelkhalik, "Wave prediction using wave rider position measurements and NARX network in wave energy conversion," *Applied Ocean Research*, vol. 82, pp. 10–21, Jan. 2019, doi: 10.1016/J.APOR.2018.10.016.

[27]   W. Wang, J. Taylor, and B. Bala, "Exploiting the Power of Levenberg-Marquardt Optimizer with Anomaly Detection in Time Series," Nov. 2021, doi: 10.48550/arxiv.2111.06060.

[28]   M. Kayri, "Predictive Abilities of Bayesian Regularization and Levenberg–Marquardt Algorithms in Artificial Neural Networks: A Comparative Empirical Study on Social Data," *Mathematical and Computational Applications 2016, Vol. 21, Page 20*, vol. 21, no. 2, p. 20, May 2016, doi: 10.3390/MCA21020020.

[29]   M. F. Møller, "A scaled conjugate gradient algorithm for fast supervised learning," *Neural Networks*, vol. 6, no. 4, pp. 525–533, Jan. 1993, doi: 10.1016/S0893-6080(05)80056-5.

[30]   B. Mohammadi, S. Mehdizadeh, F. Ahmadi, N. T. T. Lien, N. T. T. Linh, and Q. B. Pham, "Developing hybrid time series and artificial intelligence models for estimating air temperatures," *Stochastic Environmental Research and Risk Assessment*, vol. 35, no. 6, pp. 1189–1204, Jun. 2021, doi: 10.1007/S00477-020-01898-7/TABLES/6.

[31]   P. Coulibaly, F. Anctil, R. Aravena, and B. Bobée, "Artificial neural network modeling of water table depth fluctuations," *Water Resources Research*, vol. 37, no. 4, pp. 885–896, Apr. 2001, doi: 10.1029/2000WR900368.

[32]   F. di Nunno and F. Granata, "Groundwater level prediction in Apulia region (Southern Italy) using NARX neural network," *Environmental Research*, vol. 190, p. 110062, Nov. 2020, doi: 10.1016/J.ENVRES.2020.110062.

[33]   M. Mostafaei, H. Javadikia, and L. Naderloo, "Modeling the effects of ultrasound power and reactor dimension on the biodiesel production yield: Comparison of prediction abilities between response surface methodology (RSM) and adaptive neuro-fuzzy inference system (ANFIS)," *Energy*, vol. 115, pp. 626–636, Nov. 2016, doi: 10.1016/j.energy.2016.09.028.

[34]   D. Chicco, M. J. Warrens, and G. Jurman, "The coefficient of determination R-squared is more informative than SMAPE, MAE, MAPE, MSE and RMSE in regression analysis evaluation," *PeerJ Computer Science*, vol. 7, pp. 1–24, 2021, doi: 10.7717/PEERJ-CS.623.

[35]   T. Chai and R. R. Draxler, "Root mean square error (RMSE) or mean absolute error (MAE)? -Arguments against avoiding RMSE in the literature," *Geoscientific Model Development*, vol. 7, no. 3, pp. 1247–1250, 2014, doi: 10.5194/gmd-7-1247-2014.

[36]   D. J. Biau, "In brief: Standard deviation and standard error," *Clinical Orthopaedics and Related Research*, vol. 469, no. 9, pp. 2661–2664, 2011, doi: 10.1007/s11999-011-1908-9.

[37]   M. Mostafaei, "ANFIS models for prediction of biodiesel fuels cetane number using desirability function," *Fuel*, vol. 216, pp. 665–672, Mar. 2018, doi: 10.1016/j.fuel.2017.12.025.

[38]   "Wind Turbine Scada Dataset | Kaggle." https://www.kaggle.com/datasets/berkerisen/wind-turbine-scada-dataset (accessed Mar. 28, 2022).

Current Debates on Natural and Engineering Sciences 3